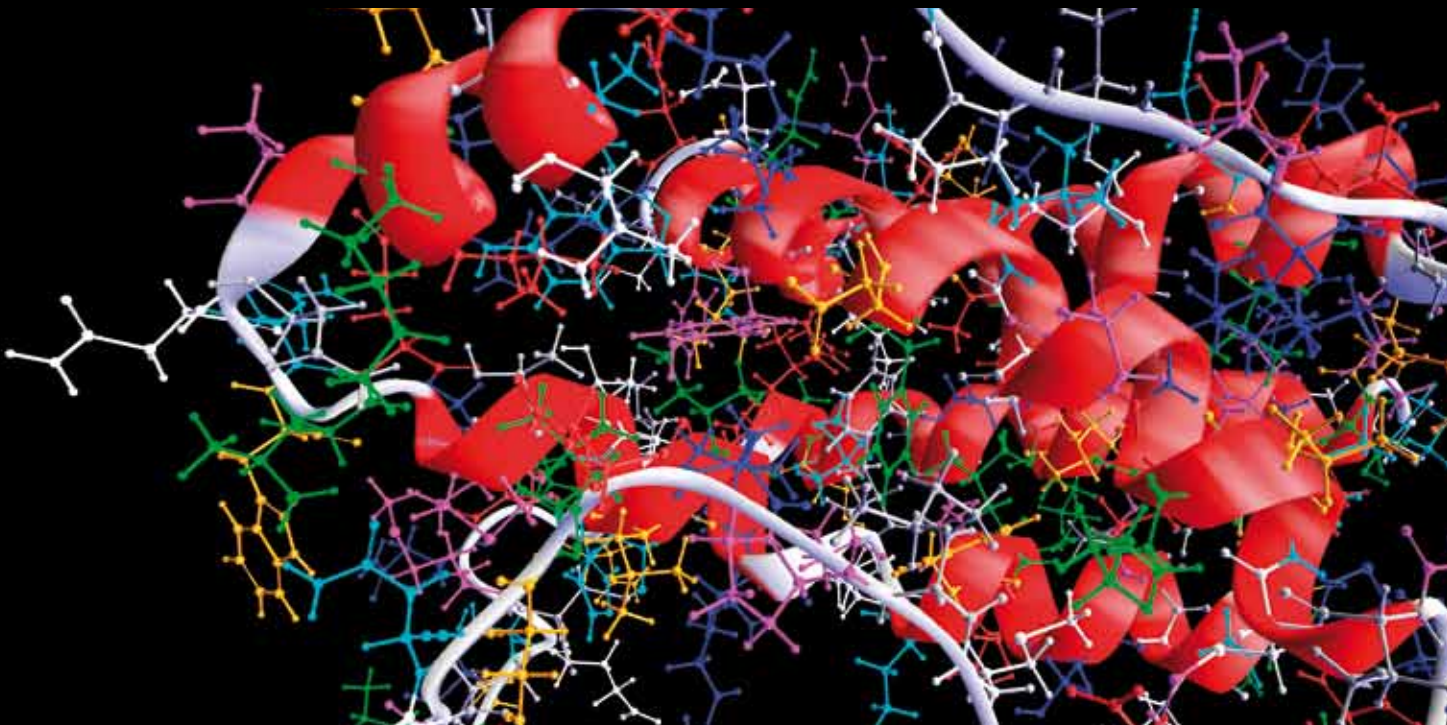


COMPUTATIONAL AND MATHEMATICAL METHODS IN MEDICINE

# COMPUTATIONAL ANALYSIS of CARDIOVASCULAR HEMODYNAMICS

GUEST EDITORS: EUN BO SHIM, THOMAS HELDT, AKIRA AMANO, AND KYEHAN RHEE





---

# **Computational Analysis of Cardiovascular Hemodynamics**

Computational and Mathematical Methods in Medicine

---

# **Computational Analysis of Cardiovascular Hemodynamics**

Guest Editors: Eun Bo Shim, Thomas Heldt, Akira Amano,  
and Kyehan Rhee



---

Copyright © 2012 Hindawi Publishing Corporation. All rights reserved.

This is a special issue published in “Computational and Mathematical Methods in Medicine.” All articles are open access articles distributed under the Creative Commons Attribution License, which permits unrestricted use, distribution, and reproduction in any medium, provided the original work is properly cited.

## Editorial Board

Zvia Agur, Israel  
Emil Alexov, USA  
Gary C. An, USA  
Georgios Archontis, Cyprus  
Pascal Auffinger, France  
Facundo Ballester, Spain  
Dimos Baltas, Germany  
Chris Bauch, Canada  
Maxim Bazhenov, USA  
Niko Beerenwinkel, Switzerland  
Philip Biggin, UK  
Michael Breakspear, Australia  
Thierry Busso, France  
Carlo Cattani, Italy  
Bill Crum, UK  
Timothy David, New Zealand  
Gustavo Deco, Spain  
Carmen Domene, UK  
Wim Van Drongelen, USA  
Frank Emmert-Streib, UK  
Ricardo Femat, Mexico  
Alfonso T. García-Sosa, Estonia  
Kannan Gunasekaran, USA

Damien R. Hall, Japan  
William F. Harris, South Africa  
Vassily Hatzimanikatis, USA  
Volkhard Helms, Germany  
J.-H. S. Hofmeyr, South Africa  
Seiya Imoto, Japan  
Bleddyn Jones, UK  
Lawrence A. Kelley, UK  
Lev Klebanov, Czech Republic  
Ina Koch, Germany  
David Liley, Australia  
Quan Long, UK  
Yoram Louzoun, Israel  
Jianpeng Ma, USA  
C.-M. C. Ma, USA  
Reinoud Maex, France  
Francois Major, Canada  
Simeone Marino, USA  
Ali Masoudi-Nejad, Iran  
Ramit Mehr, Israel  
Seth Michelson, USA  
Michele Migliore, Italy  
Karol Miller, Australia

Ernst Niebur, USA  
Kazuhisa Nishizawa, Japan  
Martin Nowak, USA  
Markus Owen, UK  
Hugo Palmans, UK  
Lech S. Papiez, USA  
Jean Pierre Rospars, France  
David James Sherman, France  
Sivabal Sivaloganathan, Canada  
Stephen W. Smye, UK  
Merryn H. Tawhai, New Zealand  
Elisabeth Tillier, Canada  
Nestor V. Torres, Spain  
Anna Tramontano, Italy  
Nelson J. Trujillo-Barreto, Cuba  
Kutlu O. Ulgen, Turkey  
Nagarajan Vaidehi, USA  
Edelmira Valero, Spain  
Jinliang Wang, UK  
Jacek Waniewski, Poland  
Guang Wu, China  
Henggui Zhang, UK

# Contents

**Computational Analysis of Cardiovascular Hemodynamics**, Eun Bo Shim, Thomas Heldt, Akira Amano, and Kyeihan Rhee

Volume 2012, Article ID 260396, 2 pages

**A Numerical Method of Reduced Complexity for Simulating Vascular Hemodynamics Using Coupled 0D Lumped and 1D Wave Propagation Models**, Wilco Kroon, Wouter Huberts, Marielle Bosboom, and Frans van de Vosse

Volume 2012, Article ID 156094, 10 pages

**Relationship between Concentration Difference of Different Density Lipoproteins and Shear Stress in Atherosclerosis**, Wei Meng, Fengxu Yu, Huaqing Chen, Jianmin Zhang, Eryong Zhang, Yingqiang Guo, and Yingkang Shi

Volume 2012, Article ID 135256, 7 pages

**Therapeutic Vascular Compliance Change May Cause Significant Variation in Coronary Perfusion: A Numerical Study**, S. Nobari, R. Mongrain, E. Gaillard, R. Leask, and R. Cartier

Volume 2012, Article ID 791686, 10 pages

**Hemodynamics of Cerebral Aneurysms: Computational Analyses of Aneurysm Progress and Treatment**, Woowon Jeong and Kyeihan Rhee

Volume 2012, Article ID 782801, 11 pages

**Finite Element Modelling of Pulsatile Blood Flow in Idealized Model of Human Aortic Arch: Study of Hypotension and Hypertension**, Paritosh Vasava, Payman Jalali, Mahsa Dabagh, and Pertti J. Kolari

Volume 2012, Article ID 861837, 14 pages

**Computational Fluid Dynamics Analysis of the Effect of Plaques in the Left Coronary Artery**, Thanapong Chaichana, Zhonghua Sun, and James Jewkes

Volume 2012, Article ID 504367, 9 pages

**Weighted Least-Squares Finite Element Method for Cardiac Blood Flow Simulation with Echocardiographic Data**, Fei Wei, John Westerdale, Eileen M. McMahon, Marek Belohlavek, and Jeffrey J. Heys

Volume 2012, Article ID 371315, 9 pages

**The Need of Slanted Side Holes for Venous Cannulae**, Joong Yull Park

Volume 2012, Article ID 854938, 7 pages

## Editorial

# Computational Analysis of Cardiovascular Hemodynamics

Eun Bo Shim,<sup>1</sup> Thomas Heldt,<sup>2</sup> Akira Amano,<sup>3</sup> and Kyeihan Rhee<sup>4</sup>

<sup>1</sup>Kangwon National University, Chuncheon-si 200-701, Republic of Korea

<sup>2</sup>Massachusetts Institute of Technology, Cambridge, MA 02139, USA

<sup>3</sup>Ritsumeikan University, Kyoto 603-8577, Japan

<sup>4</sup>Myongji University, Yongin-si 449-728, Republic of Korea

Correspondence should be addressed to Eun Bo Shim, ebshim@kangwon.ac.kr

Received 29 July 2012; Accepted 29 July 2012

Copyright © 2012 Eun Bo Shim et al. This is an open access article distributed under the Creative Commons Attribution License, which permits unrestricted use, distribution, and reproduction in any medium, provided the original work is properly cited.

## 1. Introduction

The human body requires a complex circulatory system to supply nutrients to, and to remove metabolic waste products from, its tissues. Given this primary purpose, circulatory function is closely related to the hemodynamic characteristics of blood vessels. This includes not only macroscale fluid dynamics, but also mass transfer in the microvasculature. Many experimental and clinical studies have examined these characteristics of vascular function. Over the past 50 years, mathematical modeling has become a powerful adjunct to such studies, as modeling provides a rational framework within which to analyze the cardiovascular system.

Many mathematical models of the cardiovascular system have been developed since Grodins [1] published the first system-level dynamic cardiovascular model in 1959. Today, models of cardiovascular function exist on nearly every biological time and length scale. The design of such models naturally depends on the purpose of the underlying scientific questions, and the methodologies employed vary accordingly. Some subjects that have been extensively studied include hemodynamic models of specific vascular beds, such as the coronary or cerebral circulation [2]; the distributed impedance of the arterial and pulmonary trees [3]; lumped models of the integrated cardiovascular system [4]; detailed models of the fluid-structure interaction in specific vascular beds [5]. This special issue focuses on physiological and computational issues as they relate to the development of vascular models.

## 2. Brief Introduction of the Papers

Hemodynamic modeling draws upon the interdisciplinary field of vascular physiology, system engineering, fluid

dynamics, and computer science. While the papers in this special issue reflect the broad constituency of this field, the main focus rests with the computational analysis of hemodynamic models.

The contribution by W. Jeong and K. Rhee reviews models dedicated to understanding the development, progression, and rupture of cerebral aneurysms. S. Nobari and coworkers utilize fluid-structure interaction models to study the effect of increased vascular stiffness on coronary blood flow. The contribution by J. Y. Park addresses the practical question of how to design a venous cannula for optimized flow. The study by P. Vasava and co-workers focuses on the variation in wall shear stress with hypo- and hypertension in a finite-element model of the aortic arch. W. Meng and coworkers model the effects of varying low-density lipoprotein (LDL) and high-density lipoprotein (HDL) concentrations on the wall shear stress of the carotid bifurcation. W. Kroon and coworkers present a novel scheme to couple one- and zero-dimensional wave propagation models. Finally, I. Chaichana, Z. Sun, and J. Jewkes analyze the effects of simulated plaques in a model of the left coronary artery.

## 3. Concluding Remark

Modeling studies like these provide an integrated framework to understanding vascular function. Research in computational modeling of the circulation will increase our understanding of normal vascular physiology and its pathophysiological aberrations in disease. The main motivation of the special issue was to highlight current and original research in computational modeling of cardiovascular hemodynamics and thus to encourage the applications of computational

models of cardiovascular hemodynamics to clinical cases. We think the contributions in this issue achieve this goal.

*Eun Bo Shim  
Thomas Heldt  
Akira Amano  
Kyeihan Rhee*

## References

- [1] F. S. Grodins, "Integrative cardiovascular physiology: a mathematical synthesis of cardiac and blood vessel hemodynamics," *The Quarterly Review of Biology*, vol. 34, no. 2, pp. 93–116, 1959.
- [2] T. Ejaz, T. Takemae, Y. Kosugi, and M. Hongo, "The high zero-flow pressure phenomenon in coronary circulation: a simulation study," *Frontiers of Medical and Biological Engineering*, vol. 11, no. 4, pp. 335–340, 2002.
- [3] J. R. LaCourse, G. Mohanakrishnan, and K. Sivaprasad, "Simulations of arterial pressure pulses using a transmission line model," *Journal of Biomechanics*, vol. 19, no. 9, pp. 771–780, 1986.
- [4] H. H. Hardy, R. E. Collins, and R. E. Calvert, "A digital computer model of the human circulatory system," *Medical and Biological Engineering and Computing*, vol. 20, no. 5, pp. 550–564, 1982.
- [5] M. R. Kaazempur-Mofrad, M. Bathe, H. Karcher et al., "Role of simulation in understanding biological systems," *Computers and Structures*, vol. 81, no. 8–11, pp. 715–726, 2003.

## Research Article

# A Numerical Method of Reduced Complexity for Simulating Vascular Hemodynamics Using Coupled 0D Lumped and 1D Wave Propagation Models

Wilco Kroon,<sup>1,2</sup> Wouter Huberts,<sup>2,3</sup> Marielle Bosboom,<sup>2,3</sup> and Frans van de Vosse<sup>3</sup>

<sup>1</sup>Department of Surgery, Maastricht University Medical Center, 6202 AZ Maastricht, The Netherlands

<sup>2</sup>Department of Biomedical Engineering, Maastricht University, P.O. Box 616, 6200 MD Maastricht, The Netherlands

<sup>3</sup>Department of Biomedical Engineering, Eindhoven University of Technology, 5600 MB Eindhoven, The Netherlands

Correspondence should be addressed to Wilco Kroon, wilco.kroon@maastrichtuniversity.nl

Received 31 August 2011; Revised 11 December 2011; Accepted 13 January 2012

Academic Editor: Akira Amano

Copyright © 2012 Wilco Kroon et al. This is an open access article distributed under the Creative Commons Attribution License, which permits unrestricted use, distribution, and reproduction in any medium, provided the original work is properly cited.

A computational method of reduced complexity is developed for simulating vascular hemodynamics by combination of one-dimensional (1D) wave propagation models for the blood vessels with zero-dimensional (0D) lumped models for the microcirculation. Despite the reduced dimension, current algorithms used to solve the model equations and simulate pressure and flow are rather complex, thereby limiting acceptance in the medical field. This complexity mainly arises from the methods used to combine the 1D and the 0D model equations. In this paper a numerical method is presented that no longer requires additional coupling methods and enables random combinations of 1D and 0D models using pressure as only state variable. The method is applied to a vascular tree consisting of 60 major arteries in the body and the head. Simulated results are realistic. The numerical method is stable and shows good convergence.

## 1. Introduction

Blood flow involves pressure and flow waves that propagate through the vascular system. As a compromise between computational demand and physical detail, one-dimensional (1D) network models have been used to study pressure and flow waveforms under normal and pathological conditions [1]. This modeling approach has been applied to the systemic arterial system [2–6], the coronary tree [7, 8], and the cerebral vascular tree [9, 10].

These 1D network models consist of elements that locally describe the relation between pressure and flow. Relations between pressure, area, and flow in the blood vessels are given by the 1D wave propagation equations, that is, 1D partial differential equations of mass and momentum which are derived by integrating the Navier-Stokes equation over the cross-sectional area of the blood vessel [11]. As vessel caliber decreases and the number of vessels increases towards the periphery, a point is reached where it is no longer attainable to model the vessels individually. At this point the vasculature

is truncated and contribution of the distal vasculature to pressure and flow is described by 0D lumped models, such as the windkessel model [5, 6, 12] or the structured tree model [3].

To solve the system of equations derived from the 0D and 1D models and simulate propagation of pressure and flow waves through the vascular system, various, rather complex, algorithms exist. Regarding the 1D wave propagation equations, all numerical methods start from the same relation between pressure, area, and flow or cross-sectional mean velocity. First differences between the numerical methods arise with the state variables chosen to remain. With area and pressure related via a constitutive relation of the vessel wall, the result is either a pressure-flow [2, 8], area-velocity [13], area-flow [3], or pressure-velocity formulation [9, 11, 14, 15]. A second source of differences is the choice for spatial discretization of the equations. Methods include finite difference [3, 8] and spectral/finite element schemes [2, 13]. The result is a set of ordinary differential equations in which the state variables have to be solved in time. Thirdly, different

methods are used to enforce continuity of pressure and flow across vessel bifurcations and at the interface between the vessels and the periphery. Methods include weak coupling of 0D and 1D equations [15, 16], computation of Riemann invariants [9, 14], or adding penalty equations [2].

The contribution of this study is to develop a simplified numerical method in which pressure is the only state variable. In this approach, the 1D wave propagation and 0D lumped model equations are cast into the same form. As such, 1D and 0D models are combined without the need to specify additional coupling equations. This allows for flexible model building from 0D and 1D elements for simulation of pressure and flow in a vascular network. For illustration, the numerical method proposed is applied to simulate pressure and flow waveforms in a vascular tree composed of 60 major arteries in the body and the head.

## 2. Method

**2.1. Pressure-Flow Relation in Large Blood Vessels (1D).** In large arteries, blood pressure  $p$  (Pa), blood flow  $q$  ( $\text{m}^3 \cdot \text{s}^{-1}$ ), wall shear stress  $\tau_w$  (Pa), and vessel cross-sectional area  $A$  ( $\text{m}^2$ ) are related by 1D equations of mass and momentum. When neglecting leakage through the vessel wall as well as gravitational forces, the balance of mass and momentum is given by (derivations can be found in, e.g., Hughes and Lubliner [11] and Van de Vosse and Stergiopoulos [1])

$$C_A \frac{\partial p}{\partial t} + \frac{\partial q}{\partial z} = 0, \quad \text{with } C_A = \frac{\partial A}{\partial p}, \quad (1)$$

$$\frac{\rho}{A} \left( \frac{\partial q}{\partial t} + \frac{\partial}{\partial z} \left( \delta \frac{q^2}{A} \right) \right) + \frac{\partial p}{\partial z} = \frac{2}{a} \tau_w. \quad (2)$$

In this  $(p, q, A)$  formulation,  $z$  (m) denotes the coordinate along the vessel axis,  $a = \sqrt{A/\pi}$  (m) denotes the vessel radius,  $C_A$  ( $\text{m}^2 \cdot \text{Pa}^{-1}$ ) denotes the vessel area-compliance, and  $\rho$  ( $\text{kg} \cdot \text{m}^{-3}$ ) denotes the blood density.

Wall shear stress  $\tau_w$  and constant  $\delta$  in (2) are estimated by assuming a velocity profile. For the choice of the velocity profile, several options are possible [1]. In this study approximate velocity profiles are assumed [2]. Using approximate velocity profiles, the wall shear stress is given by

$$\tau_w = -\frac{2\eta}{(1-\zeta_c)a} \frac{q}{A} + \frac{a}{4}(1-\zeta_c) \frac{\partial p}{\partial z}, \quad (3)$$

$$\text{with } \zeta_c = \left( \max \left[ 0, 1 - \frac{\sqrt{2}}{\alpha} \right] \right)^2.$$

with  $\eta$  ( $\text{Pa} \cdot \text{s}$ ) the blood viscosity,  $\zeta_c$  the fraction of cross-sectional area with inertia dominated flow, and  $\alpha = \sqrt{2A_0\rho/T\eta}$  the Womersley number that includes the duration of the cardiac cycle  $T$  [s], and vessel cross-sectional area  $A_0 = \pi a_0^2$  at reference pressure  $p_0$ . For approximate velocity profiles, constant  $\delta$  is given by

$$\delta = \frac{2 - 2\zeta_c(1 - \ln \zeta_c)}{(1 - \zeta_c)^2}. \quad (4)$$

The mass and momentum equations are completed with expressions for area ( $A$ ) and area compliance ( $C_A$ ) as a function of pressure. In this study, a nonlinear elastic vessel wall is assumed with pressure dependency of the area compliance  $C_A$  given by

$$C_A = C_A^p C_A^a, \quad \text{with } C_A^p = \beta_1 + \beta_2 \left( 1 + \left( \frac{p - p_1}{p_2} \right)^2 \right)^{-1},$$

$$C_A^a = \frac{2\pi(1 - \mu^2)a_0^3}{hE}, \quad (5)$$

where  $p_1$ ,  $p_2$ ,  $\beta_1$ , and  $\beta_2$  specify the pressure dependency of area-compliance (function  $C_A^p$  from Langewouters et al. [17]). Poisson ratio  $\mu$ , Youngs modulus  $E$ , and wall thickness  $h$  specify the radius dependency of the area compliance (function  $C_A^a$  from Bessems et al. [2]). An expression for the pressure dependency of cross-sectional area is obtained by integrating the area compliance with respect to pressure.

**2.2. Pressure-Flow Relation in the Periphery (0D).** The contribution of the peripheral vasculature at each arterial terminus is lumped in a three-element windkessel model [6, 18] (Figure 1(c)). Usually a single differential equation is derived that relates pressure  $p$  and flow  $q$  at the entrance of the Windkessel [2, 8, 10]:

$$\frac{\partial q}{\partial t} = \frac{1}{Z} \frac{\partial p}{\partial t} + \frac{p}{ZRC} - \left( 1 + \frac{Z}{R} \right) \frac{q}{ZC}, \quad (6)$$

with  $Z$  the characteristic impedance,  $R$  the peripheral resistance, and  $C$  the peripheral compliance. However, in adopting this equation, it is implicitly assumed that the venous exit pressure is zero. As such, the model's range of application is limited to that specific situation. A more general approach is to limit the Windkessel equations to those that relate pressure drops across the different elements that make up the windkessel model. Using the proposed discretization as shown in Figure 2,

$$\frac{1}{Z}(p_2 - p_3) = q_3, \quad \frac{1}{R}(p_3 - p_5) = q_5, \quad (7)$$

$$C \left( \frac{\partial p_3}{\partial t} - \frac{\partial p_4}{\partial t} \right) = q_7.$$

**2.3. Numerical Methods.** To determine pressure and flow in the vascular network, the 1D pressure-flow relations for blood vessels in (1) and (2) and the 0D pressure-flow relations for the periphery in (7) are solved in a fully coupled manner. Full coupling is achieved by casting the equations into the same discrete form.

For each of the subelements of the windkessels, two nodal point pressures and two nodal point flows are defined (Figure 2). A critical choice is that nodal point flows are both directed *inwards*. Combination of (7) with its counterpart

$$\frac{1}{Z}(p_3 - p_2) = q_4, \quad \frac{1}{R}(p_5 - p_3) = q_6,$$

$$C \left( \frac{\partial p_4}{\partial t} - \frac{\partial p_3}{\partial t} \right) = q_8 \quad (8)$$

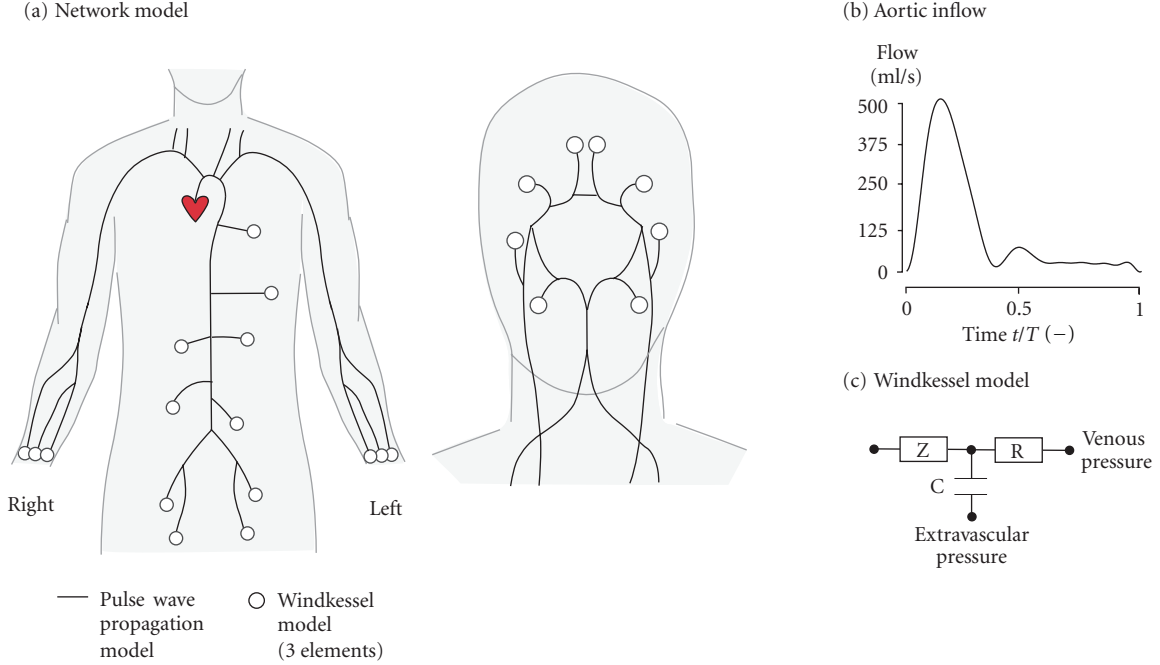


FIGURE 1: (a) Network model of 60 major arteries used to test the numerical method proposed. Adopted from Mulder et al. [10]. (b) Aortic inflow is prescribed [3]. (c) Windkessel boundary conditions at the periphery.

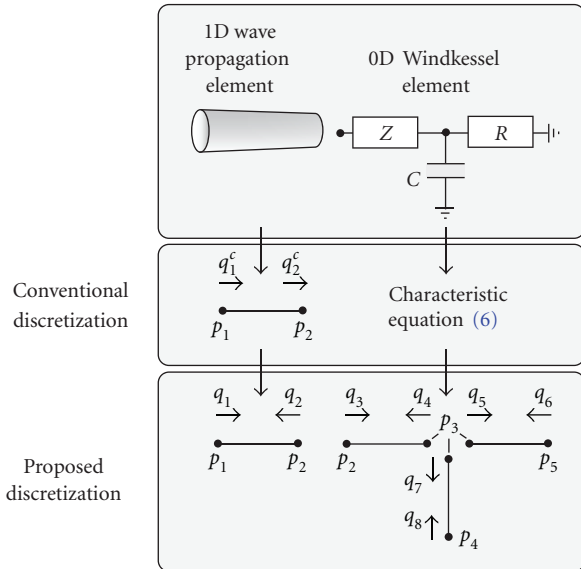


FIGURE 2: Proposed discretization for 1D wave propagation and 0D Windkessel elements. Notice the reversal of the flow in the second node with respect to the conventional discretization (indicated by superscript c).

yields (Appendix A)

$$\underline{C}_e \frac{\partial p_e}{\partial t} + \underline{R}_e^r p_e = \underline{q}_e, \quad (9)$$

where columns  $\underline{p}_e$  and  $\underline{q}_e$  contain the nodal point pressure and flows, respectively. Matrix  $\underline{C}_e$  contains the peripheral

compliance  $C$  and matrix  $\underline{R}_e^r$  contains reciprocals of the characteristic impedances and peripheral resistances. A second-order backward difference scheme is used to step forward in time with time step  $\Delta t$ . As a result the windkessel equations are written as

$$\underline{K}_e^{0D} p_e^{t+\Delta t} = f_e^{0D} + q_e^{t+\Delta t}, \quad (10)$$

with

$$\underline{K}_e^{0D} = \frac{3}{2\Delta t} \underline{C}_e + \underline{R}_e^r, \quad (11)$$

$$f_e^{0D} = -\underline{C}_e \left( -\frac{2}{\Delta t} p_e^t + \frac{1}{2\Delta t} p_e^{t-\Delta t} \right).$$

Before, Huberts et al. [19] presented a method in which the wave propagation equations for each vessel segment were cast into a lumped model consisting of resistances, compliances, and inductances, that is, the same blocks that make up the windkessel. This approach was benchmarked with the spectral element method by Bessems et al. [2]. Here an analogous, yet more direct approach is followed without the need for deriving a lumped parameter model, leading to a simplified implementation.

First, the wave propagation equations are linearized using estimates of area compliance, cross-sectional area, wall shear stress, and convective acceleration as obtained from a previous time step (indicated by symbol  $\hat{\bullet}$ ):

$$\hat{C}_A \frac{\partial p}{\partial t} + \frac{\partial q}{\partial z} = 0, \quad (12)$$

$$\frac{\rho}{\hat{A}} \frac{\partial q}{\partial t} + \frac{\partial p}{\partial z} = \frac{2}{\hat{a}} \hat{\tau}_w - \frac{\rho}{\hat{A}} \frac{\partial}{\partial z} \left( \delta \frac{\hat{q}^2}{\hat{A}} \right).$$

Subsequently, the vessel segments are divided into smaller two-noded elements of approximate size  $\Delta z$ . The actual size  $\Delta z_e$  of the elements as used for the discretization can differ from  $\Delta z$  and between vessel segments as given by

$$\Delta z_e = \frac{l}{\max[\text{round}(l/\Delta z), 1]} \quad (13)$$

with  $l$  the length of the vessel segment. Subsequently, a trapezium rule is used to spatially integrate the equations along the vessel axis and to express the equations in terms of nodal point pressures and flows. In this discretization step, nodal point flows for each element are also chosen to direct *inwards* (Figure 2). Once more, a second-order backward difference scheme is used to step forward in time. Consequently, mass and momentum equations are written as (Appendix B)

$$\underline{K}_e^{1D} \underline{p}_e^{t+\Delta t} = \underline{f}_e^{1D} + \underline{q}_e^{t+\Delta t}. \quad (14)$$

By defining both flows as being directed inwards, continuity of pressure and flow at the 0D-1D interfaces and the 1D-1D interfaces (e.g., bifurcations) is automatically satisfied in the process of assembling the element equations into the large system of equations (Appendix C). As a result, the assembled large system of equations is given by:

$$\underline{K} \underline{p}^{t+\Delta t} = \underline{f} + \underline{q}_e^{ex,t+\Delta t}, \quad (15)$$

where  $\underline{q}_e^{ex,t+\Delta t}$  contains a zero value for each node, except for nodes where external flow is prescribed. This system of equations is solved once pressure boundary conditions and external flows are given.

Note that any nonlinearity with respect to flow makes stiffness matrix  $\underline{K}$  flow dependent, thus requiring that flows are recomputed after each pressure computation. This can easily be done by using (10) or (14) at the element level; that is,

$$\underline{q}_e^{t+\Delta t} = \underline{K}_e^{(\bullet)} \underline{p}_e^{t+\Delta t} - \underline{f}_e^{(\bullet)}, \quad (\bullet) = \{0D, 1D\}. \quad (16)$$

As such, for all elements both nodal point flows are computed.

After pressures and flows are computed, the simulation proceeds to the next time step. The process is repeated until cardiac cycle time  $T$  is reached. At this point, it is checked whether the simulation is in a hemodynamic steady state. Hemodynamic steady state is considered if the nodal point maximum relative root-mean-squared norm, denoted  $\varepsilon_k$ , of both pressure and flow is less than  $10^{-3}$ . For  $\varepsilon_k$ ,

$$\varepsilon_k(\bullet) = \max_n \left( \sqrt{\frac{\sum_{t=0}^{t=T} [(\bullet)_{n,k}^t - (\bullet)_{n,k-1}^t]^2}{\sum_{t=0}^{t=T} [(\bullet)_{n,k-1}^t]^2}} \right), \quad (\bullet) = \{p, q\}, \quad (17)$$

with  $k$  the cardiac cycle number and  $n$  the nodal point number. A schematic overview of the complete algorithm is shown in Figure 3.

## 2.4. Simulation

**2.4.1. Choice of Model Parameters.** The numerical method is applied to simulate hemodynamics in an arterial tree composed of the 60 major arteries in the body and the head (Figure 1(a)). Blood density  $\rho$  and blood viscosity  $\eta$  are assumed to be  $1.05 \text{ kg}\cdot\text{m}^{-3}$  and  $4.5 \cdot 10^{-3} \text{ Pa}\cdot\text{s}$ , respectively. Reference transmural pressure ( $p_0$ ) is set to 13.3 kPa. Pressure dependency of the area compliance is specified according to parameters,  $p_1 = 2.7 \text{ kPa}$ ,  $p_2 = 4 \text{ kPa}$ ,  $\beta_1 = 0.4$ , and  $\beta_2 = 5.0$  [8]. Notice that these parameters imply that at reference pressure the compliance reduces to  $C_A = C_A^q$ . Assuming incompressible vessel wall material renders  $\mu = 0.5$ . Values for vessel length, wall thickness, radius, and Young's modulus as well as for the windkessel parameters are taken from Mulder et al. [10, Tables 2 and 3].

Aortic inflow is considered as the only external flow and is prescribed according to the waveform as depicted in Figure 1(b). Cardiac cycle time is set to  $T = 1 \text{ s}$ . Venous and extravascular pressures in the windkessels are set to 0 kPa.

**2.4.2. Simulations Performed.** To assess the convergence behavior of the proposed numerical method with respect to temporal and spatial discretization, a series of simulations is done with combinations of element sizes ( $\Delta z$ ) of approximately 2.5, 10, and 40 mm and time steps ( $\Delta t$ ) of 1, 2, 4, and 8 ms. Each simulation is started with zero pressures and flows.

For each of the simulations, the hemodynamic convergence norm  $\varepsilon$  is determined as a function of cardiac cycle number. Upon convergence, pressure and flow waveforms are visualized for the aorta, the left leg, the left arm, and in the brain. The influence of spatial and temporal discretization on simulated pressure and flow waveforms is quantified by relative root-mean-square difference  $\varepsilon$ , as given by

$$\varepsilon(\bullet) = \max_n \left( \sqrt{\frac{\sum_{t=0}^{t=T} [(\bullet)_n^t - (\bullet)_{n,REF}^t]^2}{\sum_{t=0}^{t=T} [(\bullet)_{n,REF}^t]^2}} \right), \quad (\bullet) = \{p, q\}. \quad (18)$$

In the computation of  $\varepsilon$ , waveforms as obtained with the most dense mesh and smallest time step are used as reference (indicated by subscript REF).

## 3. Results

For most simulations pressure and flow have converged after 12 cardiac cycles (Figure 4). At all intermediate cardiac cycles, the pressure norm is approximately an order of magnitude lower than that of the flow. Element size appears not to effect the decrease in  $\varepsilon$ -norm as a function of cardiac cycle number; that is, no visual discrimination between element sizes is possible. Convergence is slightly slower for larger time steps, but only in case of the largest time step ( $\Delta t = 8.0 \text{ ms}$ ) an additional cardiac cycle is required.

Figure 5 shows the simulated pressure and flow waveforms. It is shown that the amplitude of the pressure wave increases towards the periphery. Furthermore, relative height

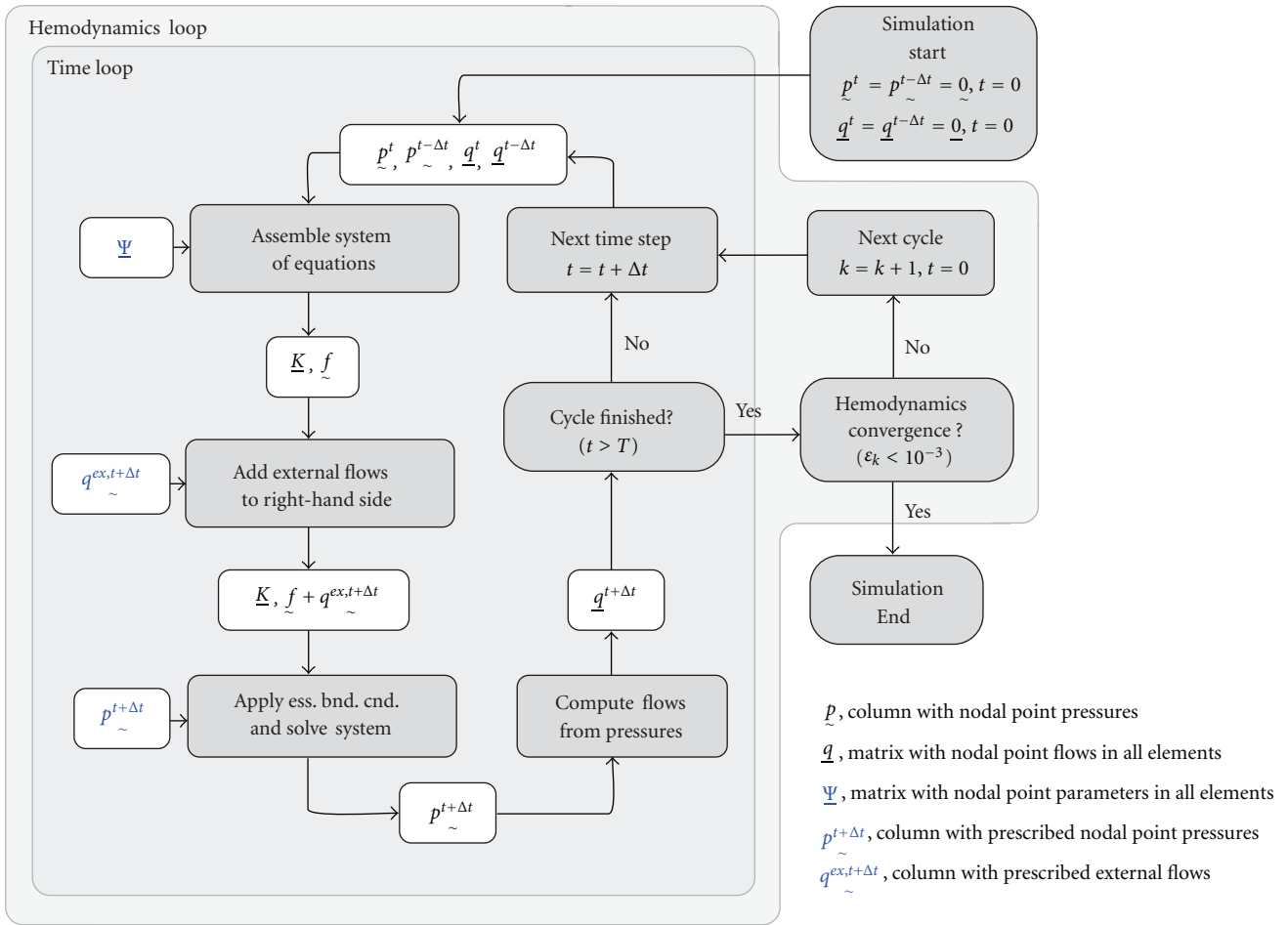


FIGURE 3: Schematic overview of the numerical method used to compute pressures and flows. During a “time loop,” a cardiac cycle with cycle time  $T$  is simulated with time step  $\Delta t$ . Subsequently, a hemodynamic convergence criterion ( $\epsilon_k$ ) is computed to assess whether pressure and flow waveforms are in steady state. If not, subsequent cardiac cycles are simulated in a “hemodynamics loop” until convergence is achieved.

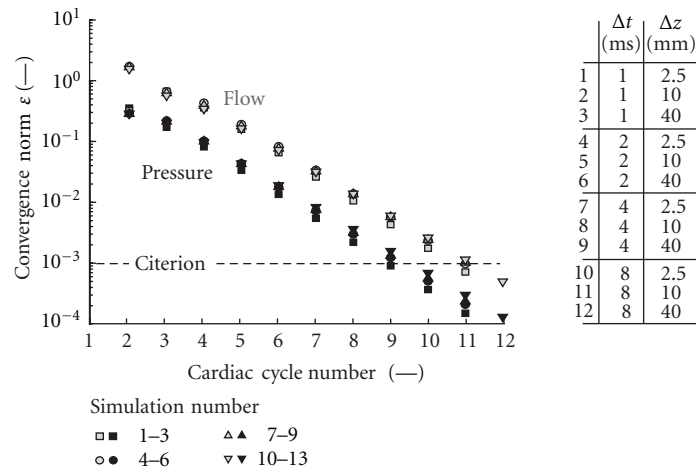


FIGURE 4: Convergence behavior for the proposed method for different time step and element sizes. Results obtained with the same time step, but different element sizes are indistinguishable.

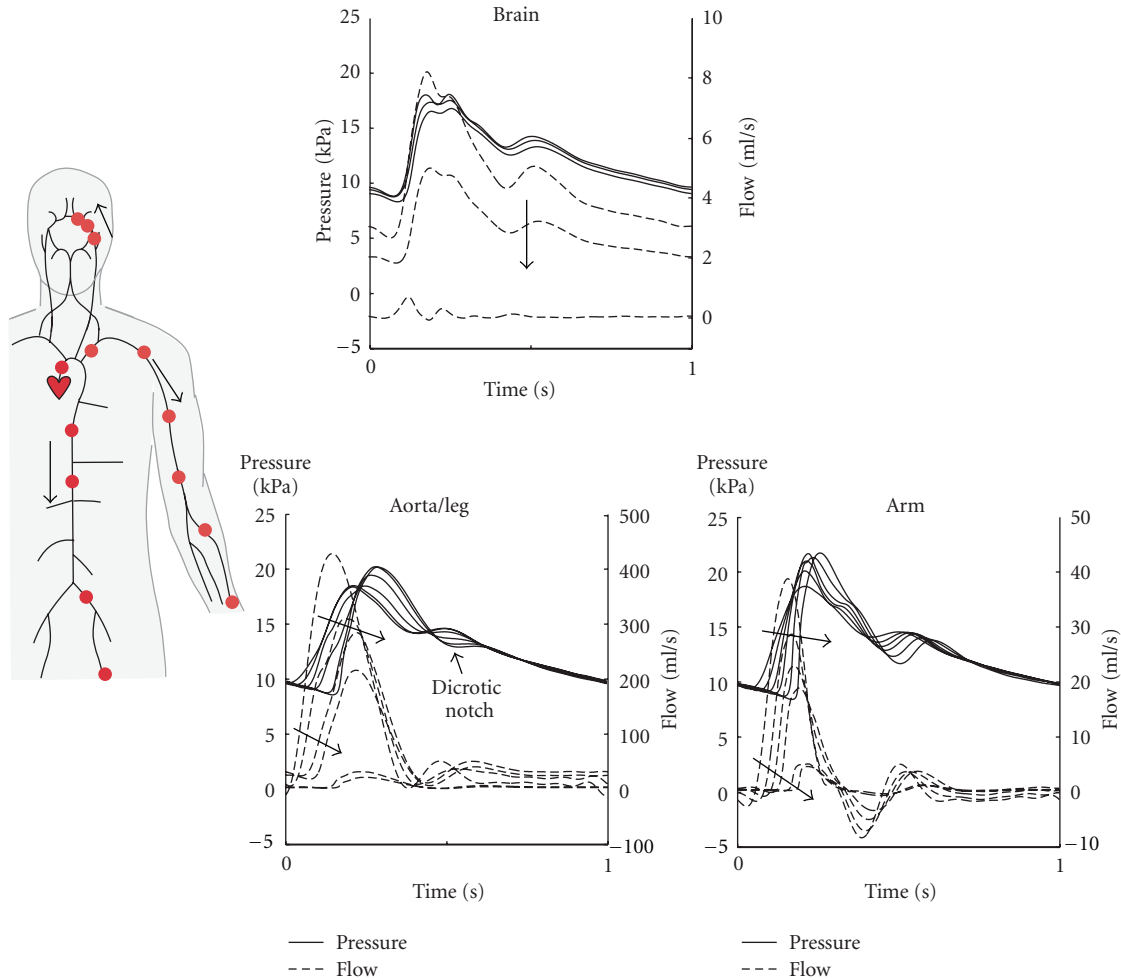


FIGURE 5: Computed pressure and flow waveforms in the aorta, the arm, and the brain. Results are shown as obtained using the simulation with element size  $\Delta z = 2.5$  mm and time step  $\Delta t = 1$  ms. The arrows indicate increase in distance from the aortic root.

of the dicrotic notch with respect to the pressure pulse decreases towards the periphery. Arteries near the periphery such as those in the arm show reversal of flow during a part of the cardiac cycle.

As shown in Figure 6, the influence of time step size on the computed waveforms (1) is typically one order of magnitude lower for pressures than for flows and (2) increases towards the periphery; that is, the largest flow difference occurs in the anterior communicating artery in the brain and the largest pressure difference in ulnar artery in the arm (Figure 6(b)). Element size has only a minor effect on the computed pressure and flow waveforms as compared to the effect of the time step (Figure 6(a)). Using an element size of 40 mm instead of 2.5 mm at the smallest time step increases the  $\epsilon$ -norm of flow by less than  $5 \cdot 10^{-3}$ . Taking a time step of 2 ms instead of 1 ms at the smallest element size leads to an increase of approximately  $8 \cdot 10^{-2}$ . Increasing the time step to 8 ms causes damping of the pressure and flow waveforms.

#### 4. Discussion

In this study, a simplified numerical method was developed for time-domain simulation of blood pressure and flow waveforms in the vascular system that couples nonlinear one-dimensional (1D) wave propagation models for the blood vessels to zero-dimensional (0D) lumped (windkessel) models for the periphery using pressure as degree of freedom.

To show performance of the method in a physiologic setting, the method was applied to simulate hemodynamics in a vascular network containing the 60 major arteries in the body and the brain. The specific choice of vessel behavior, velocity profile, windkessel parameters, and essential boundary conditions was beyond the scope of this study. The pressure-area relations of the bloodvessels were assumed non-linear and convective acceleration was included to assess behavior of the method in solving the model equations in its most non-linear form.

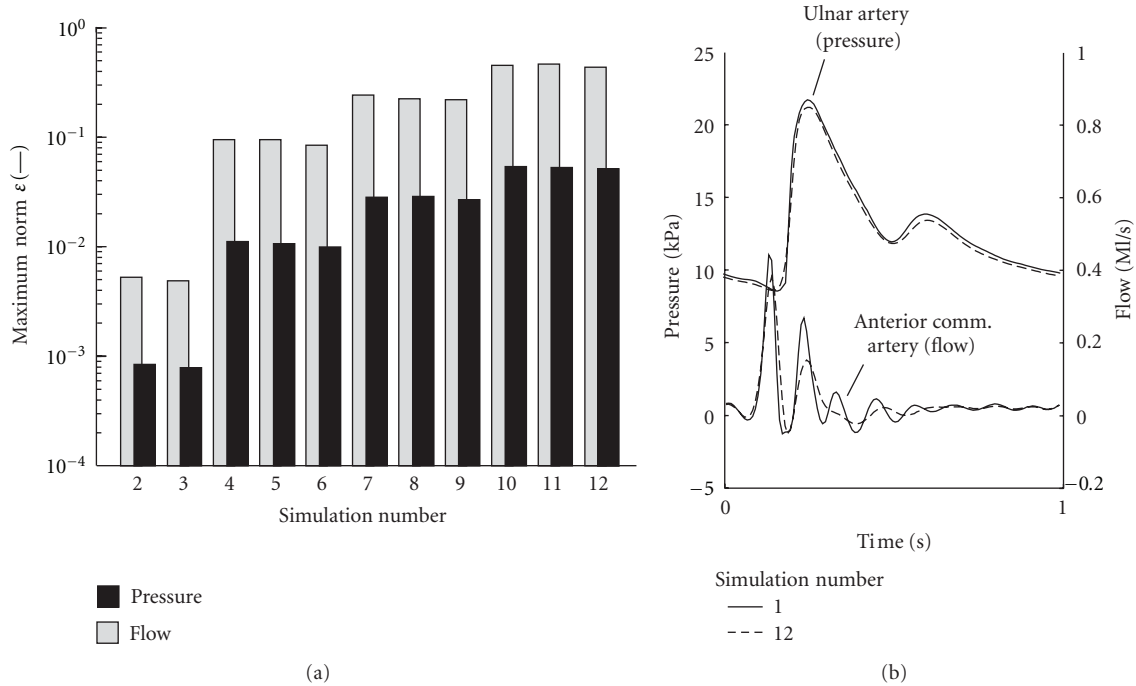


FIGURE 6: (a) Influence of element and time step size on  $\epsilon$ -norm of pressure and flow. (b) Difference in pressure and flow waveform at locations with maximal  $\epsilon$ -norm. The maximum  $\epsilon$ -norm for pressure and flow occurs at different locations.

The pressure and flow waveforms that were obtained with the method (Figure 5) are similar to those simulated [10] as well as experimentally measured by others [20]; that is, the computed waveforms demonstrate the physiological features of (1) increase in amplitude of the pressure wave and decrease in relative height of the diastolic notch with increased distance from the aortic root and (2) reversal of flow during a part of the cardiac cycle in the arteries of the arm.

**4.1. Convergence Behavior of Proposed Method.** Typically 12 cardiac cycles are needed to reach convergence when starting with zero pressure and flow conditions. This convergence is fairly independent on the element and time step size used to discretize the model equations (Figure 4). When comparing the converged situations, the time step size had a significantly larger effect on the pressure and flow waveforms than the element size (Figure 6(a)) that is, the effect of time step was typically an order of magnitude higher for flow than for pressure. Taking a time step of 8 ms introduces significant damping of the pressure and flow waves as compared to the results obtained using a time step of 1 ms (Figure 6(b)). The effect increases towards the periphery; that is, the largest root-mean-square differences are found in the ulnar artery in the arm and in the anterior communicating artery in the brain. The increase in effect of time step towards the periphery is most likely caused by the physiologic steepening of the pressure and flow waveforms towards the periphery (Figure 5). A time step of 2 ms yields an increase in relative

root-mean-square difference in flow of about  $8 \cdot 10^{-2}$ , which indicates that a time step of 1 ms is sufficiently small (Figure 6(a)).

**4.2. Benefits of Proposed Method.** As listed in the Introduction section, many different numerical methods already exist to couple the 1D wave propagation equations for the large arteries to the 0D lumped windkessel equations for the peripheral part of the vascular tree. Usually, the wave propagation equations for the vascular segments are written in discrete form using finite/spectral-element or finite-difference schemes. Such methods have the disadvantage that bifurcations require additional coupling equations to be defined in terms of the Riemann invariants or penalty functions. Furthermore, equations of the peripheral model are usually incorporated by solving a characteristic equation (such as that of the three-element windkessel in (6)) together with the wave propagation equations. The drawback of this approach is that such a characteristic equation needs to be available. This is, for instance, not the case when the terminus of the windkessels is connected to a venous circulation.

In the numerical method proposed, the windkessel and wave propagation equations are cast into the same form to strongly couple them without the need for additional coupling equations or availability of a characteristic equation. In fact, any combination of windkessel (or lumped) elements and wave propagation elements is possible, allowing for a broader application to vascular networks that combine arteries, microcirculation (periphery), and veins.

The numerical method allows for easy extension with a lumped model of the heart to study arterioventricular interaction such as done by others [21–23]. Cardiac contraction can be taken into account by specifying the ventricular pressure as (time-varying) essential boundary conditions, rather than prescribing the aortic inflow. Ventricular volume could then be updated during ejection using the aortic inflow of a time step earlier. Although in this way ventricular and aortic flow are only weakly coupled, numerical complexity is limited.

**4.3. Limitations of Proposed Method.** To cast equations for the wave propagation model into the same form as those for the windkessel model, it is required that each discrete element contains only two nodes in which both flows are directed inwards. As a consequence, higher-order elements such as those used in, for example, spectral element discretization are no longer possible. This limitation on order of approximation, however, was found to have little influence as element size appeared to be of minor importance for convergence as well as for the pressure and flow curves obtained.

As indicated by the tangent of Figure 6(a), the convergence order regarding the time step is less than second order, even though a second-order backward difference scheme was used for the time integration. This reduction in convergence order can be expected due to non-linearity of the 1D wave propagation equations but may have been amplified using estimates from a previous time step for the linearization process. Linearization by means of, for example, a Newton-Raphson scheme could have been done but was not included to further simplify (implementation of) the numerical method.

For the vascular network as presented in this study, we incorporated windkessel models for the periphery. However, the algorithm proposed is not restricted to this particular model choice. Other lumped element models such as structured tree models [3] can easily be incorporated as long as the pressure-flow relation can be cast into the same form as that for the wave propagation model. The method is also not restricted to the approximate velocity profiles as assumed in this study. Use of, for example, the Womersley velocity profiles is also possible, as the only requirement for the method to proceed in time is that area compliance, wall shear stress and convective acceleration are available at a previous time step.

## 5. Conclusion

In conclusion, a novel numerical method is developed for computation of pressure and flow waveforms in the vascular system. Using pressure as only degree of freedom, 0D lumped (windkessel) elements and 1D wave propagation elements can be randomly combined without the need for additional coupling equations. This property facilitates flexible model building from 0D and 1D elements for a wide range of applications in studying vascular hemodynamics.

## Appendices

### A. Derivation of (0D) Windkessel Element Equations

Application of definitions for nodal point pressures and flows as shown in Figure 2 yielded (7) and (8). In matrix form, these equations become

$$\begin{aligned} \frac{1}{Z} \underline{M} \begin{bmatrix} p_2 \\ p_3 \end{bmatrix} &= \begin{bmatrix} q_3 \\ q_4 \end{bmatrix}, & \frac{1}{R} \underline{M} \begin{bmatrix} p_3 \\ p_5 \end{bmatrix} &= \begin{bmatrix} q_5 \\ q_6 \end{bmatrix}, \\ \underline{C} \underline{M} \begin{bmatrix} \frac{\partial p_3}{\partial t} \\ \frac{\partial p_4}{\partial t} \end{bmatrix} &= \begin{bmatrix} q_7 \\ q_8 \end{bmatrix}, \end{aligned} \quad (\text{A.1})$$

with matrix  $\underline{M}$  defined as

$$\underline{M} = \begin{bmatrix} 1 & -1 \\ -1 & 1 \end{bmatrix}. \quad (\text{A.2})$$

Assembly of the system of equations then yields

$$\underline{C}_e \frac{\partial p_e}{\partial t} + \underline{R}_e^r p_e = q_e^{ex}, \quad (\text{A.3})$$

with

$$\underline{C}_e = \begin{bmatrix} 0 & 0 & 0 & 0 \\ 0 & C & -C & 0 \\ 0 & 0 & 0 & 0 \\ 0 & -C & C & 0 \end{bmatrix}, \quad \underline{R}_e^r = \begin{bmatrix} \frac{1}{Z} & -\frac{1}{Z} & 0 & 0 \\ -\frac{1}{Z} & \frac{1}{Z} + \frac{1}{R} & 0 & -\frac{1}{R} \\ 0 & -\frac{1}{R} & 0 & \frac{1}{R} \\ 0 & 0 & 0 & 0 \end{bmatrix}, \quad (\text{A.4})$$

and  $p_e = [p_2, p_3, p_4, p_5]^T$ , and  $q_e = [q_3, q_4 + q_5 + q_7, q_6, q_8]^T$ . Since there should be no net flow to or from node 3, the choice that nodal point flows are directed *inwards* yields  $q_4 + q_5 + q_7 = 0$ . Notice that the remaining flows  $q_3$ ,  $q_6$ , and  $q_8$  denote *external* flows. Application of a second-order backward difference scheme yields

$$\left[ k_0 \underline{C}_e + \underline{R}_e^r \right] p_e^{t+\Delta t} = \left[ \underline{C}_e \left( -k_1 p_e^t - k_2 p_e^{t-\Delta t} \right) \right] + q_e^{t+\Delta t}, \quad (\text{A.5})$$

in which  $k_0 = 3/(2\Delta t)$ ,  $k_1 = -2/\Delta t$ , and  $k_2 = 1/(2\Delta t)$ .

### B. Derivation of (1D) Blood Vessel Element Equations

To describe the linearized versions of the 1D balances of mass and momentum as given by (12) in terms of a discrete

number of points, the vessels are divided into a number of non-overlapping two-noded elements. As a consequence

$$\int (\bullet) dz \approx \sum_{e=1}^{N_e} \int_e (\bullet) dz, \quad (\text{B.1})$$

with  $N_e$  the number of elements. The trapezium rule is used to spatially integrate the element equations from node 1 to node 2. Starting with the conventional discretization with both flows directed from node 1 to node 2 as depicted in Figure 2, integration over the element domain yields

$$\begin{aligned} \int_e \hat{C}_A \frac{\partial p}{\partial t} dz &\approx \left( \hat{C}_{A,1} \frac{\partial p_1}{\partial t} + \hat{C}_{A,2} \frac{\partial p_2}{\partial t} \right) \frac{\Delta z_e}{2}, \\ \int_e \frac{\partial p}{\partial z} dz &\approx p_2 - p_1, \\ \int_e \hat{L}_A \frac{\partial q}{\partial t} dz &\approx \left( \hat{L}_{A,1} \frac{\partial q_1^c}{\partial t} + \hat{L}_{A,2} \frac{\partial q_2^c}{\partial t} \right) \frac{\Delta z_e}{2}, \\ \int_e \frac{\partial q}{\partial z} dz &\approx q_2^c - q_1^c, \quad \int_e h dz \approx (h_1 + h_2) \frac{\Delta z_e}{2}, \\ h_i &= \left( \frac{2}{\hat{a}} \hat{r}_w - \hat{L}_A \frac{\partial}{\partial z} \left( \delta \frac{\hat{q}^{c2}}{\hat{A}} \right) \right)_i \end{aligned} \quad (\text{B.2})$$

with  $\Delta z_e$  the element length and  $L_A = \rho/A$ . Superscript  $c$  is used to indicate that conventional definition of flows are adopted. In matrix form, (B.2) becomes

$$\begin{aligned} \begin{bmatrix} \hat{C}_{A,1} \frac{\Delta z_e}{2} \\ \hat{C}_{A,2} \frac{\Delta z_e}{2} \end{bmatrix}^T \frac{\partial \tilde{p}_e}{\partial t} + \begin{bmatrix} -1 \\ +1 \end{bmatrix}^T \tilde{q}_e^c &= 0, \\ \begin{bmatrix} \hat{L}_{A,1} \frac{\Delta z_e}{2} \\ \hat{L}_{A,2} \frac{\Delta z_e}{2} \end{bmatrix}^T \frac{\partial \tilde{q}_e^c}{\partial t} + \begin{bmatrix} -1 \\ +1 \end{bmatrix}^T \tilde{p}_e &= (h_1 + h_2) \frac{\Delta z_e}{2}, \end{aligned} \quad (\text{B.3})$$

where  $\tilde{p}_e = [p_1, p_2]^T$  and  $\tilde{q}_e^c = [q_1^c, q_2^c]^T$  contain nodal point pressures and flows of the element, respectively. Using the second-order backward difference scheme with time step  $\Delta t$ , (B.3) are written as

$$\underline{F}_e \tilde{p}_e^{t+\Delta t} + \underline{G}_e^c \tilde{q}_e^{c,t+\Delta t} = \tilde{h}_e, \quad (\text{B.4})$$

with

$$\begin{aligned} \underline{F}_e &= \begin{bmatrix} k_0 \hat{C}_{A,1} \frac{\Delta z_e}{2} & k_0 \hat{C}_{A,2} \frac{\Delta z_e}{2} \\ -1 & +1 \end{bmatrix}, \\ \underline{G}_e^c &= \begin{bmatrix} -1 & +1 \\ k_0 \hat{L}_{A,1} \frac{\Delta z_e}{2} & k_0 \hat{L}_{A,2} \frac{\Delta z_e}{2} \end{bmatrix}, \\ \tilde{h}_e &= \begin{bmatrix} 0 \\ (h_1 + h_2) \frac{\Delta z_e}{2} \end{bmatrix} \\ &+ \begin{bmatrix} 0 & 0 \\ \hat{L}_{A,1} \frac{\Delta z_e}{2} & \hat{L}_{A,2} \frac{\Delta z_e}{2} \end{bmatrix} \begin{pmatrix} -k_1 q_{\tilde{e}}^{c,t} - k_2 q_{\tilde{e}}^{c,t-\Delta t} \end{pmatrix} \\ &+ \begin{bmatrix} \hat{C}_{A,1} \frac{\Delta z_e}{2} & \hat{C}_{A,2} \frac{\Delta z_e}{2} \\ 0 & 0 \end{bmatrix} \begin{pmatrix} -k_1 p_{\tilde{e}}^t - k_2 p_{\tilde{e}}^{t-\Delta t} \end{pmatrix}. \end{aligned} \quad (\text{B.5})$$

Next, a switch is made to the proposed discretization as illustrated in Figure 2, in which the flow in the second node is directed inwards, that is,  $q_1 = q_1^c$  and  $q_2 = -q_2^c$ . Notice that this switch implies changing sign of the second column of  $\underline{G}_e$ . As a consequence, (B.4) becomes

$$\underline{F}_e \tilde{p}_e^{t+\Delta t} + \underline{G}_e \tilde{q}_e^{t+\Delta t} = \tilde{h}_e \quad (\text{B.6})$$

with

$$\underline{G}_e = \begin{bmatrix} G_{e,11}^c & -G_{e,12}^c \\ G_{e,21}^c & -G_{e,22}^c \end{bmatrix}, \quad \tilde{q}_e = \begin{bmatrix} q_1^c \\ -q_2^c \end{bmatrix} = \begin{bmatrix} q_1 \\ q_2 \end{bmatrix}. \quad (\text{B.7})$$

After separation of matrix  $\underline{G}_e$  from flow column  $\tilde{q}_e^{t+\Delta t}$ , the (1D) element equations finally read

$$\left[ -\underline{G}_e^{-1} \underline{F}_e \right] \tilde{p}_e^{t+\Delta t} = \left[ -\underline{G}_e^{-1} \tilde{h}_e \right] + \tilde{q}_e^{t+\Delta t}. \quad (\text{B.8})$$

### C. Assembly of Large System of Equations: Coupling (0D) and (1D) Element Equations

Notice that (A.5) and (B.8) are both of the form

$$\underline{K}_e \tilde{p}_e^{t+\Delta t} = \tilde{f}_e + \tilde{q}_e^{t+\Delta t}. \quad (\text{C.1})$$

Assembly of the large system of equations involves summation of all 1D element equations according to (B.1), as well as all 0D element equations. In doing so, element flows  $\tilde{q}_e^{t+\Delta t}$  will be added. As a consequence of all nodal point flows being directed inwards, for all internal nodes, the balance of mass yields a zero entry in the assembled flow column (denoted  $\tilde{q}^{ex,t+\Delta t}$ ). In fact, only non zero flows in external nodes will yield a non-zero entry in the assembled flow column. As a result, the assembled system of equations is given by

$$\underline{K} \tilde{p}^{t+\Delta t} = \tilde{f} + \tilde{q}^{ex,t+\Delta t}. \quad (\text{C.2})$$

Since external flows such as that at the aortic root are prescribed, the nodal point pressures are the only degrees of freedom left, and the system can be solved once the pressures at the remaining vessel or windkessel termini are prescribed.

## Acknowledgment

This study was funded by the European Commission 7th Framework Programme (ARCH ICT-224390).

## References

- [1] F. N. Van De Vosse and N. Stergiopoulos, "Pulse wave propagation in the arterial tree," *Annual Review of Fluid Mechanics*, vol. 43, pp. 467–499, 2011.
- [2] D. Bessems, M. Rutten, and F. Van De Vosse, "A wave propagation model of blood flow in large vessels using an approximate velocity profile function," *Journal of Fluid Mechanics*, vol. 580, pp. 145–168, 2007.
- [3] M. S. Olufsen, C. S. Peskin, W. Y. Kim, E. M. Pedersen, A. Nadim, and J. Larsen, "Numerical simulation and experimental validation of blood flow in arteries with structured-tree outflow conditions," *Annals of Biomedical Engineering*, vol. 28, no. 11, pp. 1281–1299, 2000.
- [4] P. Segers, N. Stergiopoulos, P. Verdonck, and R. Verhoeven, "Assessment of distributed arterial network models," *Medical and Biological Engineering and Computing*, vol. 35, no. 6, pp. 729–736, 1997.
- [5] N. Stergiopoulos, J. J. Meister, and N. Westerhof, "Evaluation of methods for estimation of total arterial compliance," *American Journal of Physiology*, vol. 268, no. 4, pp. H1540–H1548, 1995.
- [6] N. Westerhof, F. Bosman, C. J. De Vries, and A. Noordergraaf, "Analog studies of the human systemic arterial tree," *Journal of Biomechanics*, vol. 2, no. 2, pp. 121–143, 1969.
- [7] Y. Huo and G. S. Kassab, "A hybrid one-dimensional/Womersley model of pulsatile blood flow in the entire coronary arterial tree," *American Journal of Physiology*, vol. 292, no. 6, pp. H2623–H2633, 2007.
- [8] P. Reymond, F. Merenda, F. Perren, D. Rüfenacht, and N. Stergiopoulos, "Validation of a one-dimensional model of the systemic arterial tree," *American Journal of Physiology*, vol. 297, no. 1, pp. H208–H222, 2009.
- [9] J. Alastruey, K. H. Parker, J. Peiró, S. M. Byrd, and S. J. Sherwin, "Modelling the circle of Willis to assess the effects of anatomical variations and occlusions on cerebral flows," *Journal of Biomechanics*, vol. 40, no. 8, pp. 1794–1805, 2007.
- [10] G. Mulder, A. C.B. Bogaerds, P. Rongen, and F. N. van de Vosse, "The influence of contrast agent injection on physiological flow in the circle of Willis," *Medical Engineering and Physics*, vol. 33, no. 2, pp. 195–203, 2011.
- [11] T. J. R. Hughes and J. Lubliner, "On the one dimensional theory of blood flow in the larger vessels," *Mathematical Biosciences*, vol. 18, no. 1-2, pp. 167–170, 1973.
- [12] O. Frank, "Die grundform des arteriellen pulses erste abhandlung: mathematische analyse," *Zeitschrift fuer Biologie*, vol. 27, pp. 273–288, 1899.
- [13] S. J. Sherwin, V. Franke, J. Peiró, and K. Parker, "One-dimensional modelling of a vascular network in space-time variables," *Journal of Engineering Mathematics*, vol. 47, no. 3-4, pp. 217–250, 2003.
- [14] J. J. Wang and K. H. Parker, "Wave propagation in a model of the arterial circulation," *Journal of Biomechanics*, vol. 37, no. 4, pp. 457–470, 2004.
- [15] G. Pontrelli, "A multiscale approach for modelling wave propagation in an arterial segment," *Computer Methods in Biomechanics and Biomedical Engineering*, vol. 7, no. 2, pp. 79–89, 2004.
- [16] A. Quarteroni, S. Ragni, and A. Veneziani, "Coupling between lumped and distributed models for blood flow problems," *Computing and Visualization in Science*, vol. 4, pp. 111–412, 2001.
- [17] G. J. Langewouters, K. H. Wesseling, and W. J. A. Goedhard, "The static elastic properties of 45 human thoracic and 20 abdominal aortas in vitro and the parameters of a new model," *Journal of Biomechanics*, vol. 17, no. 6, pp. 425–435, 1984.
- [18] N. Stergiopoulos, D. F. Young, and T. R. Rogge, "Computer simulation of arterial flow with applications to arterial and aortic stenoses," *Journal of Biomechanics*, vol. 25, no. 12, pp. 1477–1488, 1992.
- [19] W. Huberts, A. S. Bode, W. Kroon et al., "A pulse wave propagation model to support decision-making in vascular access planning in the clinic," *Medical Engineering and Physics*, vol. 34, no. 2, pp. 233–248, 2012.
- [20] W. W. Nichols and M. F. O'Rourke, *McDonald's Blood Flow in Arteries: Theoretical, Experimental and Clinical Principles*, Hodder Arnold, London, UK, 2005.
- [21] L. Formaggia, D. Lamponi, M. Tuveri, and A. Veneziani, "Numerical modeling of 1D arterial networks coupled with a lumped parameters description of the heart," *Computer Methods in Biomechanics and Biomedical Engineering*, vol. 9, no. 5, pp. 273–288, 2006.
- [22] D. H. Fitchett, "LV-arterial coupling: interactive model to predict effect of wave reflections on LV energetics," *American Journal of Physiology*, vol. 261, no. 4, pp. 273–288, 1991.
- [23] F. Liang, S. Takagi, R. Himeno, and H. Liu, "Multi-scale modeling of the human cardiovascular system with applications to aortic valvular and arterial stenoses," *Medical and Biological Engineering and Computing*, vol. 47, no. 7, pp. 743–755, 2009.

## Research Article

# Relationship between Concentration Difference of Different Density Lipoproteins and Shear Stress in Atherosclerosis

Wei Meng,<sup>1</sup> Fengxu Yu,<sup>1</sup> Huaiqing Chen,<sup>2</sup> Jianmin Zhang,<sup>3</sup> Eryong Zhang,<sup>1</sup> Yingqiang Guo,<sup>1</sup> and Yingkang Shi<sup>1</sup>

<sup>1</sup>Department of Thoracic and Cardiovascular Surgery, West China Hospital, Sichuan University, Chengdu 610041, China

<sup>2</sup>Institute of Biomedical Engineering, West China Medical Center, Sichuan University, Chengdu 610041, China

<sup>3</sup>State Key Laboratory of Hydraulics and Mountain River Engineering, Sichuan University, Chengdu 610065, China

Correspondence should be addressed to Yingkang Shi, yingkangshi@yahoo.com

Received 15 August 2011; Revised 16 October 2011; Accepted 8 November 2011

Academic Editor: Kyehan Rhee

Copyright © 2012 Wei Meng et al. This is an open access article distributed under the Creative Commons Attribution License, which permits unrestricted use, distribution, and reproduction in any medium, provided the original work is properly cited.

Previous research has observed concentration polarization in LDL and HDL in the arterial system. However, there is no report that links this concentration polarization to the development of vascular atherosclerosis (AS). Therefore, the purpose of this study is to establish the relationship between concentration difference of LDL and HDL and shear stress using a carotid bifurcation vascular model. PTFE was employed to create the carotid bifurcation model. Endothelial cells were coated on the inner wall of the graft. In a recirculation system, HDL and LDL concentration were measured under two different ICA flow velocities at 5 different locations within our model. We report the following: (1) LDL and HDL concentration difference was observed in both high flow and low flow environments; (2) the degree of LDL and HDL concentration polarization varied depending of high flow and low flow environment; (3) absolute values of concentration difference between LDL and HDL at the inner wall surface decreased with the increase in shear stress when shear stress was more than 1.5 Pa. This variation trend would be more pronounced if shear stress were less than 0.5 Pa. Our study suggests that under the action of shear stress, concentration differences of LDL or HDL create a disturbance in the balance of atherogenic factors and anti-As factors, resulting in the occurrence of AS.

## 1. Introduction

Epidemiology has demonstrated that concentration increment of low-density lipoprotein (LDL) and concentration decrement of high-density lipoprotein (HDL) in blood are independent risk factors for the development of atherosclerosis (AS) [1, 2]. They assume opposite roles: the former is a harmful lipoprotein while the latter is protective [1–4]. In the majority of cases, AS is found to be located at the bifurcations, bends, or stenosis sites of the artery. In these areas, blood flow is disturbed resulting in flow separation and vortex zone, which is termed localization of AS [5, 6]. Studies have revealed that reasons resulting in localization of AS include the following: (1) shear stress appearing at the surface of vascular wall and (2) areas of disturbed blood flow leads to its slowing and thus, gives LDL considerable time to interact with the inner wall. As a result, an increasing number of LDL can penetrate the vascular wall.

At present, research has observed concentration polarization in LDL and HDL in the arterial system; these studies also revealed that polarization degree is related to shear stress. Lipid concentration polarization plays an important role in AS development [7–10]. In our research on HDL concentration polarization, we found that under high shear stress circumstance, HDL concentration on the inner surface of vascular wall is inversely proportional to shear stress [10]. This result appeared to contradict with the accepted protective effect of HDL. Based on this observation, the following have been assumed: AS is a result of concerted action of multiple factors and a conclusion cannot be drawn from HDL concentration of the inner surface of vascular wall alone. Under high shear stress circumstance, HDL concentration absolute value will decrease; the protective effect for preventing AS development appears to decrease. However, when integrated consideration with LDL concentration is made,

can it show the interactive function of concentration polarization of different density lipoproteins in AS development?

On the above-mentioned aspects, we studied the relationship between concentration difference of LDL and HDL on the inner surface of vascular wall and shear stress based on a carotid bifurcation vascular model which designed to mimic the configuration of the human carotid artery [10].

## 2. Material and Methods

**2.1. Experimental Model.** Semipermeable poly tetra fluoro ethylene (PTFE) was employed to create the carotid bifurcation model. The inner diameter of each region of a human carotid artery was measured by Doppler ultrasound and computerized tomography angiography (CTA) (Figures 2(c) and 2(d)). The measurements were amplified at a rate of 1:1.5 (Table 1) to create the bifurcation model of carotid artery that was subsequently coated with endothelial cells on the inner wall of the model to induce the endothelialization of the inner wall of the model as shown in Figure 1 [10, 11].

As shown in Figure 2(a), the model included the common carotid artery (CCA), external carotid artery (ECA), internal carotid artery (ICA), and internal carotid artery sinus (ICAS). The low shear stress core region and its margins were marked on the model. The low shear stress core region was marked as point 5, and the proximal and distal margins were marked as points 3 and 4 (Figure 2(b)). The measuring points of the inner diameter of the CCA and the inner diameter of the ICA were used as control points and marked as points 1 and 2 (Figure 2(b)). In addition, the final model is provided in the schematic diagram in Figure 3(a), and the schematic diagram of the experimental system was shown in Figure 3(b). The whole recirculate system was composed of the upstream reservoir, the model, the flow meter, a centrifugal pump, and the downstream reservoir, connected with tubes. The system is connected with tubing form a complete circuit. A centrifugal pump would pump the fluid from the downstream back to the upper reservoir to establish the circuit. (The fluid was conserved by a reservoir with adjustable height. Before entering the model, the fluid would pass through a segment of straight and horizontal tube. After leaving the model, the fluid flowed forwards to a downstream reservoir through tubes with flow meter. A pump would suck the fluid of the downstream reservoir back to the upper one in order to establish a circulation.) A threshold bar in the upper reservoir could automatically introduce extra fluid back into the downstream container to maintain a stable experimental water stage. The flow direction was shown by arrows (Figure 3(b)).

**2.2. Numerical Simulation Methodology.** To simplify the analysis, the following assumptions were made: (1) the circulating liquid is incompressible Newtonian fluid; (2) the flow is a steady flow; (3) the wall of bifurcation model is permeable to plasma and has a filtration rate of the order of  $10^6$  cm/s. If the volume power, heat exchange, and other physical and chemical factors are not considered then the equations provided in the footnote can be employed.

TABLE 1: The inner diameter of carotid artery measured by Doppler ultrasound and CTA and the model measurements obtained by amplifying the actual values by 1.5.

Measuring position	Measuring size (mm)	Model size (mm)
Common carotid Artery (CCA)	6.5	9.8
Internal carotid Artery (ICA)	4.9	7.4
External Carotid Artery (ECA)	4.2	6.3
Internal carotid Artery sinus (ICAS)	7.8	11.7

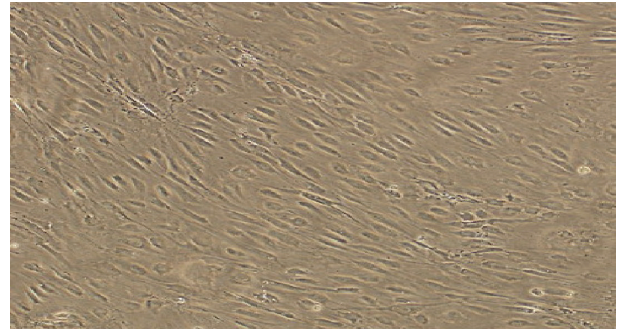


FIGURE 1: Observation of cell growth and cell arrangement with a converted microscope after implanting the inner surface of the carotid bifurcation model (magnification  $\times 100$ ).

The first formula is a continuity equation and the second formula is an equation of motion where  $u_i$  is the velocity of flow field,  $P$  is the fluid pressure,  $\rho$  is the fluid density and  $\mu$  is the fluid viscosity. Because the basic equations mentioned above are intensive non-linear equations, the Finite Volume Method (FVM) was employed as it is the most commonly used numerical method for resolving this type of mathematical problem at present [12]. The FLUENT software is hydrodynamic calculating software based on the FVM and it is the CFD software applied most widely utilized.

$$\frac{\partial u_j}{\partial x_j} = 0, \quad (1)$$

$$\rho \frac{\partial u_j u_i}{\partial x_j} = -\frac{\partial P}{\partial x_i} + \mu \frac{\partial}{\partial x_j} \left( \frac{\partial u_i}{\partial x_j} + \frac{\partial u_j}{\partial x_i} \right).$$

The boundary conditions are

$$u(x, 1, t) = 0, \quad v(x, 1, t) = \frac{V_w}{\bar{U}_0},$$

$$u(0, y, t) = U_{wm}, \quad v(0, y, t) = 0, \quad c(0, y, t) = 1. \quad (2)$$

The bifurcation model was considered as a semipermeable membrane with a filtration rate of  $V_w$ .

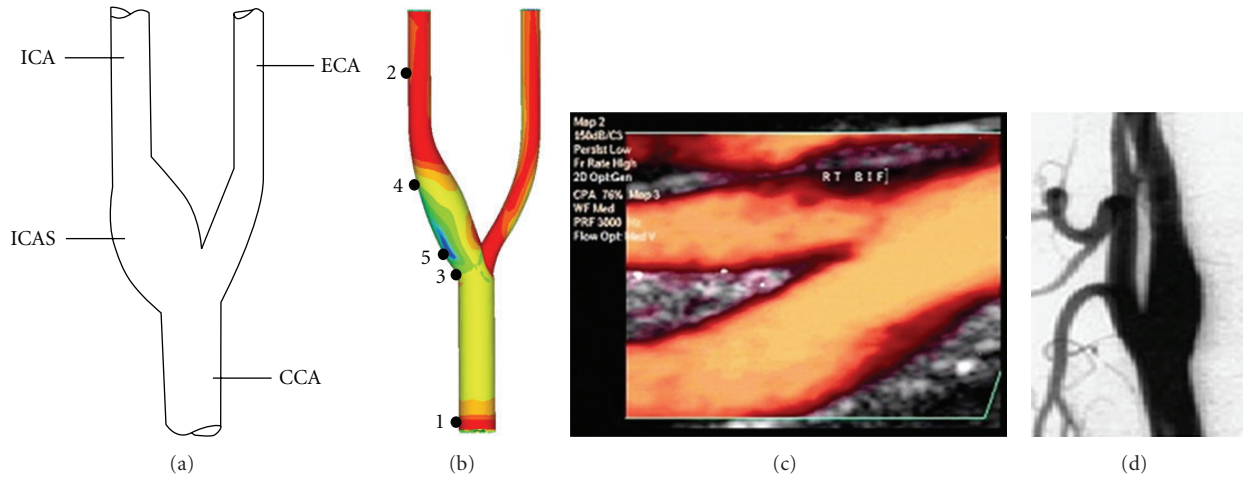


FIGURE 2: (a) Pictorial illustration of the carotid bifurcation vascular model. CCA: common carotid artery, ICA: internal carotid artery, ECA: external carotid artery, ICAS: internal carotid artery sinus. (b) The distribution of the shear stress in the carotid bifurcation vascular model. Color changes show the degree of shear stress. Blue represents the lowest shear stress while red is the highest. 1 and 2: control locations of CCA and ICA; 3 and 4: anterior and posterior edges of the low shear stress region; 5: core region of the low shear stress area. (c) The Doppler ultrasound image of carotid artery in long axis plane. (d) The CTA image of carotid artery in coronal plane.

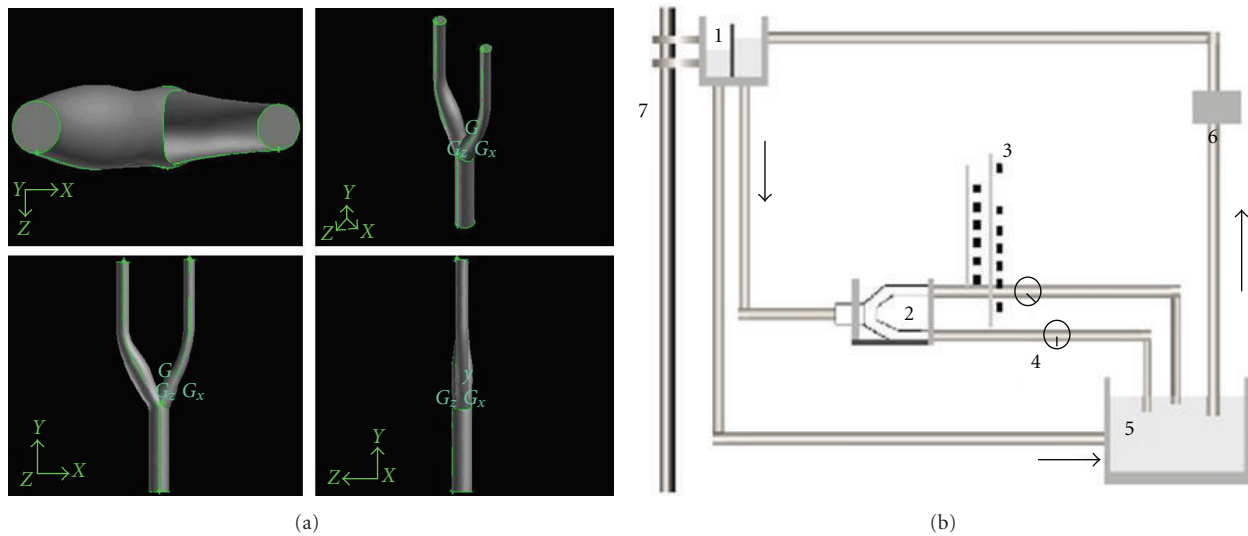


FIGURE 3: (a) Schematic diagram of the numerical simulation model (four different views angles). (b) The schematic diagram of the experiment recirculation system. Indicating points are (1) upstream reservoir, (2) carotid bifurcation vascular model, (3) manometer, (4) flow meter, (5) downstream reservoir, (6) centrifugal pump, and (7) slide pole.

2.3. *Hydrodynamic Parameters of Blood Flow.* The parameters of the blood flow in the model were controlled by the particle image velocimetry (PIV) using a type PIV-400-10 (TSI Company, Shoreview, MN, USA) and numerical simulation (NS) [13]. The average flow velocity of ICA was set at 0.559 m/s, which is the average flow velocity within the ICA measured in the human body at 150 mmHg blood pressure.

A solution prepared with 7.5% glycerol with a viscosity of 0.782 mPa.s and a density of  $1.005 \times 10^3 \text{ kg/m}^3$  (for pre run and stabilize the equipment) was measured by the Low Shear 30 (CONTRAVES LOW SHEAR 30 ISCOMETER, Swiss). This viscosity was chosen because it was the same viscosity

as the M199 culture medium used for the endothelial cells. Blood flow parameters determined were flow rate (mL/s) and velocity of the circulation liquid through the model (flow velocity, m/s).

2.4. *Separation of HDL and LDL.* Human plasma lipoproteins were collected and separated using the one-time density gradient ultracentrifugation method described by Zhang and Liu [14]. HDL and LDL bands were collected from centrifuged samples using a long syringe needle and were dialyzed in a buffer containing 0.02 mol/L Tris-HCl, 0.85% NaCl, 0.01% EDTA, and 0.01%  $\text{NaN}_3$  at pH 7.6. Dialysis was performed at 4°C in the dark for 6 hours each time

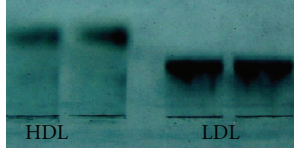


FIGURE 4: Purity of HDL and LDL banding patterns in gel electrophoresis after density gradient ultracentrifugation.

and completely repeated 4 times in order to remove sodium bromide. Collected lipoproteins were stored at 4°C following filtration (storage and dialysis were performed under a nitrogen atmosphere to avoid oxidation). Figure 4 shows the high purity of the isolated LDLs and HDLs. In total, 100 mL of circulation liquid was prepared for the experiments, including 80 ml M199 medium and 20 mL of separated human plasma lipoproteins (i.e., 10 mL LDL and 10 mL HDL). Lipoprotein concentrations were determined with an OLYMPUS automatic biochemical analyzer (OLYMPUS automatic biochemical analyzer AU2700, Japan). The concentrations of LDL and HDL in the bulk flow ( $C_0$ ) were 0.575 mmol/L and 0.242 mmol/L, respectively.

**2.5. Experimental Procedure.** HDL and LDL concentration were measured under two different ICA flow velocities at 5 different locations in the model. The low-speed group had an average ICA flow velocity of 0.559 m/s (the average flow velocity of ICA in human body under 150 mmHg blood pressure), while the high-speed group had an average ICA flow velocity of 1.451 m/s (the peak flow velocity of ICA in human body under 90 mmHg blood pressure). Hydrodynamic parameters (i.e., blood flow in the low- and high-speed groups) were measured and have been summarized in Table 2.

After allowing the model to stabilize for 30 minutes, 50  $\mu$ L samples were sequentially collected from each of the 5 locations and 5 samples were collected consecutively from each location. The samples were collected 15 minutes apart to ensure that samples were collected at a constant flow. The collected samples were individually placed in polyethylene tubes and stored protected from light in brown bottles at 4°C. Lipoprotein concentrations were measured within 4 hours of collection. The ratio of the concentration of LDL at the surface ( $C_{IS}$ ) to the concentration in bulk ( $C_{I0}$ ) was used as an index for concentration polarization of LDL. The ratio of the concentration of HDL at the surface ( $C_{HS}$ ) to the concentration in bulk ( $C_{H0}$ ) was used as an index for concentration polarization of HDL. Polarization of LDL and HDL was considered to have occurred if the ratio was greater than 1.000.

**2.6. Statistical Analysis.** The experimental result is shown in mean number  $\pm$  standard deviation ( $\bar{x} \pm s$ ). Comparison between multiple groups was performed using one-factor analysis of variance, whereas comparison between two groups involved the  $t$ -test. Data correlation contrast analysis was performed using linear regression. The result was deemed as a significant difference when  $P$  was below 0.05.

TABLE 2: Hydrodynamic parameters for low-speed and high-speed flow groups.

Group	Flow rate (mL/s)	Flow velocity (m/s)
Low-Speed	60.62	0.559
High-speed	155.93	1.451

All statistical analyses were computed using the SPSS11.5 statistics package.

### 3. Results

**3.1. The Surface Concentration of LDL and HDL at Low-Speed Flow Group.** See (Table 3).

**3.2. The Surface Concentration of LDL and HDL at High-Speed Flow Group.** From Tables 3 and 4, LDL and HDL concentration polarization on the inner surface of carotid artery bifurcation model was observed at every sampling point in both two groups.

**3.3. Relationship between Concentration Difference of HDL and LDL and Shear Stress.** LDL and HDL concentration difference on the inner surface of carotid artery bifurcation model was observed.

Absolute values of concentration difference between LDL and HDL on each sampling point of low- and high-speed flow groups (Table 5) were compared. No statistic difference was observed when absolute values of concentration difference between LDL and HDL on Sampling Points 1 and 2 were compared. However, statistical difference was noted by comparing absolute values of concentration difference between LDL and HDL on Sampling Points 3, 4, and 5;  $P$  value was less than 0.05.

Comparing the ratio of LDL concentration at the inner wall surface on each sampling point of low- and high-speed flow group to concentration in bulk flow and the ratio of HDL concentration at the inner wall surface to concentration in bulk flow, the difference value showed the following: ratio of LDL concentration at the inner wall surface in low-speed flow to concentration in bulk flow was significantly higher than HDL; the difference between these two values was a positive value. However, the ratio of LDL concentration at the inner wall surface in high-speed flow to concentration in bulk flow was significantly lower than HDL; the difference between these two values was a negative value. Statistical difference was observed by comparing difference between the ratios of LDL and HDL concentration at the inner wall surface from these two groups to concentration in bulk flow.

As demonstrated in Figure 5, absolute values of concentration difference between LDL and HDL at the inner wall surface decreased with the increase in shear stress when shear stress was less than 1.5 Pa. This variation trend would be more pronounced if shear stress were less than 0.5 Pa. After shear stress increased to 1.5 Pa, absolute values of concentration difference between LDL and HDL at the inner surface of wall remained unchanged according to shear stress.

TABLE 3: The surface concentration of LDL and HDL at low-speed flow group.

Sampling point	Shear stress (Pa)	$C_{ls}$ (mmol/L) ( $n = 5$ )	$C_{ls}/C_{l0}$	$C_{hs}$ (mmol/L) ( $n = 5$ )	$C_{hs}/C_{h0}$
1	1.921	$0.576 \pm 0.015$	1.011	$0.242 \pm 0.005$	1.008
2	1.537	$0.581 \pm 0.033$	1.049	$0.246 \pm 0.006$	1.025
3	0.448	$0.696 \pm 0.013^{**\#}$	1.221 <sup>**#</sup>	$0.276 \pm 0.005^{*\#}$	1.150 <sup>**#</sup>
4	0.297	$0.744 \pm 0.018^{**\blacktriangle}$	1.305 <sup>**\blacktriangle</sup>	$0.304 \pm 0.008^{**\blacktriangle}$	1.292 <sup>**\blacktriangle</sup>
5	0.069	$0.820 \pm 0.028^{**\blacktriangle\#\#}$	1.439 <sup>**\blacktriangle\#\#</sup>	$0.352 \pm 0.008^{**\blacktriangle\#\#}$	1.407 <sup>**\blacktriangle\#\#</sup>

\* $P < 0.05$  versus points 1 and 2, \*\* $P < 0.01$  versus points 1 and 2.

$\blacktriangle P < 0.05$  versus point 3,  $\blacktriangle\blacktriangle P < 0.01$  versus point 3

$\#P < 0.05$  versus point 4,  $\#\#P < 0.01$  versus point 4.

$C_{ls}$ : LDL concentration at surface.

$C_{hs}$ : HDL concentration at surface.

$C_{l0}$ : LDL concentration in bulk flow.

$C_{h0}$ : HDL concentration in bulk flow.

TABLE 4: The surface concentration of LDL and HDL at high-speed flow group.

Sampling point	Shear stress (Pa)	$C_{ls}$ (mmol/L) ( $n = 5$ )	$C_{ls}/C_{l0}$	$C_{hs}$ (mmol/L) ( $n = 5$ )	$C_{hs}/C_{h0}$
1	5.833	$0.576 \pm 0.015$	1.011	$0.242 \pm 0.004$	1.008
2	4.661	$0.584 \pm 0.006$	1.025	$0.244 \pm 0.006$	1.017
3	2.329	$0.584 \pm 0.152$	1.025	$0.250 \pm 0.012$	1.041*
4	1.334	$0.592 \pm 0.130\Delta$	1.042 $\Delta$	$0.252 \pm 0.008$	1.050*
5	0.896	$0.614 \pm 0.151\Delta\Delta^{**\blacktriangle\#}$	1.077 $\Delta\Delta^{*\blacktriangle\#}$	$0.262 \pm 0.008^{**\blacktriangle}$	1.092 <sup>**\blacktriangle\#</sup>

$\Delta P < 0.05$  versus point 1,  $\Delta\Delta P < 0.01$  versus point 1.

\* $P < 0.01$  versus points 2, \*\* $P < 0.01$  versus points 2.

\* $P < 0.01$  versus points 1 and 2, \*\* $P < 0.01$  versus points 1 and 2.

$\blacktriangle P < 0.05$  versus point 3,  $\blacktriangle\blacktriangle P < 0.01$  versus point 3.

$\#P < 0.05$  versus point 4,  $\#\#P < 0.01$  versus point 4.

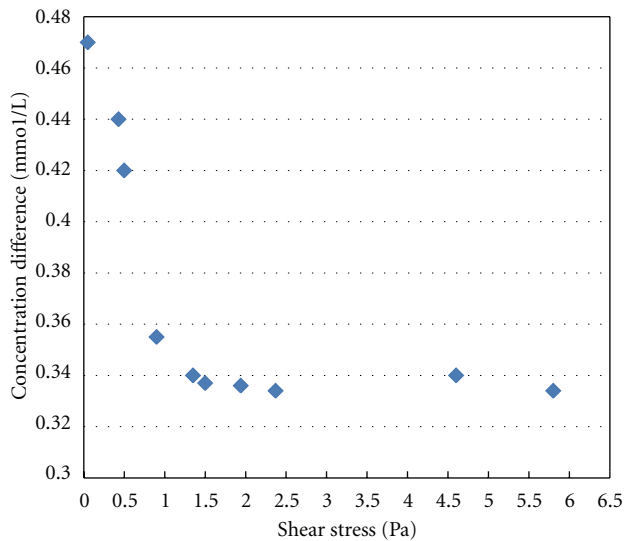


FIGURE 5: Relationship between concentration difference of HDL and LDL and shear stress.

Statistics revealed that on the inner wall surface of ICAS, absolute values of concentration difference between LDL and HDL at the inner wall surface were negatively correlated with shear stress ( $r = -29.386$ ,  $P = 0.022$ ). After shear stress increased to 1.5 Pa, concentration difference between

LDL and HDL at the inner wall surface was maintained at a relatively constant lower level. No negative correlation was observed.

Results revealed a concentration difference between LDL and HDL at the inner wall surface, particularly on the inner wall surface of ICAS.

#### 4. Discussion

Concentration increment of LDL and concentration decrement of HDL are independent risk factors for the development of AS. They assume opposite roles. While the former is a harmful lipoprotein, the latter is a protective one. The major reasons for the anti-AS mechanism of HDL are as follows: participating reverse cholesterol transcription, anti-LDL oxidation, and the protection of endothelial cells [15–22]. In the atherogenic mechanism of LDL, there are more ROS ( $O_2^-$ ,  $H_2O_2$  and ect) in the area with low shear stress because of increased expression of NADPH oxidase and defect in oxygen transfer. This accelerates LDL oxidation and generates Ox-LDL. Ox-LDL can induce expression of vascular endothelial cell MCP-1 to result in adhesion and migration of monocyte. Similarly, it can reduce expressions of antiapoptotic proteins, Bcl-2, and c-IAP-1, by combining specific receptors LOX-1 to induce cell apoptosis. Thus, concentration polarization of LDL provides pathogenic Ox-LDL with sufficient substrate, and in the setting of low shear stress environment, makes the endothelial cells in these

TABLE 5: Concentration difference between LDL and HDL on each sampling point on the inner vascular wall surface of carotid artery bifurcation model.

Sampling points	$CH_{LDL} - CH_{HDL}$ (mmol/L) ( $n = 5$ )	$RH_{LDL} - RH_{HDL}$ ( $n = 5$ )	$Cl_{LDL} - Cl_{HDL}$ (mmol/L) ( $n = 5$ )	$RL_{LDL} - RL_{HDL}$ ( $n = 5$ )
1	$0.334 \pm 0.012$	0.003	$0.334 \pm 0.029$	0.003
2	$0.340 \pm 0.016$	0.008	$0.335 \pm 0.017$	0.024
3	$0.334 \pm 0.015$	-0.016	$0.420 \pm 0.017^{**}$	0.071 <sup>▲</sup>
4	$0.340 \pm 0.016$	-0.008	$0.440 \pm 0.015^{**}$	0.013 <sup>▲▲</sup>
5	$0.352 \pm 0.020$	-0.015	$0.468 \pm 0.030^{**}$	0.032 <sup>▲</sup>

$CH_{LDL} - CH_{HDL}$ : Concentration difference between LDL and HDL at the inner wall surface in high-speed flow group.

$Cl_{LDL} - Cl_{HDL}$ : Concentration difference between LDL and HDL at the inner wall surface in low-speed flow group.

$RH_{LDL} - RH_{HDL}$ : Difference value of ratio of concentration between LDL and HDL at the inner wall surface in high-speed flow to concentration in bulk flow.

$RL_{LDL} - RL_{HDL}$ : Difference value of ratio of concentration between LDL and HDL at the inner wall surface in low-speed flow to concentration in bulk flow.

<sup>▲</sup> $P < 0.05$  versus  $RH_{LDL} - RH_{HDL}$ , <sup>▲▲</sup> $P < 0.01$  versus  $RH_{LDL} - RH_{HDL}$ ; <sup>\*\*</sup> $P < 0.01$  versus  $CH_{LDL} - CH_{HDL}$ .

areas more vulnerable to the damage, and thus facilitates occurrence of atherosclerosis [23–26].

Concentration polarization degree of HDL and LDL is correlated with shear stress. However, the degree of HDL polarization and LDL polarization is different under different shear stress. As evidenced in Table 5, under high-speed flow circumstance, shear stress at the inner wall surface of ICAS (sampling point 5) increased when low-speed flow was compared, and the LDL concentration polarization degree was lower than HDL. This indicated that concentration polarization degree of lipoprotein with different molecular weight and size is different under different shear stress. We have furthered the study on this phenomenon and proposed the concept of “concentration difference” between HDL and LDL.

According to the phenomenon observed in experiments, we compared the absolute values of LDL-HDL concentration difference at the wall surfaces of every point in low- and high-speed flow with difference value of ratio of concentration in bulk flow. Statistical results revealed that in CCA and ICA (sampling points 1 and 2), no obvious difference in absolute values of concentration difference was observed. However, in ICAS, absolute value of concentration difference between LDL and HDL at the inner wall surface in low-speed flow was significantly higher than that in high-speed flow; in the ICAS area with wall shear stress less than 0.5 Pa, the absolute value of concentration difference between LDL and HDL at the inner wall surface was negatively correlated with shear stress. In ICAS, a significant difference was observed between the difference value of ratios of LDL and HDL concentration at the inner wall surface in high- and low-speed flow to concentration in bulk flow. In low-speed flow, wall shear stress in ICAS part was lower, the difference value between the ratio of concentration of LDL at the inner wall surface to concentration in bulk flow and ratio of concentration of HDL to concentration in bulk flow was a positive value. In high-speed flow, wall shear stress in ICAS was obviously increased, the difference value between the ratio of concentration of LDL at the inner wall surface to concentration in bulk flow and ratio of concentration of HDL to concentration in bulk flow was a negative value. This indicated that concentration polarization degree of LDL was higher than HDL in low-speed flow and low shear stress, and

concentration polarization degree of HDL was higher than LDL in high-speed flow and high shear stress.

We first proposed that in the situation with certain low shear stress in the flow field, concentration polarization at the inner wall surface of lipoproteins with different molecular weights would change along with change in shear stress, resulting in inconsistent concentration profile; this is referred to as concentration difference. According to our study on concentration difference, in low stress situations, the increase in harmful LDL outweighs the increase in protective HDL. Other studies have suggested that the occurrence probability of AS angiocardopathy would increase by 1%-2% if LDL level increased by 1% or if HDL level reduced by 1% [27, 28].

## 5. Conclusion

In conclusion, we propose that the formation of AS may be secondary to an imbalance between the proatherosclerotic LDL and the antiatherosclerotic HDL. We demonstrated that in low stress environment, the increase in LDL outweighs the increase in HDL leading to AS. On the other hand, in high stress environment, the increases in HDL outweighs the increase in LDL which leads to a protective effect on atherosclerosis.

## Authors’ Contribution

Y. Guo and Y. Shi contributed equally to this paper.

## Acknowledgment

This Work Was Supported by the National Natural Science Foundation of China (81170288).

## References

- [1] A. M. Gotto Jr. and E. A. Brinton, “Assessing low levels of high-density lipoprotein cholesterol as a risk factor in coronary heart disease: a working group report and update,” *Journal of the American College of Cardiology*, vol. 43, no. 5, pp. 717–724, 2004.

- [2] A. von Eckardstein and G. Assmann, "Prevention of coronary heart disease by raising high-density lipoprotein cholesterol?" *Current Opinion in Lipidology*, vol. 11, no. 6, pp. 627–637, 2000.
- [3] J. Chen, J. L. Mehta, N. Haider, X. Zhang, J. Narula, and D. Li, "Role of caspases in Ox-LDL-induced apoptotic cascade in human coronary artery endothelial cells," *Circulation Research*, vol. 94, no. 3, pp. 370–376, 2004.
- [4] J. R. Nofer, M. Walter, and G. Assmann, "Current understanding of the role of high-density lipoproteins in atherosclerosis and senescence," *Expert Review of Cardiovascular Therapy*, vol. 3, no. 6, pp. 1071–1086, 2005.
- [5] C. G. Caro, J. M. Fitz-Gerald, and R. C. Schroter, "Arterial wall shear and distribution of early atheroma in man," *Nature*, vol. 223, no. 5211, pp. 1159–1161, 1969.
- [6] C. G. Caro, J. M. Fitz-Gerald, and R. C. Schroter, "Atheroma and arterial wall shear. Observation, correlation and proposal of a shear dependent mass transfer mechanism for atherogenesis," *Proceedings of the Royal Society of London B*, vol. 177, no. 46, pp. 109–159, 1971.
- [7] S. Wada and T. Karino, "Theoretical study on flow-dependent concentration polarization of low density lipoproteins at the luminal surface of a straight artery," *Biorheology*, vol. 36, no. 3, pp. 207–223, 1999.
- [8] S. Wada and T. Karino, "Theoretical prediction of low-density lipoproteins concentration at the luminal surface of an artery with a multiple bend," *Annals of Biomedical Engineering*, vol. 30, no. 6, pp. 778–791, 2002.
- [9] G. Wang, X. Deng, and R. Guidoin, "Concentration polarization of macromolecules in canine carotid arteries and its implication for the localization of atherogenesis," *Journal of Biomechanics*, vol. 36, no. 1, pp. 45–51, 2003.
- [10] W. Meng, F. Yu, H. Chen et al., "Concentration polarization of high-density lipoprotein and its relation with shear stress in an in vitro model," *Journal of Biomedicine and Biotechnology*, vol. 2009, Article ID 695838, 8 pages, 2009.
- [11] P. Zilla, M. Deutsch, J. Meinhart et al., "Clinical in vitro endothelialization of femoropopliteal bypass grafts: an actuarial follow-up over three years," *Journal of Vascular Surgery*, vol. 19, no. 3, pp. 540–548, 1994.
- [12] Y. Mohammed and J. F. Verhey, "A finite element method model to simulate laser interstitial thermotherapy in anatomical inhomogeneous regions," *BioMedical Engineering Online*, vol. 4, article 2, 2005.
- [13] F. Yu, Y. Shi, W. Deng, H. Chen, Q. An, and Y. Guo, "Particle image velocimetry in measuring the flow fields distribution in carotid artery bifurcation model," *Sheng Wu Yi Xue Gong Cheng Xue Za Zhi*, vol. 24, no. 1, pp. 104–109, 2007 (Chinese).
- [14] L. H. Zhang and B.W. Liu, "Isolation of human plasma lipoproteins by one-time density gradient ultracentrifugation method," *Acta Biochimica et Biophysica Sinica*, vol. 21, pp. 257–260, 1989.
- [15] P. J. Barter and K. A. Rye, "Molecular mechanisms of reverse cholesterol transport," *Current Opinion in Lipidology*, vol. 7, no. 2, pp. 82–87, 1996.
- [16] E. Boisfer, D. Stengel, D. Pastier et al., "Antioxidant properties of HDL in transgenic mice overexpressing human apolipoprotein A-II," *The Journal of Lipid Research*, vol. 43, no. 5, pp. 732–741, 2002.
- [17] P. Dimayuga, J. Zhu, S. Oguchi et al., "Reconstituted HDL containing human apolipoprotein A-I reduces VCAM-1 expression and neointima formation following periaortic cuff-induced carotid injury in apoE null mice," *Biochemical and Biophysical Research Communications*, vol. 264, no. 2, pp. 465–468, 1999.
- [18] H. Hattori, T. Kujiraoka, T. Egashira et al., "Association of coronary heart disease with pre- $\beta$ -HDL concentrations in Japanese men," *Clinical Chemistry*, vol. 50, no. 3, pp. 589–595, 2004.
- [19] X. P. Li, S. P. Zhao, X. Y. Zhang, L. Liu, M. Gao, and Q. C. Zhou, "Protective effect of high density lipoprotein on endothelium-dependent vasodilatation," *International Journal of Cardiology*, vol. 73, no. 3, pp. 231–236, 2000.
- [20] M. Navab, S. Y. Hama, G. M. Anantharamaiah et al., "Normal high density lipoprotein inhibits three steps in the formation of mildly oxidized low density lipoprotein: steps 2 and 3," *The Journal of Lipid Research*, vol. 41, no. 9, pp. 1495–1508, 2000.
- [21] J. R. Nofer, B. Levkau, I. Wolinska et al., "Suppression of endothelial cell apoptosis by high density lipoproteins (HDL) and HDL-associated lysosphingolipids," *The Journal of Biological Chemistry*, vol. 276, no. 37, pp. 34480–34485, 2001.
- [22] I. S. Yuhanna, Y. Zhu, B. E. Cox et al., "High-density lipoprotein binding to scavenger receptor-BI activates endothelial nitric oxide synthase," *Nature Medicine*, vol. 7, no. 7, pp. 853–857, 2001.
- [23] J. Hwang, M. H. Ing, A. Salazar et al., "Pulsatile versus oscillatory shear stress regulates NADPH oxidase subunit expression: implication for native LDL oxidation," *Circulation Research*, vol. 93, no. 12, pp. 1225–1232, 2003.
- [24] D. W. Crawford, L. H. Back, and M. A. Cole, "In vivo oxygen transport in the normal rabbit femoral arterial wall," *The Journal of Clinical Investigation*, vol. 65, no. 6, pp. 1498–1508, 1980.
- [25] J. A. Berliner, M. C. Territo, A. Sevanian et al., "Minimally modified low density lipoprotein stimulates monocyte endothelial interactions," *The Journal of Clinical Investigation*, vol. 85, no. 4, pp. 1260–1266, 1990.
- [26] J. Chen, J. L. Mehta, N. Haider, X. Zhang, J. Narula, and D. Li, "Role of caspases in Ox-LDL-induced apoptotic cascade in human coronary artery endothelial cells," *Circulation Research*, vol. 94, no. 3, pp. 370–376, 2004.
- [27] D. J. Gordon, J. L. Probstfield, R. J. Garrison et al., "High-density lipoprotein cholesterol and cardiovascular disease. Four prospective American studies," *Circulation*, vol. 79, no. 1, pp. 8–15, 1989.
- [28] P. W. Wilson, K. M. Anderson, W. P. Castelli, and W. B. Kannel, "Twelve-year incidence of coronary heart disease in middle-aged adults during the era of hypertensive therapy: the Framingham Offspring Study," *The American Journal of Medicine*, vol. 90, no. 1, pp. 11–16, 1991.

## Research Article

# Therapeutic Vascular Compliance Change May Cause Significant Variation in Coronary Perfusion: A Numerical Study

S. Nobari,<sup>1,2</sup> R. Mongrain,<sup>1,2,3</sup> E. Gaillard,<sup>1</sup> R. Leask,<sup>4</sup> and R. Cartier<sup>2</sup>

<sup>1</sup>Department of Biomedical Engineering, McGill University, Montreal, QC, Canada H3A 2B4

<sup>2</sup>Department of Cardiovascular Surgery, Montreal Heart Institute, Montreal, QC, Canada H1T 1C8

<sup>3</sup>Department of Mechanical Engineering, McGill University, Montreal, QC, Canada H3A 0C3

<sup>4</sup>Department of Chemical Engineering, McGill University, Montreal, QC, Canada H3A 2B2

Correspondence should be addressed to S. Nobari, soroush.nobari@mail.mcgill.ca

Received 31 August 2011; Revised 8 November 2011; Accepted 21 November 2011

Academic Editor: Thomas Heldt

Copyright © 2012 S. Nobari et al. This is an open access article distributed under the Creative Commons Attribution License, which permits unrestricted use, distribution, and reproduction in any medium, provided the original work is properly cited.

In some pathological conditions like aortic stiffening and calcific aortic stenosis (CAS), the microstructure of the aortic root and the aortic valve leaflets are altered in response to stress resulting in changes in tissue thickness, stiffness, or both. This aortic stiffening and CAS are thought to affect coronary blood flow. The goal of the present paper was to include the flow in the coronary ostia in the previous fluid structure interaction model we have developed and to analyze the effect of diseased tissues (aortic root stiffening and CAS) on coronary perfusion. Results revealed a significant impact on the coronary perfusion due to a moderate increase in the aortic wall stiffness and CAS (increase of the aortic valve leaflets thickness). A marked drop of coronary peak velocity occurred when the values of leaflet thickness and aortic wall stiffness were above a certain threshold, corresponding to a threefold of their normal value. Consequently, mild and prophylactic treatments such as smoking cessation, exercise, or diet, which have been proven to increase the aortic compliance, may significantly improve the coronary perfusion.

## 1. Introduction

In some pathological conditions like aortic stiffening and calcific aortic stenosis, the microstructure of the aortic root and the aortic valve leaflets is altered in response to stress resulting in changes in tissue thickness, stiffness, or both [1, 2].

Aortic stiffening is the consequence of changes in the properties of the arterial wall that accompany aging and arterial hypertension. Increased aortic stiffness is associated with an elevation of systolic blood pressure, a reduction in diastolic blood pressure, and thus a widened pulse pressure [3]. This widened pulse pressure leads to left ventricular hypertrophy and increases the risk of stroke and myocardial infarction [4]. Accelerated arterial stiffness has been linked to diabetes [5, 6], hyperglycemia, hyperinsulinemia, and impaired glucose tolerance [7, 8].

Aging of the aortic valve (AV) is characterized by cuspal thickening [9] and loss of extensibility (i.e., increase of stiffness) [10], which can lead to progressive changes in AV function. The most common disease of the AV is calcific

aortic stenosis (CAS), found in 2% of patients over 65 years old and in 4% of those over 85 [11]. This pathology is characterized by the occurrence of calcified nodules on the valve leaflets, which can grow over time, thickening and stiffening the leaflets and eventually critically interfering with valve opening and potentially closing [12]. Currently, the most common treatment for CAS is the calcified valve replacement by a mechanical or a bioprosthetic valve [13]. CAS is the leading single etiology of valve disease necessitating valve replacement, accounting for a major fraction of the approximately 300,000 valve replacement surgeries worldwide each year [14].

Aortic stiffening and CAS are thought to affect coronary blood flow [15, 16]. Reduced aortic distensibility (i.e., increased aortic stiffness) results in a decrease of diastolic backflow that aids coronary perfusion, disturbing thus the oxygen demand/supply balance of the myocardium [17]. The presence of a severe CAS in patients markedly reduced the coronary flow reserve (CFR), a well-known characteristic of the distensibility of the coronary arteries [16]. This reduction of CFR can be explained by the concomitance of reduced

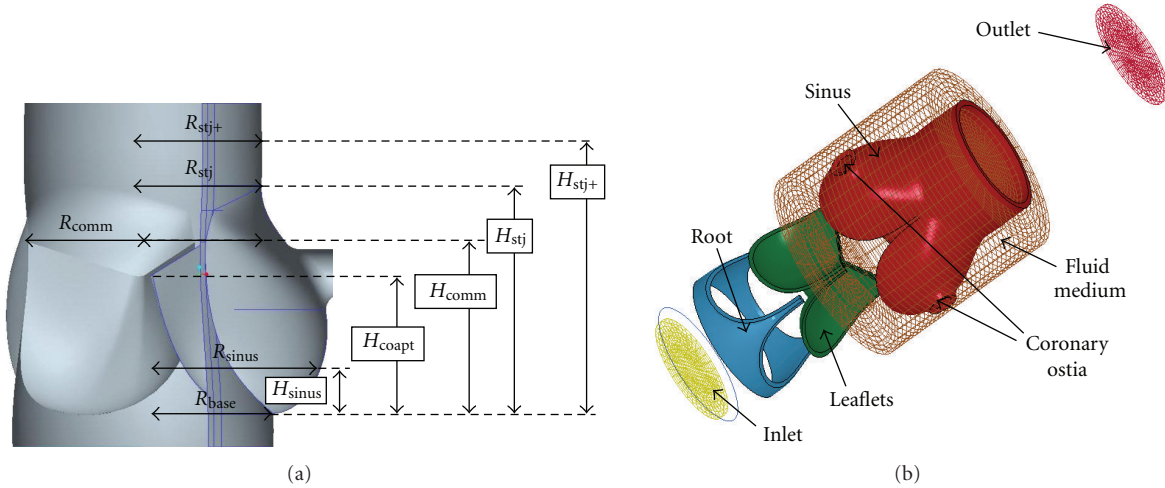


FIGURE 1: (a) Anatomical parameters used to create the 3D geometric model of the aortic root. (b) Exploded view of the final 3D CAD model.

myocardial supply as a result of decreased coronary perfusion pressure, and increased myocardial metabolic demand as a result of increased left ventricular workload.

In recent years, we have begun to address the critical area of fluid-structure interaction (FSI) and have developed our model of aortic valve including Valsalva sinuses but without coronary arteries [18]. Several other numerical studies have been carried out to improve the quality of the surgical procedures but without considering the coronary structures [19–22]. The goal of the present study was to include the flow in the coronary ostia in the previous FSI model, to analyze the effect of diseased tissues (aortic root stiffening and CAS) on coronary perfusion, and to link prophylactic treatments as smoking cessation, exercise, or diet with coronary perfusion changes. Inclusion of the coronaries will allow us to obtain hemodynamic variables related to coronary flow such as perfusion level and velocity distribution. It would also allow investigating the possible mutual effect between coronary pathologies, and aortic wall stiffening and valve dynamics. However, this bidirectionality is out of the scope of this paper since it would require the global structure of the coronary vessels. Therefore, the current paper will present the one-way interaction between aortic wall stiffening and CAS, and their effect on coronary perfusion. Even though coronary autoregulation—the intrinsic ability to maintain a constant blood flow despite changes in perfusion pressure—might mitigate some of this interaction [15, 23, 24], in a first approach, in order to simplify the analysis, autoregulation was not incorporated into the model.

## 2. Methods

The finite element software LS-DYNA (Livermore Software Technology Corporation, Livermore, CA, USA) was used to perform all FSI simulations.

**2.1. Model Geometry.** A generic, anatomically inspired 3D model of the aortic valve was derived from a combination of

imaging modalities (MRI, 3D-digitization) and pathological data as previously described by Ranga et al. [18] and Campbell et al. [25]. Dimensions for the anatomical parameters were taken as the average of various values reported in previous studies [26]. A drawing showing these parameters is presented in Figure 1(a), while Figure 1(b) shows a finalized version of the model in an exploded view along the axial direction. The model is made of two main domains, the solid and the fluid, each containing subassemblies. Three components comprise the solid medium: the aortic root, the leaflets, and the sinuses. The sinus component additionally includes a portion of the ascending aorta and the two coronary ostia. The fluid medium also consists of three components: an inlet, an outlet, and the central region. This region embeds the entire cardiac tissue to accommodate for the fluid-structure interaction. The fluid external to the aortic wall represents the pericardial fluid and is considered to be stagnant and at atmospheric. The base of the valve and inlet of the reservoir are connected together restricting the displacement in the axial direction. This guarantees that the two domains remain connected during the analysis.

The model was meshed in ANSYS, discretizing the solid components into 10,892 shell elements. These shell elements were used instead of solid brick elements because they can have several integration points allowing bending to be modeled while satisfying the physics of the model. The fluid medium, on the other hand, consisted of 24,500 hexahedral elements. This was found to be an adequate mesh density after doing mesh refinements and mesh independency tests by increasing mesh node numbers up to twice their initial value. After convergence, the percent differences in velocity results using a point-to-point Euclidean norm were less than 2.78%. This meshing was then transformed into the format of an input file including the whole geometry, material properties, boundary conditions, and loads to be analyzed in LS-DYNA.

**2.2. Material Properties.** Cardiac tissue is a highly complex material. In the context of large strains, heart tissues can

be modeled using nonlinear material properties [22, 27–29]. However, under normal physiological conditions, the strain in the aortic root varies in the range of about 10% [30, 31]. A recent study has shown that even though the stress-strain curve of the cardiac tissue is nonlinear, it can be subdivided into two linear regions: one at low strain range (below 15%) and another at high strain rates [32]. At low strain rates, this linearity is even more pronounced and a study by our group has shown that at these physiological strains the stress-strain curve of aortic tissue can essentially be considered linear [33]. Given the related advantages, we implemented a linear elastic material property to model the healthy cardiac tissue with a Young's modulus (incremental modulus) of 3.34 and 4.00 MPa for the aortic root and leaflets, respectively, and a Poisson's ratio of 0.45. These values are in the physiological range and are similar to the values used in previous studies [22, 34]. In fact, it has been shown that with this assumption the stress levels are within acceptable ranges as compared to hyperelastic modeling [35, 36]. The main reason for neglecting the viscous effects was to isolate the effect of the elastic component in the artery. This allowed us to investigate the consequence of aortic wall stiffening and valve thickening on the energy stored in this elastic component, which would ultimately affect coronary perfusion. The roll of viscous terms become significant when the smooth muscle cells are activated [37, 38]. Since the microstructure of the vessel has not been the focus of this study and the smooth muscle cells have not been considered, the viscous effects could be neglected.

As for blood, its density was set to  $1060 \text{ Kg/m}^3$ . At high levels of shear rate ( $>50 \text{ s}^{-1}$ ), the dynamic viscosity of blood varies between 3 and  $4 \text{ mPa}\cdot\text{s}$ , meaning that in general a simple Newtonian relationship may be used in studies of the larger vessels [39]. In summary, the fluid was considered Newtonian with a density of  $1060 \text{ kg} \cdot \text{m}^{-3}$  and a dynamic viscosity of  $3.5 \text{ mPa}\cdot\text{s}$ .

### 2.3. Boundary Conditions

**2.3.1. The Fluid Medium.** There are four sets of boundary conditions in the fluid medium that need to be defined. These boundary conditions are imposed at the aortic root, the ascending aorta, and the two coronary ostia. In order to account for the pulsatility of the flow, the inlet condition at the aortic root is taken to be the difference between the ventricular pressure and the aortic pressure. Therefore, the outlet of the ascending aorta has a free boundary condition, meaning fluid can flow freely, an approach borrowed from previous studies [27]. The result is that the entire system is under an overall smaller pressure and the shell elements of the solid medium are subjected to a reduced transvalvular load while maintaining the pressure gradient across the valves.

As for the two coronary ostia, it is known that the hydraulic resistance of the coronary vascular bed is largely time dependent and that much of this phenomenon is attributed to the vasocontraction of the coronary vessels [40]. This resistance is one of the controlling factors of how much flow will enter each of the coronaries. In order

to incorporate this into the model and study the effect of pathologies on coronary perfusion, two types of boundary conditions were imposed at the ostia depending if we were studying a healthy or pathological case. First, in the healthy case, clinical values of coronary flow [41] were imposed as boundary conditions. This leaves the pressure and velocity profile unconstrained and allows them to self-establish. Second, for pathological conditions, this same pressure obtained at the ostia for the healthy case is used as the new boundary condition, which will allow the flow to self-establish. This enables us to study the effect of a single parameter on the coronary perfusion. In previous studies by our group, zero coronary flow conditions were investigated and leaflet dynamics and stresses were compared to clinical data [18]. A comparison of the results from this previous study, a hypertensive case, and the current model with clinical data are presented in Section 3.1.1 and commented further in the discussion section.

**2.3.2. The Solid Medium.** In the solid medium, boundary conditions were applied at the aortic ring, the ascending aorta, the coronary ostia, and the leaflets. These boundary conditions constrain the rigid body motion (twisting, rotation, translation) but are not so limiting as to overrestrict the dynamics of the structure allowing for deformation [42]. To achieve this end, the geometry of the model contains a significant portion of the ascending aorta to fully constrain the outlet ring without affecting valvular dynamics. This constrain restricts motion and rotation in any direction at the top edge of the ascending aorta. On the other hand, at the level of the inlet ring, a constraint was applied to prevent the model from deforming and movement in the axial direction only. Hence the radial motion, and thus root expansion, was not constrained at the inlet.

The contact between leaflets was defined using CONTACT\_AUTOMATIC\_GENERAL in LS-DYNA environment, which is a single surface contact and checks for penetration along the entire length of the free (unshared) shell edges. This is a critical point in the modeling procedure since it prevents the shell elements from penetrating through each other and creating unrealistic leaflet motion. Finally, the coronary ostia were fully constrained in all rotational and translational degrees of freedom to avoid element deformation, which could possibly lead to coronary closure.

**2.4. Governing Equations.** The simulation of the complete cardiac cycle is performed using a fluid-structure interaction approach. Additionally, for the fluid flow part, the blood velocity is calculated in the context of the ALE formulation of the Navier-Stokes equations, which can be obtained by replacing the convective velocity in the standard Navier-Stokes equations by the relative velocity to the moving mesh. The general form is as follows:

$$\begin{aligned} \rho \frac{\partial v}{\partial t} + \rho(v - w) \cdot \nabla v - \nabla \cdot \sigma &= 0 \quad \text{in } \Omega_f, \\ \nabla \cdot v &= 0 \quad \text{in } \Omega_f, \end{aligned} \quad (1)$$

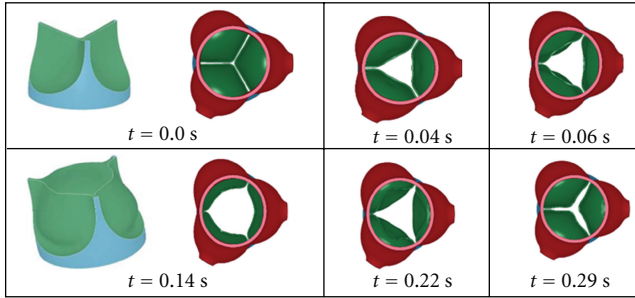


FIGURE 2: The computed opening and closing patterns of the leaflets, seen from the aorta. Note that at time  $t = 0.0$  s, the leaflets are in perfect contact. The apparent gap in the first frame corresponds to the shell (Phantom) thickness.

where  $\rho$  is the fluid density,  $v$  the velocity vector of the fluid in a fixed coordinate system,  $t$  is the time,  $w$  the velocity of the fluid medium, and  $\sigma$  the Cauchy stress tensor defined by:

$$\sigma = -pI + \tau, \quad (2)$$

where  $p$  denotes the fluid pressure and  $\tau$  the viscosity stress tensor.

The fluid-structure problem presented here consists of a fluid medium  $\Omega_f$  and an immersed solid medium  $\Omega_s$ . In order to capture the fluid-structure interaction, these two mediums need to be coupled. This coupling is obtained by applying a no slip condition

$$v_f - v_s = 0, \quad (3)$$

where  $v_f$  and  $v_s$  represent the fluid and the structure velocity, respectively, in the coupling interface.

### 3. Results

**3.1. The Solid Medium.** The engineering parameters of interest in the solid medium include the leaflet morphologies, leaflet velocities, and leaflet stresses. Although the solid medium contains the aortic root, sinuses, and ascending aorta, the most accurate clinical data available are related to the leaflets.

**3.1.1. Leaflet Morphologies and Dynamics.** Looking from the ascending aorta back towards the left ventricle, known as the short-axis view, reveals some key features. An important aspect that can be quantified clinically is the cross-sectional valve opening during the cardiac cycle. The computed leaflet morphologies during the opening and closing phases are presented in Figure 2.

For a more quantitative assessment, it is also possible to track the velocities at the leaflet tips. Some common aspects of the leaflet dynamic histories that have been clinically quantified by echocardiography studies are the rapid valve opening time (RVOT), rapid valve opening velocity (RVOV), rapid valve closing time (RVCT), rapid valve closing velocity (RVCV), and ejection time (ET). For each

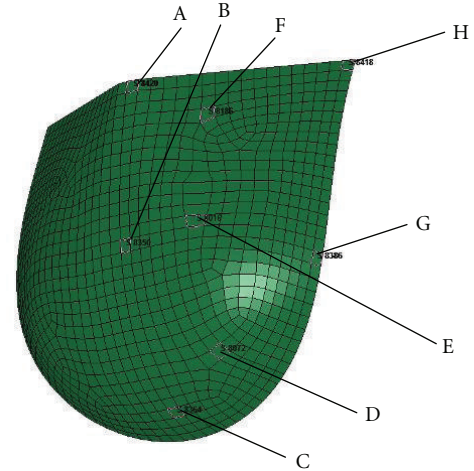


FIGURE 3: Illustration of the selected FE elements from which the von-Mises stresses are sampled.

of these five parameters, average healthy values have been determined [43–46]. These values are compared to those derived from the current model in healthy (120/80 mmHg:  $\Delta P = 40$  mmHg) and hypertensive (140/90 mmHg:  $\Delta P = 50$  mmHg) conditions and are presented in Table 1.

In the FSI study by Ranga et al. in 2006 [18], zero coronary flow was considered, and the values for RVOT, RVCT, and ET were reported as 102.5, 85, and 280 ms, respectively.

**3.1.2. Leaflet Stresses.** In this section, both the principal and von-Mises stresses are reported and examined both quantitatively and qualitatively. The principal stresses in the leaflets were observed at two instants of the cardiac cycle, one at the beginning of systole and the other one at mid-systole (0.072 seconds into the cardiac cycle). In each of these moments, a preferential direction of these stresses was noticed in a circular arrangement around the attachment edge of the leaflet. Conversely, stress in the inner area, or belly, of the leaflet was more scattered, representing a less structured environment. This particular distribution was also qualitatively similar to previous reports and known stress patterns on the leaflets [38, 47].

The stress levels were also assessed by comparing them to previously reported values under similar conditions. The locations of the elements sampled for comparison of their stress histories are given in Figure 3. These particular elements spatially match those from the previous study of the leaflet stresses during the dynamic actions of the valve by Gnyaneshwar et al. [48].

The specific values computed for the stress magnitudes at these locations for both models and their percent differences are presented in Table 2.

**3.1.3. The Fluid Medium.** Validation in the fluid medium can be accomplished to a certain degree by comparing bulk flow properties of the model to known physiological data and

TABLE 1: Comparison between FSI and echocardiography leaflet dynamics.

	Current model (healthy case)	Current model (Hypertensive case)	Echocardiography (Healthy)	% difference between the healthy case and echo
RVOT ms	53	44.6	46.0	14.14
RVOV cm/s	25.7	34.3	29.2	12.75
RVCT ms	52.7	40.1	47.0	11.43
RVCV cm/s	16.3	20.7	23.6	36.59
ET ms	276.0	248.2	329.0	17.52

(RVOT: rapid valve opening time, RVOV: rapid valve opening velocity, RVCT: rapid valve closing time, RVCV: rapid valve closing velocity, ET: ejection time) healthy case (120/80 mmHg:  $\Delta P = 40$  mmHg) and hypertensive case (140/90 mmHg:  $\Delta P = 50$  mmHg).

TABLE 2: Comparison of the maximum stress (MPa) during the cardiac cycle in selected locations represented in Figure 3 in the proposed model and Gnyaneshwar model.

Location	Proposed model	Gnyaneshwar	% difference
A	0.492	0.15	106.54
B	0.311	0.20	43.44
C	0.480	0.42	13.33
D	0.390	0.24	47.61
E	0.380	0.28	30.30
F	0.158	0.13	19.44
G	0.914	0.90	1.54
H	0.478	0.40	17.76

also by searching for known flow patterns such as diastolic recirculation regions, which are known to occur, but are more difficult to quantify.

Blood velocities were sampled in the model at three locations: the flow through the valve at the level of the commissures and the sinotubular junction as well as flow through the coronary ostia. For the first two locations, comparisons to clinical data can be made over the entire cardiac cycle regarding both the total flow ejected and the temporal distribution of this flow. For the coronary flow, the shape of the waveform is less precisely known, although certain aspects, such as the total flow and the general shape, have been documented.

The computed velocities at the STJ, commissure, left, and right ostia are provided in Figure 4 with a peak velocity of 1.41 m/s occurring at 0.087 s. The fluid exhibits a rapid acceleration followed by a deceleration slightly smaller in magnitude, which is known to be the case physiologically. Coronary perfusion data are close to the known physiological values with an overall coronary perfusion of 100 mL/min or approximately 4% of the cardiac output.

We also considered the impact of varying the stiffness of the aortic wall elastic modulus from 3.34 MPa to 60 MPa and the thickness of the aortic valve leaflets from 0.05 to 0.1 cm to simulate aortic stiffening and CAS, respectively [49, 50]. In order to allow the coronary flow to self-establish, the prescribed flows at these locations were removed and the ostia were defined as outlets with no boundary conditions. Twenty-nine and eight different values were used for aortic wall stiffness and leaflet thickness, respectively.

Figure 5 represents the peak coronary velocity with respect to different aortic wall stiffness values ranging from 3.34 to 60 MPa and leaflet thicknesses from 0.05 to 0.1 cm.

As it can be seen from the figure above, the coronary flow exhibits slight variations up to certain critical values of stiffness and thickness for which a marked drop is observed. Although interesting, this phenomenon warrants to be confirmed with clinical evidence.

#### 4. Discussion

A model of the aortic valve including flow engaging in the coronary ostia was presented in this paper. An FSI analysis was performed using explicit LS-DYNA to study the aortic stiffening and the dynamics of the valve, and their effect on the coronary flow. The ALE method was used for the FSI analysis of this study. The results from this analysis in terms of leaflet morphologies, leaflet stresses, timing during the opening and closing phases, and velocities at critical points were presented. The leaflet morphologies during the opening and closing phases, shown in Figure 2, were comparable with previous studies and the valve opens to 69% of the cross-sectional area of the aortic ring [20]. Similar time-lapse images presented by other authors have demonstrated the same qualitative triangular orifice opening and leaflet billowing [19, 20, 22, 51].

For verification, known clinical parameters of rapid valve opening and closing time and velocities were presented in Table 1. We showed that our results match the echocardiography data reasonably well. The only exception would be RVCV, in which we reported a larger percent difference. We believe the reason for this occurring could be the smooth shape of the sinus structure that we synthetically generated with pathological data. Indeed, as it was demonstrated by Katayama et al. [52], the RVCV could be sensitive to the morphology of sinuses. We also reported that the results from a hypertensive case predict a more rapid opening and closing with a higher acceleration as expected. By comparing these results to those obtained by Ranga et al. [18] without coronary flow, we showed that the zero coronary flow tended to significantly increase the opening and closing times, while the results obtained in this study were closer to the clinical data obtained from echocardiography.

Leaflet stresses were presented in Section 3.1.2, and results from our simulation were compared to the study done by Gnyaneshwar et al. [48]. Similar points were selected as

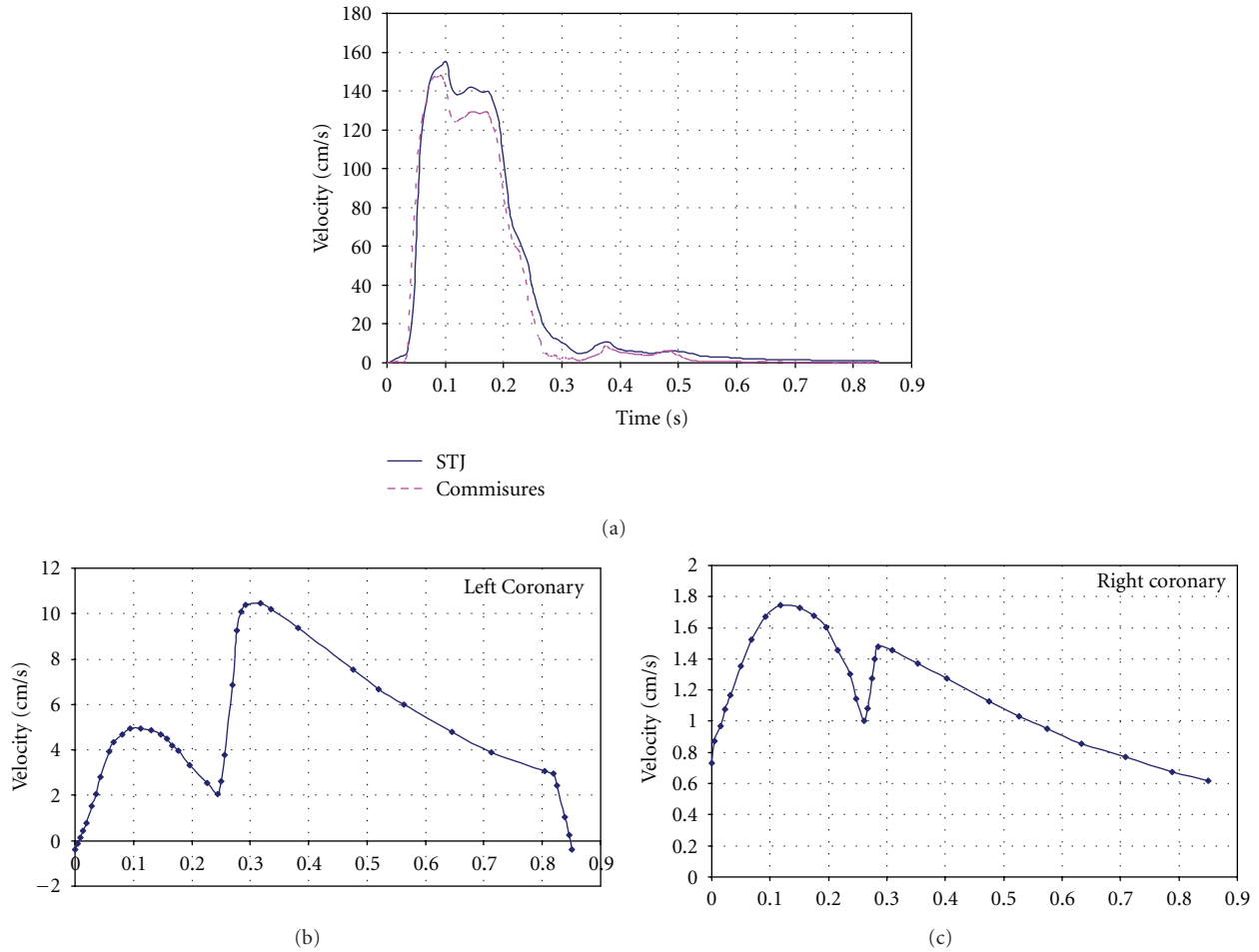


FIGURE 4: Computed velocity waveforms at (a) the STJ and commissures, (b) the left ostia and (c) the right ostia.

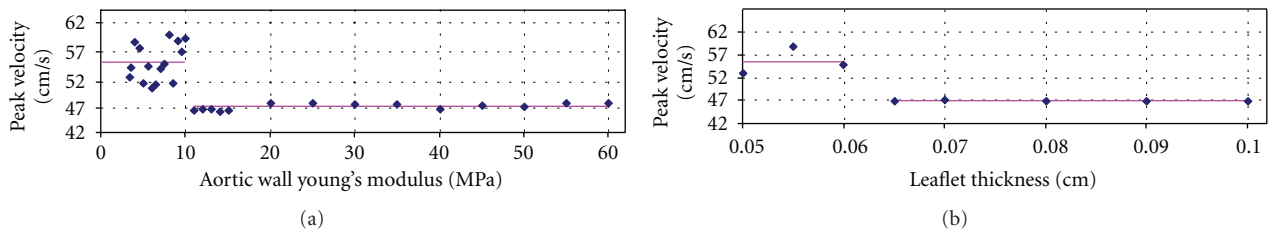


FIGURE 5: Behaviour of coronary peak velocity as a function of (a) aortic wall stiffness and (b) leaflet thickness.

to match those in the reference study. For both studies the results of stress values range between 0-1 MPa. Additionally, the models are also in agreement as to the locations of the stress minima and maxima (Figure 3). Differences were calculated, these values ranged from 0.06 MPa to 0.15 MPa with an average difference of 0.078 MPa.

Results obtained from the fluid domain including velocity at STJ or commissures were also in good agreement with previous studies. Another interesting result was obtained from a temporal examination of the velocity plots. Blood flow through commissures and STJ, in a sense, represent the bulk flow of the blood through the aortic valve. A peak velocity of 1.41 m/s occurred at 0.087 s, which is in agreement

with previous studies that have reported peak velocities of  $1.35 \pm 0.35$  m/s [35].

Results were also achieved for cases of aortic wall stiffening. These results revealed an impact of aortic wall stiffening on coronary flow. As shown in Figure 5, elastic modulus of the aortic wall was increased to a higher value than their healthy state, which caused a significant drop in coronary peak velocity after a threshold. This drop could be correlated to the decrease in coronary flow reserve (CFR) previously described in clinical studies [3, 17]. Aortic distensibility is a major determinant of left ventricular afterload [17]. Any deterioration of aortic distensibility (i.e., aortic stiffening) will result in ventricular-arterial mismatch

and left ventricular dysfunction, which may prove critical in certain stages of disease. Aortic stiffening may lead to an early return of the reflected arterial pulse wave causing an increase of systolic blood pressure (SBP) and a decrease in diastolic blood pressure (DBP), thus increasing the pulse pressure. Greater SBP increases myocardial oxygen consumption, reduces left ventricular ejection fraction, and increases left ventricular afterload inducing left ventricular hypertrophy. Myocardial blood supply depends largely on pressure throughout diastole and the duration of diastole, so the decrease of DBP can compromise coronary perfusion resulting in subepicardial ischemia. Moreover, left ventricular hypertrophy also reduces coronary flow [17].

These results showed that below a value of aortic wall elastic modulus being equivalent to three times the normal value of aortic wall elastic modulus, the peak coronary velocity remained constant. This observation could be correlated to the beneficial effects of smoking cessation, exercise, and diet on arterial compliance. Oren et al. [53] revealed, in a clinical study in 2006, that smoking cessation for 6 months significantly improved arterial stiffness. Oscillatory compliance rose from  $0.051 \pm 0.023$  to  $0.063 \pm 0.03$  mL/mmHg, which corresponds to an increase of 23%. A short time of smoking cessation has a strong effect on the arterial compliance. Exercise plays an important role on arterial compliance recovery too. Tanaka et al. [54] determined the role of habitual exercise on age-related decrease in central arterial compliance. They demonstrated that arterial compliance fell from about  $2 \text{ mm}^2/\text{mmHg}$  in sedentary healthy young subjects to values of about 1.2 to  $1.3 \text{ mm}^2/\text{mmHg}$  in middle-aged and older sedentary humans. But in the highly trained middle-aged and older subjects (on a 3-month exercise period), exercise appeared to reduce the decline in compliance with aging by about 50%. Again a short time of regular exercise has a strong effect on the arterial compliance. Finally diet has also a strong effect on arterial compliance. Nestel et al. [55] studied the impact of eating fish and fish oil on systemic arterial compliance during 4 weeks in fifteen obese people. They showed that the systemic arterial compliance rose significantly of about 85%.

Consequently, the results we obtained associated with those of Oren et al. [53], Tanaka et al. [54], and Nestel et al. [55] showed that a short period of smoking cessation, regular exercise, or diet may restore the peak coronary velocity to a normal value and therefore reestablish a good coronary perfusion.

The increase of aortic valve leaflets thickness (mimicking CAS) led to a decrease in coronary peak velocity. Above a certain threshold, a marked drop in peak velocity occurred. These results were again in agreement with previous studies [16, 56]. In patients with CAS and a normal coronary angiogram, the CFR is significantly lower [50]. The CFR capacity of the coronary arteries depends on at least three main components: (1) micro- and macrovascular resistance, (2) myocardial resistance, and (3) the effect of viscosity [57]. In some pathologic conditions like aortic stiffening and CAS, changes in one or other of these factors may lead to an impairment of the CFR capacity.

It is known that aortic compliance is reduced as the cardiac tissue becomes aged and pathological [58]. Recently it has been shown that a stiff aorta is associated with a reduction in coronary blood flow [3, 56, 59]. However, there is little information relating coronary flow and aortic stiffness in humans [60]. An explanation for the drop in coronary flow observed in our simulation could be linked to the fact that 70–90% of the coronary perfusion occurs during diastole [61, 62] and also the fact that it is during this phase that blood is driven towards the coronary arteries by the elastic recoil of aorta (Windkessel model) [63]. This elastic recoil is the potential energy stored in the walls during systole and released during diastole to aid leaflet closure and blood perfusion through coronaries. Approximately 50% of the stroke volume is directly forwarded to the peripheral circulation [64]. Peripheral resistance and elastic extension of the aortic wall are responsible for storage of the other 50% of the stroke volume, the storage volume [65]. Reduction in aortic compliance will induce an increase on the impedance to the ventricular ejection which will lead to a decrease in coronary flow [66].

For a less compliant aortic wall, the impact of the reduction in elastic recoil would be direct as less energy is stored in the wall during systole. As for the case where the leaflets have thickened, this loss in the potential energy could be linked to the increase in blood velocity through the valves (due to reduction of effective orifice area) and the associated pressure drop. In that context, we believe that the hydraulic resistance and the vessel compliance could compound to produce the observed sudden drop in the perfusion.

Several assumptions and simplifications were made in the present study. A linear elastic model was used to mimic aortic root and aortic valve leaflets behavior, which leads to a short computing time compared to nonlinear models. However, in the context of aneurismal diseases, the linear elastic model used for its simplicity and ease of calculations would need to be expanded to nonlinear elastic in order to take into account for the large deformations. In addition, to investigate the aneurysm rupture process, it would be required to generalize the assumption of an isotropic model, which is sufficient for global assessment, to anisotropic model to integrate the vascular microstructures.

As for boundary conditions, the inlet boundary condition at the ventricular level is considered to be the pressure difference between the ventricle and aorta. This is an inevitable constraint imposed on the model to avoid introducing instabilities and extensive run-times in an already complex FSI model. This assumption will cause the aortic wall to experience a smaller pressure, specifically during mid-systole. As a result aortic root expansion will be reduced, which could affect the leaflet opening and closing pattern. The percent difference observed for RVCV could also be due to this reduced expansion and loss of distensibility in the sinuses. This assumption might cause the drop observed in the coronary perfusion to have a minor shift across the range of wall stiffness and leaflet thickness studied. Moreover, the leaflets thickness was considered constant on the whole leaflet surface, whereas this one varies along the leaflet. The leaflets are the thinnest in the belly, their load-bearing part.

They become thicker towards the line of attachment and the leaflet free edge. The thickest part is the nodule of Arrantius, just below the center of the free edge [67]. Finally, the coronary ostia were only considered in this study and not the complete coronary arteries.

## 5. Conclusion

In this study, we have shown that a moderate increase in aortic stiffness and aortic leaflet thickness (CAS) will lead to a noticeable drop in coronary perfusion. Considering the fact that short-term smoking cessation, regular exercise or diet could cause a mild change in aortic compliance; this study suggests that such preventions and/or prophylactic treatments could significantly improve the coronary perfusion. The thresholding phenomena observed via a drop in the coronary flow, due to varying the stiffness and thickness of the aortic wall and leaflet tissues, are very interesting as it suggests a possible interaction between valvular and coronary diseases but warrants further analysis with exhaustive clinical data.

The incorporation of the coronary ostia improved the opening and closing valve dynamics, compared to a model without the coronary arteries. The model is sensitive enough to differentiate between normal and slightly hypertensive conditions showing distinct impact on the valves dynamics.

The proposed model that incorporated perfusions in the coronary ostia has the potential to investigate the impact of flow disturbances in the aortic root on the coronary flow and eventually the impact of coronary obstructive diseases on aortic stiffening and aortic valve leaflets dynamics. It would also be possible to examine coronary perfusion variations due to mechanical and geometric modifications of the aortic root using clinical metrics for validation of the approach. Such investigations are not possible with previously described models of the aortic root without any coronary structures.

## References

- [1] I. El-Hamamsy, A. H. Chester, and M. H. Yacoub, "Cellular regulation of the structure and function of aortic valves," *Journal of Advanced Research*, vol. 1, no. 1, pp. 5–12, 2010.
- [2] M. Safar, "Arterial stiffness: a simplified overview in vascular medicine," in *Atherosclerosis, Large Arteries and Cardiovascular Risk*, M. Safar and E. Frohlich, Eds., vol. 44, pp. 1–18, Advanced Cardiology, Basel, Switzerland, 2007.
- [3] A. Nemes, T. Forster, and M. Csanády, "Reduction of coronary flow reserve in patients with increased aortic stiffness," *Canadian Journal of Physiology and Pharmacology*, vol. 85, no. 8, pp. 818–822, 2007.
- [4] C. M. McEniery, B. J. McDonnell, A. So et al., "Aortic calcification is associated with aortic stiffness and isolated systolic hypertension in healthy individuals," *Hypertension*, vol. 53, no. 3, pp. 524–531, 2009.
- [5] A. Stella, M. Gessaroli, B. I. Cifello et al., "Elastic modulus in young diabetic patients (ultrasound measurements of pulse wave velocity)," *Angiology*, vol. 35, no. 11, pp. 729–734, 1984.
- [6] K. E. Juhani Airaksinen, P. I. Salmela, M. K. Linnaluoto, M. J. Ikaheimo, K. Ahola, and L. J. Ryhanen, "Diminished arterial elasticity in diabetes: association with fluorescent advanced glycosylation end products in collagen," *Cardiovascular Research*, vol. 27, no. 6, pp. 942–945, 1993.
- [7] J. J. Toto-Moukoko, A. Achimastos, R. G. Asmar, C. J. Hugues, and M. E. Safar, "Pulse wave velocity in patients with obesity and hypertension," *American Heart Journal*, vol. 112, no. 1, pp. 136–140, 1986.
- [8] M. Kupari, P. Hekali, P. Keto, V. P. Poutanen, M. J. Tikkanen, and C. G. Standertskjold-Nordenstam, "Relation of aortic stiffness to factors modifying the risk of atherosclerosis in healthy people," *Arteriosclerosis and Thrombosis*, vol. 14, no. 3, pp. 386–394, 1994.
- [9] Y. Sahasakul, W. D. Edwards, J. M. Naessens, and A. J. Tajik, "Age-related changes in aortic and mitral valve thickness: implications for two-dimensional echocardiography based on an autopsy study of 200 normal human hearts," *American Journal of Cardiology*, vol. 62, no. 7, pp. 424–430, 1988.
- [10] G. W. Christie and B. G. Barratt-Boyes, "Age-dependent changes in the radial stretch of human aortic valve leaflets determined by biaxial testing," *Annals of Thoracic Surgery*, vol. 60, pp. S156–S159, 1995.
- [11] S. J. Cowell, D. E. Newby, N. A. Boon, and A. T. Elder, "Calcific aortic stenosis: same old story?" *Age and Ageing*, vol. 33, no. 6, pp. 538–544, 2004.
- [12] F. Schoen and M. Edwards, "Valvular heart disease: general principles and stenosis," in *Cardiovascular Pathology*, M. Silver, A. I. Gotlieb, and F. Schoen, Eds., pp. 402–442, W. B. Saunders, 3rd edition, 2001.
- [13] F. Schoen, "Pathology of heart valve substitution with mechanical and tissue prostheses," in *Cardiovascular Pathology*, M. Silver, A. I. Gotlieb, and F. Schoen, Eds., pp. 629–677, W. B. Saunders, 3rd edition, 2001.
- [14] M. H. Yacoub and J. J. M. Takkenberg, "Will heart valve tissue engineering change the world?" *Nature Clinical Practice Cardiovascular Medicine*, vol. 2, no. 2, pp. 60–61, 2005.
- [15] M. F. O'Rourke, "How stiffening of the aorta and elastic arteries leads to compromised coronary flow," *Heart*, vol. 94, no. 6, pp. 690–691, 2008.
- [16] D. Garcia, P. G. Camici, L. G. Durand et al., "Impairment of coronary flow reserve in aortic stenosis," *Journal of Applied Physiology*, vol. 106, no. 1, pp. 113–121, 2009.
- [17] C. Stefanadis, C. Stratos, H. Boudoulas, C. Vlachopoulos, I. Kallikazaros, and P. Toutouzas, "Distensibility of the ascending aorta in coronary artery disease and changes after nifedipine administration," *Chest*, vol. 105, no. 4, pp. 1017–1023, 1994.
- [18] A. Ranga, O. Bouchot, R. Mongrain, P. Ugolini, and R. Cartier, "Computational simulations of the aortic valve validated by imaging data: evaluation of valve-sparing techniques," *Interactive Cardiovascular and Thoracic Surgery*, vol. 5, no. 4, pp. 373–378, 2006.
- [19] J. De Hart, G. W. M. Peters, P. J. G. Schreurs, and F. P. T. Baaijens, "A three-dimensional computational analysis of fluid-structure interaction in the aortic valve," *Journal of Biomechanics*, vol. 36, no. 1, pp. 103–112, 2003.
- [20] J. De Hart, F. P. T. Baaijens, G. W. M. Peters, and P. J. G. Schreurs, "A computational fluid-structure interaction analysis of a fiber-reinforced stentless aortic valve," *Journal of Biomechanics*, vol. 36, no. 5, pp. 699–712, 2003.
- [21] I. C. Howard, E. A. Patterson, and A. Yoxall, "On the opening mechanism of the aortic valve: some observations from simulations," *Journal of Medical Engineering and Technology*, vol. 27, no. 6, pp. 259–266, 2003.
- [22] C. J. Carmody, G. Burriesci, I. C. Howard, and E. A. Patterson, "An approach to the simulation of fluid-structure interaction

- in the aortic valve,” *Journal of Biomechanics*, vol. 39, no. 1, pp. 158–169, 2006.
- [23] B. J. Verhoeff, M. Siebes, M. Meuwissen et al., “Influence of percutaneous coronary intervention on coronary microvascular resistance index,” *Circulation*, vol. 111, no. 1, pp. 76–82, 2005.
- [24] K. Rajappan, O. E. Rimoldi, P. G. Camici, N. G. Bellenger, D. J. Pennell, and D. J. Sheridan, “Functional changes in coronary microcirculation after valve replacement in patients with aortic stenosis,” *Circulation*, vol. 107, no. 25, pp. 3170–3175, 2003.
- [25] I. Campbell, A. Ranga, R. Mongrain, and R. Cartier, “Coronary flow in an FSI model of the aortic valve,” in *Proceedings of the 30th Canadian Medical and Biological Engineering Conference (CMBEC 30) in the Festival of International Conferences on Caregiving, Disability, Aging and Technology (FICCDAT '07)*, Toronto, Canada, 2007.
- [26] I. H. Campbell, *A study of coronary flow in the presence of geometric and mechanical abnormalities in a fluid-structure interaction model of the aortic valve*, M.S. thesis, Department of Mechanical Engineering, McGill University, 2007.
- [27] G. G. Chew, I. C. Howard, and E. A. Patterson, “Simulation of damage in a porcine prosthetic heart valve,” *Journal of Medical Engineering and Technology*, vol. 23, no. 5, pp. 178–189, 1999.
- [28] J. Li, X. Y. Luo, and Z. B. Kuang, “A nonlinear anisotropic model for porcine aortic heart valves,” *Journal of Biomechanics*, vol. 34, no. 10, pp. 1279–1289, 2001.
- [29] A. Ranga, R. Mongrain, R. Mendes Galaz, Y. Biadillah, and R. Cartier, “Large-displacement 3D structural analysis of an aortic valve model with nonlinear material properties,” *Journal of Medical Engineering and Technology*, vol. 28, no. 3, pp. 95–103, 2004.
- [30] M. Gur, R. Yilmaz, R. Demirbag, A. Yildiz, M. Menduh Bas, and M. Polat, “Relationship between impaired elastic properties of aorta with left ventricle geometric patterns and left ventricle diastolic functions in patients with newly diagnosed essential hypertension,” *International Journal of Clinical Practice*, vol. 60, no. 11, pp. 1357–1363, 2006.
- [31] Y. Oishi, Y. Mizuguchi, H. Miyoshi, A. Iuchi, N. Nagase, and T. Oki, “A novel approach to assess aortic stiffness related to changes in aging using a two-dimensional strain imaging,” *Echocardiography*, vol. 25, no. 9, pp. 941–945, 2008.
- [32] D. Tremblay, T. Zigras, R. Cartier et al., “A comparison of mechanical properties of materials used in aortic arch reconstruction,” *Annals of Thoracic Surgery*, vol. 88, no. 5, pp. 1484–1491, 2009.
- [33] N. Choudhury, O. Bouchot, L. Rouleau et al., “Local mechanical and structural properties of healthy and diseased human ascending aorta tissue,” *Cardiovascular Pathology*, vol. 18, no. 2, pp. 83–91, 2009.
- [34] E. S. Di Martino, G. Guadagni, A. Fumero et al., “Fluid-structure interaction within realistic three-dimensional models of the aneurysmatic aorta as a guidance to assess the risk of rupture of the aneurysm,” *Medical Engineering and Physics*, vol. 23, no. 9, pp. 647–655, 2001.
- [35] A. Cataloglu, P. L. Gould, and R. E. Clark, “Validation of a simplified mathematical model for the stress analysis of human aortic heart valves,” *Journal of Biomechanics*, vol. 8, no. 5, pp. 347–348, 1975.
- [36] S. Hashim and D. Richens, “Finite element method in cardiac surgery,” *Interactive Cardiovascular and Thoracic Surgery*, vol. 5, no. 1, pp. 5–8, 2006.
- [37] F. P. Salvucci, J. Schiavone, D. Craiem, and J. G. Barra, “Arterial wall mechanics as a function of heart rate: role of vascular smooth muscle,” *Journal of Physics*, vol. 90, no. 1, Article ID 012010, 2007.
- [38] Y. Zou and Y. Zhang, “The orthotropic viscoelastic behavior of aortic elastin,” *Biomechanics and Modeling in Mechanobiology*, vol. 10, no. 5, pp. 613–625, 2010.
- [39] S. A. Berger, W. Goldsmith, and E. R. Lewis, *Introduction to Bioengineering*, Oxford University Press, Oxford, UK, 1996.
- [40] P. Sipkema, H. Yamada, and F. C. P. Yin, “Coronary artery resistance changes depend on how surrounding myocardial tissue is stretched,” *American Journal of Physiology*, vol. 270, no. 3, pp. H924–H934, 1996.
- [41] M. N. Levy and A. J. Pappano, *Cardiovascular Physiology*, Mosby Physiology Monograph Series, 9th edition, 2007.
- [42] B. J. Bellhous, “Velocity and pressure distributions in the aortic valve,” *Journal of Fluid Mechanics*, vol. 37, no. 3, pp. 587–600, 1969.
- [43] R. G. Leyh, C. Schmidtke, H. H. Sievers, and M. H. Yacoub, “Opening and closing characteristics of the aortic valve after different types of valve-preserving surgery,” *Circulation*, vol. 100, no. 21, pp. 2153–2160, 1999.
- [44] R. De Paulis, G. M. De Matteis, P. Nardi, R. Scaffa, M. M. Buratta, and L. Chiariello, “Opening and closing characteristics of the aortic valve after valve-sparing procedures using a new aortic root conduit,” *Annals of Thoracic Surgery*, vol. 72, no. 2, pp. 487–494, 2001.
- [45] T. Aybek, M. Sotiriou, T. Wöhleke et al., “Valve opening and closing dynamics after different aortic valve-sparing operations,” *Journal of Heart Valve Disease*, vol. 14, no. 1, pp. 114–120, 2005.
- [46] M. Handke, G. Heinrichs, F. Beyersdorf, M. Olschewski, C. Bode, and A. Geibel, “In vivo analysis of aortic valve dynamics by transesophageal 3-dimensional echocardiography with high temporal resolution,” *Journal of Thoracic and Cardiovascular Surgery*, vol. 125, no. 6, pp. 1412–1419, 2003.
- [47] R. A. Boerboom, N. J. B. Driessen, C. V. C. Bouten, J. M. Huyghe, and F. P. T. Baaijens, “Finite element model of mechanically induced collagen fiber synthesis and degradation in the aortic valve,” *Annals of Biomedical Engineering*, vol. 31, no. 9, pp. 1040–1053, 2003.
- [48] R. Gnyaneshwar, R. K. Kumar, and K. R. Balakrishnan, “Dynamic analysis of the aortic valve using a finite element model,” *Annals of Thoracic Surgery*, vol. 73, no. 4, pp. 1122–1129, 2002.
- [49] S. W. Rabkin, “The association of hypertension and aortic valve sclerosis,” *Blood Pressure*, vol. 14, no. 5, pp. 264–272, 2005.
- [50] K. R. Branch, K. D. O’Brien, and C. M. Otto, “Aortic valve sclerosis as a marker of active atherosclerosis,” *Current Cardiology Reports*, vol. 4, no. 2, pp. 111–117, 2002.
- [51] K. Perktold and G. Rappitsch, “Computer simulation of local blood flow and vessel mechanics in a compliant carotid artery bifurcation model,” *Journal of Biomechanics*, vol. 28, no. 7, pp. 845–856, 1995.
- [52] S. Katayama, N. Umetani, S. Sugiura, and T. Hisada, “The sinus of Valsalva relieves abnormal stress on aortic valve leaflets by facilitating smooth closure,” *Journal of Thoracic and Cardiovascular Surgery*, vol. 136, no. 6, pp. 1528–1535, 2008.
- [53] S. Oren, I. Isakov, B. Golzman et al., “The influence of smoking cessation on hemodynamics and arterial compliance,” *Angiology*, vol. 57, no. 5, pp. 564–568, 2006.
- [54] H. Tanaka, F. A. Dinunno, K. D. Monahan, C. M. Clevenger, C. A. DeSouza, and D. R. Seals, “Aging, habitual exercise, and dynamic arterial compliance,” *Circulation*, vol. 102, no. 11, pp. 1270–1275, 2000.

- [55] P. J. Nestel, S. E. Pomeroy, T. Sasahara et al., "Arterial compliance in obese subjects is improved with dietary plant n-3 fatty acid from flaxseed oil despite increased LDL oxidizability," *Arteriosclerosis, Thrombosis, and Vascular Biology*, vol. 17, no. 6, pp. 1163–1170, 1997.
- [56] A. Nemes, T. Forster, A. Varga et al., "How can coronary flow reserve be altered by severe aortic stenosis?" *Echocardiography*, vol. 19, no. 8, pp. 655–659, 2002.
- [57] D. Baumgart, M. Haude, F. Liu, J. Ge, G. Goerge, and R. Erbel, "Current concepts of coronary flow reserve for clinical decision making during cardiac catheterization," *American Heart Journal*, vol. 136, no. 1, pp. 136–149, 1998.
- [58] R. H. Mohiaddin, S. R. Underwood, H. G. Bogren et al., "Regional aortic compliance studied by magnetic resonance imaging: the effects of age, training, and coronary artery disease," *British Heart Journal*, vol. 62, no. 2, pp. 90–96, 1989.
- [59] M. C. H. Leung, I. T. Meredith, and J. D. Cameron, "Aortic stiffness affects the coronary blood flow response to percutaneous coronary intervention," *American Journal of Physiology*, vol. 290, no. 2, pp. H624–H630, 2006.
- [60] M. Saito, H. Okayama, K. Nishimura et al., "Possible link between large artery stiffness and coronary flow velocity reserve," *Heart*, vol. 94, no. 6, pp. 690–691, 2008.
- [61] H. G. Bogren, R. H. Mohiaddin, R. K. Klipstein et al., "The function of the aorta in ischemic heart disease: a magnetic resonance and angiographic study of aortic compliance and blood flow patterns," *American Heart Journal*, vol. 118, no. 2, pp. 234–247, 1989.
- [62] R. B. Gunderman, *Essential Radiology: Clinical Presentation, Pathophysiology, Imaging*, 2006.
- [63] R. H. Mohiaddin, D. N. Firmin, and D. B. Longmore, "Age-related changes of human aortic flow wave velocity measured noninvasively by magnetic resonance imaging," *Journal of Applied Physiology*, vol. 74, no. 1, pp. 492–497, 1993.
- [64] G. G. Belz, "Elastic properties and Windkessel function of the human aorta," *Cardiovascular Drugs and Therapy*, vol. 9, no. 1, pp. 73–83, 1995.
- [65] H. Bader, "Importance of the gerontology of elastic arteries in the development of essential hypertension," *Clinical Physiology and Biochemistry*, vol. 1, no. 1, pp. 36–56, 1983.
- [66] D. E. Wilcken, A. A. Charlier, J. I. Hoffman, and A. Guz, "Effects of alterations in aortic impedance on the performance of the ventricles," *Circulation Research*, vol. 14, pp. 283–293, 1964.
- [67] A. Cataloglu, R. E. Clark, and P. L. Gould, "Stress analysis of aortic valve leaflets with smoothed geometrical data," *Journal of Biomechanics*, vol. 10, no. 3, pp. 153–158, 1977.

## Review Article

# Hemodynamics of Cerebral Aneurysms: Computational Analyses of Aneurysm Progress and Treatment

**Woowon Jeong and Kyeihan Rhee**

*Department of Mechanical Engineering, Myongji University, 38-2 Nam-Dong, Yongin-Si, Kyunggi-Do 449-728, Republic of Korea*

Correspondence should be addressed to Kyeihan Rhee, [khanrhee@mju.ac.kr](mailto:khanrhee@mju.ac.kr)

Received 22 September 2011; Accepted 10 November 2011

Academic Editor: Eun Bo Shim

Copyright © 2012 W. Jeong and K. Rhee. This is an open access article distributed under the Creative Commons Attribution License, which permits unrestricted use, distribution, and reproduction in any medium, provided the original work is properly cited.

The progression of a cerebral aneurysm involves degenerative arterial wall remodeling. Various hemodynamic parameters are suspected to be major mechanical factors related to the genesis and progression of vascular diseases. Flow alterations caused by the insertion of coils and stents for interventional aneurysm treatment may affect the aneurysm embolization process. Therefore, knowledge of hemodynamic parameters may provide physicians with an advanced understanding of aneurysm progression and rupture, as well as the effectiveness of endovascular treatments. Progress in medical imaging and information technology has enabled the prediction of flow fields in the patient-specific blood vessels using computational analysis. In this paper, recent computational hemodynamic studies on cerebral aneurysm initiation, progress, and rupture are reviewed. State-of-the-art computational aneurysmal flow analyses after coiling and stenting are also summarized. We expect the computational analysis of hemodynamics in cerebral aneurysms to provide valuable information for planning and follow-up decisions for treatment.

## 1. Introduction

Aneurysm is a vascular disease characterized by local dilatation of arterial walls. Aneurysms are frequently observed in the intracranial space and exhibit fusiform or saccular shapes. Some of aneurysms may grow, and rupture of cerebral aneurysms causes intracranial hemorrhage, which is associated with high mortality and morbidity [1–3]. In order to prevent the rupture of aneurysms, interventional thromboembolization treatment via the endovascular insertion of coils and stents may be applied as a prophylactic treatment. The recent development of neuroradiological and diagnostic imaging techniques has enabled aneurysms to be detected more frequently. Since much less than 1% of cerebral aneurysms rupture on an annual basis [4, 5], the demand for accurate prediction of aneurysm growth and rupture is increasing in order to select appropriate and immediate endovascular treatment.

The initiation, progression, and rupturing of aneurysms are related to the arterial wall remodeling: it is believed that they are all related to the complex interactions between biochemical and biomechanical factors. Pathological vessel wall

remodeling involves various enzymes and proteins related to degeneration, inflammation, and repair: their expressions in arterial walls can be affected by hemodynamics. Blood flow imposes mechanical stress on the vessel wall, which may stimulate the functions of endothelial cells, affect the structural integrity of the endothelium, and affect the transport of various cells and enzymes in the blood stream to the endothelium. Therefore, hemodynamic forces and flow characteristics, such as recirculation [6], secondary flow [7], and jet impingement [8], are considered to be major mechanical factors related to the genesis and progression of vascular diseases. Among the hemodynamic parameters, wall shear stress (WSS) has been studied extensively, since endothelial cells actively sense and respond to WSS. In their recent review, Nixon et al. [9] clearly summarized the role of WSS in cerebral aneurysms and atherosclerosis.

Recent progress in medical imaging technology and improvements in computer equipment have enabled computational fluid dynamic (CFD) analysis to predict the hemodynamics of aneurysms with increased accuracy and reliability. Angiography image data can be converted to the three-dimensional (3D) vessel geometric data for computer

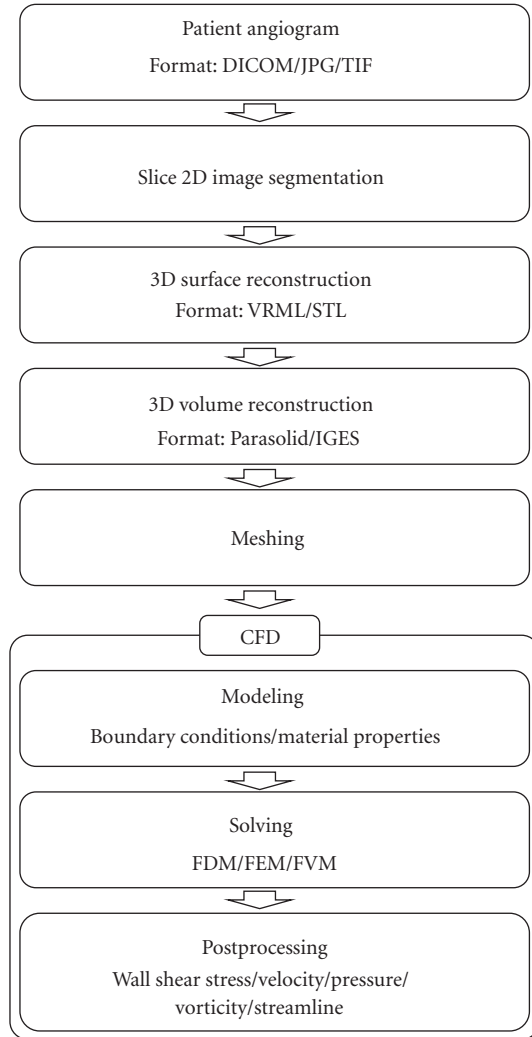


FIGURE 1: Flowchart of the computational hemodynamic analysis procedure based on patient-specific angiogram.

simulation; therefore, CFD analysis based on real aneurysm geometry has been progressed in recent years [10–14]. The basic process of computational hemodynamic analysis using a patient angiogram is illustrated in Figure 1. The sliced cross-sectional lumen images of a patient’s vasculature are obtained using various imaging modalities, such as magnetic resonance angiography (MRA), computed tomography angiography (CTA), and 3D rotational angiography. The lumen of each cross-section image can be segmented and the luminal surface is reconstructed using splines, contour tilting, or other interpolation methods. Two-dimensional segmentation is inaccurate when the vessel axis is not perpendicular to the cross-sectional surface. Furthermore, manual automatic segmentation is operator dependent while automatic segmentation using threshold may yield topological defects and inaccuracies for the image with inhomogeneous image intensities. The state-of-the-art models for unsupervised full three-dimensional segmentation have been developed [15]. A region growing segmentation with automatic thresholding [16] and a component-based approach using a

deformable model [17] are described in Cebral et al. [15] in detail. Based on the reconstructed surface contour, 3D solid-volume models are constructed using commercial 3D computer-aided design (CAD) programs. The reconstructed 3D volume models are divided into the computational grids by a meshing program. Some commercial software for preprocessing is outlined in Table 1. The governing equations of a flow fields are solved using various numerical schemes, such as the finite differential method (FDM), finite element method (FEM), finite volume method (FVM), and lattice Boltzmann method (LBM). Various commercial CFD software programs including Fluent and Ansys CFX (ANSYS, Inc., Canonsburg, PA, USA), ADINA (ADINA R&D, Inc., Watertown, MA, USA), COMSOL (COMSOL, Inc., Burlington, MA, USA), CFD-ACE (ESI Group, Paris, France), Flow-3D (Flow Science, Inc., Pasadena, CA, USA), and STAR-CD (CD-adapco, Melville, NY, USA), are available. Calculated flow field variables can be rearranged in order to show various flow characteristics of interest using postprocessing procedures.

Patient-specific CFD analysis involves imaging data process, mesh construction, computational calculations, and postprocessing. In order to avoid difficulties associated with manual and time-consuming works of using commercial CFD packages, efforts of developing in-house CFD codes have been made. The whole pipeline from medical images to flow calculations has been developed in order to eliminate manual intervention and editing of data processing. Cebral et al. [10, 15, 18, 19] developed the pipeline for simulation based hemodynamics. It consists of vessel reconstruction, unstructured grid generation, numerical solver, and postprocessing. Proper boundary conditions and material properties are imposed on the blood vessel models. Patient-specific inflow data provide important information which determines the accuracy of CFD calculations. In vivo patient-specific inflow boundary conditions can either be obtained through invasive measurement using a catheter or medical imaging. Karmonik et al. [20–22] measured blood flow waveform in cerebral arteries by phase contrast MRI, and provided the measured blood flow profile at the inlet boundary conditions for CFD simulation. They successfully simulated blood flow in cerebral arteries using 3D digital subtraction angiography and phase contrast MRI. Specifying outflow boundary condition also requires careful attentions, and the appropriate impedances of the distal vasculature for multiple outlets should be provided.

If the hemodynamic factors affecting aneurysm etiology are elucidated, CFD analysis based on the patient-specific images data will provide a better understanding and diagnosis of aneurysm progress and rupture. The performance of endovascular stents and coils can be evaluated by analyzing aneurysmal flow alteration as a result of interventional treatment. Furthermore, prediction of blood flow using CFD analysis can be used to plan interventional therapies. In this paper, we review recent computational hemodynamic studies on cerebral aneurysm initiation, growth, and rupture, as well as computational studies on aneurysmal flow alterations induced by interventional treatment with coils and stents.

TABLE 1: Some commercial preprocessing software for patient-specific CFD analysis and its role.

Software	Slice 2D image segmentation	3D surface reconstruction	3D volume reconstruction	Meshing
3DMax (Autodesk Inc., San Rafael, CA)	Yes	Yes	Yes	No
3D-Doctor (Able Software Corp., Lexington, MA)	Yes	Yes	Yes	No
Mimics (Materialise Group, Leuven, Belgium)	Yes	Yes	Yes	No
Insight Toolkit (Kitware Inc., Clifton Park, NY)	Yes	Yes	Yes	No
3D Slicer (MIT, Boston, MA)	Yes	Yes	Yes	No
SolidWorks (Dassault Systems, Concord, MA)	No	No	Yes	No
Pro-Engineer (PTC, Needham, MA)	No	No	Yes	No
CATIA (Dassault Systems, Velizy-Villacoublay, France)	No	No	Yes	No
3-matic (Materialise Group, Leuven, Belgium)	No	No	Yes	Yes
Hypermesh (Altair Engineering Inc., Troy, MI)	No	No	Yes	Yes
Gambit (ANSYS Inc., Canonsburg, PA)	No	No	Yes	Yes
ICEM-CFD (ANSYS Inc., Canonsburg, PA)	No	No	Yes	Yes
Gridgen (Pointwise Inc., Fort Worth, TX)	No	No	Yes	Yes

## 2. Aneurysm Initiation

Most cerebral aneurysms are observed at arterial bifurcations and branches or at the outer walls of arterial curvatures [23, 24]. The localized occurrence of cerebral aneurysms prompted the hemodynamic research on aneurysm formation. Since CFD analysis provides detailed hemodynamic information at bifurcations [25, 26] and the outer walls of curved arteries [27, 28], many studies have attempted to identify an appropriate hemodynamic parameter correlated with pathological aneurysm formation.

Flow impingement on the apex of bifurcations and sharply curved vessels generates unstable helical flow patterns near the impinging wall. Repetitive flow impingement against the vessel wall under pulsatile flows may induce fatigue, potentially causing morphological and functional changes in the endothelium may occur in this region. The distributions of pressure and shear stress near the impingement point are shown in Figure 2. The local pressure increase at the impingement point is caused by the conversion of fluid kinetic energy to static wall pressure. Previous studies reported that the local pressure increases at arterial bifurcations and bends are less than 1-2% of intravascular pressure [29, 30]. However, high spatial pressure gradients may affect endothelial remodeling.

WSS near the impingement point is high (hundreds of dyne/cm<sup>2</sup> [31]), and its spatial gradient is also very large. Previous studies using animal experiments have demonstrated that high WSS contributes to the genesis of cerebral aneurysms via degenerative changes in endothelium [32, 33]. Other studies have also shown that elevated WSS affects to the various degenerative changes of vessel walls [34–40].

Meng et al. [26] surgically created carotid bifurcations in a dog animal model and found that the spatial histological features of walls are correlated with hemodynamic variables calculated by CFD analysis. Their results show that the localization of destructive wall remodeling, which resembles the initiation of aneurysms, is correlated with a combination

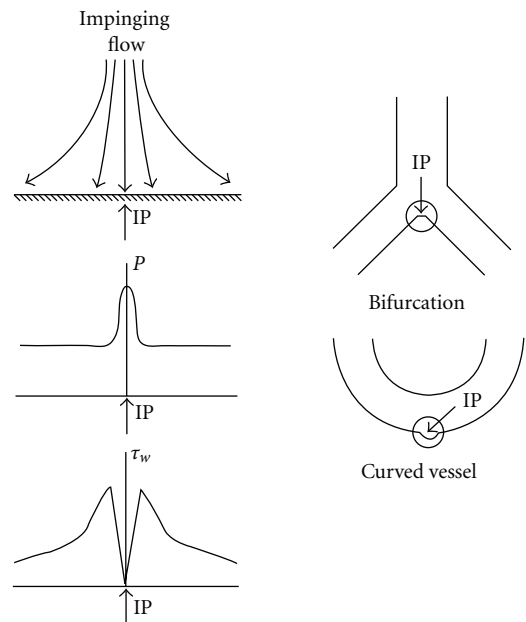


FIGURE 2: Schematic of pressure ( $P$ ) and WSS ( $\tau_w$ ) distribution near the jet impingement point (IP) of curved and bifurcated blood vessels.

of high WSS and a high WSS gradient. Mantha et al. [37] constructed computational models of carotid artery lateral aneurysms based on the patient 3D angiography data, and performed CFD analysis was performed for the parent vessel prior to aneurysm formation. They found significant correlations between the temporal directional changes of WSS and the location of aneurysm formation.

Since the endothelium senses WSS and actively responds to mechanical stress [34–36, 38, 40], vascular remodeling that initiates aneurysm formation may be related to high WSS magnitude or high spatial and temporal variations in WSS. Although it is difficult to pinpoint the hemodynamic

variables responsible for aneurysm initiation, complex flow fields near the flow impingement point, where high WSS magnitude, high temporal and spatial WSS gradients, and high pressure gradients are probably part of the prerequisite hemodynamic environment related to the initiation of cerebral aneurysms.

### 3. Aneurysm Growth

Histological studies have revealed degeneration of the intima and thinning of the media in the aneurysm vessel wall [39, 41]. Furthermore, various proteolytic enzyme secretions such as elastase [42] and matrix metalloproteinase [43] contribute to degenerative wall remodeling. Pathological wall remodeling processes, which are related to the secretion of various enzymes, along with the inflammatory response of endothelium [44] and apoptosis of smooth muscle cells [45, 46], may be affected by hemodynamics [47]. CFD studies have been performed to investigate the hemodynamic factors affecting aneurysm growth. Many CFD studies have been performed on the growth and rupture of aneurysms using not only the ideal curved and bifurcated blood vessel models [31, 48–51], but also aneurysm models based on real patient data obtained by MRI or CT imaging [13, 14, 52, 53].

Feng et al. [54, 55] simulated the deformation and growth of an aneurysm bleb of a curved vessel in a simplified cerebral artery model. They assumed that aneurysm growth was related to degeneration of the arterial wall caused by high WSS. Aneurysm formation was modeled as vessel wall deformation due to reduced wall stiffness using fluid solid interaction (FSI). The WSS distributions were calculated, and the Young's modulus of the arterial wall was assumed to be reduced if the WSS was larger than the threshold value. The drawback of their methodology is that the mechanical properties of an arterial wall could not be modeled as a simple function of WSS. Furthermore, arterial remodeling could not be simply modeled by using a vessel wall expansion model based on FSI, and the temporal progression of aneurysm growth was not considered. Boussel et al. [56] calculated the WSS of the intracranial aneurysm on the basis of the patient's MR angiography data, and correlated WSS with aneurysm growth by using MR images at 2 different time points (mean  $16.4 \pm 7.4$  months between the 2 time points): they found a significant correlation between low time-averaged WSS and aneurysm growth.

Atherosclerotic vascular wall changes due to low and oscillatory WSS have been studied extensively, and the role of hemodynamics on atherogenesis is well established [57–59]. Although vessel wall remodeling in aneurysm growth is different from atherosclerotic wall remodeling [46, 60], inflammatory responses due to disturbed flow or decreased WSS may affect the aneurysm growth and rupture via degenerative vascular wall remodeling. Low WSS ( $<4$  dyne/cm<sup>2</sup>) causes endothelial proliferation [61] and apoptosis [62]. Moreover, low WSS induced by slow flow recirculation in the complex flow fields in the aneurysmal bifurcations [53, 63] is positively correlated with aneurysm growth. One study found that the WSS of the aneurysms is significantly lower than that of the surrounding vasculature [53]. Furthermore,

a relationship between local aneurysm growth and areas of low WSS at the intraluminal surface was found using patient aneurysm models [53, 56].

The complex flow patterns accompanying low and oscillating WSS may be correlated with aneurysm growth. Slight out-pouching of the aneurysm wall may induce a disturbed flow region, and aneurysm growth can be accelerated due to low and oscillatory WSS in the expanded blood vessel via a positive feedback mechanism. Vascular wall remodeling maintaining the WSS at a constant level favors the high WSS hypothesis of aneurysm growth. However, it cannot explain aneurysm growth, because intracranial arteries have different vessel wall structures from the arteries in which arterial remodeling is observed [64–67].

### 4. Aneurysm Rupture

Aneurysm rupture occurs when wall tension exceeds the mechanical strength of wall tissue. Wall tension is proportional to the intramural pressure and radius, and inversely proportional to the walls thickness of a spherical balloon. Therefore, high pressure, large aneurysm size, and thin wall increase wall tension. Local weakening of the aneurysm wall, which is characterized by thinning of the media and a lack of collagen fibers, is closely related to the pathological wall remodeling. Furthermore, the hemodynamic environment may affect the wall remodeling process. Therefore, hemodynamic forces, including high pressure and WSS, may directly influence wall breakage, while low WSS and disturbed flow patterns may affect the aneurysm wall weakening via wall remodeling over an extended period.

Strong flow impingement is suspected as a hemodynamic factor responsible for aneurysm rupture. Cebal et al. [52] performed a CFD study using 62 patient-specific models. They found out that flow patterns are more complex and the impingement jet is narrower in ruptured aneurysms compared to unruptured aneurysms. Recently, the same group extended the previous study by including 210 intracranial aneurysms in 128 consecutive patients and more hemodynamic characteristics were investigated [68]. A quantitative hemodynamic study showed that concentrated inflow jets, small impingement regions, complex flow patterns, and unstable flow patterns were correlated with a clinical history of prior aneurysm rupture. Therefore, strong inflow jets from the parent vessel to the aneurysm sac might provide a hemodynamic environment prone to aneurysm rupture. Blood impingement on the wall generates impact force and high WSS, which could affect the fatigue of the vessel wall. The site of flow impact includes locally elevated pressure and a high WSS gradient. The contribution of pressure elevation due to the impinging flow jet is small [31, 69], but the effect of impact force remains unknown. Shojima et al. [53] calculated the WSS in the human middle cerebral artery using CFD analysis. They reported that the spatially averaged WSS of the aneurysm region at the peak systole is significantly higher (approximately 2 times higher) in ruptured models than that in unruptured models. High spatially averaged WSS in the ruptured cases is due to the high WSS at the body or the neck of aneurysm caused by direct flow

stream from a parent artery. Therefore, high WSS may not be correlated with aneurysm rupture. The WSS at the tip of the aneurysm, where it is more vulnerable to rupture, is lower in the ruptured cases. But their computational results may not detect secondary flows and other detailed features of the intraaneurysmal flow pattern because the computational vessel models reconstructed in their study are extremely truncated. Castro et al. [18] studied the influence of the upstream parent artery geometry on intraaneurysmal hemodynamics. They showed that the reconstructed models using the truncated parent vessel underestimated the WSS and shifted the impact zone to the neck. Therefore, further studies should be required to clarify the effects of low and high WSS on aneurysm rupture.

Complex unstable flow accompanying low and oscillatory flow may be responsible for vessel wall remodeling associated with rupture [70], since it is correlated with apoptotic wall remodeling [62]. Valencia et al. [71] showed that low WSS regions are larger in ruptured aneurysms than in unruptured ones. They also report a linear correlation between the average WSS on the aneurysm sac at peak systole with the area index, which was defined as the ratio between the aneurysm area and the artery areas. Lu et al. [72] performed CFD analysis using 3D reconstructed angiograms of both ruptured and unruptured cerebral aneurysms. In the ruptured group, the proportion of low WSS areas ( $<1.5$  Pa) to the whole area of the aneurysm was significantly lower, while the oscillatory shear index was significantly higher. Therefore, large spatial and temporal variations in WSS within the complex unstable flow in the aneurysm sac might be related to aneurysm rupture.

Pressure may be a hemodynamic parameter influencing aneurysm rupture. Previous studies demonstrated that the complex flow pattern of the flow impingement around the aneurysm results in elevated pressure at the aneurysm [30, 48, 69], although it is very low compared to systemic pressure. A large pressure gradient along a wall near the impingement point may affect endothelial functioning and remodeling. Torii et al. [73, 74] studied the effects of high blood pressure on WSS in aneurysm models using image-based FSI modeling. Their results show that hypertensive blood pressure causes significant changes in WSS distribution on the aneurysm wall. Thus, hypertension may affect aneurysm wall damage.

Since aneurysm rupture is not correlated with the abnormally high local stress, a loss of wall integrity due to vascular wall remodeling and increased wall tension due to systemic pressure may be responsible for aneurysm rupture. Isaksen et al. [75] calculated wall tension and displacement using FSI for the elastic cerebral aneurysm wall. They show that the areas of maximum wall tension and displacement are located where aneurysms are most vulnerable to rupture. Local changes of wall thickness and mechanical property caused by aneurysm wall remodeling were not considered since they assumed a uniform aneurysm wall thickness. Local wall thickness and the properties of the aneurysm wall are hard to measure, which limits the estimation of wall tension.

## 5. Aneurysm Coiling

Until the early 1990s, surgical clipping was used to obliterate the aneurysm sac. However, endovascular treatments such as coil embolization and stenting have been used since the development of nonsurgical endovascular approaches. Coils packed into the aneurysm sac induce flow stasis and thrombus formation [76–78], and scar tissue forms as a result of the foreign body reaction completing the aneurysmal occlusion [76, 79, 80]. It is difficult to completely fill an aneurysmal cavity due to the complex shape of the aneurysm sac and coil compaction due to hemodynamic force. Incomplete embolization induces residual flow from the parent vessel and contributes to the recurrence of the aneurysm. Accordingly, hemodynamics after coil embolization is a highly relevant factor for predicting the recurrence and regrowth of aneurysms.

Byun and Rhee [81] studied hemodynamic changes due to partially blocked lateral aneurysms, and investigated the effects of aneurysm shape and parent vessel geometry using CFD analysis. A computer simulation of a terminal aneurysm was also performed, and the effects of coil density were explored [76]. Since aneurysm wall remodeling and flow stasis may be important, aneurysmal WSS was investigated taking fluid (blood) and solid (vessel wall) interactions into consideration [82]. In these analyses, coils were modeled as a solid material (block element); these analyses might be valid for completely thromboembolized coils.

In order to investigate the flow inside the coil, the coil was modeled as a porous medium. CFD analysis was performed using aneurysm images of the real patient, and the influence of multiple coils on intra-aneurysmal hemodynamics was investigated [83, 84]. Porous medium modeling might be useful in the early stage of coil insertion, but the thrombus formation inside of a coil bundle should be modeled during the embolization process after endovascular treatment. Computational simulation of the blood clotting inside the idealized lateral aneurysm model was performed on the basis of the viscosity model defined as a function of both residence time and clotting fluid concentration [85]. However, further refinement of the clotting model is required, since its validation is incomplete.

The interaction between hemodynamics and the coil is the major physical cause of coil compaction and dislocation, which induce the recanalization and growth of the aneurysm. The interaction between coils and flow has been simulated. One application of these simulations is to simulate coil deployment during the initial stage of coil intervention. The results from such simulations may help provide patient-specific guidelines for coil selection and predict postoperative prognosis. Recently, Wei et al. [86] simulated coil deployment and deformation while considering reactive fluid force, and computed flow fields for coil filled and coil free domains. Since simulations of aneurysmal hemodynamics in the interaction between coils and flow are limited, further studies should be performed to elucidate the role of hemodynamics on coil compaction and dislocation.

## 6. Aneurysm Stenting

Stents have been used as scaffolds to keep coils in the cavities of fusiform and wide-neck aneurysms. At present, it is believed that stents alone can be used to reduce the flow from the parent artery and to thromboembolize the aneurysm sac. Although thromboembolization with stents may be less effective than that with coils, the advantages of stenting include the ability to stabilize the aneurysm without touching the aneurysm sac and to block the aneurysm neck by inducing neointima formation over the stent surface. Predicting the hemodynamic changes after stenting could be helpful for designing and selecting stents effective for aneurysm embolization.

Flow patterns, vorticity, slip velocity, and WSS are relevant hemodynamic parameters affecting the thromboembolization efficiency of stents. Flow visualization methods have been used in aneurysm phantom models to elucidate the effects of stent porosity [87–90]. Quantitative experimental methods using particle image velocimetry [91, 92] and laser Doppler velocimetry [93, 94] have also been used to evaluate alterations in hemodynamics according to different vessel geometries and stent designs.

Computational analyses have been performed to elucidate the flow field alterations caused by stents and to evaluate their ability to divert flow and induce stasis inside of aneurysmal cavities [95, 96]. Patient-specific aneurysm models have also been analyzed to elucidate the flow alterations caused by stenting [11, 70, 97–102]. Recently, Cebra et al. [103] performed CFD analysis on the cerebral aneurysms which are apparently successfully treated using a stent but have been complicated by later aneurysm hemorrhage. They showed that flow diversion stent can cause intra-aneurysmal pressure increase, which can potentially lead to rupture. Among the challenges in the CFD simulation of stented aneurysms, there are major difficulties related to the meshing of stents due to the scale differences between the artery and stent strut thickness. Some adaptive embedding techniques have been developed to resolve such meshing difficulties [104–106]: vessel walls are treated with body-fitted unstructured grids, and stents are embedded in the grids; furthermore, adaptive meshing refinement is performed near the stents.

The flow of stented lateral and terminal aneurysms have been simulated by modeling a stent as a porous medium [107]. In this study, a rough model of stent geometry can reproduce flow features quantitatively as well as qualitatively. LBMs considering velocity reduction caused by stent implantation in advance using the stent positioning effect have also been developed to predict the thromboembolization of stented aneurysms [108–110]. The simulation of stent deployment is also challenging. In some models, an elastic cylindrical support surface is generated along the parent vessel that deforms until it comes into contact with the vessel wall [104, 111]. The inlet and outlet boundary conditions, as well as the parent vessel wall elasticity before and after the stenting, should be specified accurately. Further studies are required to model stent deployment as well as vessel wall and flow field alterations due to stenting, neointima formation along the stent, and thromboembolization modeling.

## 7. Discussion and Conclusions

Experimental hemodynamic studies have been performed using various cerebral aneurysm models in order to investigate the role of fluid dynamics in the etiology of aneurysms [48, 94, 111–115] and endovascular treatment [31, 105, 116]. These studies have attempted to find correlations between complex hemodynamic variables and cerebral aneurysm formation, growth and rupture with idealized model geometries. Hemodynamic alterations after stenting and coiling are also observed in *in vitro* models [81, 90] as well as in surgically created aneurysms in animal models [117]. Since the details of flow patterns are significantly affected by vessel and aneurysm geometries, realistic vascular geometry is believed to be one of the most important factors for precisely analyzing flow in aneurysms and arteries.

Recently, detailed patients' vessel geometries have become available as a result of the progress of high-resolution angiography techniques. Moreover, and the recent advances in information technology have enabled the prediction of hemodynamics in patient-specific blood vessels using CFD analysis. Difficulties in accurately determining blood vessel geometry from patient angiograms are related to the segmentation of the lumen, defining the calculation domain, and computational mesh formation. Since these difficulties require a great deal of manual, time-consuming, and operator-dependent work to be overcome, efforts for developing in-house codes for patient-specific CFD analyses have been made.

Other difficulties in CFD analysis are related to defining the material properties and boundary conditions for realistic *in vivo* arterial blood flow. The consideration of the rheological viscosity characteristics of blood and vessel wall elasticity in arterial blood flow analysis has remained controversial over the last few decades. Even though non-Newtonian viscosity characteristics are not important for analyzing blood flow in large arteries [11, 118–121], they may influence the WSS distributions in aneurysmal flow [10]. The implementation of non-Newtonian viscosity laws in CFD calculations requires relatively insignificant efforts and computational loads, although validating the viscosity law in complex flow fields may be difficult. Taking the wall elasticity of arteries into consideration in computational analysis requires additional information on vessel radial wall motion, local wall properties, and pressure waveforms—all of which are difficult to obtain. CFD analysis using dynamic angiography has been attempted [122–124] to define radial vessel wall motion. Specifying outflow boundary conditions also requires careful attentions, and the appropriate impedances of the distal vasculature for multiple outlets should be provided.

Even though accurate vessel geometry can be obtained using high-resolution medical imaging modalities and hemodynamic analysis can be performed with the help of state-of-the-art computing techniques, the application of hemodynamic parameters for predicting aneurysm growth and rupture is still limited. Although information regarding vessel wall structure is very useful, it is difficult to obtain *in vivo* information of aneurysm wall structures. A vascular

wall-remodeling model based on cell mechanobiology has been developed on the basis of FSI [125–127]. In this particular growth and remodeling model, hemodynamic analysis provides the wall tractions for wall mechanics computation to refine wall properties and geometries. The solution iterated between fluid and solid wall mechanics, and stress mediated-growth and aneurysmal remodeling have been analyzed. Modeling the changes in properties, configurations, and mass fractions of the aneurysmal wall due to mechanical stress requires further study [49, 125, 128]. Moreover, difficulties related to adaptive mesh generation [129–131] and boundary conditions for describing wall traction should be considered when computationally analyzing vascular wall remodeling.

Patient-specific hemodynamic simulations would provide valuable information for planning and follow-up decisions in cerebral aneurysm treatment. Additional effort is required to develop fast and accurate computational methodologies using high-resolution medical images to apply CFD simulation in cerebral aneurysm diagnostic and intervention planning tools. In addition, fundamental mechanobiological studies on the effects of hemodynamics on aneurysm growth, rupture, and thromboembolization should be performed in order to refine and complete the computational modeling.

## Acknowledgment

This paper was supported by a Grant from the Korean Health Technology R&D Project, Ministry of Health and Welfare, Republic of Korea (A111101).

## References

- [1] M. Kaminogo, M. Yonekura, and S. Shibata, “Incidence and outcome of multiple intracranial aneurysms in a defined population,” *Stroke*, vol. 34, no. 1, pp. 16–21, 2003.
- [2] F. H. H. Linn, G. J. E. Rinkel, A. Algra, and J. Van Gijn, “Incidence of subarachnoid hemorrhage: role of region, year, and rate of computed tomography: a meta-analysis,” *Stroke*, vol. 27, no. 4, pp. 625–629, 1996.
- [3] H. R. Winn, J. A. Jane, J. Taylor, D. Kaiser, and A. G. W. Britz, “Prevalence of asymptomatic incidental aneurysms: review of 4568 arteriograms,” *Journal of Neurosurgery*, vol. 96, no. 1, pp. 43–49, 2002.
- [4] S. Juvela, “Natural history of unruptured intracranial aneurysms: risks for aneurysm formation, growth, and rupture,” *Acta Neurochirurgica, Supplement*, no. 82, pp. 27–30, 2002.
- [5] D. O. Wiebers, “Unruptured intracranial aneurysms: natural history, clinical outcome, and risks of surgical and endovascular treatment,” *Lancet*, vol. 362, no. 9378, pp. 103–110, 2003.
- [6] J. Cao and S. E. Rittgers, “Particle motion within in vitro models of stenosed internal carotid and left anterior descending coronary arteries,” *Annals of Biomedical Engineering*, vol. 26, no. 2, pp. 190–199, 1998.
- [7] S. Z. Zhao, X. Y. Xu, A. D. Hughes et al., “Blood flow and vessel mechanics in a physiologically realistic model of a human carotid arterial bifurcation,” *Journal of Biomechanics*, vol. 33, no. 8, pp. 975–984, 2000.
- [8] A. P. Yoganathan, J. Ball, Y. R. Woo et al., “Steady flow velocity measurements in a pulmonary artery model with varying degrees of pulmonic stenosis,” *Journal of Biomechanics*, vol. 19, no. 2, pp. 129–146, 1986.
- [9] A. M. Nixon, M. Gunel, and B. E. Sumpio, “The critical role of hemodynamics in the development of cerebral vascular disease: a review,” *Journal of Neurosurgery*, vol. 112, no. 6, pp. 1240–1253, 2010.
- [10] J. R. Cebal, M. A. Castro, S. Appanaboyina, C. M. Putman, D. Millan, and A. F. Frangi, “Efficient pipeline for image-based patient-specific analysis of cerebral aneurysm hemodynamics: technique and sensitivity,” *IEEE Transactions on Medical Imaging*, vol. 24, no. 4, pp. 457–467, 2005.
- [11] D. A. Steinman, J. S. Milner, C. J. Norley, S. P. Lownie, and D. W. Holdsworth, “Image-based computational simulation of flow dynamics in a giant intracranial aneurysm,” *American Journal of Neuroradiology*, vol. 24, no. 4, pp. 559–566, 2003.
- [12] C. A. Taylor and D. A. Steinman, “Image-based modeling of blood flow and vessel wall dynamics: applications, methods and future directions,” *Annals of Biomedical Engineering*, vol. 38, no. 3, pp. 1188–1203, 2010.
- [13] R. Torii, M. Oshima, T. Kobayashi, K. Takagi, and T. E. Tezduyar, “Fluid-structure interaction modeling of a patient-specific cerebral aneurysm: influence of structural modeling,” *Computational Mechanics*, vol. 43, no. 1, pp. 151–159, 2008.
- [14] A. Valencia, D. Ledermann, R. Rivera, E. Bravo, and M. Galvez, “Blood flow dynamics and fluid-structure interaction in patient-specific bifurcating cerebral aneurysms,” *International Journal for Numerical Methods in Fluids*, vol. 58, no. 10, pp. 1081–1100, 2008.
- [15] J. R. Cebal, M. A. Castro, O. Soto, R. Löhner, and N. Alperin, “Blood-flow models of the circle of Willis from magnetic resonance data,” *Journal of Engineering Mathematics*, vol. 47, no. 3-4, pp. 369–386, 2003.
- [16] J. R. Cebal and R. Lhner, “From medical images to anatomically accurate finite element grids,” *International Journal for Numerical Methods in Engineering*, vol. 51, no. 8, pp. 985–1008, 2001.
- [17] P. J. Yim, J. J. Cebal, R. Mullick, H. B. Marcos, and P. L. Choyke, “Vessel surface reconstruction with a tubular deformable model,” *IEEE Transactions on Medical Imaging*, vol. 20, no. 12, pp. 1411–1421, 2001.
- [18] M. A. Castro, C. M. Putman, and J. R. Cebal, “Computational fluid dynamics modeling of intracranial aneurysms: effects of parent artery segmentation on intra-aneurysmal hemodynamics,” *American Journal of Neuroradiology*, vol. 27, no. 8, pp. 1703–1709, 2006.
- [19] P. Yim, K. DeMarco, M. A. Castro, and J. Cebal, “Characterization of shear stress on the wall of the carotid artery using magnetic resonance imaging and computational fluid dynamics,” *Studies in Health Technology and Informatics*, vol. 113, pp. 412–422, 2005.
- [20] C. Karmonik, C. Yen, O. Diaz, R. Klucznik, R. G. Grossman, and G. Benndorf, “Temporal variations of wall shear stress parameters in intracranial aneurysms-importance of patient-specific inflow waveforms for CFD calculations,” *Acta Neurochirurgica*, vol. 152, no. 8, pp. 1391–1398, 2010.
- [21] C. Karmonik, C. Yen, R. G. Grossman, R. Klucznik, and G. Benndorf, “Intra-aneurysmal flow patterns and wall shear stresses calculated with computational flow dynamics in an anterior communicating artery aneurysm depend on knowledge of patient-specific inflow rates,” *Acta Neurochirurgica*, vol. 151, no. 5, pp. 479–485, 2009.

- [22] M. Spiegel, T. Redel, Y. J. Zhang et al., "Tetrahedral vs. polyhedral mesh size evaluation on flow velocity and wall shear stress for cerebral hemodynamic simulation," *Computer Methods in Biomechanics and Biomedical Engineering*, vol. 14, no. 1, pp. 9–22, 2011.
- [23] F. Bonneville, N. Sourour, and A. Biondi, "Intracranial Aneurysms: an overview," *Neuroimaging Clinics of North America*, vol. 16, no. 3, pp. 371–382, 2006.
- [24] A. L. Rhoton, "Aneurysms," *Neurosurgery*, vol. 51, no. 4, pp. 121–158, 2002.
- [25] L. Gao, Y. Hoi, D. D. Swartz, J. Kolega, A. Siddiqui, and H. Meng, "Nascent aneurysm formation at the basilar terminus induced by hemodynamics," *Stroke*, vol. 39, no. 7, pp. 2085–2090, 2008.
- [26] H. Meng, Z. Wang, Y. Hoi et al., "Complex hemodynamics at the apex of an arterial bifurcation induces vascular remodeling resembling cerebral aneurysm initiation," *Stroke*, vol. 38, no. 6, pp. 1924–1931, 2007.
- [27] T. A. Altes, H. J. Cloft, J. G. Short et al., "Creation of saccular aneurysms in the rabbit: a model suitable for testing endovascular devices," *American Journal of Roentgenology*, vol. 174, no. 2, pp. 349–354, 2000.
- [28] N. H. Fujiwara, H. J. Cloft, W. F. Marx, J. G. Short, M. E. Jensen, and D. F. Kallmes, "Serial angiography in an elastase-induced aneurysm model in rabbits: evidence for progressive aneurysm enlargement after creation," *American Journal of Neuroradiology*, vol. 22, no. 4, pp. 698–703, 2001.
- [29] H. Meng, E. Metaxa, Z. Wang et al., "Vascular response to impinging blood flow," in *Proceedings of the BMES Annual Fall Meeting*, Baltimore, MD, USA, 2005.
- [30] M. Shojima, M. Oshima, K. Takagi et al., "Role of the bloodstream impacting force and the local pressure elevation in the rupture of cerebral aneurysms," *Stroke*, vol. 36, no. 9, pp. 1933–1938, 2005.
- [31] Y. Hoi, H. Meng, S. H. Woodward et al., "Effects of arterial geometry on aneurysm growth: three-dimensional computational fluid dynamics study," *Journal of Neurosurgery*, vol. 101, no. 4, pp. 676–681, 2004.
- [32] S. Fukuda, N. Hashimoto, H. Naritomi et al., "Prevention of rat cerebral aneurysm formation by inhibition of nitric oxide synthase," *Circulation*, vol. 101, no. 21, pp. 2532–2538, 2000.
- [33] S. Kondo, N. Hashimoto, H. Kikuchi, F. Hazama, I. Nagata, and H. Kataoka, "Cerebral aneurysms arising at nonbranching sites: an experimental study," *Stroke*, vol. 28, no. 2, pp. 398–404, 1997.
- [34] S. Chien, S. Li, and J. Y. J. Shyy, "Effects of mechanical forces on signal transduction and gene expression in endothelial cells," *Hypertension*, vol. 31, no. 1, pp. 162–169, 1998.
- [35] P. F. Davies, "Flow-mediated endothelial mechanotransduction," *Physiological Reviews*, vol. 75, no. 3, pp. 519–560, 1995.
- [36] P. F. Davies, K. A. Barbee, M. V. Volin et al., "Spatial relationships in early signaling events of flow-mediated endothelial mechanotransduction," *Annual Review of Physiology*, vol. 59, pp. 527–549, 1997.
- [37] A. Mantha, C. Karmonik, G. Benndorf, C. Strother, and R. Metcalfe, "Hemodynamics in a cerebral artery before and after the formation of an aneurysm," *American Journal of Neuroradiology*, vol. 27, no. 5, pp. 1113–1118, 2006.
- [38] J. Y. J. Shyy, "Mechanotransduction in endothelial responses to shear stress: review of work in Dr. Chien's laboratory," *Biorheology*, vol. 38, no. 2-3, pp. 109–117, 2001.
- [39] W. E. Stehens, "Histopathology of cerebral aneurysms," *Archives of neurology*, vol. 8, pp. 272–285, 1963.
- [40] O. Traub and B. C. Berk, "Laminar shear stress: mechanisms by which endothelial cells transduce an atheroprotective force," *Arteriosclerosis, Thrombosis, and Vascular Biology*, vol. 18, no. 5, pp. 677–685, 1998.
- [41] W. E. Stehens, "Etiology of intracranial berry aneurysms," *Journal of Neurosurgery*, vol. 70, no. 6, pp. 823–831, 1989.
- [42] D. Chyatte and I. Lewis, "Gelatinase activity and the occurrence of cerebral aneurysms," *Stroke*, vol. 28, no. 4, pp. 799–804, 1997.
- [43] G. Bruno, R. Todor, I. Lewis, and D. Chyatte, "Vascular extracellular matrix remodeling in cerebral aneurysms," *Journal of Neurosurgery*, vol. 89, no. 3, pp. 431–440, 1998.
- [44] H. D. Intengan and E. L. Schiffrin, "Vascular remodeling in hypertension: roles of apoptosis, inflammation, and fibrosis," *Hypertension*, vol. 38, no. 3, pp. 581–587, 2001.
- [45] A. Hara, N. Yoshimi, and H. Mori, "Evidence for apoptosis in human intracranial aneurysms," *Neurological Research*, vol. 20, no. 2, pp. 127–130, 1998.
- [46] S. Kondo, N. Hashimoto, H. Kikuchi, F. Hazama, I. Nagata, and H. Kataoka, "Apoptosis of medial smooth muscle cells in the development of saccular cerebral aneurysms in rats," *Stroke*, vol. 29, no. 1, pp. 181–189, 1998.
- [47] B. L. Langille, "Arterial remodeling: relation to hemodynamics," *Canadian Journal of Physiology and Pharmacology*, vol. 74, no. 7, pp. 834–841, 1996.
- [48] A. C. Bursleson, C. M. Strother, V. T. Turitto, H. H. Batjer, S. Kobayashi, and R. E. Harbaugh, "Computer modeling of intracranial saccular and lateral aneurysms for the study of their hemodynamics," *Neurosurgery*, vol. 37, no. 4, pp. 774–784, 1995.
- [49] I. Chatziprodromou, A. Tricoli, D. Poulikakos, and Y. Ventiokos, "Haemodynamics and wall remodeling of a growing cerebral aneurysm: a computational model," *Journal of Biomechanics*, vol. 40, no. 2, pp. 412–426, 2007.
- [50] Y. Hoi, S. H. Woodward, M. Kim, D. B. Taulbee, and H. Meng, "Validation of CFD simulations of cerebral aneurysms with implication of geometric variations," *Journal of Biomechanical Engineering*, vol. 128, no. 6, pp. 844–851, 2006.
- [51] B. Utter and J. S. Rossmann, "Numerical simulation of saccular aneurysm hemodynamics: influence of morphology on rupture risk," *Journal of Biomechanics*, vol. 40, no. 12, pp. 2716–2722, 2007.
- [52] J. R. Cebal, M. A. Castro, J. E. Burgess, R. S. Pergolizzi, M. J. Sheridan, and C. M. Putman, "Characterization of cerebral aneurysms for assessing risk of rupture by using patient-specific computational hemodynamics models," *American Journal of Neuroradiology*, vol. 26, no. 10, pp. 2550–2559, 2005.
- [53] M. Shojima, M. Oshima, K. Takagi et al., "Magnitude and role of wall shear stress on cerebral aneurysm: computational fluid dynamic study of 20 middle cerebral artery aneurysms," *Stroke*, vol. 35, no. 11, pp. 2500–2505, 2004.
- [54] Y. Feng, S. Wada, K. I. Tsubota, and T. Yamaguchi, "The application of computer simulation in the genesis and development of intracranial aneurysms," *Technology and Health Care*, vol. 13, no. 4, pp. 281–291, 2005.
- [55] Y. Feng, S. Wada, K. I. Tsubota, and T. Yamaguchi, "Growth of intracranial aneurysms arised from curved vessels under the influence of elevated wall shear stress—a computer simulation study," *JSME International Journal, Series C*, vol. 47, no. 4, pp. 1035–1042, 2004.
- [56] L. Bousset, V. Rayz, C. McCulloch et al., "Aneurysm growth occurs at region of low wall shear stress: patient-specific

- correlation of hemodynamics and growth in a longitudinal study,” *Stroke*, vol. 39, no. 11, pp. 2997–3002, 2008.
- [57] S. Glagov, C. Zarins, D. P. Giddens, and D. N. Ku, “Hemodynamics and atherosclerosis. Insights and perspectives gained from studies of human arteries,” *Archives of Pathology and Laboratory Medicine*, vol. 112, no. 10, pp. 1018–1031, 1988.
- [58] D. N. Ku, D. P. Giddens, C. K. Zarins, and S. Glagov, “Pulsatile flow and atherosclerosis in the human carotid bifurcation. Positive correlation between plaque location and low and oscillating shear stress,” *Arteriosclerosis, Thrombosis, and Vascular Biology*, vol. 5, no. 3, pp. 293–302, 1985.
- [59] C. K. Zarins, D. P. Giddens, and B. K. Bharadvaj, “Carotid bifurcation atherosclerosis. Quantitative correlation of plaque localization with flow velocity profiles and wall shear stress,” *Circulation Research*, vol. 53, no. 4, pp. 502–514, 1983.
- [60] J. Frösen, A. Piippo, A. Paetau et al., “Remodeling of saccular cerebral artery aneurysm wall is associated with rupture: histological analysis of 24 unruptured and 42 ruptured cases,” *Stroke*, vol. 35, no. 10, pp. 2287–2293, 2004.
- [61] A. M. Malek, S. L. Alper, and S. Izumo, “Hemodynamic shear stress and its role in atherosclerosis,” *Journal of the American Medical Association*, vol. 282, no. 21, pp. 2035–2042, 1999.
- [62] D. Kaiser, M. A. Freyberg, and P. Friedl, “Lack of hemodynamic forces triggers apoptosis in vascular endothelial cells,” *Biochemical and Biophysical Research Communications*, vol. 231, no. 3, pp. 586–590, 1997.
- [63] A. A. Valencia, A. M. Guzmán, E. A. Finol, and C. H. Amon, “Blood flow dynamics in saccular aneurysm models of the basilar artery,” *Journal of Biomechanical Engineering*, vol. 128, no. 4, pp. 516–526, 2006.
- [64] A. Kamiya and T. Togawa, “Adaptive regulation of wall shear stress to flow change in the canine carotid artery,” *The American Journal of Physiology*, vol. 239, no. 1, pp. H14–H21, 1980.
- [65] P. C. Smiesko and V. Johnson, “The arterial lumen is controlled by flow-related shear stress,” *Physiology*, vol. 8, pp. 34–38, 1993.
- [66] F. Tronc, M. Wassef, B. Esposito, D. Henrion, S. Glagov, and A. Tedgui, “Role of NO in flow-induced remodeling of the rabbit common carotid artery,” *Arteriosclerosis, Thrombosis, and Vascular Biology*, vol. 16, no. 10, pp. 1256–1262, 1996.
- [67] C. K. Zarins, M. A. Zatina, and D. P. Giddens, “Shear stress regulation of artery lumen diameter in experimental atherogenesis,” *Journal of Vascular Surgery*, vol. 5, no. 3, pp. 413–420, 1987.
- [68] J. R. Cebral, F. Mut, J. Weir, and C. M. Putman, “Association of hemodynamic characteristics and cerebral aneurysm rupture,” *American Journal of Neuroradiology*, vol. 32, no. 2, pp. 264–270, 2011.
- [69] G. N. Foutarakis, H. Yonas, and R. J. Scwabassi, “Saccular aneurysm formation in curved and bifurcating arteries,” *American Journal of Neuroradiology*, vol. 20, no. 7, pp. 1309–1317, 1999.
- [70] J. R. Cebral, M. Hernandez, and A. F. Frangi, “Computational analysis of blood flow dynamics in cerebral aneurysms from CTA and 3D rotational angiography image data,” in *Proceedings of the International Congress on Computational Bioengineering*, pp. 191–198, Zaragoza, Spain, 2003.
- [71] A. Valencia, H. Morales, R. Rivera, E. Bravo, and M. Galvez, “Blood flow dynamics in patient-specific cerebral aneurysm models: the relationship between wall shear stress and aneurysm area index,” *Medical Engineering and Physics*, vol. 30, no. 3, pp. 329–340, 2008.
- [72] G. Lu, L. Huang, X. L. Zhang et al., “Influence of hemodynamic factors on rupture of intracranial aneurysms: patient-specific 3D mirror aneurysms model computational fluid dynamics simulation,” *American Journal of Neuroradiology*, vol. 32, no. 7, pp. 1255–1261, 2011.
- [73] R. Torii, M. Oshima, T. Kobayashi, K. Takagi, and T. E. Tezduyar, “Fluid-structure interaction modeling of aneurysmal conditions with high and normal blood pressures,” *Computational Mechanics*, vol. 38, no. 4-5, pp. 482–490, 2006.
- [74] R. Torii, M. Oshima, T. Kobayashi, K. Takagi, and T. E. Tezduyar, “Influencing factors in image-based fluid-structure interaction computation of cerebral aneurysms,” *International Journal for Numerical Methods in Fluids*, vol. 65, no. 1–3, pp. 324–340, 2011.
- [75] J. G. Isaksen, Y. Bazilevs, T. Kvamsdal et al., “Determination of wall tension in cerebral artery aneurysms by numerical simulation,” *Stroke*, vol. 39, no. 12, pp. 3172–3178, 2008.
- [76] C. Groden, J. Laudan, S. Gatchell, and H. Zeumer, “Three-dimensional pulsatile flow simulation before and after endovascular coil embolization of a terminal cerebral aneurysm,” *Journal of Cerebral Blood Flow and Metabolism*, vol. 21, no. 12, pp. 1464–1471, 2001.
- [77] S. I. Stiver, P. J. Porter, R. A. Willinsky, and M. C. Wallace, “Acute human histopathology of an intracranial aneurysm treated using Guglielmi detachable coils: case report and review of the literature,” *Neurosurgery*, vol. 43, no. 5, pp. 1203–1207, 1998.
- [78] H. Tenjin, S. Fushiki, Y. Nakahara et al., “Effect of Guglielmi detachable coils on experimental carotid artery aneurysms in primates,” *Stroke*, vol. 26, no. 11, pp. 2075–2080, 1995.
- [79] M. B. Horowitz, P. D. Purdy, D. Burns, and D. Bellotto, “Scanning electron microscopic findings in a basilar tip aneurysm embolized with Guglielmi detachable coils,” *American Journal of Neuroradiology*, vol. 18, no. 4, pp. 688–690, 1997.
- [80] S. Shimizu, A. Kurata, M. Takano et al., “Tissue response of a small saccular aneurysm after incomplete occlusion with a Guglielmi detachable coil,” *American Journal of Neuroradiology*, vol. 20, no. 4, pp. 546–548, 1999.
- [81] H. S. Byun and K. Rhee, “CFD modeling of blood flow following coil embolization of aneurysms,” *Medical Engineering and Physics*, vol. 26, no. 9, pp. 755–761, 2004.
- [82] S. Ahmed, I. D. Sutalo, and H. Kavnoudias, “Hemodynamics and stress distribution in a cerebral aneurysm partially blocked with coils,” in *Proceedings of the 5th International Conference on CFD in the Process Industries CSIRO*, pp. 13–15, Melbourne, Australia, 2006.
- [83] N. M. P. Kakalis, A. P. Mitsos, J. V. Byrne, and Y. Ventikos, “The haemodynamics of endovascular aneurysm treatment: a computational modelling approach for estimating the influence of multiple coil deployment,” *IEEE Transactions on Medical Imaging*, vol. 27, no. 6, Article ID 4531637, pp. 814–824, 2008.
- [84] A. P. Mitsos, N. M. P. Kakalis, Y. P. Ventikos, and J. V. Byrne, “Haemodynamic simulation of aneurysm coiling in an anatomically accurate computational fluid dynamics model: technical note,” *Neuroradiology*, vol. 50, no. 4, pp. 341–347, 2008.
- [85] A. Narracott, S. Smith, P. Lawford et al., “Development and validation of models for the investigation of blood clotting in idealized stenoses and cerebral aneurysms,” *Journal of Artificial Organs*, vol. 8, no. 1, pp. 56–62, 2005.
- [86] Y. Wei, S. Cotin, J. Allard, L. Fang, C. Pan, and S. Ma, “Interactive blood-coil simulation in real-time during aneurysm

- embolization,” *Computers and Graphics*, vol. 35, no. 2, pp. 422–430, 2011.
- [87] K. Baráth, F. Cassot, D. A. Rüfenacht, and J. H. D. Fasel, “Anatomically shaped internal carotid artery aneurysm in vitro model for flow analysis to evaluate stent effect,” *American Journal of Neuroradiology*, vol. 25, no. 10, pp. 1750–1759, 2004.
- [88] K. Baráth, F. Cassot, J. H. D. Fasel, M. Ohta, and D. A. Rüfenacht, “Influence of stent properties on the alteration of cerebral intra-aneurysmal haemodynamics: flow quantification in elastic sidewall aneurysm models,” *Neurological Research*, vol. 27, no. 1, pp. S120–S128, 2005.
- [89] B. B. Lieber, A. P. Stancampiano, and A. K. Wakhloo, “Alteration of hemodynamics in aneurysm models by stenting: influence of stent porosity,” *Annals of Biomedical Engineering*, vol. 25, no. 3, pp. 460–469, 1997.
- [90] K. Rhee, M. H. Han, and S. H. Cha, “Changes of flow characteristics by stenting in aneurysm models: influence of aneurysm geometry and stent porosity,” *Annals of Biomedical Engineering*, vol. 30, no. 7, pp. 894–904, 2002.
- [91] B. B. Lieber, V. Livescu, L. N. Hopkins, and A. K. Wakhloo, “Particle image velocimetry assessment of stent design influence on intra-aneurysmal flow,” *Annals of Biomedical Engineering*, vol. 30, no. 6, pp. 768–777, 2002.
- [92] S. C. M. Yu and J. B. Zhao, “A steady flow analysis on the stented and non-stented sidewall aneurysm models,” *Medical Engineering and Physics*, vol. 21, no. 3, pp. 133–141, 1999.
- [93] T. M. Liou, W. C. Chang, and C. C. Liao, “LDV measurements in lateral model aneurysms of various sizes,” *Experiments in Fluids*, vol. 23, no. 4, pp. 317–324, 1997.
- [94] S. Tateshima, Y. Murayama, J. P. Villablanca et al., “In vitro measurement of fluid-induced wall shear stress in unruptured cerebral aneurysms harboring blebs,” *Stroke*, vol. 34, no. 1, pp. 187–192, 2003.
- [95] M. Aenis, A. P. Stancampiano, A. K. Wakhloo, and B. B. Lieber, “Modeling of flow in a straight stented and non-stented side wall aneurysm model,” *Journal of Biomechanical Engineering*, vol. 119, no. 2, pp. 206–212, 1997.
- [96] M. Ohta, S. G. Wetzel, P. Dantan et al., “Rheological changes after stenting of a cerebral aneurysm: a finite element modeling approach,” *CardioVascular and Interventional Radiology*, vol. 28, no. 6, pp. 768–772, 2005.
- [97] J. R. Cebral, M. Hernandez, A. F. Frangi, C. M. Putman, R. Pergolizzi, and J. E. Burgess, “Subject-specific modeling of intracranial aneurysms,” in *Medical Imaging*, Proceedings of SPIE, pp. 319–327, 2004.
- [98] J. R. Cebral and R. Löhner, “Flow visualization on unstructured grids using geometrical cuts, vortex detection and shock surfaces,” in *Proceedings of the 39th AIAA Aerospace Sciences Meeting and Exhibit*, Reno, Nev, USA, 2001.
- [99] J. R. Cebral and R. Löhner, “From medical images to anatomically accurate finite element grids,” *International Journal for Numerical Methods in Engineering*, vol. 51, no. 8, pp. 985–1008, 2001.
- [100] L. D. Jou, C. M. Quick, W. L. Young et al., “Computational approach to quantifying hemodynamic forces in giant cerebral aneurysms,” *American Journal of Neuroradiology*, vol. 24, no. 9, pp. 1804–1810, 2003.
- [101] R. Löhner, “Regridding surface triangulations,” *Journal of Computational Physics*, vol. 126, no. 1, pp. 1–10, 1996.
- [102] R. Löhner, “Automatic unstructured grid generators,” *Finite Elements in Analysis and Design*, vol. 25, no. 1-2, pp. 111–134, 1997.
- [103] J. R. Cebral, F. Mut, M. Raschi et al., “Aneurysm rupture following treatment with flow-diverting stents: computational hemodynamics analysis of treatment,” *American Journal of Neuroradiology*, vol. 32, pp. 27–33, 2011.
- [104] S. Appanaboyina, F. Mut, R. Löhner, C. Putman, and J. Cebral, “Simulation of intracranial aneurysm stenting: techniques and challenges,” *Computer Methods in Applied Mechanics and Engineering*, vol. 198, no. 45-46, pp. 3567–3582, 2009.
- [105] S. Appanaboyina, F. Mut, R. Löhner, C. M. Putman, and J. R. Cebral, “Computational fluid dynamics of stented intracranial aneurysms using adaptive embedded unstructured grids,” *International Journal for Numerical Methods in Fluids*, vol. 57, no. 5, pp. 475–493, 2008.
- [106] J. R. Cebral and R. Löhner, “Efficient simulation of blood flow past complex endovascular devices using an adaptive embedding technique,” *IEEE Transactions on Medical Imaging*, vol. 24, no. 4, pp. 468–476, 2005.
- [107] L. Augsburger, P. Reymond, D. A. Rüfenacht, and N. Stergiopulos, “Intracranial stents being modeled as a porous medium: flow simulation in stented cerebral aneurysms,” *Annals of Biomedical Engineering*, vol. 39, pp. 850–863, 2011.
- [108] B. Chopard, R. Ouared, D. A. Rüfenacht, and H. Yilmaz, “Lattice Boltzmann modeling of thrombosis in giant aneurysms,” *International Journal of Modern Physics C*, vol. 18, no. 4, pp. 712–721, 2007.
- [109] B. Chopard, R. Ouared, and D. A. Rüfenacht, “A lattice Boltzmann simulation of clotting in stented aneurysms and comparison with velocity or shear rate reductions,” *Mathematics and Computers in Simulation*, vol. 72, no. 2–6, pp. 108–112, 2006.
- [110] R. Ouared, B. Chopard, B. Stahl, D. A. Rüfenacht, H. Yilmaz, and G. Courbebaisse, “Thrombosis modeling in intracranial aneurysms: a lattice Boltzmann numerical algorithm,” *Computer Physics Communications*, vol. 179, no. 1–3, pp. 128–131, 2008.
- [111] S. Tateshima, J. Grinstead, S. Sinha et al., “Intraaneurysmal flow visualization by using phase-contrast magnetic resonance imaging: feasibility study based on a geometrically realistic in vitro aneurysm model,” *Journal of Neurosurgery*, vol. 100, no. 6, pp. 1041–1048, 2004.
- [112] Y. P. Gobin, J. L. Counord, P. Flaud, and J. Duffaux, “In vitro study of haemodynamics in a giant saccular aneurysm model: influence of flow dynamics in the parent vessel and effects of coil embolisation,” *Neuroradiology*, vol. 36, no. 7, pp. 530–536, 1994.
- [113] T. M. Liou and S. N. Liou, “A review on in vitro studies of hemodynamic characteristics in terminal and lateral aneurysm models,” *Proceedings of the National Science Council, Republic of China. Part B, Life sciences*, vol. 23, no. 4, pp. 133–148, 1999.
- [114] T. Satoh, K. Onoda, and S. Tsuchimoto, “Visualization of intraaneurysmal flow patterns with transluminal flow images of 3D MR angiograms in conjunction with aneurysmal configurations,” *American Journal of Neuroradiology*, vol. 24, no. 7, pp. 1436–1445, 2003.
- [115] H. Ujiie, H. Tachibana, O. Hiramatsu et al., “Effects of size and shape (aspect ratio) on the hemodynamics of saccular aneurysms: a possible index for surgical treatment of intracranial aneurysms,” *Neurosurgery*, vol. 45, no. 1, pp. 119–130, 1999.
- [116] A. J. Ringer, D. K. Lopes, A. S. Boulos, L. R. Guterman, and L. N. Hopkins, “Current techniques for endovascular treatment

- of intracranial aneurysms,” *Seminars in Cerebrovascular Diseases and Stroke*, vol. 1, pp. 39–51, 2001.
- [117] S. H. Kim, M. H. Han, I. K. Yu, S. H. Lee, and K. H. Chang, “Experimental model for creation of carotid artery aneurysms in dogs,” *Journal of the Korean Radiological Society*, vol. 35, pp. 703–707, 1996.
- [118] K. Perktold, R. Peter, and M. Resch, “Pulsatile non-Newtonian blood flow simulation through a bifurcation with an aneurysm,” *Biorheology*, vol. 26, no. 6, pp. 1011–1030, 1989.
- [119] K. Perktold and G. Rappitsch, “Computer simulation of local blood flow and vessel mechanics in a compliant carotid artery bifurcation model,” *Journal of Biomechanics*, vol. 28, no. 7, pp. 845–856, 1995.
- [120] D. A. Steinman, “Image-based computational fluid dynamics modeling in realistic arterial geometries,” *Annals of Biomedical Engineering*, vol. 30, no. 4, pp. 483–497, 2002.
- [121] G. R. Stuhne and D. A. Steinman, “Finite-element modeling of the hemodynamics of stented aneurysms,” *Journal of Biomechanical Engineering*, vol. 126, no. 3, pp. 382–387, 2004.
- [122] L. Dempere-Marco, E. Oubel, M. Castro, C. Putman, A. Frangi, and J. Cebral, “CFD analysis incorporating the influence of wall motion: application to intracranial aneurysms,” *Lecture Notes in Computer Science*, vol. 4191, pp. 438–445, 2006.
- [123] E. Oubel, M. De Craene, C. M. Putman, J. R. Cebral, and A. F. Frangi, “Analysis of intracranial aneurysm wall motion and its effects on hemodynamic patterns,” in *Medical Imaging*, vol. 6511 of *Proceedings of SPIE*, p. 65112A, San Diego, Calif, USA, February 2007.
- [124] K. Takizawa, C. Moorman, S. Wright et al., “Patient-specific arterial fluid-structure interaction modeling of cerebral aneurysms,” *International Journal for Numerical Methods in Fluids*, vol. 65, no. 1–3, pp. 308–323, 2011.
- [125] C. A. Figueroa, S. Baek, I. E. Vignon-Clementel, J. D. Humphrey, and C. A. Taylor, “Towards patient-specific modeling I: hemodynamics in a growing aneurysm,” in *Medical Imaging*, vol. 6143 of *Proceedings of SPIE*, p. 61430K, San Diego, Calif, USA, 2006.
- [126] R. L. Gleason and J. D. Humphrey, “A mixture model of arterial growth and remodeling in hypertension: altered muscle tone and tissue turnover,” *Journal of Vascular Research*, vol. 41, no. 4, pp. 352–363, 2004.
- [127] R. L. Gleason and J. D. Humphrey, “Effects of a sustained extension on arterial growth and remodeling: a theoretical study,” *Journal of Biomechanics*, vol. 38, no. 6, pp. 1255–1261, 2005.
- [128] S. Baek, C. A. Figueroa, C. A. Taylor, and J. D. Humphrey, “Towards patient-specific modeling II. Biomechanics of a growing aneurysm,” in *Medical Imaging*, vol. 6143 of *Proceedings of SPIE*, p. 61432C, San Diego, Calif, USA, 2006.
- [129] R. A. Peattie, T. J. Riehle, and E. I. Bluth, “Pulsatile flow in fusiform models of abdominal aortic aneurysms: flow fields, velocity patterns and flow-induced wall stresses,” *Journal of Biomechanical Engineering*, vol. 126, no. 4, pp. 438–446, 2004.
- [130] S. Prakash and C. R. Ethier, “Requirements for mesh resolution in 3D computational hemodynamics,” *Journal of Biomechanical Engineering*, vol. 123, no. 2, pp. 134–144, 2001.
- [131] A. V. Salsac, S. R. Sparks, and J. C. Lasheras, “Hemodynamic changes occurring during the progressive enlargement of abdominal aortic aneurysms,” *Annals of Vascular Surgery*, vol. 18, no. 1, pp. 14–21, 2004.

## Research Article

# Finite Element Modelling of Pulsatile Blood Flow in Idealized Model of Human Aortic Arch: Study of Hypotension and Hypertension

Paritosh Vasava,<sup>1</sup> Payman Jalali,<sup>1</sup> Mahsa Dabagh,<sup>1</sup> and Pertti J. Kolari<sup>2</sup>

<sup>1</sup> Faculty of Technology, Lappeenranta University of Technology, P.O. Box 20, 53851 Lappeenranta, Finland

<sup>2</sup> South Karelian Institute, Lappeenranta University of Technology, P.O. Box 20, 53851 Lappeenranta, Finland

Correspondence should be addressed to Paritosh Vasava, vasava@lut.fi

Received 31 August 2011; Accepted 17 October 2011

Academic Editor: Eun Bo Shim

Copyright © 2012 Paritosh Vasava et al. This is an open access article distributed under the Creative Commons Attribution License, which permits unrestricted use, distribution, and reproduction in any medium, provided the original work is properly cited.

A three-dimensional computer model of human aortic arch with three branches is reproduced to study the pulsatile blood flow with Finite Element Method. In specific, the focus is on variation of wall shear stress, which plays an important role in the localization and development of atherosclerotic plaques. Pulsatile pressure pulse is used as boundary condition to avoid flow entry development, and the aorta walls are considered rigid. The aorta model along with boundary conditions is altered to study the effect of hypotension and hypertension. The results illustrated low and fluctuating shear stress at outer and inner wall of aortic arch, proximal wall of branches, and entry region. Despite the simplification of aorta model, rigid walls and other assumptions results displayed that hypertension causes lowered local wall shear stresses. It is the sign of an increased risk of atherosclerosis. The assessment of hemodynamics shows that under the flow regimes of hypotension and hypertension, the risk of atherosclerosis localization in human aorta may increase.

## 1. Introduction

Atherosclerosis is the disease of large arteries (carotid, aorta, and other proximal arteries) and tends to localize in regions of curvature and branching in arteries. Caro et al. [1, 2] and DeBakey et al. [3] categorized aortic arch, major branches of aortic arch, and abdominal aorta as susceptible sites for creation and development of atherosclerosis. The complex anatomies of arteries are often associated with abnormal flow dynamics and stress distributions. Ku et al. [4], Nerem [5], Tarbell [6], and Zarins et al. [7] have reported that atherosclerosis is more prone to occur in regions of low shear stress and oscillating shear stress increases the risk of atherosclerosis localization. Fry [8] demonstrated that under acute elevation of shear stress the endothelial layer of arterial wall may damage and increases its permeability for lipids. These studies prove that there is a positive correlation between low and fluctuating wall shear stress and risk of development of atherosclerosis.

The human aorta has complex anatomy with curvature, branching, and distal tapering. Caro [2] and Fry [8] have shown that the human aortic arch is vulnerable to localization of atherosclerosis due to the complex anatomy of aorta. In his work, Utepov [10] has demonstrated the tapering of arteries as one of the risk factors for manifestation of atherosclerosis. Kilner et al. [11] detected, in vivo, the complicated helical and retrograde flow caused by the aortic arch and pulsatile nature of the inflow of blood from left ventricle of heart. Thus the complex arterial flow mechanics in aorta may promote the early development atherosclerotic plaque. The blood flow in thoracic aorta models has been also studied numerically [12–19]. However, some of studies neglected the three major of branches of aortic arch. Towfiq [9] and Dabagh et al. [20] have shown that the aorta size is subjected to change with blood pressure. But no attention has been made on studying the corresponding influence on the blood flow features. Moreover, the effect of blood pressure on changing the aorta geometry has also been ignored.

TABLE 1: Details of computational geometries measure in mm under normal pressure conditions.

Artery geometric measure (in mm)	Geometry	
Ascending aorta	Lumen diameter ( $B_1$ )	25.0
	Length ( $L_1$ )	18.0
Aortic arch	Arch radius ( $R$ )	32.5
	Lumen diameter ( $B_2$ )	25.0
Descending aorta	Length ( $L_2$ )	75.0
	Lumen diameter ( $B'_2$ )	20.0
Brachiocephalic artery (BA)	Diameter ( $A_1$ )	8.8
	Length ( $L_1$ )	28.0
	Diameter ( $A'_1$ )	8.8
Left common carotid artery (LCA)	Diameter ( $A_2$ )	8.8
	Length ( $L_2$ )	28.0
	Diameter ( $A'_2$ )	8.5
Left subclavian artery (LSA)	Diameter ( $A_3$ )	9.9
	Length ( $L_3$ )	28.0
	Diameter ( $A'_3$ )	9.9
Distance between BA and LCA ( $d_1$ )		3.6
Distance between LCA artery and LSA ( $d_2$ )		4.7

In the present study, we have reconstructed a three-dimensional (3D) aorta model adopted from the literature. The aorta model includes three major branches (brachiocephalic artery, left carotid artery and left subclavian artery) in the aortic arch. The pulsatile blood flow through three 3D model of aortic arch was simulated with incompressible Navier-Stokes equations. The governing equations along with boundary conditions are solved with Finite element method- (FEM-) based code Comsol Multiphysics V3.4. The idealized aorta model along with inlet pressure profile was further modified to simulate aorta under hypotension and hypertension conditions. Though the transient variation of blood pressure within a cardiac cycle causes instantaneous deformation of the aorta wall, which in turn may affect the blood flow features (two-way coupling between wall deformation and blood flow), such effects are ignored in this study. Because of the critical role played by the shear stress in arterial wall diseases, the wall shear stress (WSS) is studied extensively within branches and through the arch of aorta. Moreover, the velocity profiles across various cross sections of aortic arch and branches are investigated. The first objective of present study is to find out how the aortic geometry is connected with the blood flow development and the shear stress distribution in the aorta wall. The second objective is to realize how blood pressure and its associated wall deformation affect the distribution of WSS, the flow profiles, and the volumetric outflow across branches. Therefore, this study seeks the role of aortic arch geometry (with branches) and the mean blood pressure on the resulting transient blood flow only when the wall of aorta is rigid. However, one should note that the corresponding results might be different than what we observe in reality due to the flexibility of real wall and the complexity of the real aorta geometry.

## 2. Materials and Methods

The idealized model of human aorta was reconstructed based on aorta model used by Shahcheranhi et al. [18]. The model is constructed in six parts, namely, ascending aorta, aortic arch, descending aorta, and three branches (brachiocephalic artery, left common carotid artery, and left subclavian artery). The simplification of the geometry is basically associated with neglecting the undetermined curvature of the abdominal part of aorta and torsion of ascending aorta, as the original aorta models were reconstructed from the computed tomographic (CT) images. Moreover, there may be minor differences in original aorta models and aorta models used in this study due to different design module used for reconstruction purpose. Figure 1(a) illustrates the schematic diagram of aorta with the details of geometric measures given in Table 1. The aorta model was modified for two working pressures inside the aorta mimicking the hypotension (65–105 mmHg) and hypertension (100–140 mmHg) conditions. The variation of the inlet cross-sectional area versus pressure is demonstrated in Figure 1(b), which has been used in the construction of the geometry under the effect of hypotension and hypertension conditions.

The blood is assumed to be a Newtonian fluid. The assumption of Newtonian fluid for blood with a constant viscosity is feasible in large arteries. Although some works such as Khanfar et al. [21] showed that the non-Newtonian assumption of blood affects the blood flow in aorta aneurysms, their simulations did not display significant differences in shear stress calculated from Newtonian and non-Newtonian simulations. The driving force for the blood flow in an artery is the pressure gradient along the artery. Thus the pulsatile pressure-inlet boundary condition (with zero viscous stress) was used at inlet and outlets. The outflow

TABLE 2: Values of coefficients for polynomial used as pressure waveform ( $\times 10^5$ ).

$C_1$	$C_2$	$C_3$	$C_4$	$C_5$	$C_6$	$C_7$	$C_8$
0.5601	0.1882	-1.4424	1.2239	-0.426	0.0664	-0.00492	0.000432

from left ventricle of heart is not always uniform as flow disturbance is induced by aortic valve. Although an exact effect of tricuspid aortic valve cannot be exactly mimicked, with the deployment of pressure-inlet boundary condition we can avoid uniform inflow at inlet of aorta which has been typically used in several works. Thus the pressure-inlet boundary condition in the present study will be more realistic. In the present study, a pulsatile pressure is deployed as inlet and outlet boundary conditions. An eighth degree polynomial was used to reproduce the inlet pressure pulse in mmHg from the data given by Conlon et al. [22] as

$$f(t) = \begin{cases} \sum_{i=1}^9 C_i(t - 0.85n)^i + 79.20 & \text{if } t \in [0.85n, 0.85(n+1) - 0.34], \\ -61.50(t - 0.85n) + 131.47 & \text{if } t \in [0.85(n+1) - 0.34, 0.85(n+1)], \end{cases} \quad (1)$$

where  $n$  is the cardiac cycle number varying from 1 to 4. The polynomial coefficients  $C_i$  are introduced in Table 2. The period of systole and diastole in the pressure pulse took 0.35 s and 0.5 s, respectively. The pressure pulse at the inlet of ascending aorta is shown under normal pressure condition in Figure 1(c). For boundary conditions at the outlets, the pressure pulse is multiplied by a certain coefficient that represents pressure drop between inlet and respective outlet. The coefficients for respective branch outlets are obtained by a separate series of steady-state simulations with flat velocity at inlet and target mass flow at outlet. Li [23] has suggested that in large arteries it is reasonable to assume that the blood close to artery moves with same speed as that of wall. Thus over the walls of aorta, no-slip boundary condition is applied. Under transient condition and the assumption of incompressible flow with Newtonian rheology, the flow of blood in the aorta is governed by the continuity and Navier-Stokes equations

$$\nabla \cdot \mathbf{u} = 0, \quad (2)$$

$$\rho \frac{\partial \mathbf{u}}{\partial t} + \rho(\mathbf{u} \cdot \nabla) \mathbf{u} = -\nabla p + \mu \nabla \cdot (\nabla \mathbf{u} + (\nabla \mathbf{u})^T), \quad (3)$$

where  $\mathbf{u}$  denotes fluid velocity vector and  $p$  represents hydrostatic pressure. Also,  $\rho$  is the density of blood taken as  $1060 \text{ kg/m}^3$  and  $\mu$  is the dynamic viscosity of blood that is a constant as  $0.005 \text{ Pa}\cdot\text{s}$ .

To ensure periodic nature of the flow, the simulations were performed for four cardiac cycles (pressure pulse) where each cycle is 0.85 s. The results from fourth cardiac cycles are discussed in the results section. The governing equations were discretized with Backwards Difference Method, which is known to be a very stable method for discretization. The set of governing (2)-(3) along with

boundary conditions were solved by means of the FEM method provided in COMSOL Multiphysics, v. 3.4. The mesh grid for each aorta case was refined subsequently to obtain mesh-independent-results. The computational mesh utilized in primary simulations consisted of nearly 35000 to 42000 tetrahedral elements. The mesh grid was refined till the resulting distributions of the flow and WSS were qualitatively identical: spatially and temporally. The final mesh grid consisted of nearly 140000 grid elements. To further increase accuracy and reliability of the solutions, the local variations of flow variable within the grid elements were predicted by quadratic piecewise functions. Memory friendly iterative solvers GMRES and FGMRES were used for solving the discretized governing equations. The residual for solution was kept at  $1 \times 10^{-4}$  and the simulations progressed with a time step of 0.001 s. A steady-state simulation with 80 mmHg pressure was performed with direct solver UMFPACK and was used as an initial guess for the transient simulations. The transient simulations were performed with personal computer with 3 GHz Core 2 Duo processor with 3 GB of RAM.

The aorta model used in the current study was adopted from the literature and thus lacked some features of realistic aorta, for example, curvature in descending aorta. The study was focused on flow dynamics in aortic arch and three major branches, thus the branches of thoracic aorta were neglected. In real aorta, the branch entry regions have blunt corners; however, this feature of aorta model was not included due to lack of exact measurements. This feature of aorta model was also found missing in the original works [13, 18]. Due to limited memory available for computation, the fluid-structure interaction could not be included in the current set of simulation. The reported study is mainly focused on understanding the effects of hypotension and hypertension on the flow and WSS distributions. The reported study is mainly focused on understanding the effects of hypotension and hypertension on the flow and WSS distributions. Although it is indicative that assumption of rigid wall in blood flow simulation may underestimate temporal and spatial flow and wall motion, the aorta walls were assumed to be rigid for flow simulations under all three pressure regimes. Long-term hypertension can cause thickening of arterial wall and loss of elasticity of arterial wall [24]. Thus, aorta walls can be assumed rigid under hypertensive flow regime. The assumption of rigid artery wall in other two cases is acceptable as earlier works [21, 25–27] have demonstrated that the arterial compliance does not influence general characteristics of flow and WSS significantly. Moayeri and Zendehebudi [25] compared hemodynamic characteristics of blood flow through arterial stenosis with and without distensible walls numerically. The comparison revealed no difference between WSS distributions for the rigid and deformable walls during systole and diastole. Zhao et al. [27]

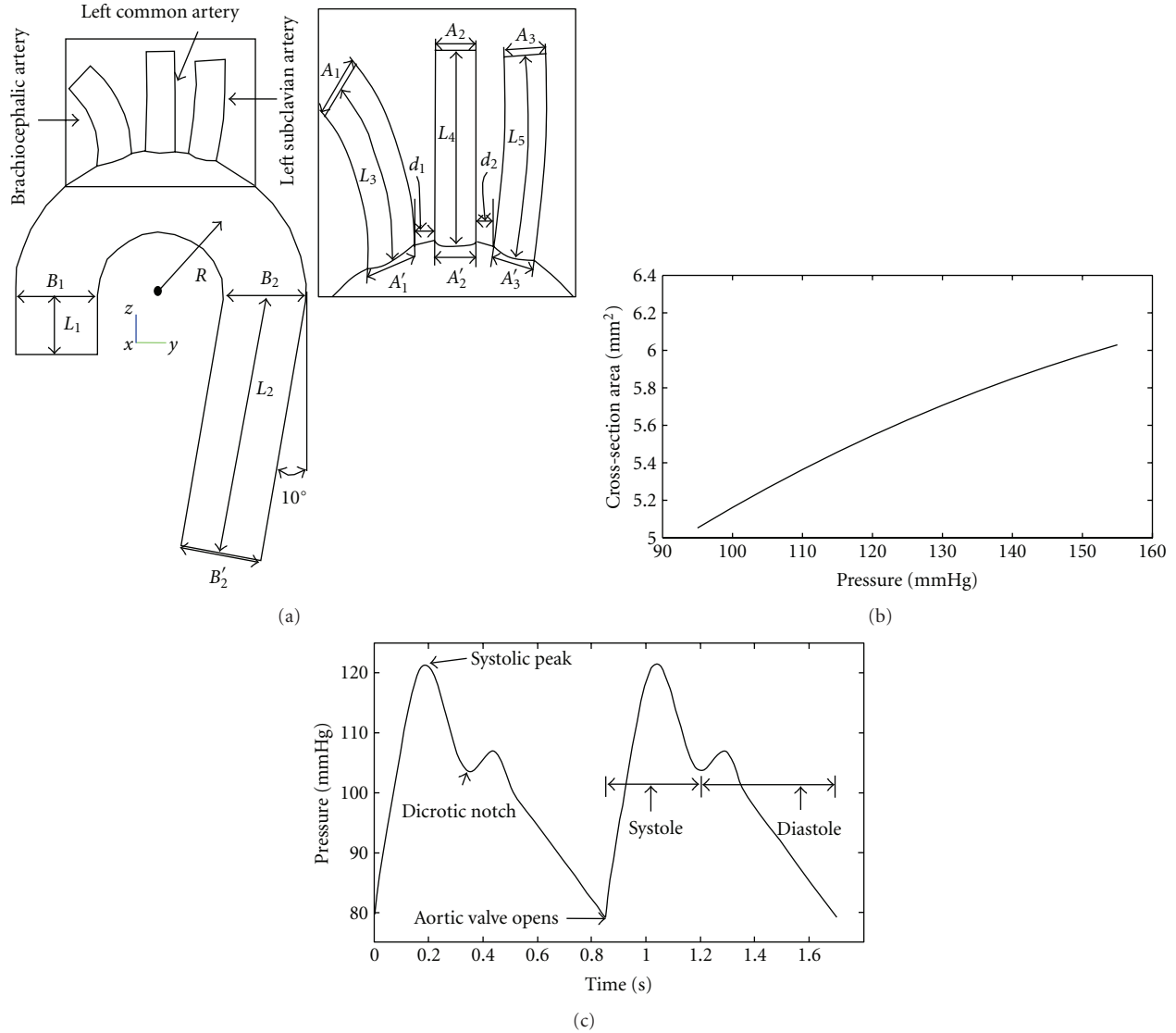


FIGURE 1: (a) Schematic diagram of 3D aortic arch model (Inset: a zoomed region around branches with definitions of lengths, diameters, and distances also common with the two other geometries), (b) the plot of luminal cross-sectional area of ascending aorta versus pressure estimated from Towfiq et al. [9]. (c) Pressure pulse at the inlet of ascending aorta under normal pressure condition.

studied the influence of wall distensibility on WSS numerically and did not find any significant difference between the WSS in rigid and compliant models. It is of notice that Zhao used an angiogram-based model of carotid bifurcation for their experiments. The localization of atherosclerosis is often localized in regions of low and oscillating WSS, flow stagnation, or recirculation. The elongation of separated flow region and local migration of recirculation or stagnant flow region may influence the localization of atherosclerosis only locally.

### 3. Results and Discussion

The axial velocity distributions and peripheral WSS at peak systolic time instance  $t = 0.18$  s are compared.

**3.1. The Distributions of Pressure, Flow Field, and WSS for Normal Pressure Case.** The pressure iso-contours and distribution of velocity across the coronal plane captured at time  $t = 0.18$  s are shown in Figures 2(a) and 2(c), respectively. In aortic arch high pressure is distributed on the upper aortic arch while low pressure is distributed at the inner curvature of the arch. The most prominent feature of pressure distribution is the maximum pressure distributed at the branch entry region of three branches. The maximum pressure is distributed on the distal side of three branch entry regions, while relatively lower pressure is distributed on the proximal side of the branching regions.

The axial flow in ascending aorta is marginally skewed towards the outer wall of the aorta. The marginal skewness persists close to the proximal aortic arch as well. In the aortic arch, the flow close to the inner aortic arch slows

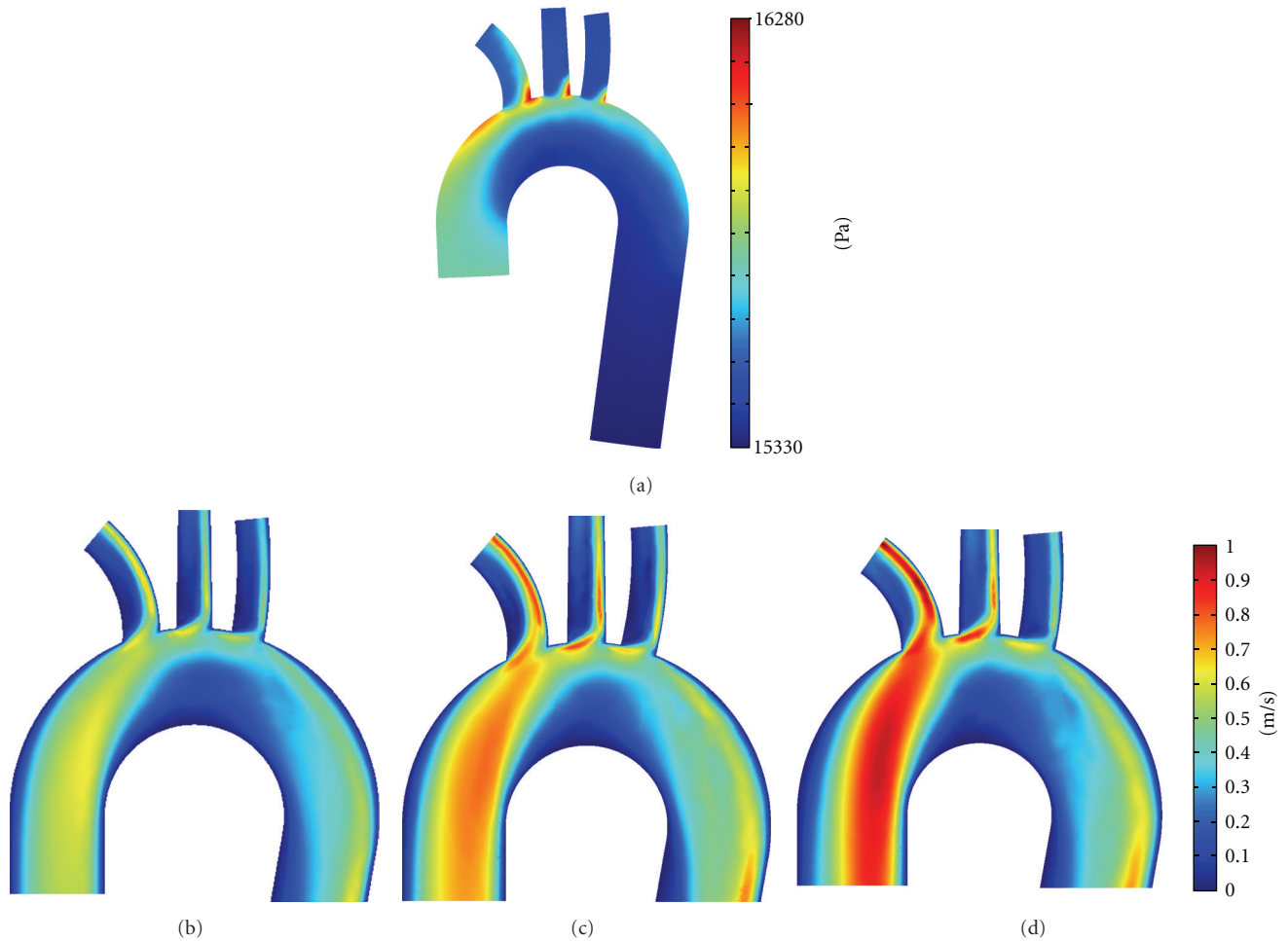


FIGURE 2: (a) Distribution of pressure for normal pressure regime, velocity distributions across the symmetry plane of the aorta model under (b) hypotension, (c) normal pressure, and (d) hypertension at peak systolic at time instance  $t = 0.18$  s.

down while the flow in the upper aortic arch accelerates. At the flow stagnation region in the aortic arch, the velocity of the flow is less than  $0.01$  m/s, which may account for longer particle residence time of blood cells and thus the localization of atherosclerosis. The pressure gradient across the branch entry region causes the maximum velocity of magnitude about  $0.72$  m/s on the proximal side of the branch entry region of brachiocephalic artery (Figure 2(c)). The flow separation and secondary flow motion in aortic arch affects the flow in distal aortic arch as well. In region after the left subclavian artery (the third branch), the flow profiles display more tendency to the distal wall. The flow in distal aortic arch and descending aorta is extremely skewed towards the inner wall. To obtain details of the secondary flow motion in the aortic arch and branches, velocity profiles across axial cross-sections of the aortic arch and branches (as shown in Figure 3(a)) were captured. The axial flow profiles for normal pressure case are demonstrated in Figures 3(b)–3(j). At section-A (Figure 3(b)), the flow is skewed towards the inner wall of the aortic arch. The aortic arch curvature induces secondary flow motion, which were captured at sections-B and C. The flow near outer wall of the arch

is directed towards the inner wall of the arch causing  $\epsilon$ - and C-shaped velocity distributions at sections B and C, respectively. At sections B and C, the flow is concentrated substantially around the outer wall of the arch. It is also of notice that the flow velocity retards as it moves from top towards the bottom of the axial section.

The axial flow distributions at sections D, F, and H suggest significant disturbance at the branch entry regions. This is demonstrated in Figures 3(e), 3(g), and 3(j). This is caused by the bifurcating flow coupled with pressure gradient across branch entry region. At sections D, F, and H, maximum velocity is distributed towards the distal side of the branch. The pressure gradient across the axial cross-section of branches causes flow separation and secondary flow patterns in branches as well. In Figure 2(c), it can be noticed that the flow in branches is skewed towards the proximal walls. The skewness of the flow causes flow stagnations close to the proximal walls of respective branches. It is also noticeable that at the axial sections at the branch exit region (sections E, G, and I), the flow remains localized towards the distal wall. The pressure gradient between proximal and distal wall is highest in brachiocephalic artery, moderate in

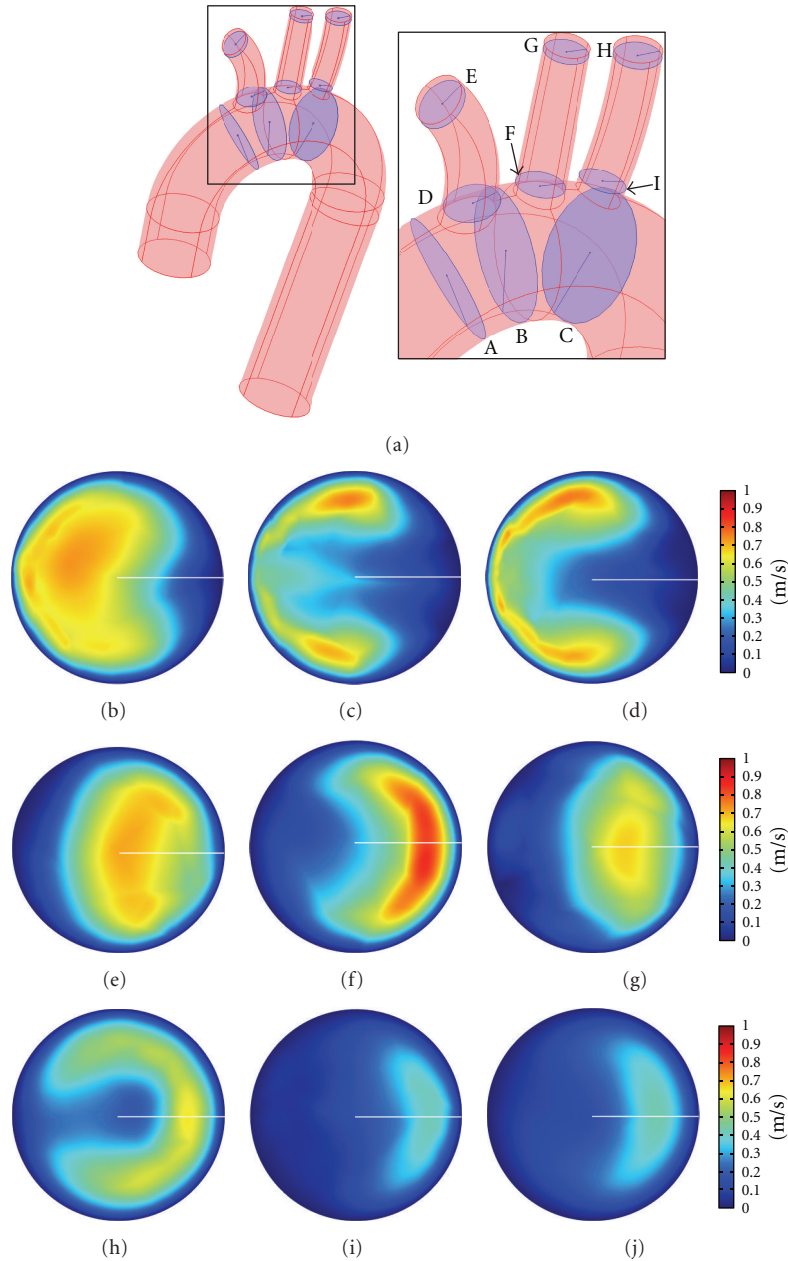


FIGURE 3: (a) Axial cross-sections within the aortic arch and branches; axial velocity profiles across axial cross-section, (b) A, (c) B, (d) C, (e) D, (f) E, (g) F, (h) G, (i) H, and (j) I in the aortic arch model captured at peak systolic time  $t = 0.18$  s.

left carotid artery, and lowest in left subclavian artery. The effect of weakening pressure gradient is also evident in axial flow profiles in sections E, G, and I. It can be observed that the magnitude of velocity is highest in brachiocephalic artery (section E), moderate in moderate in left carotid artery (section G), and lowest in left subclavian artery (section I). During reconstruction of aorta model, the effect of tapering is incorporated in the carotid artery. The tapering effect causes overlapping of pathlines close to outlet of the carotid artery. As a result of this, the axial flow distribution in section G is almost O-shaped, while in sections E and I the axial flow distributions are C-shaped.

The distribution of velocity in vicinity of the walls is crucial for the calculating WSS, as low and fluctuating WSS are known to be the key parameters of the development of atherosclerotic plaques. Higher WSS is also known to be closely related to aorta dissection. Ku [24] has reported that skewness in axial profiles can cause alteration and oscillation of local WSS, which can cause localization of atherosclerosis. The distributions of WSS at peak systole for aorta model under normal pressure regime are presented in Figure 4. The distributions are shown in two view angles with full and low range of WSS. The anterior and posterior views in Figure 4(a) and Figure 4(b) suggest lower WSS distributed

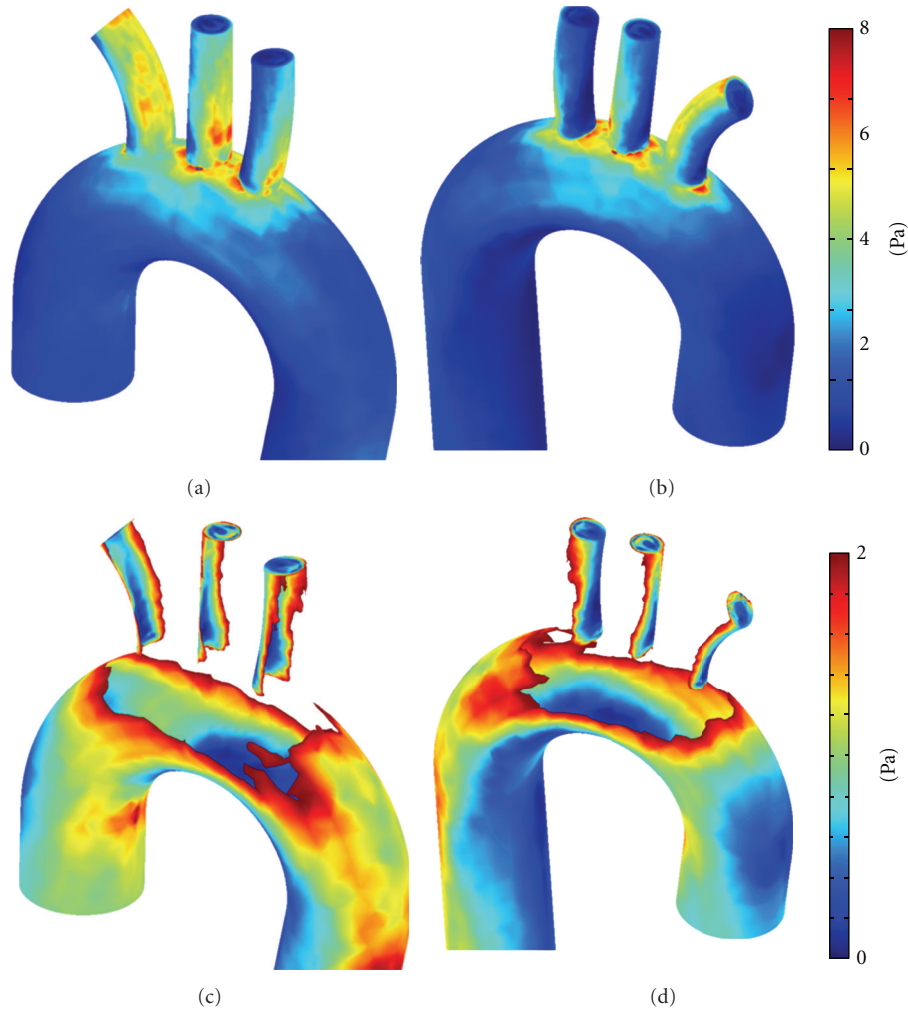


FIGURE 4: Anterior (a, c) and posterior (b, d) views of aorta model showing WSS distribution over the aortic arch and branches at time  $t = 0.18$  s.

on the proximal walls of branches and the higher WSS distributed on distal walls of branches. On lowering down the scale we also realized extremely low WSS distributed at the outer wall or ascending aorta and inner wall of the aortic arch (Figure 4(c) and Figure 4(d)). The demonstrated distribution of flow and WSS were in qualitative agreement with the earlier numerical [13, 18, 28] and experimental [5] works.

To further analyze the WSS distributions quantitatively, circumferential WSS captured at axial cross-sections D–I is plotted as polar plots in Figure 5. In sections D, E, and I of branches, the low values of WSS are distributed in the angular domain from  $90^\circ$  to  $270^\circ$  counterclockwise, while the higher values of WSS are distributed on the opposite domain, that is, from  $270^\circ$  to  $90^\circ$  counterclockwise. The distributions of circumferential WSS at axial sections close to branch outlets follows cardioids-like pattern.

In order to get stable values, WSS is averaged peripherally for brachiocephalic left carotid, and left subclavian arteries. An area weighted average is obtained for 10 arc sections over each branch. The arch sections are essentially of arc length of

2.6 mm. The peripherally average WSS for brachiocephalic, left carotid and left subclavian arteries is presented in Figure 5(g). To avoid errors in averaging due to extreme WSS values close to branch entry and exit, WSS values close to the branch entry and exit regions are excluded from averaging. The values of mean WSS display limited variation along each branch which is about 3.5 Pa for brachiocephalic, 2.5 Pa for left carotid, and 1.5 Pa for left subclavian branches. As the lower WSS is blamed for the development of atherosclerotic plaques, the brachiocephalic artery displays more vulnerability to the development of plaques than the two others arteries. This conclusion is in agreement with earlier works [2, 3], where the brachiocephalic artery is determined as one of the predominant sites for localization of atherosclerosis plaque. However, Figure 5(g) shows a contradictory relation in a first glance, which indicates an average WSS can behave completely different than the local one. Also, an overall view through Figures 4(a)–4(d) and Figures 5(a)–5(g) indicates that the variation of WSS from distal to proximal side of arteries could be more relevant factor than WSS for the development of plaques. This variation is significantly

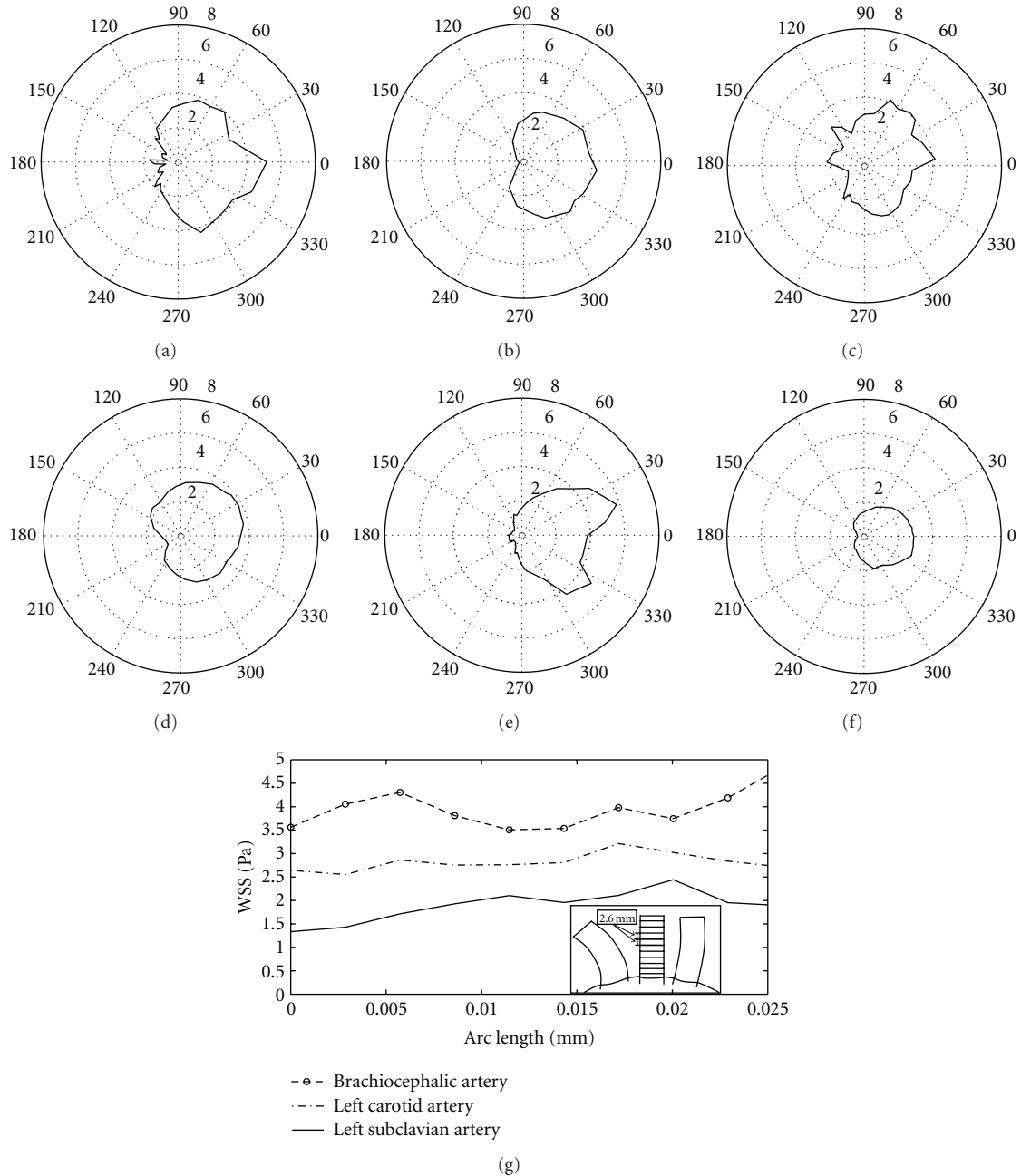


FIGURE 5: Polar plot of peripheral WSS distribution over the axial section (a) D, (b) E, (c) F, (d) G, (e) H, (f) I, and (g) WSS averaged over length of branch arteries at time  $t = 0.18$  s.

large for the brachiocephalic artery. It should be noted that there are several other factors not studied here such as the geometry of aortic arch (patient-specific data associated with the shape of arch and branches with local details of the wall surface) and the flexibility of the aorta wall. Such factors will be studied through our next papers.

The mass flow rate across branch outlets followed distribution similar to outlet boundary condition. The flow rates were fairly the same in all three branches as it was observed for WSS, too. The reason behind similarity of mass flow rates is also the fact that the actual boundary condition was determined from equal mass flow rate condition.

*3.2. Effect of Hypotension and Hypertension on the Distributions of Flow Field and WSS.* The effect of pressure on flow parameters is studied by changing the dimensions of the aorta model based on the pressure-lumen area relation in aorta from Towfiq et al. [9]. Moreover, the boundary conditions are also modified to mimic hypotension and hypertension pressure regimes. The flow distributions in coronal plane are shown in Figures 2(b) and 2(d), while axial flow distributions across sections A–I (as shown in Figure 3(a)) are demonstrated in Figures 6 and 7. The distributions of pressure under the regimes of hypotension and hypertension were qualitatively identical to normal

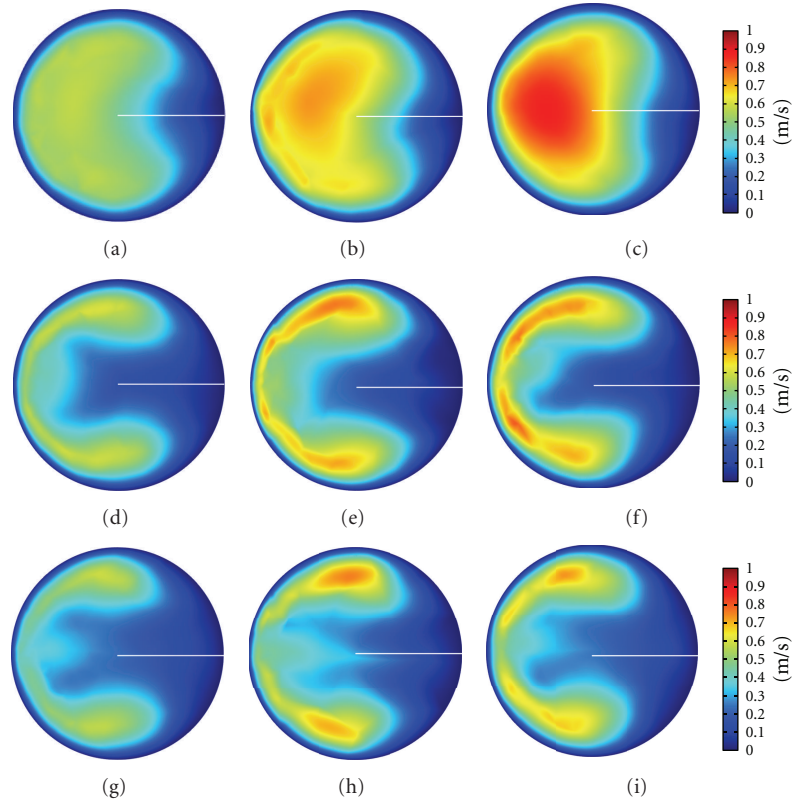


FIGURE 6: Axial velocity distributions at the axial cross-sections (a, b, c) A, (d, e, f) B, and (g, h, i) C (as shown in Figure 3(a)) through aortic arch at time  $t = 0.18$  s, where a, d, and g correspond to hypotension; b, e and h correspond to normal pressure; c, f and i correspond to hypertension.

pressure case (shown in Figure 2(a)) and thus are not discussed here.

The flow distributions demonstrated in Figures 2(b), 2(c), and 2(d) are qualitatively identical. Like the velocity distribution across the coronal planes, the axial velocity distributions in respective axial sections shown in Figures 6 and 7 are also qualitatively identical. However, the comparison revealed that the velocity distributions are quantitative different and directly influenced by the hypotension and hypertension pressure regimes. The scale of velocity magnitude is high for hypertension case than that in hypotension and normal pressure cases. The velocity distributions in sagittal and axial planes are most pronounced and amplified for hypertension case. The maximum velocity magnitude of 1.1 m/s observed in the hypertension case is 51% lower than the maximum velocity of hypotension case. Also the maximum velocity magnitude of 0.72 m/s observed in the normal pressure case is about 26% lower than the maximum velocity of hypotension case. Highly accelerated axial flow under hypertension regime is also evident in the axial flow distributions in aortic arch and three branches demonstrated in Figure 6 and Figure 7, respectively. The velocity distributions at sections A (Figures 6(a)–6(c)), D (Figures 7(a)–7(c)), and F (Figures 7(j)–7(l)) for hypertension case are almost parabolic with maximum velocity at the localized at the centre of the respective

sections. On the other hand, the axial velocity distributions at sections A, D, and F for hypotension and normal case are nonuniform and with spatial nonuniformity. Higher axial velocity in normal pressure and hypertension case implicate dominant axial flow. Due to the dominant axial flow, the secondary flow patterns in hypotension are weaker while during hypertension secondary flow patterns intensify. The spatial variation in velocity fields are expected to affect the WSS distributions.

Within the branches, the flow is skewed toward the proximal walls, and the effect of hypotension and hypertension affects both the profile and the magnitude of velocity. Again the velocity profiles for hypertension case are more pronounced and amplified. Also amongst all the axial sections, maximum velocity magnitude is observed in section E (Figures 7(g)–6(i)), which lies in vicinity of outlet of brachiocephalic artery, for hypertension case.

The effect of pressure regimes on WSS is closely investigated. The peripheral WSS for hypotension, normal pressure and hypertension is presented in form of polar plots in Figure 8. It can be noticed in Figure 8 that the magnitude of peripheral WSS does not change proportional to the pressure regimes. The WSS magnitude under hypertension condition is lower than that observed for normal cases while qualitatively the distributions are similar. Interestingly, for hypertension case, the values of WSS shown in Figure 8(c),

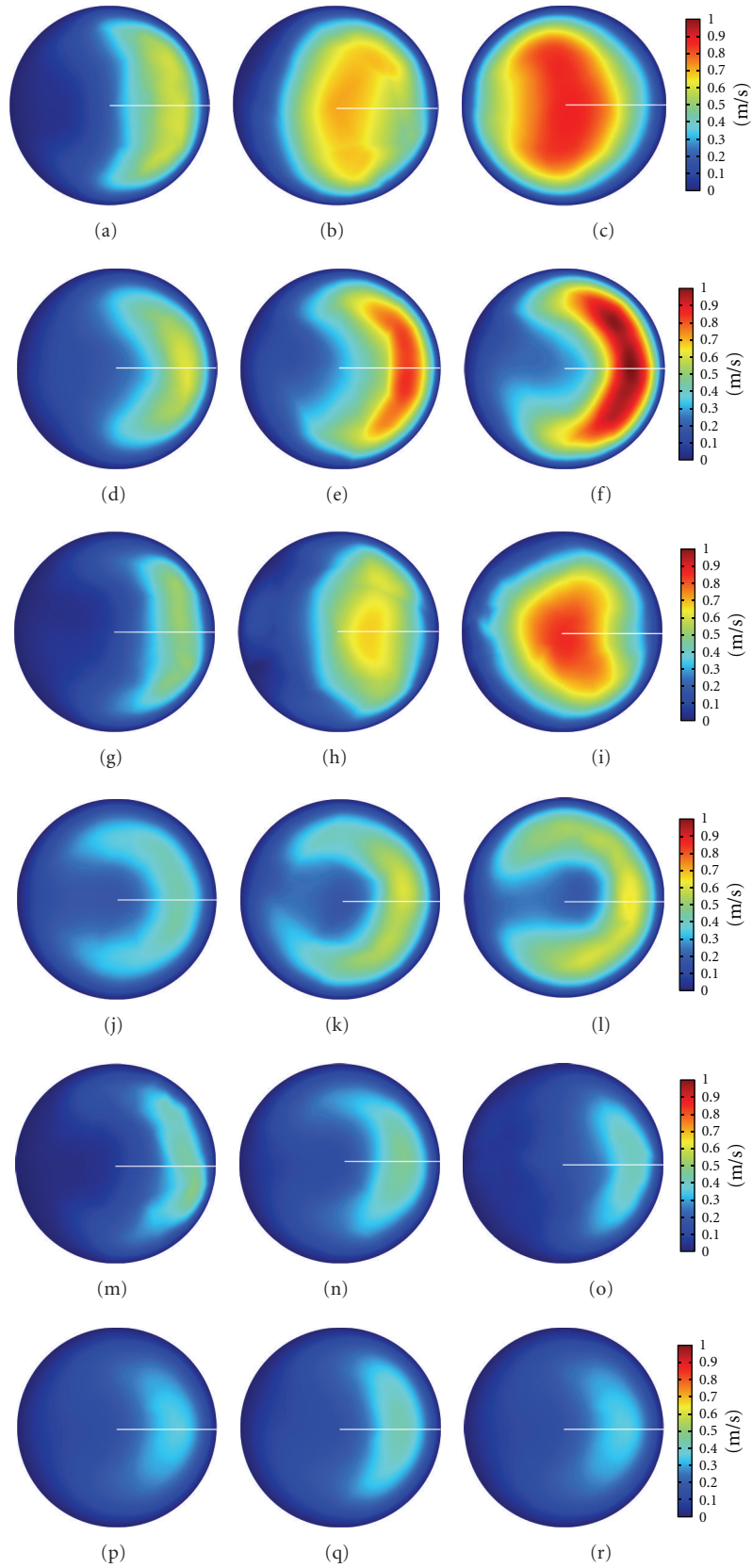


FIGURE 7: Axial velocity distributions at the axial cross-sections (a, b, c) D, (d, e, f) E, (g, h, i) F, (j, k, l) G, (m, n, o) H, (p, q, r) I (as shown in Figure 3(a)) through aortic arch at time  $t = 0.18$  s, where a, d, g, j, m, and p correspond to hypotension; b, e, h, k, n, and q correspond to normal pressure; c, f, i, l, o and r correspond to hypertension.

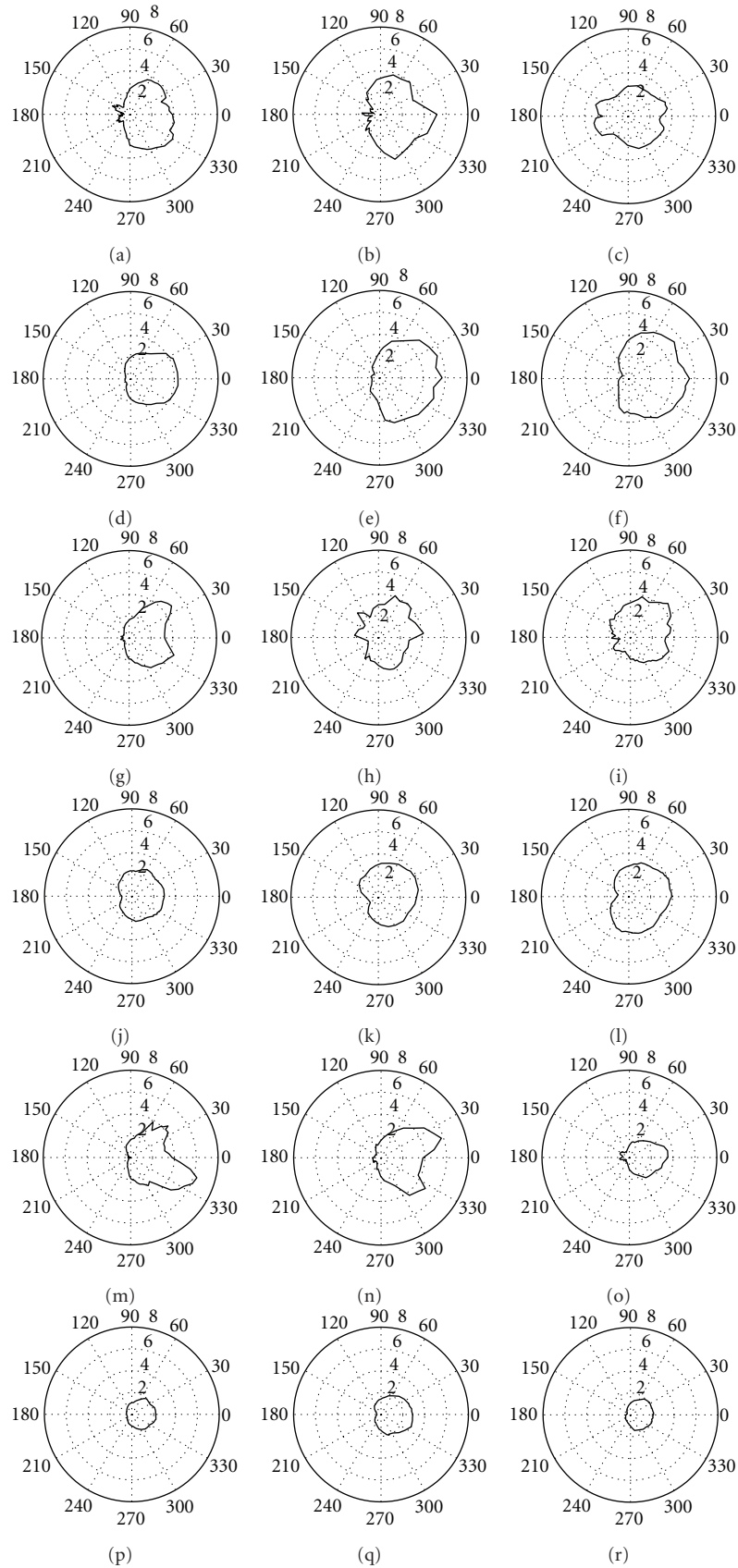


FIGURE 8: Polar plot of peripheral WSS distribution at the axial cross-sections (a, b, c) D, (d, e, f) E, (g, h, i) F, (j, k, l) G, and (m, n, o) H, and (p, q, r) I (as shown in Figure 3(a)) through aortic arch at time  $t = 0.18$  s. Where a, d, g, j, m, and p correspond to hypotension; b, e, h, k, n, and q correspond to normal pressure; c, f, i, l, o, and r correspond to hypertension.

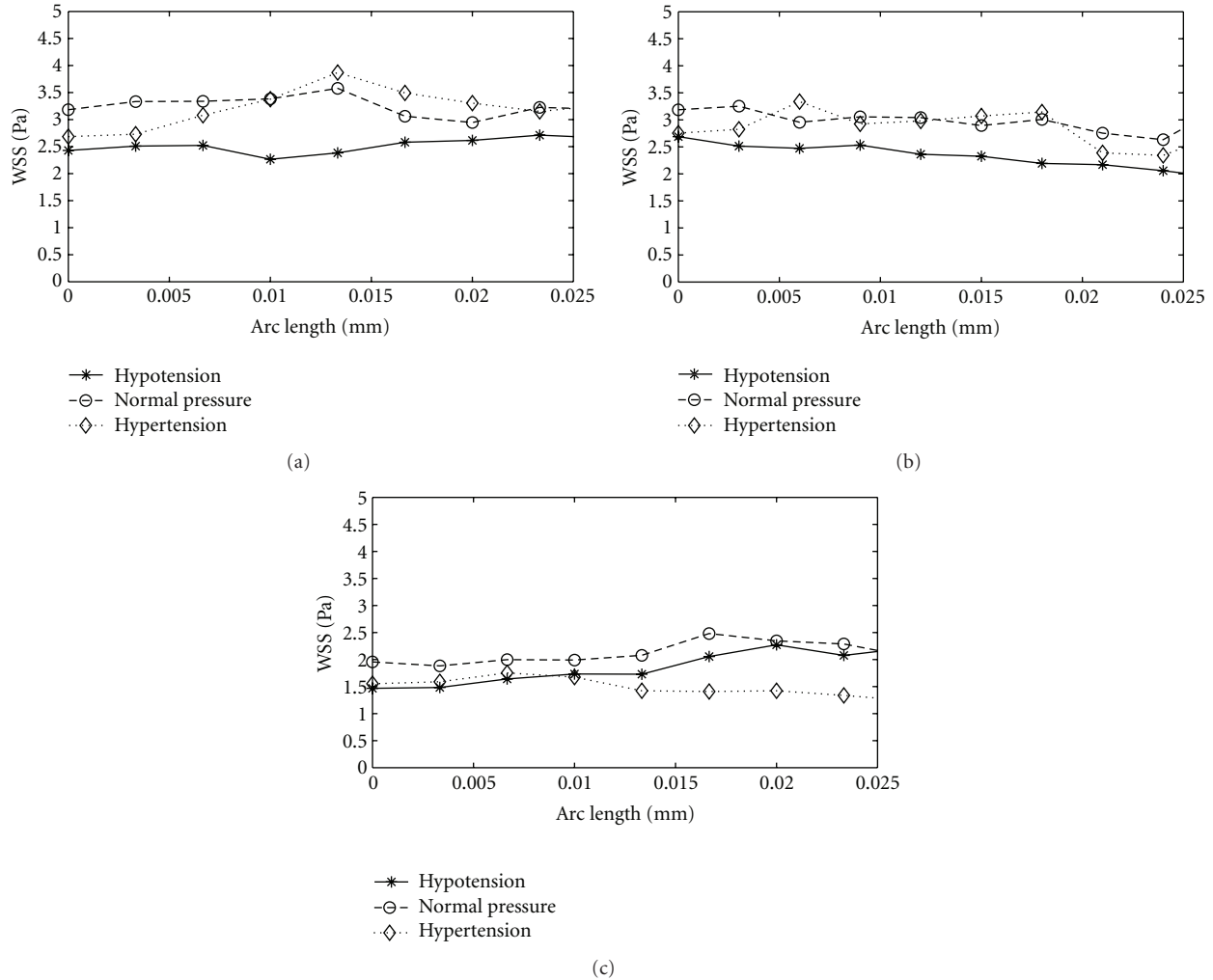


FIGURE 9: The average WSS along the (a) brachiocephalic, (b) left carotid, and (b) left subclavian branches of geometry G3 at peak systolic pressure of 80 mmHg (hypotension), 100 mmHg (normal), and 120 mmHg (hypertension) conditions.

8(i), and 8(o) are, respectively, lower than WSS shown in Figure 8(b), 8(h), and 8(n). These correspond to the amplified velocity observed in Figure 7(c), 7(i), and 7(o). Relatively lower WSS at the branch entry regions and inner aortic arch may play a role in altering vascular biology and the localization of atherosclerosis [4, 6].

The aorta is under greater peripheral stresses during hypertension. Dabagh et al. [29] have reported that due to the change in the morphology of endothelial cells higher rates of mitosis or apoptosis are expected, which increases the number of LDL pathways over endothelium. Thus an elevated risk of developing atherosclerotic plaques is anticipated under hypertensive conditions. It is also instructive to look at the variation of mean WSS through different sections along the branches. In order to get stable values, WSS is averaged along the length of the brachiocephalic, left carotid, and left subclavian branches for aorta model in Figure 9. It can be seen that the levels of WSS corresponding to hypertension do not considerably surpass those of normal pressure along each branch, but they may even go lower. As mentioned earlier, this can potentially boost the penetration

of LDL macromolecules across the arterial wall. Figure 9 indicates that the average peripheral WSS is almost invariant along the branch though its peripheral distribution is not uniform. Note that the hypertensive wall is under higher strain while its shear stress is either unchanged or lower than what normally exist. According to Dabagh et al. [29], this can potentially boost the penetration of LDL macromolecules across the arterial wall.

#### 4. Conclusions

In the present study, an idealized model of human aorta was reconstructed with measurements from the literature. Pulsatile blood flow in aorta model was simulated with FEM-based numerical solver. The aorta model along with boundary condition was modified to mimic the effect of hypotension and hypertension. The flow dynamic in the work displayed a reasonable qualitative agreement with other earlier works. Figures 4, 5, and 8 illustrate extremely low WSS at outer wall of aortic arch, proximal wall of branches, entry region of branches, and inner aortic arch. Low and oscillating

shear stress are associated with risk of developing atherosclerosis, thus the listed sites are susceptible to localization of atherosclerosis. This conclusive observation is also consistent with earlier studies. The study has provided the fundamental understanding of the flow dynamics dependence on the artery geometry and the blood pressure in human aorta. Results reveal that the hemodynamics is significantly affected by the anatomy of aorta, which emphasizes on the patient-specific factor of the aorta geometry in developing atherosclerosis. The anatomy and orientation of branches have a significant role in flow distribution and flow dynamics. On the other hand, the blood pressure affects the site of low WSS. It also appeared that the magnitude of WSS decreases under hypertension. It is associated with the deformation of aorta under high pressure. Our simulations were based on pressure-inlet boundary condition in the inlet and pressure-outlet boundary condition at the outlets, which reproduced developed flow profiles from the inlet section. The results show the fact that flow dynamics may be more complex when the geometry of aorta varies under pressure. A very important feature for our future study is the coupling the blood flow in aorta with wall deformation under elevated pressures to analyze the blood hemodynamics more precisely. To overcome limitations offered by idealized aorta models, computed-tomography- (CT-) scans-based realistic aorta will be used in future simulations.

## Conflict of Interests

There are no conflicts of interests.

## Acknowledgments

Authors P. Vasvasa, M. Dabagh and P. Jalalia would like to thank the financial support from the Academy of Finland (Grant no.123938). P. Vasvasa also acknowledges the support from The Finnish Graduate School in Computational Fluid Dynamics.

## References

- [1] C. G. Caro, J. M. Fitz-Gerald, and R. C. Schroter, "Arterial wall shear and distribution of early atheroma in man," *Nature*, vol. 223, no. 5211, pp. 1159–1161, 1969.
- [2] C. G. Caro, J. M. Fitz-Gerald, and R. C. Schroter, "Atheroma and arterial wall shear. Observation, correlation and proposal of a shear dependent mass transfer mechanism for atherogenesis," *Proceedings of the Royal Society of London Series B*, vol. 177, no. 46, pp. 109–159, 1971.
- [3] M. E. DeBakey, G. M. Lawrie, and D. H. Glaeser, "Patterns of atherosclerosis and their surgical significance," *Annals of Surgery*, vol. 201, no. 2, pp. 115–131, 1985.
- [4] D. N. Ku, D. P. Giddens, C. K. Zarins, and S. Glagov, "Pulsatile flow and atherosclerosis in the human carotid bifurcation. Positive correlation between plaque location and low and oscillating shear stress," *Arteriosclerosis*, vol. 5, no. 3, pp. 293–302, 1985.
- [5] R. Nerem, "Atherosclerosis and the role of wall shear stress," in *Flow Dependent Regulation of Vascular Function*, J. A. Bevan, G. Kaley, and G. M. Rubany, Eds., Oxford University Press, New York, NY, USA, 1995.
- [6] J. M. Tarbell, "Mass transport in arteries and the localization of atherosclerosis," *Annual Review of Biomedical Engineering*, vol. 5, pp. 79–118, 2003.
- [7] C. K. Zarins, D. P. Giddens, B. K. Bharadvaj, V. S. Sottiurai, R. F. Mabon, and S. Glagov, "Carotid bifurcation atherosclerosis. Quantitative correlation of plaque localization with flow velocity profiles and wall shear stress," *Circulation Research*, vol. 53, no. 4, pp. 502–514, 1983.
- [8] D. L. Fry, "Acute vascular endothelial changes associated with increased blood velocity gradients," *Circulation Research*, vol. 22, no. 2, pp. 165–197, 1968.
- [9] B. A. Towfiq, J. Weir, and J. M. Rawles, "Effect of age and blood pressure on aortic size and stroke distance," *British Heart Journal*, vol. 55, no. 6, pp. 560–568, 1986.
- [10] Y. Y. Utepov, "Correlation between anatomic parameters of the aorta and manifestations of atherosclerosis," *Bulletin of Experimental Biology and Medicine*, vol. 124, no. 8, pp. 729–734, 1997.
- [11] P. J. Kilner, G. Z. Yang, R. H. Mohiaddin, D. N. Firmin, and D. B. Longmore, "Helical and retrograde secondary flow patterns in the aortic arch studied by three-directional magnetic resonance velocity mapping," *Circulation*, vol. 88, no. 5 I, pp. 2235–2247, 1993.
- [12] F. Gao, Z. Guo, M. Sakamoto, and T. Matsuzawa, "Fluid-structure interaction within a layered aortic arch model," *Journal of Biological Physics*, vol. 32, no. 5, pp. 435–454, 2006.
- [13] T. Kim, A. Y. Cheer, and H. A. Dwyer, "A simulated dye method for flow visualization with a computational model for blood flow," *Journal of Biomechanics*, vol. 37, no. 8, pp. 1125–1136, 2004.
- [14] D. Mori, T. Hayasaka, and T. Yamaguchi, "Modeling of the human aortic arch with its major branches for computational fluid dynamics simulation of the blood flow," *JSME International Journal, Series C*, vol. 45, no. 4, pp. 997–1002, 2002.
- [15] L. Morris, P. Delassus, A. Callanan et al., "3-D numerical simulation of blood flow through models of the human aorta," *Journal of Biomechanical Engineering*, vol. 127, no. 5, pp. 767–775, 2005.
- [16] M. Nakamura, S. Wada, and T. Yamaguchi, "Computational analysis of blood flow in an integrated model of the left ventricle and the aorta," *Journal of Biomechanical Engineering*, vol. 128, no. 6, pp. 837–843, 2006.
- [17] J. Y. Park, C. Y. Park, C. M. Hwang, K. Sun, and B. Goo Min, "Pseudo-organ boundary conditions applied to a computational fluid dynamics model of the human aorta," *Computers in Biology and Medicine*, vol. 37, no. 8, pp. 1063–1072, 2007.
- [18] N. Shahcheranhi, H. A. Dwyer, A. Y. Cheer, A. I. Barakat, and T. Rutaganira, "Unsteady and three-dimensional simulation of blood flow in the human aortic arch," *Journal of Biomechanical Engineering*, vol. 124, no. 4, pp. 378–387, 2002.
- [19] C. A. Taylor, T. J. R. Hughes, and C. K. Zarins, "Finite element modeling of three-dimensional pulsatile flow in the abdominal aorta: relevance to atherosclerosis," *Annals of Biomedical Engineering*, vol. 26, no. 6, pp. 975–987, 1998.
- [20] M. Dabagh, P. Jalali, Y. T. Konttinen, and P. Sarkomaa, "Distribution of shear stress over smooth muscle cells in deformable arterial wall," *Medical and Biological Engineering and Computing*, vol. 46, no. 7, pp. 649–657, 2008.
- [21] K. M. Khanafer, P. Gadhoke, R. Berguer, and J. L. Bull, "Modeling pulsatile flow in aortic aneurysms: effect of non-New-

- tonian properties of blood,” *Biorheology*, vol. 43, no. 5, pp. 661–679, 2006.
- [22] M. J. Conlon, D. L. Russell, and T. Mussivand, “Development of a mathematical model of the human circulatory system,” *Annals of Biomedical Engineering*, vol. 34, no. 9, pp. 1400–1413, 2006.
- [23] K.-J. Li, *Dynamics of the Vascular System*, World Scientific, Singapore, 2004.
- [24] D. N. Ku, “Blood flow in arteries,” *Annual Review of Fluid Mechanics*, vol. 29, pp. 399–434, 1997.
- [25] M. S. Moayeri and G. R. Zendejbudi, “Effects of elastic property of the wall on flow characteristics through arterial stenoses,” *Journal of Biomechanics*, vol. 36, no. 4, pp. 525–535, 2003.
- [26] D. Zeng, E. Boutsianis, M. Ammann, K. Boomsma, S. Wildermuth, and D. Poulidakos, “A study on the compliance of a right coronary artery and its impact on wall shear stress,” *Journal of Biomechanical Engineering*, vol. 130, no. 4, Article ID 041014, 11 pages, 2008.
- [27] S. Z. Zhao, X. Y. Xu, A. D. Hughes et al., “Blood flow and vessel mechanics in a physiologically realistic model of a human carotid arterial bifurcation,” *Journal of Biomechanics*, vol. 33, no. 8, pp. 975–984, 2000.
- [28] C. Y. Wen, A. S. Yang, L. Y. Tseng, and J. W. Chai, “Investigation of pulsatile flowfield in healthy thoracic aorta models,” *Annals of Biomedical Engineering*, vol. 38, no. 2, pp. 391–402, 2010.
- [29] M. Dabagh, P. Jalali, and J. M. Tarbell, “The transport of LDL across the deformable arterial wall: the effect of endothelial cell turnover and intimal deformation under hypertension,” *American Journal of Physiology*, vol. 297, no. 3, pp. H983–H996, 2009.

## Research Article

# Computational Fluid Dynamics Analysis of the Effect of Plaques in the Left Coronary Artery

Thanapong Chaichana,<sup>1</sup> Zhonghua Sun,<sup>1</sup> and James Jewkes<sup>2</sup>

<sup>1</sup>Discipline of Medical Imaging, Department of Imaging and Applied Physics, Curtin University, GPO Box, U1987, Perth, WA 6845, Australia

<sup>2</sup>Fluid Dynamics Research Group, Department of Mechanical Engineering, Curtin University, Perth, WA 6845, Australia

Correspondence should be addressed to Zhonghua Sun, z.sun@curtin.edu.au

Received 30 September 2011; Revised 8 November 2011; Accepted 9 November 2011

Academic Editor: Kyeihan Rhee

Copyright © 2012 Thanapong Chaichana et al. This is an open access article distributed under the Creative Commons Attribution License, which permits unrestricted use, distribution, and reproduction in any medium, provided the original work is properly cited.

This study was to investigate the hemodynamic effect of simulated plaques in left coronary artery models, which were generated from a sample patient's data. Plaques were simulated and placed at the left main stem and the left anterior descending (LAD) to produce at least 60% coronary stenosis. Computational fluid dynamics analysis was performed to simulate realistic physiological conditions that reflect the *in vivo* cardiac hemodynamics, and comparison of wall shear stress (WSS) between Newtonian and non-Newtonian fluid models was performed. The pressure gradient (PSG) and flow velocities in the left coronary artery were measured and compared in the left coronary models with and without presence of plaques during cardiac cycle. Our results showed that the highest PSG was observed in stenotic regions caused by the plaques. Low flow velocity areas were found at postplaque locations in the left circumflex, LAD, and bifurcation. WSS at the stenotic locations was similar between the non-Newtonian and Newtonian models although some more details were observed with non-Newtonian model. There is a direct correlation between coronary plaques and subsequent hemodynamic changes, based on the simulation of plaques in the realistic coronary models.

## 1. Introduction

Coronary artery disease (CAD) is the leading cause of death in advanced countries. The most common cause of CAD is atherosclerosis which is caused by the presence of plaques on the artery wall, resulting in the lumen stenosis. Plaques have been particularly associated with blood clots and compromise blood flow to the myocardium. This occurs when the coronary plaques suddenly rupture; if a clot cannot be treated in time, then the heart muscle will be impaired due to ischemic changes, leading to myocardial ischemia or infarction or, more severely, necrosis [1]. Therefore, an early detection and diagnosis of CAD is particularly important for reduction of the mortality and subsequent complications [1].

The natural history of coronary plaque is dependent not only on the formation and progression of atherosclerosis, but also on the vascular remodelling response. If the local wall shear stress is low, a proliferative plaque will form. Local inflammatory response will stimulate the formation

of so-called “vulnerable plaque” which is prone to rupture with superimposed thrombus formation. The vast majority of these inflamed high-risk plaques cannot be detected by anatomic and myocardial perfusion imaging. Since the progression and development of vulnerable plaque is associated with low wall shear stress and the presence of expansive remodelling, measurement of these characteristics *in vivo* will enable risk stratification for the entire coronary circulation [2].

The wall shear stress (WSS), wall pressure, and blood flow changes in the human body cannot be measured directly on blood vessels, whereas computational fluid dynamics (CFD) can provide alternative ways to diagnose CAD [3]. The WSS factor in the coronary artery is known to play a significant role in the early formation of CAD [4]. In addition, the WSS at the local vessel wall can demonstrate a predisposition for atherosclerosis development for various anatomical sections, thus enabling the prediction of coronary disease [5].

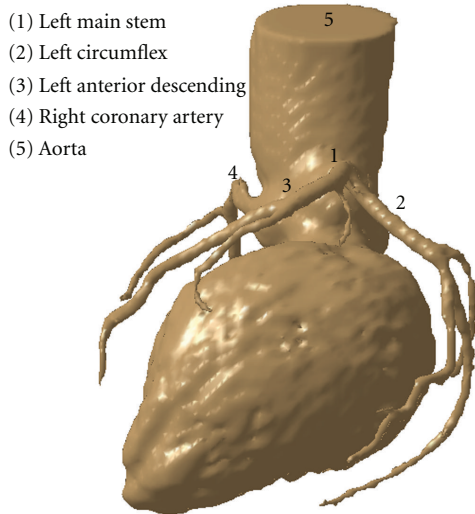


FIGURE 1: 3D CT visualisation of a normal left coronary artery with side branches in a patient with suspected coronary artery disease.

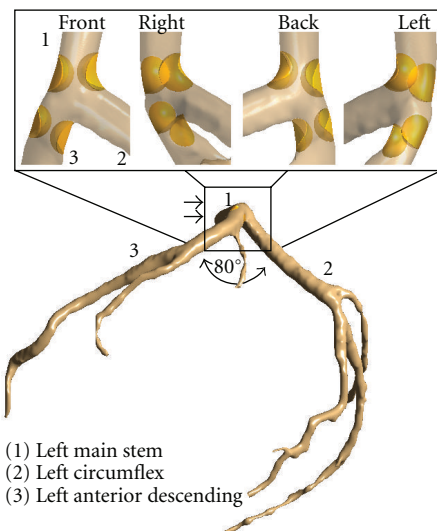


FIGURE 2: Plaque distribution in left coronary artery model is simulated at the left main stem and ostium of left anterior descending. Double arrows indicate that rectangle is an effective plaque location (EPL).

CFD allows for efficient and accurate computations of hemodynamic features of both normal and abnormal situations in the cardiovascular system, *in vivo* simulation of coronary artery flow changes [3–6]. CFD is different from medical imaging visualisation as medical imaging techniques such as coronary angiography or computed tomography angiography provide anatomic alterations of the coronary artery wall due to the presence of plaques, thus allowing only assessment of the degree of lumen changes such as stenosis or occlusion [7, 8]. In contrast, CFD analysis enables the identification of hemodynamic changes in the coronary artery, even before the plaques are actually formed at the artery wall or can occlude the vessels. Therefore, to

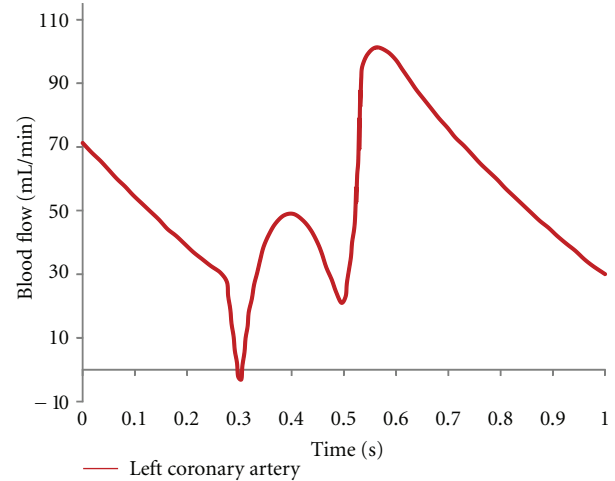


FIGURE 3: Cardiac pulsatile velocity at left main stem is applied for computational fluid dynamic simulation at the left coronary artery.

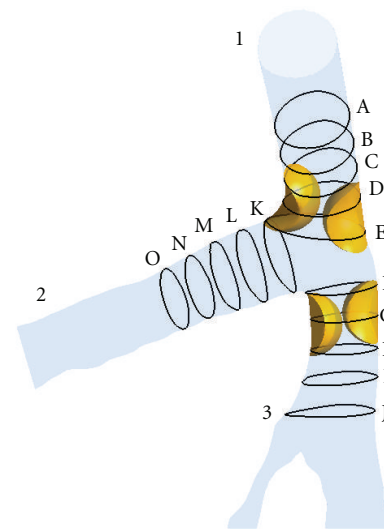


FIGURE 4: The EPL posterior view at left coronary artery model represents the cross-sectional positions of pre- and postplaque simulated models.

some extent, CFD allows early detection of coronary artery disease and improves the understanding of the progression of plaques, which are considered of paramount importance to clinical treatment. The purpose of this study was to investigate the hemodynamic effect of plaques in the left coronary artery by using CFD analysis. Simulated plaques were inserted into the left main stem and left anterior descending coronary arteries (taken from a selected patient’s data), and hemodynamic analysis was performed to correlate the effect of presence of plaques with subsequent flow changes to the coronary main and side branches.

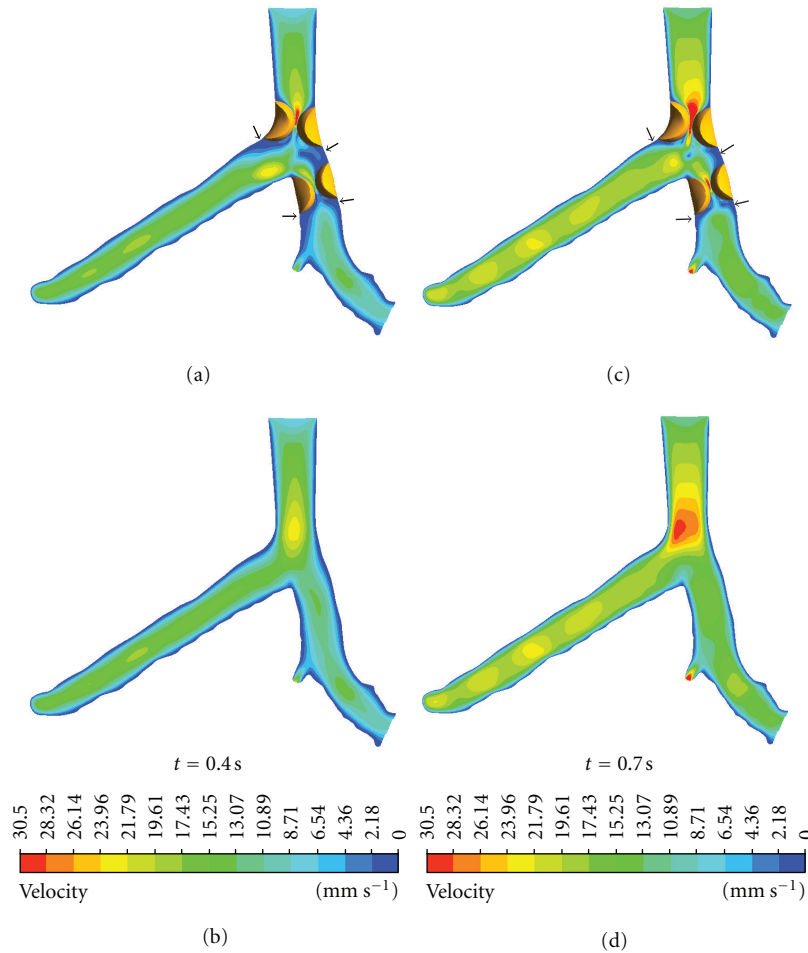


FIGURE 5: Flow velocity observed in pre- and postplaque simulated models during systolic peak of 0.4 s and midsystolic phase of 0.7 s. Arrows indicate the anatomic locations where plaques could spread into areas with low flow velocity.

## 2. Materials and Methods

**2.1. Patient Data Selection for Generation of Left Coronary Artery Model.** A sample patient suspected of CAD who underwent multislice CT angiography was selected, and the patient's volume CT data was used to generate a 3D coronary model. The original CT data was saved in digital imaging and communication in medicine (DICOM) format and then transferred to a workstation equipped with Analyze 7.0 (Analyze Direct, Inc., Lexana, KS, USA) for image after-processing and segmentation. Three-dimensional (3D) volume data was postprocessed and segmented using a semiautomatic method with a CT number thresholding technique [9, 10], and manual editing was performed in some slices to remove soft tissues and artefacts. The segmented model was produced with a special focus on the left coronary artery (LCA) and its branches. The 3D LCA model was saved in "STL format" for further reconstruction purposes. Figure 1 shows the anatomical details of the left coronary artery.

**2.2. Realistic Plaques Modelling.** The actual plaques and degree of lumen stenosis on coronary artery wall were

simulated at the left main stem (LMS) and the left anterior descending (LAD), as these artery branches are the common locations where plaques tend to form and induce myocardial ischemic changes [7, 11]. The plaques produced a lumen narrowing of approximately 60% diameter at the LMS and LAD, since more than 50% lumen stenosis leads to significant hemodynamic changes to flow within the coronary artery [12]. Figure 2 is the segmented LCA model showing various views of the position of the plaques at the left coronary artery.

**2.3. Generation of Computational Models.** The surface of LCA model with and without plaques (Figure 2) was prepared by using Blender version 2.48 (Blender Institute, Amsterdam, Netherlands). A gentle B-spline smoothing technique was applied between the left main trunk and side branches to reduce any potential nonphysical behaviour induced by sharp edges [13]. The surface models consisting of plaques and normal coronary arteries were converted into solid models and saved in "STL format" for the additional creation of meshing elements. Both models were used to create hexahedral and tetrahedral meshes to perform the CFD simulations. The hexahedral mesh configuration for

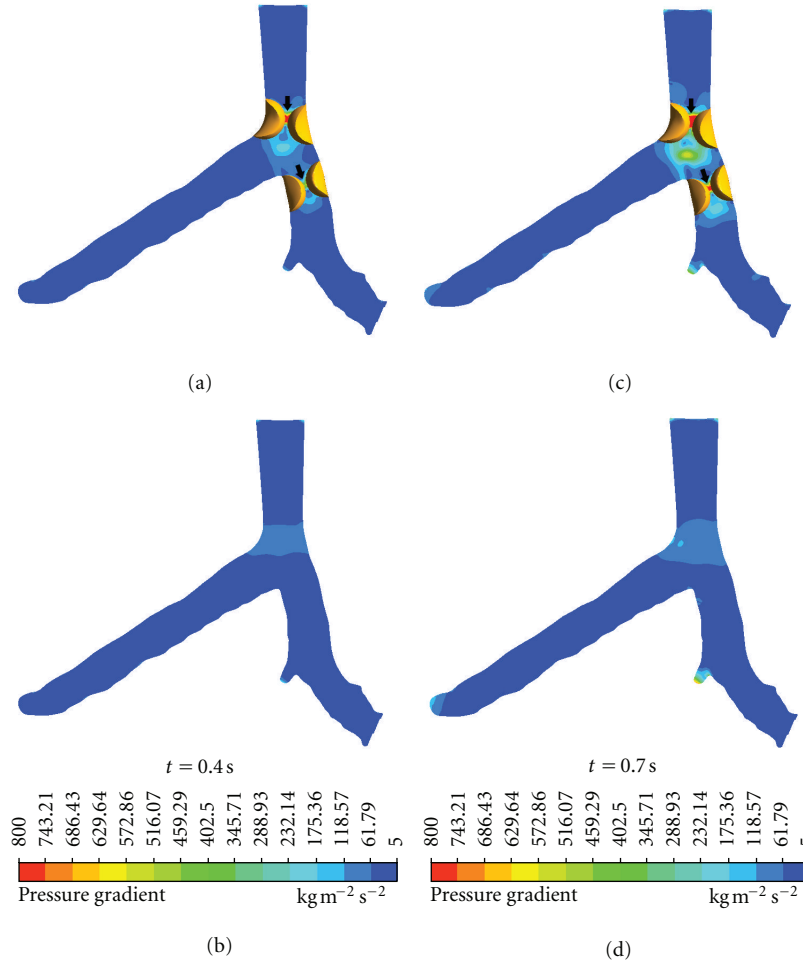


FIGURE 6: Pressure gradient observed in coronary models with and without plaques during systolic peak of 0.4 s and middiastolic phase of 0.7 s. Arrows indicate the high PSG locations where plaques may induce potential rupture or further atherosclerotic changes.

the LCA model without plaques was 949,289 elements and 1,062,280 nodes, while the hexahedral mesh configuration for the LCA model with plaques was 928,311 elements and 1,041,936 nodes. The tetrahedral mesh configuration was 15,519 nodes and 78,618 elements. The meshes were generated using ANSYS ICEM CFD version 12 (ANSYS, Inc., Canonsburg, PA, USA), with details having been described in previous studies [6, 14, 15]. Finally, both mesh models were saved in “GTM format” for CFD computation.

**2.4. Application of Physiological Parameters.** In order to ensure that our analysis reflects the realistic simulation of *in vivo* conditions, realistic physiological boundary conditions were applied for 3D numerical analysis. The transient simulation was performed using accurate hemodynamic rheological and material properties, as described in a previous study [16]. Figure 3 shows the pulsatile flow rates [17] at the aorta, reconstructed using a Fourier series [18] in Matlab (MathWorks, Inc. Natick, MA, USA). This Fourier series was applied using ANSYS CFX Command Language programming to define velocity and pressure boundary conditions. Pulsatile velocity was applied as an inlet boundary condition

at the left main stem, and a zero pressure gradient was applied at the left anterior descending and left circumflex outlet boundaries [19]. Appropriate rheological parameters were applied with a blood density of  $1060 \text{ kg/m}^3$  and blood viscosity of  $0.0035 \text{ Pa s}$  [20, 21]. The blood flow was assumed to be laminar and a no-slip condition was applied at the walls. Plaque was assumed to be a rigid body [22]. Blood was assumed to be a Newtonian and incompressible fluid [4, 23]. In addition, the comparison of WSS between Newtonian and non-Newtonian models has been considered, especially at the stenotic locations [24]. A non-Newtonian blood model was simulated using the generalized power law [4, 25] which is defined as

$$\mu = \lambda(\dot{\gamma}) |\dot{\gamma}|^{n(\dot{\gamma})-1},$$

$$\lambda(\dot{\gamma}) = \mu_{\infty} + \Delta\mu \exp \left[ - \left( 1 + \frac{|\dot{\gamma}|}{a} \right) \exp \left( \frac{-b}{|\dot{\gamma}|} \right) \right], \quad (1)$$

$$n(\dot{\gamma}) = n_{\infty} - \Delta n \exp \left[ - \left( 1 + \frac{|\dot{\gamma}|}{c} \right) \exp \left( \frac{-d}{|\dot{\gamma}|} \right) \right],$$

where  $\mu_{\infty} = 0.035$ ,  $n_{\infty} = 1.0$ ,  $\Delta\mu = 0.25$ ,  $\Delta n = 0.45$ ,  $a = 50$ ,  $b = 3$ ,  $c = 50$ , and  $d = 4$ . Generalized power law model

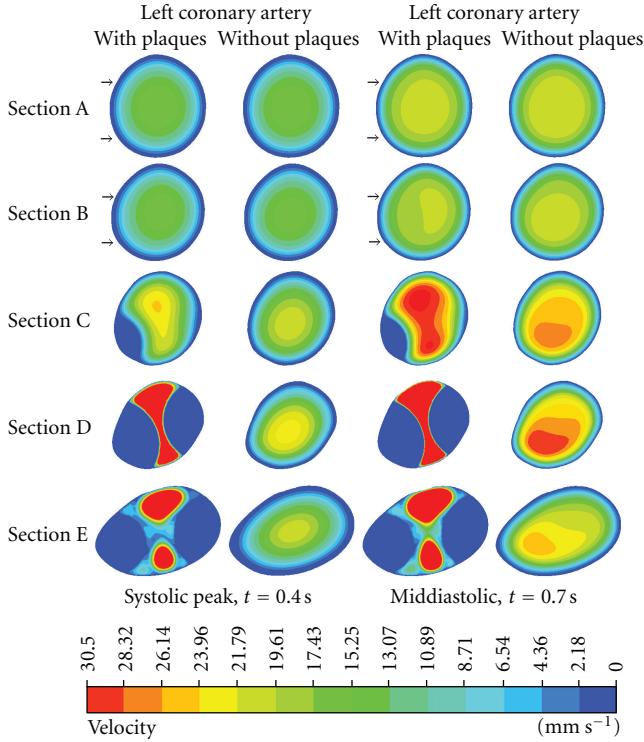


FIGURE 7: Cross-sectional views of A–E at the left main stem. Flow velocity observed with and without presence of plaque models during systolic peak of 0.4 s and middiastolic phase of 0.7 s. Arrows at Sections A and B refer to the normal flow pattern prior to the location of plaques, while flow pattern changes at the postplaque locations.

fits experimental stress-strain measurements over the range of strain rates,  $\dot{\gamma}$ ,  $0.1 < \dot{\gamma} < 1000 \text{ s}^{-1}$  [25].

**2.5. Performance of Computational Hemodynamic Analysis.** The Navier-Stokes equations were solved using the ANSYS CFX CFD package (version 12—ANSYS, Inc.), on a Microsoft Windows 7 32-bit machine, 6 MB RAM with an Xeon W3505 2.53 GHz CPU. The CFD simulation was run for 80 timesteps, representing 1.0 second of pulsatile flow, (0.0125 seconds per timestep), with each timestep converged to a residual target of less than  $1 \times 10^{-4}$  by approximately 100 iterations. The CFD solution was fully converged by approximately 8,000 time iterations per LCA model. The calculation time for each LCA model was approximately 2 hours. The configuration of this simulation is similar to previously published simulations [6, 14, 15]. Flow velocity, cross-sections of velocity pattern, and pressure gradient were calculated and visualised using ANSYS CFD-Post version 12 (ANSYS, Inc.). Figure 4 represents the area of interest at the left coronary bifurcation and shows measurement positions of cross-sections of the models with and without plaques. The sectional planes were separated into 3 groups: Sections A–E, Sections F–J, and Sections K–O. The distance between sections in each group was approximately 0.5 millimetres. The parameter used to characterise the impact of plaques at the coronary bifurcation on hemodynamic flow was

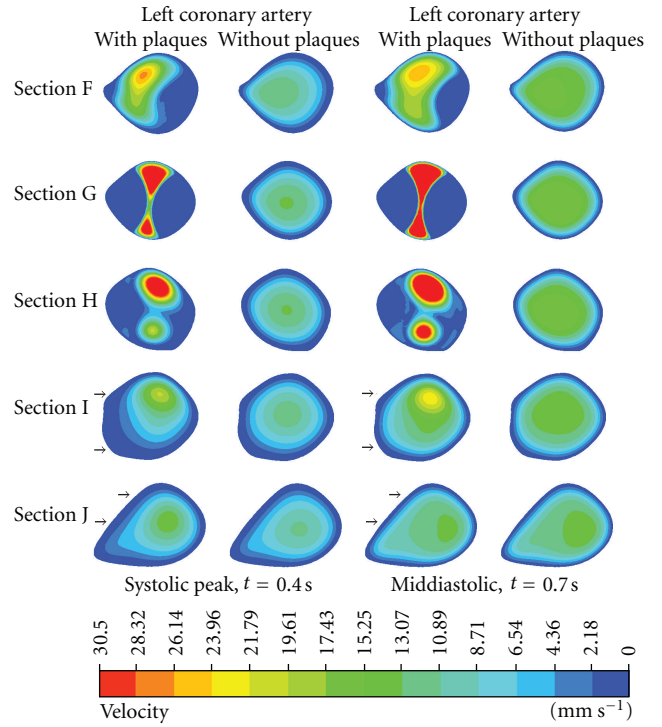


FIGURE 8: Cross-sectional views of F–J at the left anterior descending. Flow velocity observed with and without presence of plaque models during systolic peak of 0.4 s and middiastolic phase of 0.7 s. Arrows point to the low flow velocity areas at post-plaque locations due to interference of plaques.

calculated as the magnitude of local pressure gradient [26, 27], which is defined as

$$\text{PSG} = \sqrt{\left(\frac{\partial p}{\partial u}\right)^2 + \left(\frac{\partial p}{\partial v}\right)^2 + \left(\frac{\partial p}{\partial w}\right)^2}, \quad (2)$$

where  $p$  is the pressure in the area of interest,  $u$ ,  $v$ , and  $w$  are the Cartesian  $x$ ,  $y$ , and  $z$  coordinates in the direction of blood flow velocity. The local PSG is calculated by taking the time derivative of the local pressure. Finally, the value of PSG oscillated in relation to the percentage of plaques in the coronary lumen [28].

### 3. Results

The realistic left coronary artery models with plaques and without plaques were successfully performed with CFD analysis under *in vivo* physiological conditions during the systolic and diastolic phases. Peak systolic velocity and pressure were reached at a time of 0.4 sec, and middiastolic phase was reached at a time of 0.7 sec during the cardiac cycles, respectively. The analysis demonstrates a strong relationship between hemodynamic change and plaques at the left coronary artery.

**3.1. CFD Analysis of the Left Coronary Artery: 2D Visualization.** Flow velocity increased significantly in the presence

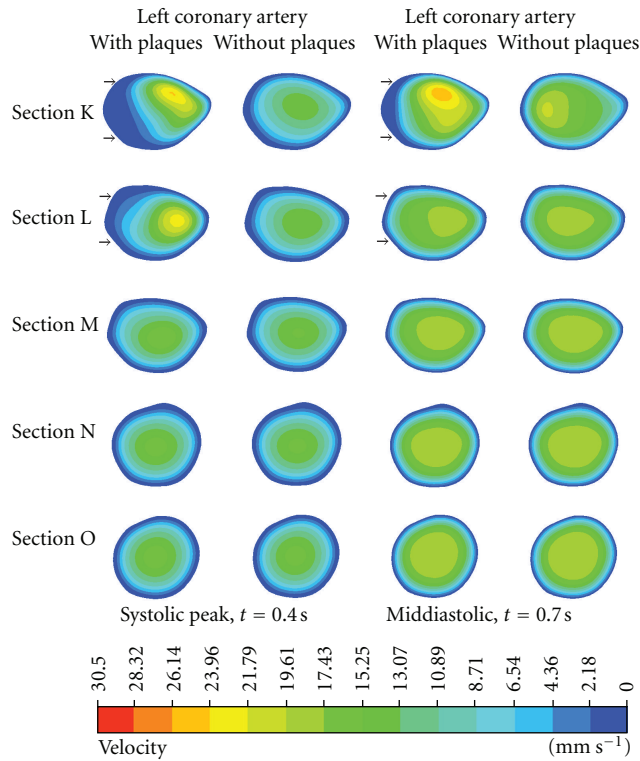


FIGURE 9: Cross-sectional views of K–O at the left circumflex. Flow velocity observed with and without presence of plaque models during systolic peak of 0.4 s and middiastolic phase of 0.7 s. Arrows indicate that the low flow velocity areas are present in the proximal segment of left circumflex due to the effect of plaques located at the left main stem.

of plaques due to resultant lumen stenosis. Poststenotic recirculation was observed in the LMS and LAD according to the CFD analysis, at the locations where plaques were present, as shown in Figure 5. Similarly, the pressure gradient (PSG) increased significantly at the LMS and LAD ostium, as shown in Figure 6. Measured PSG values at peak systolic and diastolic phases ranged from  $459.29\text{--}800\text{ kg/m}^2\text{ s}^2$  to  $345.71\text{--}629.64\text{ kg/m}^2\text{ s}^2$ , corresponding to the LMS, LAD, and LCx in the presence of plaques. In contrast, in the absence of plaques, measured PSG values were significantly lower than those measured with presence of plaques, and these values ranged from  $61.79\text{--}118.57\text{ kg/m}^2\text{ s}^2$  to  $5\text{--}61.79\text{ kg/m}^2\text{ s}^2$ .

**3.2. CFD Analysis of Left Coronary Artery-Cutting Plane Visualisation.** Flow velocity was visualised inside the LMS at Sections A–E, as shown in Figure 7. Flow patterns in both the pre and poststenotic cases were similar to those observed in Sections A and B (velocity ranged from 0 to  $17.43\text{ mm s}^{-1}$ ). However, the flow velocity increased in Sections C–E (velocity ranged from  $23.96$  to  $30.50\text{ mm s}^{-1}$ ), at the location of plaques during the systolic peak. In addition, the flow pattern was affected by the presence of plaques, which started from Sections A–E as observed in the poststenotic region, during the middiastolic phase, with velocity increasing from  $28.32$  to  $30.50\text{ mm s}^{-1}$ .

Figure 8 demonstrates the hemodynamic effect of plaques inside the LAD with cutting views of Sections F–J. Poststenotic velocity reached its highest value in Sections F–H during peak systolic and middiastolic phases, with measured velocity ranging from  $28.32$  to  $30.50\text{ mm s}^{-1}$ . Furthermore, a recirculation region was apparent at the postplaque locations in Sections I and J. The velocity increased slightly with measured values ranging from  $17.43$  to  $23.96\text{ mm s}^{-1}$  as observed in the post-stenotic regions.

Figure 9 represents the result of flow changes observed in the LCx from where plaques were situated in the LMS. Again, the recirculation location was obviously present in Sections K and L, located at postplaque positions. Flow velocity was found to slightly increase, ranging from  $17.43$  to  $26.14\text{ mm s}^{-1}$  in both systolic peak and middle diastolic phases. Furthermore, velocity changes were not observed in Sections M–O as shown in the pre and post-stenotic regions with very similar flow patterns and velocity measured ranging from 0 to  $21.79\text{ mm s}^{-1}$ .

**3.3. CFD Analysis of the Left Coronary Artery: Wall Shear Stress Comparisons.** Analysis of WSS was particularly focused at the stenotic locations with comparison of non-Newtonian and Newtonian fluid models. Figure 10 compares WSS with different fluid viscosities at the left coronary model with presence of plaques. WSS contour values ranged from 0 Pa to  $3.50\text{ Pa}$  as observed in both fluid viscosity models. WSS was different due to presence of plaques at LMS branch at peak systolic phase, ranging from  $0.50\text{ Pa}$  to  $1.75\text{ Pa}$  with non-Newtonian model (Figure 10(a)) and ranging from  $0.50\text{ Pa}$  to  $1.0\text{ Pa}$  with Newtonian model (Figure 10(b)). Similar results of WSS values ranging from  $1.50\text{ Pa}$  to  $3.50\text{ Pa}$  with both viscosity models (Figures 10(c) and 10(d)) were found at middiastolic phase at plaques positions in LMS branch. WSS changes at stenotic locations in LAD were compared at peak systolic phases, ranging from  $0.50\text{ Pa}$  to  $1.0\text{ Pa}$  with non-Newtonian model (Figure 10(a)) and from  $0.50\text{ Pa}$  to  $0.75\text{ Pa}$  with Newtonian model (Figure 10(b)). WSS values at plaques positions in LAD were compared at middiastolic phases, ranging from  $1.50\text{ Pa}$  to  $3.50\text{ Pa}$  with non-Newtonian model (Figure 10(c)) and from  $1.50\text{ Pa}$  to  $3.25\text{ Pa}$  with Newtonian model (Figure 10(d)).

## 4. Discussion

This study shows that coronary plaques produce a significant impact on the subsequent flow changes in the coronary artery, in addition to the local hemodynamic interference due to the presence of plaques. This is clinically important as further potential effects could result from the plaques' interference, leading to adverse effects on the coronary artery, such as lumen stenosis or worsening of atherosclerosis.

It is well known that plaques most commonly form in the coronary bifurcation and coronary angulation, and that this is an important factor that has been found to be related to the development of atherosclerosis, as confirmed by our and other studies [6, 12, 29–31]. Multislice CT angiography and intravascular ultrasound have been widely used to detect

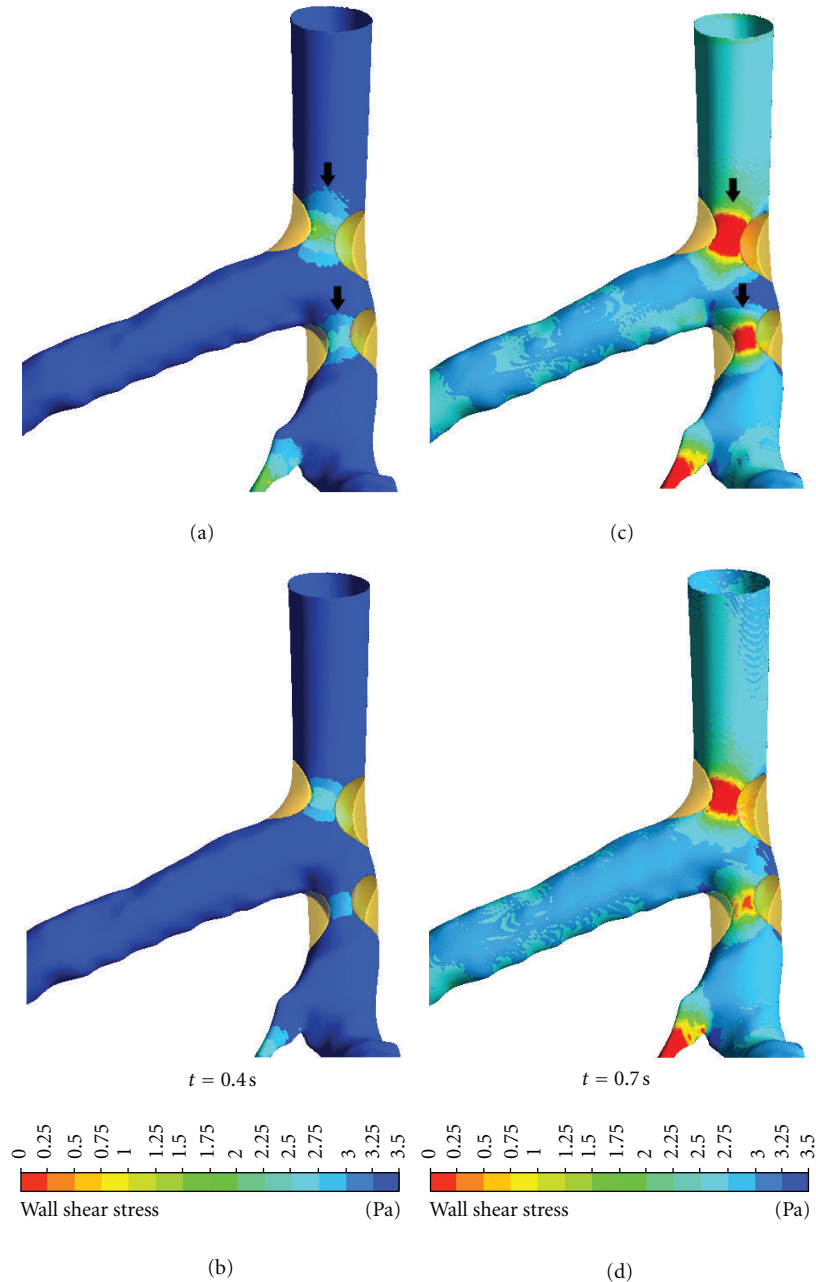


FIGURE 10: Comparison of WSS between non-Newtonian (a, c) and Newtonian (b, d) models observed in realistic coronary artery with presence of plaques during systolic peak of 0.4 s and middiastolic phase of 0.7 s. Arrows identify the different WSS at stenotic locations.

and characterise plaques in the coronary arteries [7, 32]. Despite promising results having been achieved with imaging modalities, the limitations of these techniques were restricted to image visualisation and identification of coronary lumen changes due to presence of plaques, and no information is available about the interference of plaques with blood flow. In contrast, CFD overcomes those limitations by enabling the analysis of coronary blood flow and rheological factors [6, 14, 15]. This study investigated two important factors: PSG and flow velocity and qualified the impact of plaques on flow changes to the coronary arteries. The static wall

pressure does not reflect the velocity profile from the flow axis to the blood wall [27, 33]. In the clinical situation, the PSG magnitude has been used to judge the risk of severity of plaques [28]. The highest PSG area may be relevant to potential coronary plaque rupture. In this study, the CFD analysis of the LCA with presence of plaques showed that the highest PSG was displayed in the locations at both LMS and LAD where plaques were simulated (Figure 6), with measured PSG value ranging from 743.21 to 800 kg/m<sup>2</sup> s<sup>2</sup>.

The presence of plaques in the coronary artery is responsible for obstructing blood flow to the myocardium,

consequently affecting the flow velocity [27]. Moreover, plaques influencing hemodynamic change may lead to the further distribution of plaques. Since velocity is the main component of local WSS and acts in the same direction as local WSS, which means that flow velocity is low when the WSS is low, as observed in a previous study [6], our analysis in this study has proposed explicitly hemodynamic changes inside the LCA surrounding the plaque locations (the so-called effective plaque location (EPL)) (Figure 2). In Sections A–E (Figure 7), we found that the flow velocity fluctuated in post-stenotic regions during cardiac cycles, and this could lead to abnormalities at the coronary wall, responsible for atherosclerosis. In Sections I–L (Figures 8 and 9), flow recirculation occurred, and the region of low velocity was observed within a short distance from the plaques. Consequently, plaques could generate an effect that spread into an area of low flow velocity as demonstrated in Sections I–L, matching with an area of low velocity in Figure 5, with measured low velocity value ranging from 0 to  $2.18 \text{ mm s}^{-1}$ . This is confirmed by our previous analysis [6] showing that progression of plaques developed at a low-flow region. Our analysis provides insight into the effect of plaques on subsequent coronary flow changes although further studies are needed to verify our preliminary findings. WSS in non-Newtonian model was found to be similar to that observed in Newtonian model at plaques locations although more details were demonstrated in non-Newtonian model, as shown in Figure 10. The effect of plaques in left coronary is obviously shown in Newtonian model, and this is adequate for analysis of the plaque effect. The comparison of WSS between different viscosity models is confirmed by previous studies [4, 24]. A non-Newtonian model was simulated using the generalized power law as it has been reported to produce similar WSS effects to Newtonian model on coronary flow changes [4].

There are some limitations in our study that should be addressed. Firstly, realistic left coronary models, both pre and post-stenotic, were assumed to have a rigid wall rather than elastic wall; therefore, the simulation does not fully reflect the realistic physiological situation as the coronary wall moves during cardiac cycles. Secondly, the assumption of a Newtonian blood model becomes important especially in low flow and low wall shear stress regions. Nevertheless, a previous study has shown that the assumption of a Newtonian model is reasonable in this configuration [4]. Thirdly, the realistic plaques position may be affected by left coronary side branches that have not been evaluated in this study. Thus, future studies will use coronary models with a more realistic idealized geometry, extended to evaluate the effect of side branches.

In conclusion, we studied the effect of simulated plaques in the realistic left coronary artery on hemodynamic changes at the locations of plaques, as well as pre and post-stenotic regions inside the coronary artery. There is a direct effect of plaques in the left coronary artery on hemodynamic changes such as recirculation flow, low flow velocity regions, wall shear stress, and wall pressure gradient, indicating the potential for plaques to rupture, causing atherosclerosis. Further studies focusing on the realistic plaque's effect on

coronary side branches should be performed to verify our results.

## References

- [1] Australian Institute of Health and Welfare, "The tenth biennial health report of the Australian Institute of Health and Welfare," AIHW, Canberra, Australia, 2006.
- [2] F. J. Rybicki, S. Melchionna, D. Mitsouras et al., "Prediction of coronary artery plaque progression and potential rupture from 320-detector row prospectively ECG-gated single heart beat CT angiography: lattice Boltzmann evaluation of endothelial shear stress," *International Journal of Cardiovascular Imaging*, vol. 25, no. 2, pp. 289–299, 2009.
- [3] S. K. Shanmugavelayudam, D. A. Rubenstein, and W. Yin, "Effect of geometrical assumptions on numerical modeling of coronary blood flow under normal and disease conditions," *Journal of Biomechanical Engineering*, vol. 132, no. 6, article 061004, 2010.
- [4] B. M. Johnston, P. R. Johnston, S. Corney, and D. Kilpatrick, "Non-Newtonian blood flow in human right coronary arteries: steady state simulations," *Journal of Biomechanics*, vol. 37, no. 5, pp. 709–720, 2004.
- [5] J. V. Soulis, T. M. Farmakis, G. D. Giannoglou, and G. E. Louridas, "Wall shear stress in normal left coronary artery tree," *Journal of Biomechanics*, vol. 39, no. 4, pp. 742–749, 2006.
- [6] T. Chaichana, Z. Sun, and J. Jewkes, "Computation of hemodynamics in the left coronary artery with variable angulations," *Journal of Biomechanics*, vol. 44, no. 10, pp. 1869–1878, 2011.
- [7] Z. Sun and Y. Cao, "Multislice CT angiography assessment of left coronary artery: correlation between bifurcation angle and dimensions and development of coronary artery disease," *European Journal of Radiology*, vol. 79, no. 2, pp. e90–e95, 2011.
- [8] Z. Sun, F. J. Dimpudus, J. Nugroho, and J. D. Adipranoto, "CT virtual intravascular endoscopy assessment of coronary artery plaques: a preliminary study," *European Journal of Radiology*, vol. 75, no. 1, pp. e112–e119, 2010.
- [9] Z. Sun, R. J. Winder, B. E. Kelly, P. K. Ellis, and D. G. Hirst, "CT virtual intravascular endoscopy of abdominal aortic aneurysms treated with suprarenal endovascular stent grafting," *Abdominal Imaging*, vol. 28, no. 4, pp. 580–587, 2003.
- [10] Z. Sun, R. J. Winder, B. E. Kelly, P. K. Ellis, P. T. Kennedy, and D. G. Hirst, "Diagnostic Value of CT Virtual Intravascular Endoscopy in Aortic Stent-Grafting," *Journal of Endovascular Therapy*, vol. 11, no. 1, pp. 13–25, 2004.
- [11] G. Y. Cho, C. W. Lee, M. K. Hong, J. J. Kim, S. W. Park, and S. J. Park, "Effects of stent design on side branch occlusion after coronary stent placement," *Catheterization and Cardiovascular Interventions*, vol. 52, no. 1, pp. 18–23, 2001.
- [12] V. Fuster, "Lewis A. Conner memorial lecture: mechanisms leading to myocardial infarction: insights from studies of vascular biology," *Circulation*, vol. 90, no. 4 I, pp. 2126–2146, 1994.
- [13] X. He and D. N. Ku, "Flow in T-bifurcations: effect of the sharpness of the flow divider," *Biorheology*, vol. 32, no. 4, pp. 447–458, 1995.
- [14] Z. Sun and T. Chaichana, "Fenestrated stent graft repair of abdominal aortic aneurysm: hemodynamic analysis of the effect of fenestrated stents on the renal arteries," *Korean Journal of Radiology*, vol. 11, no. 1, pp. 95–106, 2010.

- [15] Z. Sun and T. Chaichana, "Investigation of the hemodynamic effect of stent wires on renal arteries in patients with abdominal aortic aneurysms treated with suprarenal stent-grafts," *CardioVascular and Interventional Radiology*, vol. 32, no. 4, pp. 647–657, 2009.
- [16] T. Frauenfelder, M. Lotfey, T. Boehm, and S. Wildermuth, "Computational fluid dynamics: hemodynamic changes in abdominal aortic aneurysm after stent-graft implantation," *CardioVascular and Interventional Radiology*, vol. 29, no. 4, pp. 613–623, 2006.
- [17] W. Nichols and M. O'Rourke, *McDonald's Blood Flow in Arteries*, Hodder Arnold, London, UK, 2005.
- [18] S. Smith, *The Scientist and Engineer's Guide to Digital Signal Processing*, Technical Publishing, Poway, Calif, USA, 1997.
- [19] E. Wellnhofer, J. Osman, U. Kertzscher, K. Affeld, E. Fleck, and L. Goubergrits, "Flow simulation studies in coronary arteries-Impact of side-branches," *Atherosclerosis*, vol. 213, no. 2, pp. 475–481, 2010.
- [20] E. Boutsianis, H. Dave, T. Frauenfelder et al., "Computational simulation of intracoronary flow based on real coronary geometry," *European Journal of Cardio-thoracic Surgery*, vol. 26, no. 2, pp. 248–256, 2004.
- [21] W. Milnor, *Hemodynamics*, Williams & Wilkins, Baltimore, Md, USA, 1989.
- [22] Z. Sun, B. Mwiapatayi, T. Chaichana, and C. Ng, "Hemodynamic effect of calcified plaque on blood flow in carotid artery disease: a preliminary study - Hemodynamic effect of calcified plaque," in *Proceedings of the 3rd International Conference on Bioinformatics and Biomedical Engineering (iCBBE '09)*, pp. 1–4, June 2009.
- [23] A. Borghi, N. B. Wood, R. H. Mohiaddin, and X. Y. Xu, "Fluid-solid interaction simulation of flow and stress pattern in thoracoabdominal aneurysms: a patient-specific study," *Journal of Fluids and Structures*, vol. 24, no. 2, pp. 270–280, 2008.
- [24] W. W. Jeong and K. Rhee, "Effects of surface geometry and non-newtonian viscosity on the flow field in arterial stenoses," *Journal of Mechanical Science and Technology*, vol. 23, no. 9, pp. 2424–2433, 2009.
- [25] P. D. Ballyk, D. A. Steinman, and C. R. Ethier, "Simulation of non-newtonian blood flow in an end-to-side anastomosis," *Biorheology*, vol. 31, no. 5, pp. 565–586, 1994.
- [26] L. C. Cheng, J. M. Robertson, and M. E. Clark, "Numerical calculations of plane oscillatory non uniform flow. II. Parametric study of pressure gradient and frequency with square wall obstacles," *Journal of Biomechanics*, vol. 6, no. 5, pp. 521–538, 1973.
- [27] D. Garcia, L. Kadem, D. Savéry, P. Pibarot, and L. G. Durand, "Analytical modeling of the instantaneous maximal transvalvular pressure gradient in aortic stenosis," *Journal of Biomechanics*, vol. 39, no. 16, pp. 3036–3044, 2006.
- [28] H. V. Anderson, G. S. Roubin, and P. P. Leimgruber, "Measurement of transstenotic pressure gradient during percutaneous transluminal coronary angioplasty," *Circulation*, vol. 73, no. 6, pp. 1223–1230, 1986.
- [29] S. H. Han, J. Puma, H. M. Garcia-Garcia et al., "Tissue characterisation of atherosclerotic plaque in coronary artery bifurcations: an intravascular ultrasound radiofrequency data analysis in humans," *EuroIntervention*, vol. 6, no. 3, pp. 313–320, 2010.
- [30] A. I. Gziut, "Comparative analysis of atherosclerotic plaque distribution in the left main coronary artery and proximal segments of left anterior descending and left circumflex arteries in patients qualified for percutaneous coronary angioplasty," *Annales Academiae Medicae Stetinensis*, vol. 52, no. 2, pp. 51–63, 2006.
- [31] T. Asakura and T. Karino, "Flow patterns and spatial distributions of atherosclerotic lesions in human coronary arteries," *Circulation Research*, vol. 66, no. 4, pp. 1045–1066, 1990.
- [32] F. J. H. Gijzen, J. J. Wentzel, A. Thury et al., "A new imaging technique to study 3-D plaque and shear stress distribution in human coronary artery bifurcations in vivo," *Journal of Biomechanics*, vol. 40, no. 11, pp. 2349–2357, 2007.
- [33] H. W. Sung, P. S. Yu, C. H. Hsu, and J. C. Hsu, "Can cardiac catheterization accurately assess the severity of aortic stenosis? An in vitro pulsatile flow study," *Annals of Biomedical Engineering*, vol. 25, no. 5, pp. 896–905, 1997.

## Research Article

# Weighted Least-Squares Finite Element Method for Cardiac Blood Flow Simulation with Echocardiographic Data

Fei Wei,<sup>1</sup> John Westerdale,<sup>2</sup> Eileen M. McMahon,<sup>2</sup> Marek Belohlavek,<sup>2</sup> and Jeffrey J. Heys<sup>1</sup>

<sup>1</sup>Chemical and Biological Engineering Department, Montana State University, Bozeman, MT 59717, USA

<sup>2</sup>Mayo Clinic, Scottsdale, AZ 85259, USA

Correspondence should be addressed to Jeffrey J. Heys, jeff.heys@gmail.com

Received 1 August 2011; Revised 5 October 2011; Accepted 9 October 2011

Academic Editor: Eun Bo Shim

Copyright © 2012 Fei Wei et al. This is an open access article distributed under the Creative Commons Attribution License, which permits unrestricted use, distribution, and reproduction in any medium, provided the original work is properly cited.

As both fluid flow measurement techniques and computer simulation methods continue to improve, there is a growing need for numerical simulation approaches that can assimilate experimental data into the simulation in a flexible and mathematically consistent manner. The problem of interest here is the simulation of blood flow in the left ventricle with the assimilation of experimental data provided by ultrasound imaging of microbubbles in the blood. The weighted least-squares finite element method is used because it allows data to be assimilated in a very flexible manner so that accurate measurements are more closely matched with the numerical solution than less accurate data. This approach is applied to two different test problems: a flexible flap that is displaced by a jet of fluid and blood flow in the porcine left ventricle. By adjusting how closely the simulation matches the experimental data, one can observe potential inaccuracies in the model because the simulation without experimental data differs significantly from the simulation with the data. Additionally, the assimilation of experimental data can help the simulation capture certain small effects that are present in the experiment, but not modeled directly in the simulation.

## 1. Introduction

The physics of blood flow in the left ventricle of the heart has traditionally been studied using either experimental measurement of flow properties (e.g., ultrasound or magnetic resonance imaging) or computational fluid dynamic models. Experimental approaches are generally limited to obtaining flow information at only few spatial locations and using time-averaged properties. Computational models require assumptions along the mathematical domain boundaries, and they include numerical approximation error and model error. In many cases, however, it is desirable to have the more comprehensive spatial and temporal data provided by computational fluid dynamics combined with the data provided by experimental measurement. The weighted least-square finite element method (WLSFEM) is a computational modeling approach that allows experimental data to be assimilated into the model in a flexible framework so that the numerical approximation matches the more accurate experimental data while, at the same time, not being contaminated by errors in the noisier experimental data. The

application of this method to the simulation of blood flow in the left ventricle is examined here.

One approach that we have used previously for obtaining experimental blood flow data in the left ventricle is echocardiographic particle imaging velocimetry (echo PIV) [1–7]. For this approach, microbubbles are introduced into the blood, and they are imaged using 2D brightness (B)-mode ultrasound scans. These images are acquired at a rate of approximately 60 frames/sec, and the microbubble concentration is kept low enough that individual bubbles can be tracked between frames. Using cross-correlation analysis, the particle displacement between two images in sequence can be calculated, and, after dividing by the time span between images, PIV software can calculate the two velocity components tangential to the imaging plane. Echo PIV has been used as a research tool for nearly a decade, and it has been validated by multiple research groups [1, 7]. The flow velocity data provided by echo PIV is useful, but there is a strong interest in using the data to determine additional flow property information such as pressure gradients and viscous energy losses. The problem is that the calculation of these,

or almost any other additional flow property, requires full 3-dimensional velocity data. The data from echo PIV are limited to a single 2D plane. As a result, 2D ultrasound scans provide only 2 components of a 3D velocity field.

A complementary approach to echo PIV that could allow the approximation of all 3 components of the 3D velocity field is to use computational fluid dynamics to simulate blood flow in the left ventricle. A number of computational models have been developed specifically to model blood flow in the heart (c.f., [8, 9] and references therein). Many of these models also predict the motion of the heart wall and simulate the blood-tissue interaction (e.g., [10–12]). The enforcement of boundary conditions with most computational fluid dynamics approaches, such as the finite element or finite volume methods, is achieved by strongly enforcing the velocity (i.e., exactly matching the experimental velocity data) at nodes within the discretization mesh or grid [13, 14]. There are two problems with strong enforcement of the experimental data at the nodes: (1) the experimental data might not be known at the exact location of the nodal mesh points so some type of interpolation is required, and (2) the errors in the experimental data will be propagated throughout the 3D domain and contaminate the numerical approximation at all nodes throughout the computational domain [15]. What is needed is a computational fluid dynamics approach that can assimilate velocity data anywhere in the domain, not just at computational nodes, and an approach that can weakly enforce the experimental data with a weighting that is varied depending upon the accuracy of the experimental data.

In an earlier paper, we developed the WLSFEM for the assimilation of data when solving partial differential equations, including the steady Navier-Stokes equations [15]. This paper extends that work in a number of different ways so that the method can be applied to the simulation of blood flow in the left ventricle using echo PIV data. The greatest change is caused by the fact that we now have a moving fluid domain so a pseudosolid domain mapping technique is developed to handle the deforming fluid mesh. The mathematical approach that we have developed and the numerical implementation are described in the next section. This approach is then applied to two different example problems: a moving flag problem and blood flow in the left ventricle.

## 2. Methods

The physical phenomena of interest here are typically modeled by partial differential equations. In particular, incompressible, Newtonian fluids are modeled by the Navier-Stokes equations, which are generally considered appropriate for modeling blood flow in the heart [16, 17] and are given by:

$$\begin{aligned} \sqrt{\text{Re}} \left( \frac{\partial \mathbf{v}}{\partial t} + \mathbf{v} \cdot \nabla \mathbf{v} \right) &= -\nabla p + \frac{1}{\sqrt{\text{Re}}} \nabla^2 \mathbf{v}, \\ \nabla \cdot \mathbf{v} &= 0, \end{aligned} \quad (1)$$

where  $\mathbf{v}$  is the dimensionless velocity,  $p$  is the dimensionless pressure, and  $\text{Re}$  is the Reynolds number. It should be noted

that the Reynolds number is not written only on the viscous or convective terms, as it normally is, but the equation is instead scaled so that the Reynolds number appears on both terms. The Navier-Stokes equation is generally considered appropriate for modeling blood flow in the heart [16, 17]. The WLSFEM begins by defining new variables so that all second-order equations can be rewritten as systems of first-order equations. There are a number of different options available for rewriting the Navier-Stokes equations as a first-order system, and this choice can significantly impact the properties of the resulting discrete approximation [18–20]. For the particular problems of interest here, accurate mass conservation is of importance, so a modified vorticity approach is used [21]. This approach begins by defining a new variable, called the vorticity, by

$$\boldsymbol{\omega} = -\nabla \times \mathbf{v}, \quad (2)$$

and another new variable,  $\mathbf{r}$ , by

$$\mathbf{r} = \nabla p + \frac{\sqrt{\text{Re}}}{2} \nabla |\mathbf{v}|^2 = \nabla \left( \frac{\sqrt{\text{Re}}}{2} |\mathbf{v}|^2 + p \right), \quad (3)$$

which is often referred to as the gradient of the total pressure. Using these two new variables, the Navier-Stokes equations (1) can be rewritten as the following system of first-order equations:

$$\begin{aligned} \nabla \times \mathbf{v} + \boldsymbol{\omega} &= 0, \\ \nabla \cdot \mathbf{v} &= 0, \\ \frac{1}{\sqrt{\text{Re}}} \nabla \times \boldsymbol{\omega} - \mathbf{r} - \sqrt{\text{Re}} \left( \mathbf{v} \times \boldsymbol{\omega} + \frac{\partial \mathbf{v}}{\partial t} \right) &= 0, \\ \nabla \cdot \boldsymbol{\omega} &= 0, \\ \nabla \times \mathbf{r} &= 0, \\ \nabla \cdot \mathbf{r} - \sqrt{\text{Re}} (\boldsymbol{\omega} \cdot \boldsymbol{\omega}) - \text{Re} (\mathbf{v} \cdot \mathbf{r}) &= 0. \end{aligned} \quad (4)$$

In the least-squares finite element method, this system of equations is cast as an optimization problem based on the functional:

$$\begin{aligned} G(\mathbf{v}, \boldsymbol{\omega}, \mathbf{r}) &= \|\nabla \times \mathbf{v} + \boldsymbol{\omega}\|_{0,\Omega}^2 + \|\nabla \cdot \mathbf{v}\|_{0,\Omega}^2 \\ &+ \left\| \frac{1}{\sqrt{\text{Re}}} \nabla \times \boldsymbol{\omega} - \mathbf{r} - \sqrt{\text{Re}} \left( \mathbf{v} \times \boldsymbol{\omega} + \frac{\partial \mathbf{v}}{\partial t} \right) \right\|_{0,\Omega}^2 \\ &+ \|\nabla \cdot \boldsymbol{\omega}\|_{0,\Omega}^2 + \|\nabla \times \mathbf{r}\|_{0,\Omega}^2 \\ &+ \left\| \nabla \cdot \mathbf{r} - \sqrt{\text{Re}} (\boldsymbol{\omega} \cdot \boldsymbol{\omega}) - \text{Re} (\mathbf{v} \cdot \mathbf{r}) \right\|_{0,\Omega}^2 \\ &+ \frac{w_\Gamma}{h} \|\mathbf{v} - g_1\|_{0,\Gamma}^2 + \frac{1}{h} \|\boldsymbol{\omega} - g_2\|_{0,\Gamma}^2 \\ &+ \frac{w_{\text{PIV}}}{h} \|\mathbf{v} - g_{\text{PIV}}\|_{0,\Gamma_{\text{PIV}}}^2, \end{aligned} \quad (5)$$

where  $\|\cdot\|_{0,\Omega}^2$  is the  $L^2$ -norm on the 3D fluid domain and  $(w/h) \|\cdot\|_{0,\Gamma}^2$  is the weighted  $L^2$ -norm along the 2D

boundary surfaces ( $\Gamma$ ) or 2D surfaces, where PIV data is given ( $\Gamma_{\text{PIV}}$ ). The PIV plane is simply a 2-dimensional cross-section that is typically somewhat near the middle of the 3-dimensional domain ( $\Gamma_{\text{PIV}}$ ), where as the other boundaries ( $\Gamma$ ) are all on the surface of the 3-dimensional domain. The weighted  $L^2$ -norm, used along the boundary surfaces, is an approximation of the  $H^{1/2}$ -norm that deemphasizes oscillatory components (i.e., noisy components) relative to the  $H^{1/2}$ -norm [22]. The functions  $g_1$ ,  $g_2$ , and  $g_{\text{PIV}}$  are the given boundary or PIV data, that is, to be weakly matched by the numerical approximation of the solution. For example,  $g_1$  is set to the surface displacement rate along no-slip boundaries. The function  $g_2$  is only set along boundaries where the normal vorticity is known, such as along walls. It is also straightforward to enforce this data strongly on the finite element space so that it is matched exactly by the approximate solution, but that is not an optimal strategy if the data contains errors, which is generally true for experimental data. Finally, the PIV data,  $g_{\text{PIV}}$ , can be either 2- or 3-dimensional data, but the PIV method is typically limited to providing 2-dimensional data, so that is the focus here. The spatial location of the PIV data does not need to be the same as the computational mesh node locations. The data can be located anywhere within the computational domain.

The boundary functional weights,  $w_\Gamma$  and  $w_{\text{PIV}}$ , should be chosen so that the weight value is larger in regions where the given data,  $g$ , is known more accurately and smaller in the regions where the data contains more noise. Along the heart walls, for example, we know that the fluid velocity is equal to the velocity of the wall, but the wall location is not known precisely so there is still some error. In the problems of interest here, the PIV data typically contains larger errors than the boundary data, so we would expect  $w_\Gamma > w_{\text{PIV}}$ , which would result in an approximate solution that more closely matches the boundary data than the PIV data. In [15] it was shown that the boundary functional weight should be chosen by

$$w \approx \frac{1}{\sigma^2}, \quad (6)$$

where  $\sigma$  is the standard deviation in the given data. To simplify this process, we typically set the boundary functional weight to 1.0 for the most accurate boundary data, and then the other boundary functional weights are set relative to the most accurate data. The vorticity is typically determined from the velocity data, and boundary conditions on the vorticity are weighted consistently with the accuracy of the velocity data.

When modeling blood flow in the left ventricle, or any fluid-structure interaction problem, the shape of the fluid domain is continuously changing. There are a number of numerical strategies for addressing the changing domain shape, including the generation of a new mesh every time step or grid mapping using equations such as the Winslow generator [23, 24]. Another straightforward method is to solve a compressible elasticity problem over the fluid domain and use the solution from the elasticity problem to move the nodes of the finite element mesh. This approach is often referred to as a pseudosolid domain mapping technique

[25, 26]. The linear, compressible elasticity equation can be written as

$$\lambda \nabla (\nabla \cdot \mathbf{u}) + \nabla^2 \mathbf{u} = 0, \quad (7)$$

where  $\mathbf{u}$  is the displacement and  $\lambda$ , which is typically set to 1.0, is a Lamé coefficient related to Poisson's ratio. Similar to the Navier-Stokes equation, this equation also must be rewritten as a first-order system of equations by defining a matrix of new variables,  $U$ , equal to the gradient of  $\mathbf{u}$ . The full first-order system is

$$\begin{aligned} U - \nabla \mathbf{u} &= 0, \\ \lambda \nabla (\text{tr}(U)) + \nabla \cdot U n &= 0, \\ \nabla \times U &= 0, \end{aligned} \quad (8)$$

where  $\text{tr}(U)$  is the trace of  $U$ . The equations in the first-order system are combined into the functional

$$\begin{aligned} G_u(\mathbf{u}, U) &= \|U - \nabla \mathbf{u}\|_{0,\Omega}^2 + \|\lambda \nabla (\text{tr}(U)) + \nabla \cdot U\|_{0,\Omega}^2 \\ &+ \|\nabla \times U\|_{0,\Omega}^2 + \frac{1}{h} \|\mathbf{u} - g_u\|_{0,\Gamma}^2, \end{aligned} \quad (9)$$

where  $g_u$  is the given boundary displacement. It is important to note that moving the finite element mesh can create an additional, artificial convection that must be subtracted from the actual convective velocity in the Navier-Stokes equation [25].

The WLSFEM has a number of computational and algorithmic advantages for the problem of solving the Navier-Stokes equations and pseudosolid domain mapping equations with assimilated data:

- (i) it provides tremendous flexibility in handling the additional conditions imposed by the experimental data, including the ability to weight data based on the accuracy of the experimental data, that is, accurate data can be weighted and matched more closely by the CFD solution while less accurate data is only loosely matched by the CFD approximation;
- (ii) the mathematical framework of least-squares minimization leads to symmetric positive definite matrices, which generally allows for efficient algebraic multigrid solvers [27];
- (iii) the functional itself provides a natural sharp local error estimator, which could enable effective adaptive refinement [28, 29].

To solve the least-squares problem, the equations in the functional ( $G$ ) are first linearized so that the solution can be found using a Gauss-Newton approach. The least-squares weak form is converted into a linear system of equations by choosing a finite element basis. All the results presented here utilized a triquadratic finite element basis. The WLSFEM allows the solution spaces for the variables to be chosen independently, and there is no restrictive stability condition (i.e., inf-sup condition) to satisfy [30]. As a result, all variables in the reformulation of the Navier-Stokes equations

or the linear elasticity equation can be approximated with the same basis.

All simulations were performed using the ParaFOS code, written by the authors. The code imports hexahedral meshes from the Cubit mesh generation package (Sandia National Laboratory). The finite element meshes are then partitioned using the Metis graph partitioning library [31]. The software is designed to run on distributed memory clusters using the MPI library for communication. The linear matrix problem generated during each Gauss-Newton step is solved using the hypre library of solvers (from the Center for Applied Scientific Computing, Lawrence Livermore National Laboratory, see [32]). Specifically, the BoomerAMG parallel algebraic multigrid solver is used as a preconditioner for a conjugate gradient iteration.

### 3. Results

To test the WLSFEM on problems with moving domains and PIV data assimilation, two different test problems are examined. The first problem is a flexible flap that is displaced by a fluid jet, and optical PIV is used to obtain experimental data. The second problem is a simulation of blood flow in the left ventricle of a pig using echo PIV data. It is this second problem that was the primary motivation for the development of the numerical modeling approach described here.

*3.1. Moving Flap.* The experimental apparatus consisted of a cellulose acetate flap (taken from an overhead transparency) that was fixed on one end and placed in a 15.4 cm cube filled with water and contrast agent particles (Figure 1). A centrifugal pump was used to generate a jet of water with a diameter of 2.2 cm for a duration of 200 ms. Additional details regarding the experimental setup can be found in [33]. For the numerical simulation, the experimental system was nondimensionalized and the simulation was run using a Reynolds number of 1000 based on the inlet tube diameter, which is small enough to ensure that no turbulent effects are present.

A sample image from the moving flap experiment is shown in Figure 1, and the velocity data obtained from PIV data analysis is overlaid on the image. Because the experiment used an optical PIV technique, the seeding particles can be seen in the fluid. To simulate this model experiment, a cubic domain was meshed using hexahedral finite elements, and the flap in the no-flow or rest position was defined by a 2-dimensional surface within the cubic volume. The location of the flap at various time points during the experiment could be determined from the experimental images that were used for PIV analysis. The flap in each image was interpolated with a 5th order polynomial, and these polynomials were used to specify the displacement of the flap surface in the WLSFEM simulation at each time step. As the flap surface moved, the pseudosolid domain mapping technique was used to deform the finite element mesh in response to the flap motion (Figure 2). To clarify, the simulation did not model the solid flap because experimental data was available for specifying

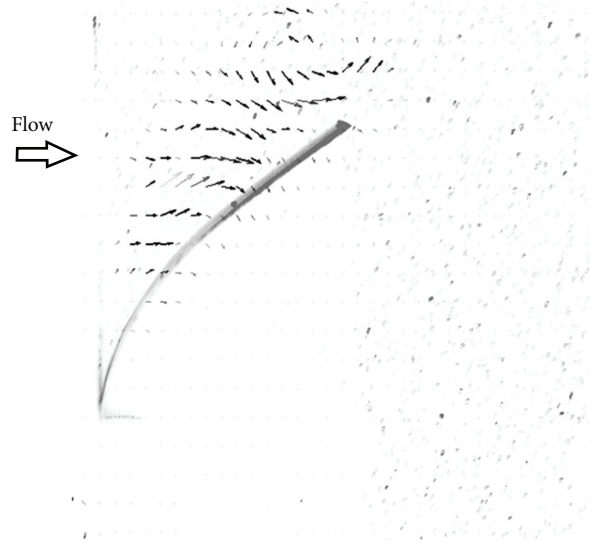


FIGURE 1: Image from the flap displacement PIV experiment. The flap (grey) is displaced by a jet of fluid, and the flow velocity is determined using PIV. The optical PIV particles appear as speckles, and the velocities are shown using arrows.

the flap location, but the simulation did include the impact of the flap on the fluid through the boundary conditions on the fluid (i.e., the no-slip boundary condition on the flap surface). The other boundary conditions used in the simulation were no-slip boundary conditions on the walls of the cubic domain except for the right surface of the domain, which was set to a natural boundary condition because the actual experimental system allowed outflow along this surface. The inlet velocity was set to a paraboloid with a total flow rate equal to the experimentally measured flow rate.

The WLSFEM algorithm was based on implicit time stepping, so from a numerical stability standpoint, any time step size could be used in the simulation. Here we used the same time step size in the simulation as was available from the PIV data, 20 msec. This means that PIV data was available at every time point in the simulation. If a simulation uses more time steps than are available from PIV data, then some simulation time steps cannot use assimilated PIV data or they must use interpolated PIV data. Based on error estimated by the experimentalists and the PIV software, a boundary functional weight of  $w_{PIV} = 1.0$  was used for most simulations. This implies that the PIV data had a standard error similar to that of the flap displacement rate estimate and inflow velocity estimates. Figure 2 shows the simulation prediction for the velocity along a single plane in the 3-dimensional domain at two different time points. Specifically, the visualized plane is the same plane as the PIV data plane (recall the PIV data is typically restricted to a single plane) so that the differences between the PIV data and simulation prediction can clearly be seen. The simulation prediction of the velocity field is similar to the original PIV data, but it also contained less high-frequency variation (i.e., the simulation with the PIV data assimilated gave a smoother velocity field).

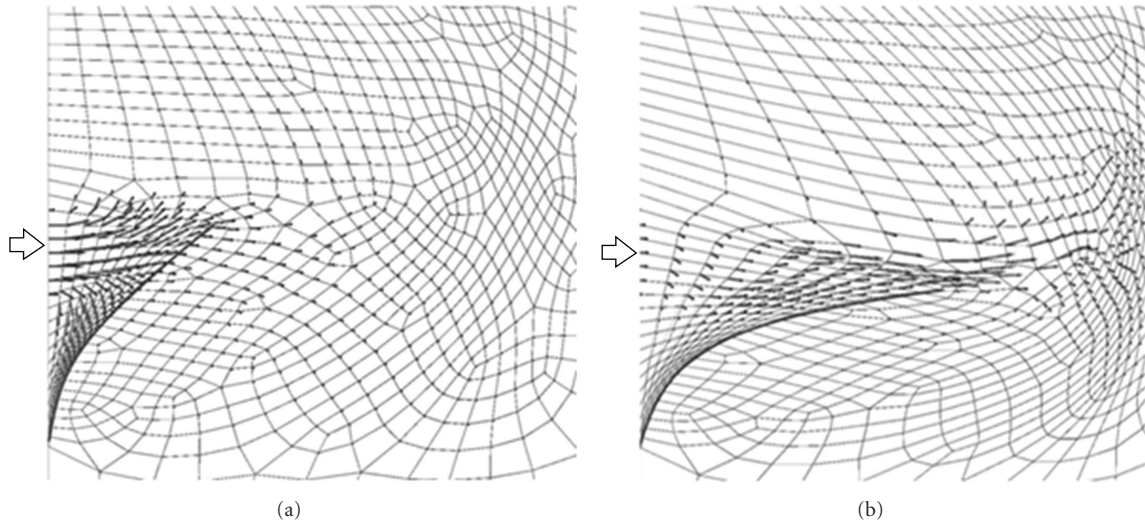


FIGURE 2: WLSFEM simulation of the moving flap experiment at (a) 0.0 sec and (b) 0.2 sec. The finite element grid deforms in response to the moving flap, and the PIV data is assimilated into the simulation with a boundary functional weight of 1.0.

It is difficult to quantitatively compare the simulation predictions with and without PIV data included, but one measure is to calculate the magnitude of the velocity at every node along a surface (in this case the PIV surface) and sum those magnitudes. Figure 3 shows this “total velocity” at every time step for different values of  $w_{PIV}$ . A high velocity burst is seen at the beginning when the pump is turned on, then the total velocity decreases until the jet has expanded into larger parts of the domain. When  $w_{PIV} = 0.0$ , no PIV data is included in the simulation, and the total velocity tends to be the lowest at every time step. As  $w_{PIV}$  is increased, the total velocity along the PIV plane appears to converge to slightly higher values. The reason for the increase in total velocity as the boundary data weight is increased is that more high-frequency variation from the PIV data appears in the simulation result. If this same comparison is made for planes other than the PIV plane, the results are qualitatively similar, but the difference between the velocity with and without PIV data is dampened the further the plane is from the PIV plane. This is clearly a result of the fact that the further one is from the PIV plane, the less the velocity is influenced by the PIV data.

3.2. *Left Ventricle.* The PIV data for the left ventricle simulation was obtained in previous studies using an open-chest pig [4, 34, 35]. The PIV data was obtained at a higher temporal resolution (approximately 60 Hz) than the simulation time step size (50 msec.), so only a subset of the PIV data corresponding to the simulation time steps was used. A typical ultrasound image from the experiment is shown in Figure 4, and this image was obtained in the late diastole phase (i.e., near the end of the filling phase). The microbubbles in the blood appear as white spots in this image, and the bubbles appear much larger than their actual dimensions due to scattering. The ultrasound probe is placed epicardially near the apex of the heart, and most of the left

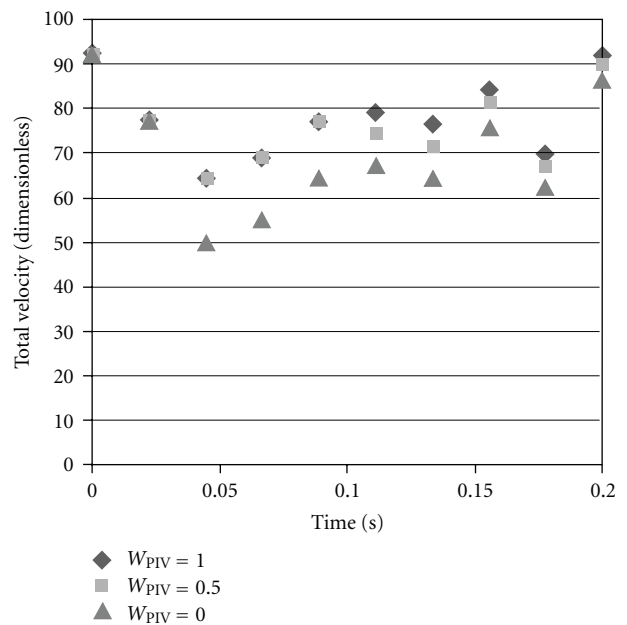


FIGURE 3: The sum of the  $L^2$ -norm of every velocity vector along the PIV plane in the simulation versus the weight on the PIV data term in the functional. Slightly lower velocities are predicted by the simulation if the PIV data are not assimilated ( $w_{PIV} = 0.0$ ), and including the PIV data gives slightly higher velocities. These higher velocities are partially due to high-frequency noise in the PIV data.

ventricle is visible within the scanned region. The lack of data from outside the scanned region is not a concern because the WLSFEM can incorporate whatever data are available, and it does not have a minimum quantity of data requirement. The velocity data obtained from PIV analysis of the bubble motion are shown in Figure 4(b). The inflow from the left atrium is visible in the upper part of the domain, and a vortex

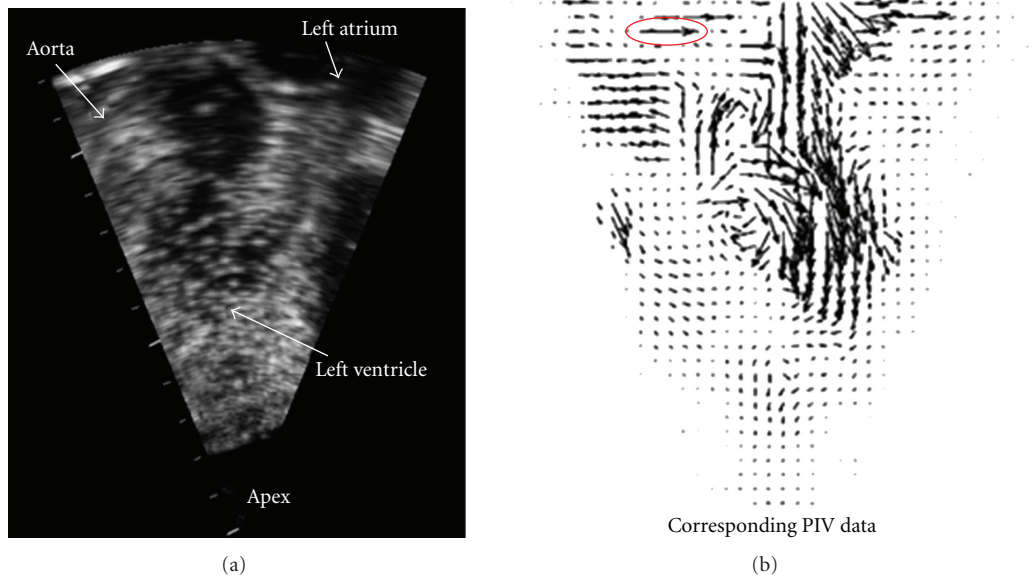


FIGURE 4: An ultrasound image showing microbubbles inside the left ventricle of the heart of a pig (left). The ultrasound probe is on the external side of the heart wall near the apex. The PIV data corresponding to the bubble motion is shown on the right. The data clearly contains some errors (e.g., the circled vector).

can be seen near the center of the domain. During systole, the blood is ejected through the outflow tract and aorta, partially captured in the upper left of the image domain.

The WLSFEM simulation of the left ventricle required that the location of the heart walls be specified. The left ventricle was assumed to have a half-ellipsoid geometry, which is a common geometric approximation [36–38], and the motion of the heart walls was based on the measured ejection fraction of the heart and the motion observed in the ultrasound scans. The motion of the walls in the simulation is somewhat distorted by the fact that the upper surface was not allowed to move so that the cross-sectional area of the inlet (mitral valve) and outlet (aortic valve) could be kept constant. This restriction could be relaxed in the future as more experimental data becomes available. The blood velocity along the inlet was specified based on the PIV data, and the outlet flow rate was not specified (a natural boundary condition was set on the outlet). Along the heart walls, the velocity was set using a no-slip boundary condition (i.e., the fluid velocity was set equal to the wall displacement rate). The simulation was based on the dimensionless Navier-Stokes equation, and the Reynolds number was set to 1000 based on data from the pig experiments.

The simulation begins at the start of diastole, the filling of the ventricle, and the velocity along a single plane (the PIV plane) during early diastole is shown in Figure 5. The heart walls have only moved a small amount at this point in the simulation, and most of the blood flow is still near the inlet located on the right side of the upper surface. Simulations were run with  $w_{PIV} = 0.0$  and  $w_{PIV} = 2.0$  to explore the differences between including the PIV data and not including the data. The weight of 2.0 implies that the PIV data is actually more accurate than the velocity data along the walls,

which is inaccurate because the wall location is not accurately known, and the inlet, which is also based on PIV data but is farther from the ultrasound probe. For the early time point shown in Figure 5, there are only small differences in the simulation when the PIV data are included or not included. It appears that the PIV data may have smaller velocities away from the inlet, but these differences are still very small.

The PIV data has a larger impact on the simulation at later time points. Figure 6 shows the simulation results during late diastole when the left ventricle has stopped filling. In the simulation without PIV data, Figure 6(a), there is a very weak vortex in the upper center of the ventricle, but the velocities are relatively slow in general. This vortex has been identified as potentially important for the efficient pumping of the heart [4, 39]. When PIV data are assimilated into the simulation (Figure 6(b) with  $w_{PIV} = 2.0$ ), we see a stronger vortex and more chaotic flows in general. It appears that something may be missing from the pure numerical model (no PIV data) that is causing a higher velocity vortex. There are a number of possible reasons for this, but we will only discuss what we believe are the three most likely explanations. First, the simulation does not include the mitral valve, and the drag force applied to the blood by the valve flaps may cause a stronger vortex than would be observed without the valve. This is a very interesting result because it suggests that by properly incorporating experimental data into a simulation, we can potentially capture effects (like valves or body motion) that are often neglected in simplified numerical models. A second possibility is that the estimated Reynolds number is low and the simulation should have been run at a higher Reynolds number with greater inertial forces. Simulations run with a Reynolds number of 2000 and no PIV data showed a

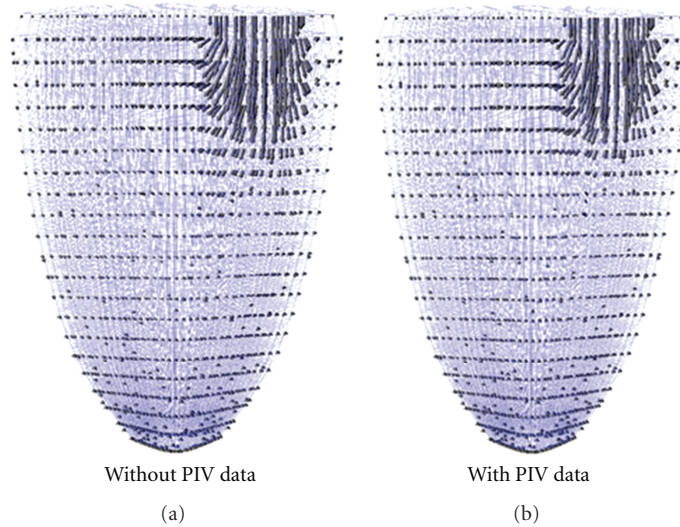


FIGURE 5: WLSFEM simulations of blood flow in the left ventricle at  $t = 0.1$  sec (early diastole in our model). The left figure is the simulation without PIV data ( $w_{PIV} = 0.0$ ), and the right figure incorporates the PIV data ( $w_{PIV} = 2.0$ ). The PIV data has very little impact on the numerical simulation.

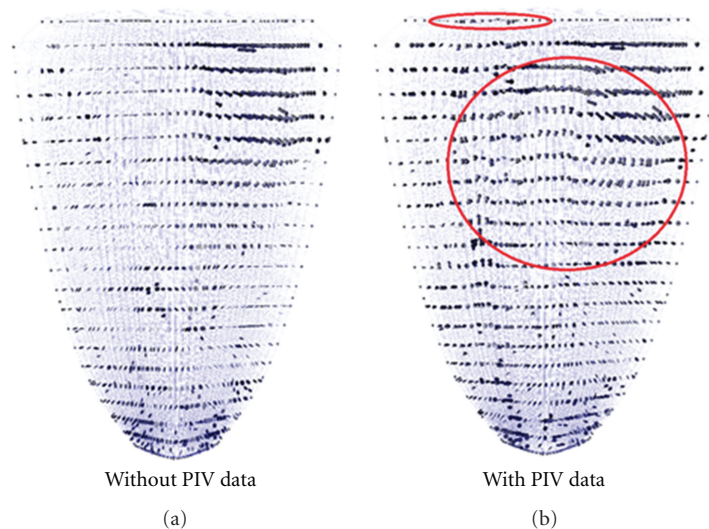


FIGURE 6: WLSFEM simulation of flow in the left ventricle at  $t = 0.5$  sec (late diastole in our model). The velocity in the left figure (a) is not impacted by the PIV data, but the figure on the right includes assimilated PIV data ( $w_{PIV} = 2.0$ ). The PIV data have a clear impact on the simulation and allow it to capture physics that may not be modeled correctly without the PIV data. For example, the simulation does not capture the effects of the mitral valve.

slightly stronger vortex than Figure 6(a), but it was still not as strong as the figure with PIV data, and it is impossible to justify a doubling of the Reynolds number estimate. A third possibility is that the idealized geometry of the left ventricle (a half-ellipsoid) resulted in a somewhat inaccurate flow field at later time points.

#### 4. Conclusions

The challenge of assimilating experimental data into a computational simulation is very widespread. The general problem of interest here is solving the Navier-Stokes

equations on a moving domain with additional experimental data provided by PIV experiments. In particular, the goal is the simulation of blood flow in the left ventricle with the assimilation and inclusion of 2-dimensional echo PIV data obtained using microbubbles. The WLSFEM used here is particularly well suited for this assimilation of data problem because of the flexibility in incorporating experimental data that are weighted based on accuracy. Accurate data can be closely matched with the simulation result, and less accurate data is not closely matched. The WLSFEM approach is demonstrated on two different test problems: (1) a flap that is displaced by a jet of fluid, and (2) blood flow in

the left ventricle of the pig. By applying different weights to the PIV data, one can observe quantitative differences between the simulation without PIV data and the simulation that matches the PIV data more or less accurately. These comparisons can reveal inaccuracies in the model such as inaccurate boundary conditions or missing physics. The incorporation of PIV data can assist the simulation by capturing some effects that are not directly modeled. For example, in the left ventricle model presented here, the mitral valve was not modeled directly, but the effects of the valve on the blood flow could be partially captured by the simulation through the incorporated PIV data. There are other methods for incorporating experimental data into a numerical simulation, but the WLSFEM method is a flexible and efficient option for this class of problems.

## Acknowledgments

This work was supported by NSF Grant DMS-0811275 and the Flight Attendant Medical Research Institute.

## References

- [1] H. B. Kim, J. R. Hertzberg, and R. Shandas, "Development and validation of echo PIV," *Experiments in Fluids*, vol. 36, no. 3, pp. 455–462, 2004.
- [2] H. R. Zheng, L. Liu, L. Williams, J. R. Hertzberg, C. Lanning, and R. Shandas, "Real time multicomponent echo particle image velocimetry technique for opaque flow imaging," *Applied Physics Letters*, vol. 88, no. 26, Article ID 261915, 2006.
- [3] P. Jiamsripong, A. M. Calleja, M. S. Alharthi et al., "Impact of acute moderate elevation in left ventricular afterload on diastolic transmitral flow efficiency: analysis by vortex formation time," *Journal of the American Society of Echocardiography*, vol. 22, no. 4, pp. 427–431, 2009.
- [4] P. Jiamsripong, A. M. Calleja, M. S. Alharthi et al., "Increase in the late diastolic filling force is associated with impaired transmitral flow efficiency in acute moderate elevation of left ventricular afterload," *Journal of Ultrasound in Medicine*, vol. 28, no. 2, pp. 175–182, 2009.
- [5] P. Jiamsripong, M. S. Alharthi, A. M. Calleja et al., "Impact of pericardial adhesions on diastolic function as assessed by vortex formation time, a parameter of transmitral flow efficiency," *Cardiovascular Ultrasound*, vol. 8, no. 1, article 42, 2010.
- [6] J. C. Adams, P. Jiamsripong, M. Belohlavek et al., "Potential role of Reynolds number in resolving Doppler- and catheter-based transvalvular gradient discrepancies in aortic stenosis," *Journal of Heart Valve Disease*, vol. 20, no. 2, pp. 159–164, 2011.
- [7] J. Westerdale, M. Belohlavek, E. M. McMahon, P. Jiamsripong, J. J. Heys, and M. Milano, "Flow velocity vector fields by ultrasound particle imaging velocimetry: in vitro comparison with optical flow velocimetry," *Journal of Ultrasound in Medicine*, vol. 30, no. 2, pp. 187–195, 2011.
- [8] C. A. Taylor and C. A. Figueroa, "Patient-specific modeling of cardiovascular mechanics," *Annual Review of Biomedical Engineering*, vol. 11, pp. 109–134, 2009.
- [9] S. S. Khalafvand, E. Y. K. Ng, and L. Zhong, "CFD simulation of flow through heart: a perspective review," *Computer Methods in Biomechanics and Biomedical Engineering*, vol. 14, no. 1, pp. 113–132, 2011.
- [10] D. M. McQueen and C. S. Peskin, "A three-dimensional computer model of the human heart for studying cardiac fluid dynamics," *Computer Graphics*, vol. 34, no. 1, pp. 56–60, 2000.
- [11] A. I. Veress, W. P. Segars, B. M. Tsui, and G. T. Gullberg, "Incorporation of a left ventricle finite element model defining infarction into the XCAT imaging phantom," *IEEE Transactions on Medical Imaging*, vol. 30, no. 4, pp. 915–927, 2011.
- [12] J. J. Heys, C. G. DeGroof, T. A. Manteuffel, and S. F. McCormick, "First-order system least-squares (FOSLS) for modeling blood flow," *Medical Engineering and Physics*, vol. 28, no. 6, pp. 495–503, 2006.
- [13] P. M. Gresho, R. L. Sani, and M. S. Engelman, *Incompressible Flow and the Finite Element Method*, vol. 2, John Wiley & Sons, Chichester, UK, 2000.
- [14] R. J. LeVeque, *Finite Volume Methods for Hyperbolic Problems*, Cambridge Texts in Applied Mathematics, Cambridge University Press, Cambridge, UK, 2002.
- [15] J. J. Heys, T. A. Manteuffel, S. F. McCormick, M. Milano, J. Westerdale, and M. Belohlavek, "Weighted least-squares finite elements based on particle imaging velocimetry data," *Journal of Computational Physics*, vol. 229, no. 1, pp. 107–118, 2010.
- [16] B. E. Griffith, R. D. Hornung, D. M. McQueen, and C. S. Peskin, "An adaptive, formally second order accurate version of the immersed boundary method," *Journal of Computational Physics*, vol. 223, no. 1, pp. 10–49, 2007.
- [17] T. J. Pedley, "Mathematical modelling of arterial fluid dynamics," *Journal of Engineering Mathematics*, vol. 47, no. 3-4, pp. 419–444, 2003.
- [18] J. J. Heys, E. Lee, T. A. Manteuffel, and S. F. McCormick, "On mass-conserving least-squares methods," *SIAM Journal on Scientific Computing*, vol. 28, no. 5, pp. 1675–1693, 2006.
- [19] P. B. Bochev, "Analysis of least-squares finite element methods for the navier-stokes equations," *SIAM Journal on Numerical Analysis*, vol. 34, no. 5, pp. 1817–1844, 1997.
- [20] B. N. Jiang, "A least-squares finite-element method for incompressible Navier-Stokes problems," *International Journal for Numerical Methods in Fluids*, vol. 14, no. 7, pp. 843–859, 1992.
- [21] J. J. Heys, E. Lee, T. A. Manteuffel, and S. F. McCormick, "An alternative least-squares formulation of the Navier-Stokes equations with improved mass conservation," *Journal of Computational Physics*, vol. 226, no. 1, pp. 994–1006, 2007.
- [22] P. G. Ciarlet, *The Finite Element Method for Elliptic Problems*, Classics in Applied Mathematics, Society for Industrial and Applied Mathematics, Philadelphia, Pa, USA, 2002.
- [23] P. M. Knupp and S. Steinberg, *Fundamentals of Grid Generation*, CRC Press, Boca Raton, Fla, USA, 1994.
- [24] J. J. Heys, T. A. Manteuffel, S. F. McCormick, and J. W. Ruge, "First-order system least squares (FOSLS) for coupled fluid-elastic problems," *Journal of Computational Physics*, vol. 195, no. 2, pp. 560–575, 2004.
- [25] J. J. Heys, V. H. Barocas, and M. J. Taravella, "Modeling passive mechanical interaction between aqueous humor and iris," *Journal of Biomechanical Engineering*, vol. 123, no. 6, pp. 540–547, 2001.
- [26] P. A. Sackinger, P. R. Schunk, and R. R. Rao, "A Newton-Raphson pseudo-solid domain mapping technique for free and moving boundary problems: a finite element implementation," *Journal of Computational Physics*, vol. 125, no. 1, pp. 83–103, 1996.
- [27] Z. Q. Cai, T. A. Manteuffel, and S. F. McCormick, "First-order system least squares for second-order partial differential

- equations: part II,” *SIAM Journal on Numerical Analysis*, vol. 34, no. 2, pp. 425–454, 1997.
- [28] J. M. Fiard, T. A. Manteuffel, and S. F. McCormick, “First-order system least squares (FOSLS) for convection-diffusion problems: numerical results,” *SIAM Journal on Scientific Computing*, vol. 19, no. 6, pp. 1958–1979, 1998.
- [29] J. Nolting, T. Manteuffel, S. McCormick, J. Ruge, and G. Sanders, “Further results on error estimators for local refinement with first-order system least squares (FOSLS),” *Numerical Linear Algebra with Applications*, vol. 17, no. 2-3, pp. 387–413, 2010.
- [30] P. Bochev, Z. Cai, T. A. Manteuffel, and S. F. McCormick, “Analysis of velocity-flux first-order system least-squares principles for the navier-stokes equations: part I,” *SIAM Journal on Numerical Analysis*, vol. 35, no. 3, pp. 990–1009, 1998.
- [31] G. Karypis and V. Kumar, “A fast and high quality multilevel scheme for partitioning irregular graphs,” *SIAM Journal on Scientific Computing*, vol. 20, no. 1, pp. 359–392, 1998.
- [32] R. D. Falgout and U. M. Yang, “Hypr: a library of high performance preconditioners,” in *Proceedings of the Computational Science (ICCS ’02)*, vol. 2331 of *Lecture Notes in Computational Science Part III*, pp. 632–641, April 2002.
- [33] J. Westerdale, M. Belohlavek, E. McMahon, P. Jiamsripong, J. Heys, and M. Milano, “Elasticity estimation using optical PIV velocity fields,” *Journal of Fluids and Structures*. In press.
- [34] P. P. Sengupta, J. Korinek, M. Belohlavek et al., “Left ventricular structure and function: basic science for cardiac imaging,” *Journal of the American College of Cardiology*, vol. 48, no. 10, pp. 1988–2001, 2006.
- [35] P. P. Sengupta, V. K. Krishnamoorthy, J. Korinek et al., “Left ventricular form and function revisited: applied translational science to cardiovascular ultrasound imaging,” *Journal of the American Society of Echocardiography*, vol. 20, no. 5, pp. 539–551, 2007.
- [36] P. Bagnoli, N. Malagutti, D. Gastaldi et al., “Computational finite element model of cardiac torsion,” *International Journal of Artificial Organs*, vol. 34, no. 1, pp. 44–53, 2011.
- [37] F. B. Sachse, G. Seemann, M. B. Mohr, and A. V. Holden, “Mathematical modeling of cardiac electro-mechanics: from protein to organ,” *International Journal of Bifurcation and Chaos*, vol. 13, no. 12, pp. 3747–3755, 2003.
- [38] R. G. Wise, C. L. H. Huang, A. I. M. Al-Shafei, T. A. Carpenter, and L. D. Hall, “Geometrical models of left ventricular contraction from MRI of the normal and spontaneously hypertensive rat heart,” *Physics in Medicine and Biology*, vol. 44, no. 10, pp. 2657–2676, 1999.
- [39] M. Gharib, E. Rambod, A. Kheradvar, D. J. Sahn, and J. O. Dabiri, “Optimal vortex formation as an index of cardiac health,” *Proceedings of the National Academy of Sciences of the United States of America*, vol. 103, no. 16, pp. 6305–6308, 2006.

## Research Article

# The Need of Slanted Side Holes for Venous Cannulae

**Joong Yull Park**

*School of Mechanical Engineering, College of Engineering, Chung-Ang University, Seoul 156-756, Republic of Korea*

Correspondence should be addressed to Joong Yull Park, [jrpark@cau.ac.kr](mailto:jrpark@cau.ac.kr)

Received 1 September 2011; Accepted 9 October 2011

Academic Editor: Eun Bo Shim

Copyright © 2012 Joong Yull Park. This is an open access article distributed under the Creative Commons Attribution License, which permits unrestricted use, distribution, and reproduction in any medium, provided the original work is properly cited.

Well-designed cannulae must allow good flow rate and minimize nonphysiologic load. Venous cannulae generally have side holes to prevent the rupture of blood vessel during perfusion. Optimizing side hole angle will yield more efficient and safe venous cannulae. A numerical modeling was used to study the effect of the angle ( $0^{\circ}$ – $45^{\circ}$ ) and number (0–12) of side holes on the performance of cannulae. By only slanting the side holes, it increases the flow rate up to 6% (in our models). In addition, it was found that increasing the number of side holes reduces the shear rate up to 12% (in our models). A new parameter called “penetration depth” was introduced to describe the interfering effect of stream jets from side holes, and the result showed that the  $45^{\circ}$ -slanted side holes caused minimum interfering for the flow in cannula. Our quantitative hemodynamic analysis study provides important guidelines for venous cannulae design.

## 1. Introduction

Cannula is one of the most primary tools for cardiac surgery, especially when the extracorporeal blood circulatory device is expected. A special care should be given in design of venous cannulae because, as opposed to arterial cannulae, they generally have side holes to improve hydraulic performance in suction of blood. This is particularly important in consideration of (1) that minimizing buffer volume for venous reservoir is required for better clinical outcome and (2) that a low central venous pressure limits an active control of blood flow rate for extracorporeal devices. Considering that the improvement of venous cannulae means a more stable and higher flow under lower venous pressure condition, the optimization of the side holes parameters (size, angle, position, arrangement, shape, etc.) is to be a practical target for improving the efficacy and safety of venous cannulae. In practical medical/animal test cases, doctors frequently suffers from the reduced intake volume to the extracorporeal system due to unstable blood suction through the venous cannulae; here, it should be noted that the side holes contribute to prevention of rupture of blood vessel (obstruction of cannula) during perfusion [1]. For the evaluation of performance of cannulae, the “M-number” (or “catheter number”) has been widely used [2];

the M-number is a single dimensionless number that is based on a Reynolds friction factor correlation and describes the pressure-flow relationship in a cannula. However, it only shows the bulk performance of cannulae and does not characterize other hemodynamic local phenomena such as vortices, flow stagnation/separation, and mechanical stress. Without deep understanding and close observation on the local flow in cannula, it is hardly possible to design and evaluate the cannulae appropriately.

From that point of view, computational fluid dynamics (CFD) models have many beneficial features such as visualization of local phenomenon, solutions for all physics parameters, low cost, and fast, to name a few. Grigioni et al. proposed a full-scale computational model for a cannula with side holes to predict the mechanical blood trauma and emphasized that a small shear stress can be a possible clinical problem [3, 4]. Also Park et al. examined the effect of the number and position of side holes on flow rate and shear stress using CFD and proposed an appropriate design of venous cannula with staggered array of side holes in view point of flow rate and shear rate [5]. However, none of previous studies have shown the effect of the slant angle of side holes in venous cannulae, while the angle of cannula side holes should be included as a primary parameter for the design and the study on its effects on hemodynamics

such as local flow pattern, overall flow rate, and shear stress.

Mechanical stress and chemical agonists (e.g., platelet agonists that alter platelet shape and aggregation properties) can activate platelets and induce the release of additional platelet agonists, such as adenosine diphosphate (ADP) and thromboxane A2 (TxA2) [6]. Activated platelets, while important for wound healing, tend to stick to foreign surfaces and can cause significant problems for cannulae, valves, stents, oxygenators, tubes, and other artificial circulatory devices. Therefore, mechanical stress should be reduced as much as possible, and close observation is needed even at small shear rate (SR) values because the formation of rigid microaggregates can occur to low ADP concentrations (0.25–2.0 mmol) [3]. In addition, cumulative effects of blood cell damage can lead to clinical problems [3, 7, 8]. Thus, the results of our study of SR (Figure 5(b)) can guide the use and design of cannulae. These results show that increasing the number of side holes generally reduces the mechanical load placed on blood cells. Thus, in no side hole (NSH) cannulae, all flow proceeds from tip to outlet and all blood cells are exposed to a certain amount of mechanical load. As the number of side holes increases, a greater amount of blood joins the main stream from side holes, resulting in a reduction of exposure to mechanical load. Thus, increasing the number of side holes reduces the mean SR.

Knowing that the primary goals of cannula design is to achieve higher flow rates with lower shear stress to blood cells, here I report the effect of the angle of venous cannula side holes on flow rate, most primarily, by use of three-dimensional (3D) simulations and also studied flow patterns and shear rate distributions. Four different side hole angles (0°, 15°, 30°, 45°) and four different numbers of side holes (0, 4, 8, 12) were selected to investigate the effect of venous cannula design on function. Based on my previous study that shows a slight better performance found in staggered array of side holes [5], I adopted the staggered array for this study. For understanding the reason of the angle effect, I also proposed a new parameter, named “penetration depth (PD),” that explains a flow-mixing relationship between the main stream and the other streams from side holes. I formed a hypothesis that the smoother mixing pattern (lower PD) should be guaranteed for a better hemodynamic performance (higher flow rate and lower mechanical load) of venous cannula. Our results provide insight into the consequences of cannula design on mechanical stresses to blood cells and provide guidance for the future design of venous cannulae. Most practically, I claim that all the side holes should have a slanted feature for a better performance in clinical cases such extracorporeal circulatory system operation.

## 2. Materials and Methods

**2.1. Cannula Geometry and Computational Models.** Table 1 shows the geometrical parameters of the venous cannula used in our modeling. It was assumed that the cannula (inner diameter: 7 mm) was concentrically placed in a blood vessel of 20 mm diameter, similar to the size of the iliac vena cava [9] (Figure 1(a)). The models include no side hole model

TABLE 1: Geometrical dimensions of model cannulae and blood vessel.

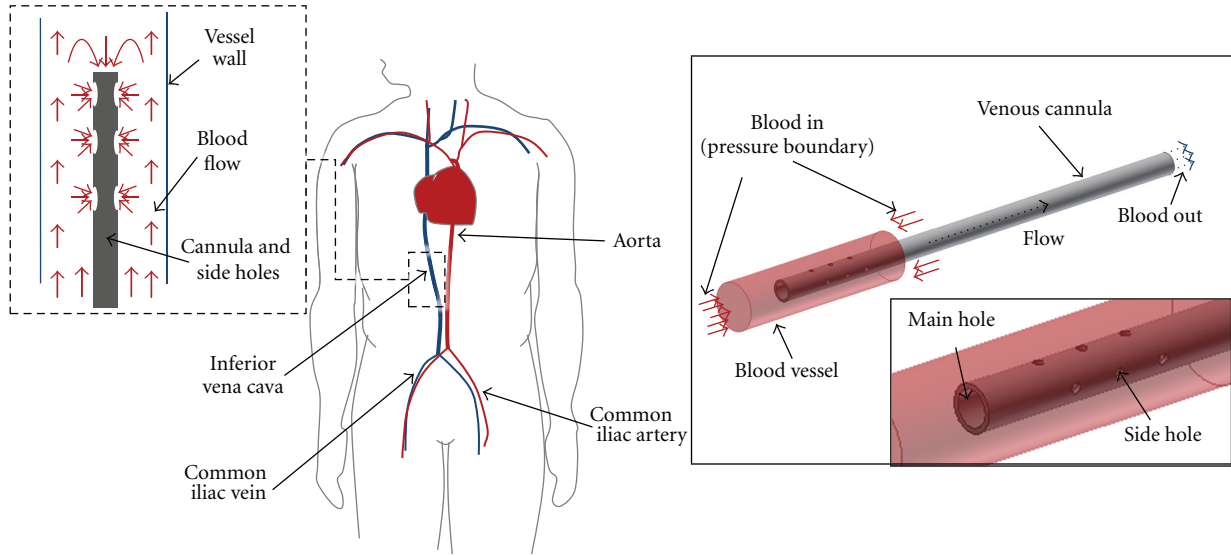
Length	200 mm
Inner diameter	7 mm
Wall thickness	1 mm
Side hole diameter	2 mm
Side hole interval	10 mm
Array type	Staggered array
Angle of side holes	0°, 15°, 30° and 45°
Number of side holes	0 (no side holes), 4, 8 and 12
Blood vessel diameter	20 mm
Blood vessel length	80 mm

(NSH) and staggered array models (SA) [5] with different numbers (4, 8, and 12) and angles (0°, 15°, 30°, and 45°) of side holes (Figure 1(b)). The angle ( $\theta$ ) represents the rotation of the hole from its original vertical position (Figure 1(c)), with the hole diameter (2 mm) kept constant. Each model was named as “number of side holes-angle of side holes” (e.g., 12H-30°) and considered 13 different cannula designs.

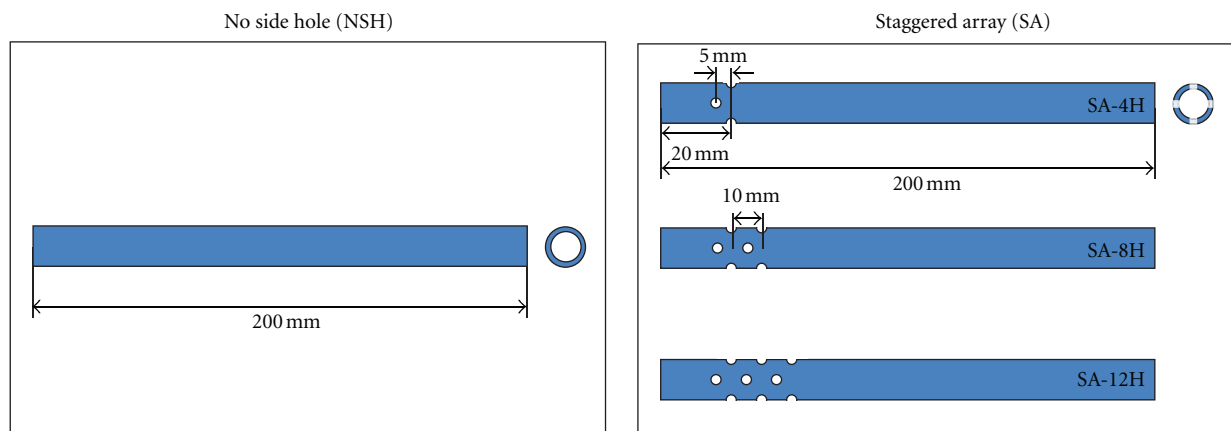
A finite volume method (FVM) model was created using a commercial program, FLUENT 6 (Fluent Inc.). In view of the cross-sectional symmetry of our cannula models, it was only necessary to simulate one-fourth of the geometry (Figure 2); a structured grid system was used for the inner cannula and pyramid/prismatic grids were used for the outer cannula region. I used the 60,000 grid counts for 12H models; typical grid spacing was about 0.2 mm near the side holes (see insets, Figure 2). It was considered a model to have converged on the result when the residuals of momentum and continuity equations reached  $10^{-12}$ .

Flow was assumed to be laminar and steady, and blood (density of 1060 kg/m<sup>3</sup>, dynamic viscosity of 0.0035 kg/m·s) was assumed to be a homogeneous, incompressible Newtonian fluid. The Navier-Stokes flow motion equations and the continuity equation were used for modeling. Gravitational effects were not considered. The pressure boundary conditions were set at the proximal/distal inlets of the blood vessel and at the outlet of the cannula (right, Figure 1(a)). The pressure at the inlet was 10 mmHg and the pressure at the outlet was 0 mmHg, making the operative pressure difference ( $\Delta P$ ) 10 mmHg. This choice of  $\Delta P$  was based on the practical reasons that the most favorable condition is when natural drainage volume is sufficient for the operation of extracorporeal circulatory system, and that the average venous pressure can be assumed to be 10 mmHg; it should be noted that the active drainage by operation of a circulatory pump system may cause higher pressure difference. Symmetric conditions were imposed to the  $xy$ -plane and the  $yz$ -plane (Figure 2). No slip boundary conditions were imposed at the blood vessel wall and at the internal and external walls of the cannula.

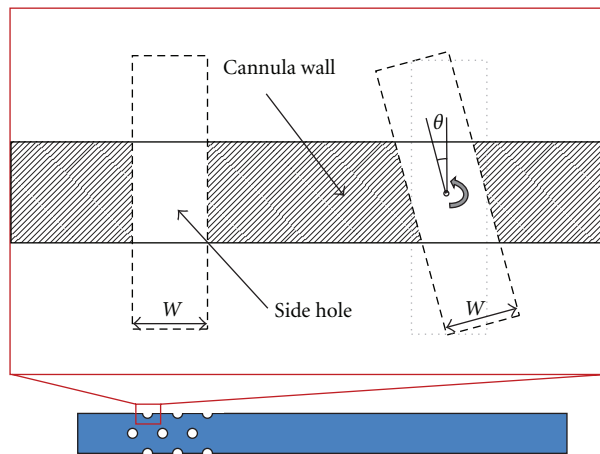
As a supportive analysis, the flow distribution within the 2D cannula models was first visualized to evaluate the effect of side hole angle (Figure 3(a)). An axisymmetric model was used and the dimensions were same as 3D models. A fixed



(a)



(b)



(c)

FIGURE 1: (a) A venous cannula inserted in the inferior vena cava was calculated (left). A computational domain was constructed in 3D (right). (b) Illustrations of cannula: NSH and SA models. (c) Cross-sectional view of side holes; left: vertically upright ( $0^\circ$ ) side hole; middle: inclined side hole of angle  $\theta$  created by rotating the upright side hole geometry; right: inclined side hole of angle  $\theta$  created by distorting the upright side hole geometry. All illustrations are not to scale except the 3D computational domain in (a).

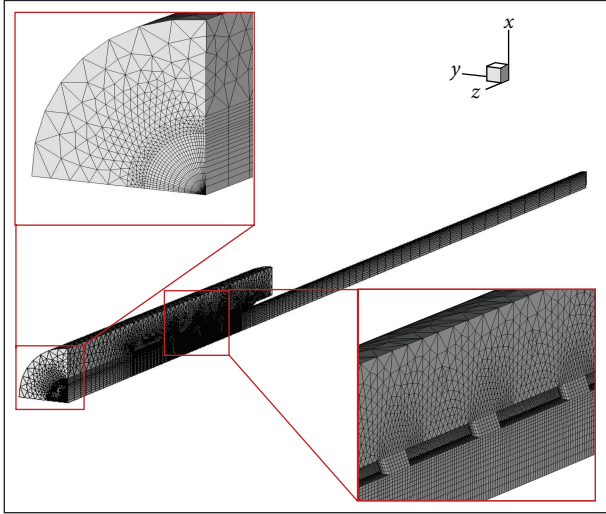


FIGURE 2: Grid system for model 12H-30° cannula. Insets show detailed views of the local mesh; pyramid grids are used for blood vessel part and structured grids for cannula. Also this figure shows that the 0.2 mm grid spacing is used near the side holes while a gradual increased spacing was applied to the distal area.

flow rate was applied to the outer inlets, while the pressure boundary was applied to the inlet of cannula.

**2.2. Shear Rate.** Apart from the flow rate, shear rate (SR), a scalar quantity, is another important hemodynamic factor that must be considered in the design and evaluation of medical devices through which blood flows. SR represents the rate of change of velocity and is equivalent to the first derivative of strain. In this paper, mean SR is a volume-averaged value of shear rates in the inner cannula space. I did not try to construct a very dense grid system to determine precise peak SR values. Mean SR appeared to be more meaningful, since the duration of maximum SR was observed only near the edge of side holes.

**2.3. Penetration Depth.** The angle of side holes may affect the direction of flow through the side holes. This flow can be described as “penetrating” the main stream, and thus disturbs the stream in the cannula. Therefore, apart from flow rate and SR, it was proposed a supportive parameter, “penetration depth (PD).” The PD is a penetrating distance of the stream coming through a side hole. Higher PD values mean that the main stream get disturbed greater by the flow streams from side holes. Therefore, the cannula design having lower PD values should be pursued.

### 3. Results and Discussion

In 2D cannula models, it was clearly showed that the angle of cannula side holes has a significant effect to the flow pattern in cannula. Corresponding to each geometry patterns (I, II, and III) shown in Figure 1(c), PD was 1.87, 1.48, and 1.29 mm (Figure 3(b)), and the flow rate was 2.83, 3.2, and 3.49 kg/s (note that this is 2D simulation). Here it was thus

found that the geometry pattern II was not efficient as III and dropped in 3D modeling studies. Note that the bigger side hole size of pattern II (than that of pattern III) may allow a higher side hole flow rate; however, it should not be interpreted as the net flow of the pattern II cannula is also higher than that of the pattern III cannula.

In 3D cannula models, it was observed the disturbing pattern of flow. Figure 4 shows the flow trajectory of a typical cannula (12H-45°); in this figure, the flow pattern outside the cannula was suppressed to clarify the flow distribution inside. The flow from side holes disturbed the main stream in the center of cannula, and thus the minimization of such disturbance should be achieved in new designs of venous cannulae. I evaluated the effect of the number and angle of side holes on cannula flow rates and SRs. As previously reported [5], the cannulae with no side holes (NSH) had the highest flow rate (2.03 L/min) (Figure 5). The flow rates of cannulae in which the side holes had no slant (0°) decreased as the number of side holes increased from 4 to 12 (blue dash-dot line, Figure 5(a)). However, by only slanting side holes, the flow rate increased about 3–5%. I also compared the SR of cannulae with different designs. NSH cannula had the highest SR ( $619 \text{ s}^{-1}$ ) (Figure 5(b)). As the number of side holes increased to 12, the SR decreased by 11%. It is clear that the SR is strongly related to the amount of flow rate, however, the higher number of side holes are effective in reducing the shear stress. In addition, although wall shear stress is not dealt with in this research directly, it should be noted that the wall shear stress level is proportional to SR level in cannulae [5].

In agreement with the results of our previous studies [5, 10], it was found that flow rates in cannulae do not increase as the number of side holes increases from 4 to 12 (Figure 5(a)). It is very important to know that side holes can contribute to the safety of the cannulae, but have no “always-positive” effect on flow rate. A counterintuitive finding was that side holes possibly contribute to the perfusion of cannulae. Our side hole models had about 6–14% lower flow rate than the control (NSH) model (inset, Figure 5(a)). This may be because side holes disturb the flow pattern, with “tangled” streamlines appearing near the side holes (Figure 4). Cannula side holes appear to adversely affect the flow rate through a cannula [5]. However, in line with the results of previous studies [5, 10], the present study shows that a greater number (12 in our models) of side holes can recover the flow rate in some degree when the high side hole angle is presented (30° and 45° in our models).

Our results showed that smoother flow pattern occurs as the angle of cannula side holes increases, resulting in higher flow rate (Figure 5(a)) and higher shear stress (Figure 5(b)). It is clear that the benefits of flow rate compensate the shear stress gained; however, a special care must be taken to minimize the shear rate. I claim that this can be achieved by slanting side hole. As the velocity contours of the 12H-45° models show (Figure 6(a)), the strength of flow from a side hole toward the center of the main stream (expressed as a PD) gets smaller from PD = 4.6 to 3.58 mm as the side hole angle increases from 0° to 15° and 45° (Figures 6(b)–6(d)). A deeper penetration of this flow will decrease the

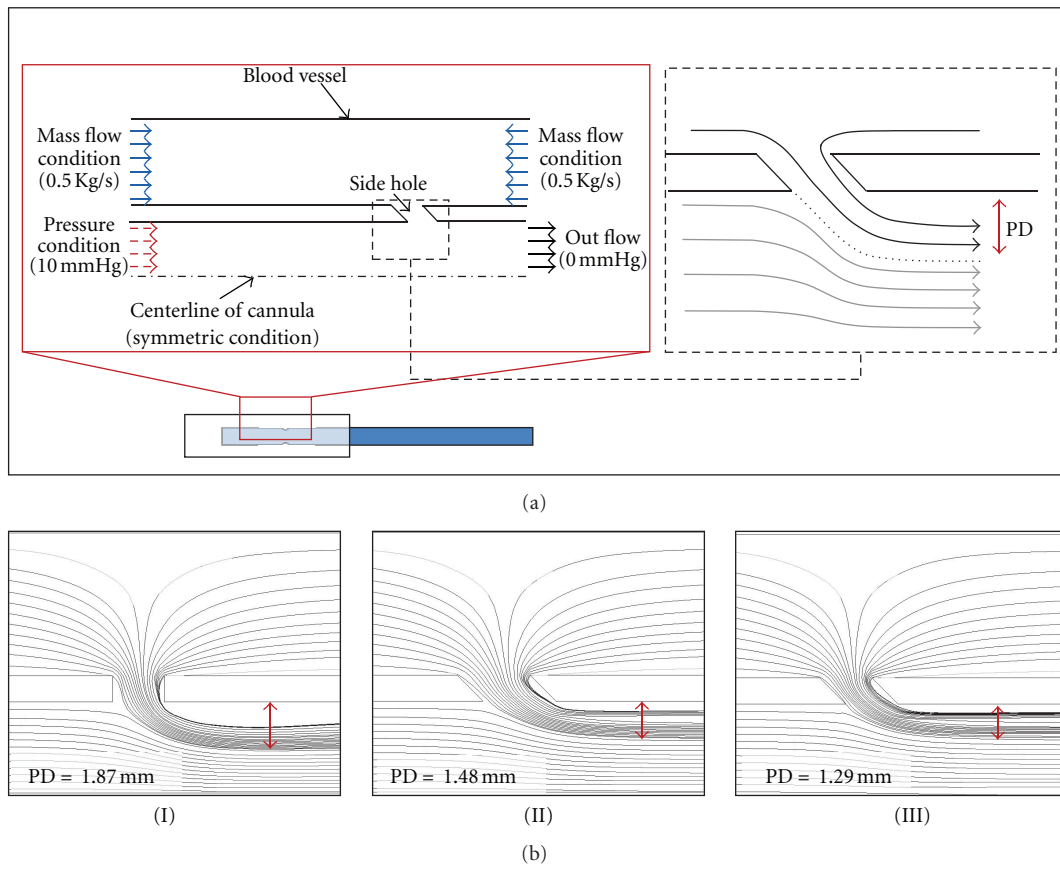


FIGURE 3: 2D simulation results. (a) 2D computational geometry was constructed using the same dimensions from 3D model. However, to show clearly the effect of PD, different boundary conditions were applied; same pressure boundary was applied to the cannula inlet, and mass flow boundary was applied to the inlets from the blood vessel. (b) Therefore, the flow through the main inlet of cannula tip is dependent on PD value. By changing the angle to  $45^\circ$ , more amount of flow can be transferred to the main stream while the same flow rate is supplied through the side holes because of the application of mass flow inlet condition at the vessel part. Note that “I, II, and III” are the corresponding notations used in Figure 1(c).

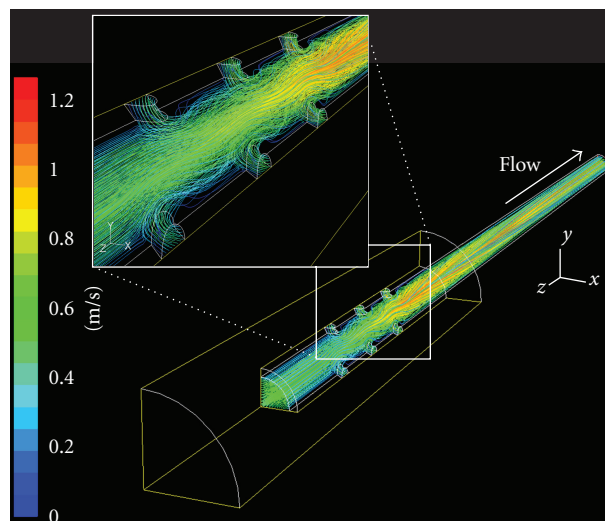


FIGURE 4: Streamlines of  $12H-45^\circ$ , with noticeable disturbance near the side holes. Inset shows detailed features of the entangled streamlines near the side holes.

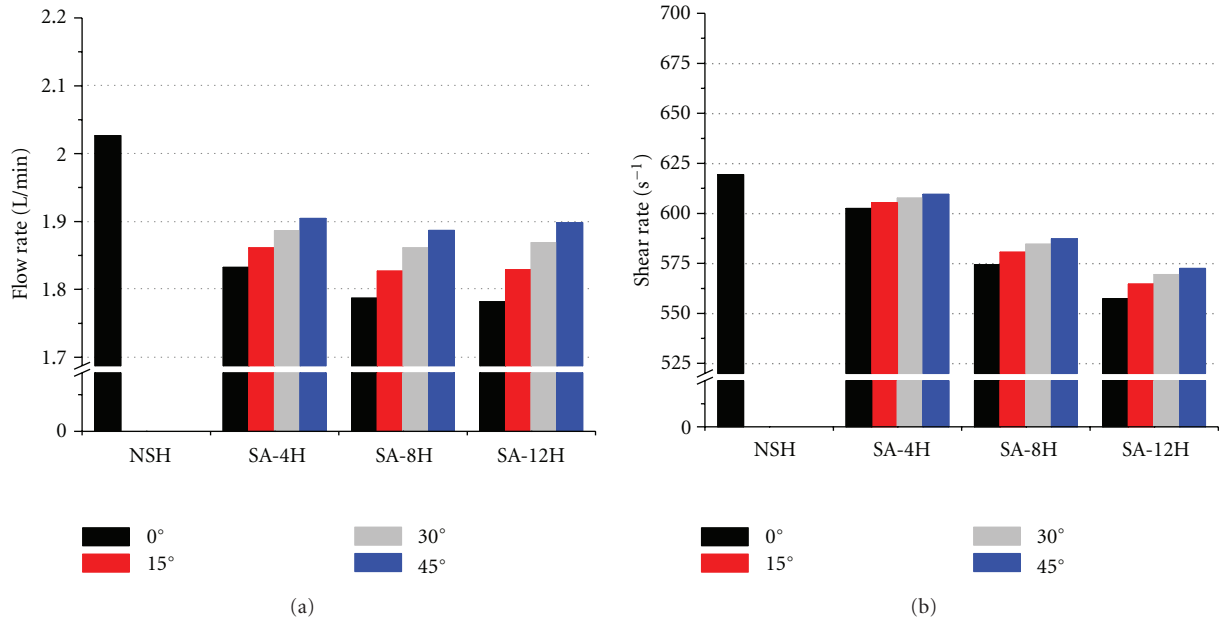


FIGURE 5: (a) Flow rates through different SA cannula models (inset shows the reduction of flow rate for each model compared to the NSH model). (b) Shear rates through different SA cannula models (inset shows the reduction of shear rate for each model compared to the NSH model).

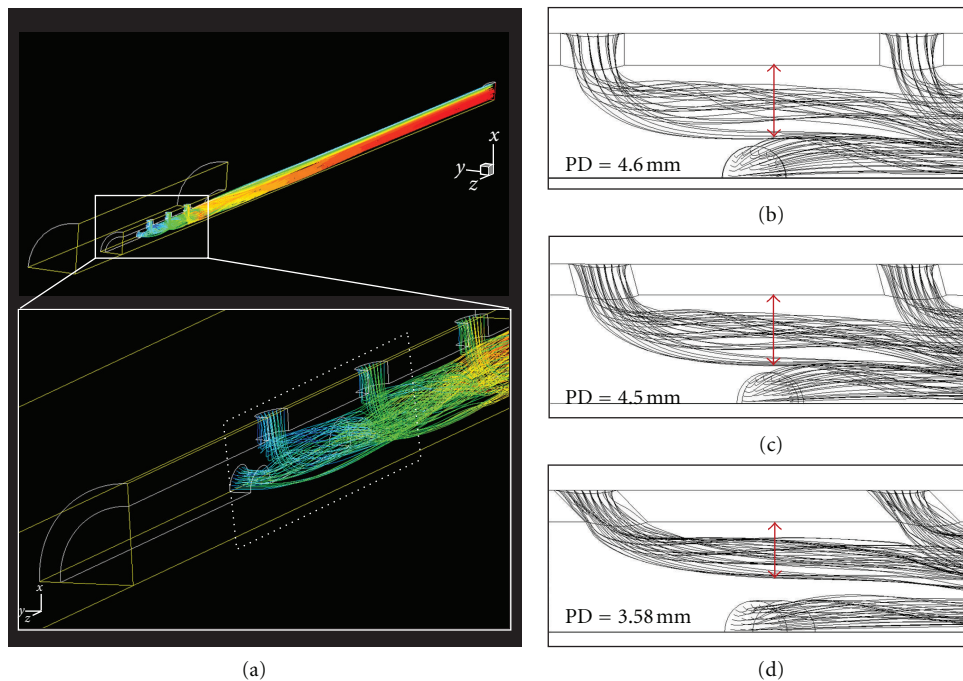


FIGURE 6: Effect of slanted side angle. (a) A typical model, 12H-45°, is presented to show the flow path distribution from the side holes. Inset is the zoomed feature near side holes. (b–d) PD reduces as the side hole angle increases, resulting in higher flow rate.

net flow rate through a cannula, and this is accompanied by a flow rate increase from 1.78 to 1.9 L/min. PD is inversely proportional to the side hole angle, resulting in an increased flow rate for more sharply angled side holes. This also applied to all of our other models with side holes. Thus, PD can be used to determine the effect of the side hole parameters

on flow through a cannula. Table 2 shows the PDs in each model.

With regard to flow rate, the best cannula design is the NSH model. However, since side holes allow for safer implementation of cannulae, cannulae with 4–12 side holes appear to be good alternatives. The SRs of the 12H-0°

TABLE 2: Penetration depth in cannula models.

Cannula model	PD
4H-0°, -15°, -30°, and -45°	4.8, 4.62, 4.4 and 3.65 mm
8H-0°, -15°, -30°, and -45°	4.7, 4.6, 4.35 and 3.6 mm
12H-0°, -15°, -30°, and -45°	4.6, 4.5, 4.32 and 3.58 mm

cannula ( $557.2 \text{ s}^{-1}$ ) were the lowest. Ideal cannula design/use may depend on the unique requirements imposed by specific clinical situations. However, the 12H-45° cannula seems to have the best design for general use because it is associated with minor loss in flow rate and has moderately small SRs (Figure 5(a)).

Our study has several limitations. First, it was assumed a steady-state system with constant pressure boundary, concentrically poised cannula, and rigid blood vessel walls. I suggest that the especially the elasticity of the blood vessels be considered in future work because this can affect the rupture and closing of cannula side holes. Regardless, the general conclusions of our quantitative comparative study about the number and angle of cannula side holes remain valid.

#### 4. Conclusion

In this study, 3D numerical analysis was used to investigate the effect of the angle of side holes. The primary target of our study is to improve the blood flow rate by slanting the side hole, and this can be additionally adapted with any other major improvement in cannula designs, and thus, I claim that all the side holes should be equipped at a hydrodynamically designed angle for better clinical outcomes. It cannot be too emphasized when considering that it can be a life-threatening problem for patients during medical operations. In particular, our study has two significant findings. First, when the side hole angle was 0°, a smaller number of side holes was associated with higher flow rate, while a larger number of side holes was associated with reduced mechanical SR. Second, when the side hole angle is 45°, a larger number of side holes allow a higher flow rate and greater reduction of SR. Therefore, there appear to be definite advantages of venous cannulae with a large number of side holes at an acute angle. I suggest that cannula design also depends on the clinical features of individual cases and should be based on a deeper understanding of cannula hemodynamics. Further study should be continued for improvement other parameters such as side hole shape and spacing.

#### Conflict of Interests

The authors declares no conflict of interests.

#### Acknowledgment

This study was supported by Chung-Ang University grant (2011).

#### References

- [1] A. P. Simons, Y. Ganushchak, P. Wortel et al., "Laboratory performance testing of venous cannulae during inlet obstruction," *Artificial Organs*, vol. 32, no. 7, pp. 566–571, 2008.
- [2] J. P. Montoya, S. I. Merz, and R. H. Bartlett, "A standardized system for describing flow/pressure relationships in vascular access devices," *ASAIO Transactions*, vol. 37, no. 1, pp. 4–8, 1991.
- [3] M. Grigioni, C. Daniele, U. Morbiducci et al., "Computational model of the fluid dynamics of a cannula inserted in a vessel: incidence of the presence of side holes in blood flow," *Journal of Biomechanics*, vol. 35, no. 12, pp. 1599–1612, 2002.
- [4] M. Grigioni, C. Daniele, U. Morbiducci, G. di Benedetto, G. D'Avenio, and V. Barbaro, "Potential mechanical blood trauma in vascular access devices: a comparison of case studies," *International Journal of Artificial Organs*, vol. 25, no. 9, pp. 882–891, 2002.
- [5] J. Y. Park, C. Y. Park, and B. G. Min, "A numerical study on the effect of side hole number and arrangement in venous cannulae," *Journal of Biomechanics*, vol. 40, no. 5, pp. 1153–1157, 2007.
- [6] P. Tandon and S. L. Diamond, "Hydrodynamic effects and receptor interactions of platelets and their aggregates in linear shear flow," *Biophysical Journal*, vol. 73, no. 5, pp. 2819–2835, 1997.
- [7] K. K. Yeleswarapu, J. F. Antaki, M. V. Kameneva, and K. R. Rajagopal, "A mathematical model for shear-induced hemolysis," *Artificial Organs*, vol. 19, no. 7, pp. 576–582, 1995.
- [8] R. Zimmer, A. Steegers, R. Paul, K. Affeld, and H. Reul, "Velocities, shear stresses and blood damage potential of the leakage jets of the Medtronic Parallel(TM) bileaflet valve," *International Journal of Artificial Organs*, vol. 23, no. 1, pp. 41–48, 2000.
- [9] M. R. Prince, R. A. Novelline, C. A. Athanasoulis, and M. Simon, "The diameter of the inferior vena cava and its implications for the use of vena caval filters," *Radiology*, vol. 149, no. 3, pp. 687–689, 1983.
- [10] H. D. Polaschegg, K. Sodemann, and B. Estabrook, "Investigation of the effect of catheter side holes on flow properties and outwash of the locking solution," in *Proceedings of the 2nd Symposium on Angioaccess for Hemodialysis*, vol. 195, Vascular Access Society, Maastricht, The Netherlands, 1999.